Gesellschaft für Anlagen- und Reaktorsicherheit (GRS) mbH

Impact of climate change on far-field and biosphere processes for a HLW-repository in rock salt

GRS - 241

Gesellschaft für Anlagen- und Reaktorsicherheit (GRS) mbH

Impact of climate change on far-field and bisophere processes for a HLW-repository in rock salt

Ulrich Noseck
Christine Fahrenholz
Eckhard Fein
Judith Flügge
Gerhard Pröhl
Anke Schneider

März 2009

Remark:

This report, with the German title „Wissenschaftliche Grundlagen zum Nachweis der Langzeitsicherheit von Endlagern (Kurztitel WiGru5)“, was prepared under the contract No. 02 E 9954 with the Federal Ministry of Economics and Technology (BMWi).

The work was conducted by the Gesellschaft für Anlagen- und Reaktorsicherheit (GRS) mbH.

The authors are responsible for the content of this report.

GRS - 241
ISBN 978-3-939355-15-1

Keywords:
biosphere, climate, climate change, glacial, hydrogeology, interglacial, permafrost, radioactive waste, safety assessment, transport

Preface

The assessment of the long-term safety of a repository for radioactive or hazardous waste requires a comprehensive system understanding and capable and qualified numerical tools. All relevant processes which contribute to mobilisation and release of contaminants from the repository, transport through the host rock and adjacent rock formations as well as exposition in the biosphere have to be implemented in the programme package. The objective of the project “Scientific basis for the assessment of the long-term safety of repositories”, identification number 02 E 9954, was to follow national and international developments in this area, to evaluate research projects, which contribute to knowledge, model approaches and data, and to perform specific investigations to improve the methodologies of the long-term safety assessment.

This project, founded by the German Federal Ministry of Economics and Technology (BMWi), was performed in the period from 1st November 2004 to 31st July 2008. The results of the key topics investigated within the project are published in the following reports:

GRS-report 222: About the role of vapour transport during bentonite re-saturation

GRS-report 238: Elemente eines Safety Case zur Realisierung eines Endlagers in Deutschland

GRS-report 239: Chemical effects in the near field of a HLW repository in rock salt

GRS-report 240: Safety and Performance indicators for repositories in clay and salt formations

GRS-report 241: Impact of climate change on far-field and biosphere processes for HLW repositories in rock salt

GRS-report 242: Gase in Endlagern im Salz

The results of the whole project are summarised in the overall final report:

GRS-report 237: Assessment of the long-term safety of repositories. Scientific basis

Acknowledgment

We thank Antje Schwalb, Klaus-Dieter Meyer and Andrey Ganopolski for fruitful discussions and helpful comments.

Contents

1 Introduction

An essential part of demonstrating long-term safety in safety case for a repository with radioactive wastes is the long-term safety analysis which uses numerical models for the description of possible evolutions of the repository system, so-called scenarios. These model calculations are aimed at achieving a comprehensive understanding of the system behaviour and determining potential consequences for the population.

Due to the high radiotoxicity of the wastes over very long periods of time, correspondingly long periods are to be considered. For the German safety criteria, it was proposed that the safety case should cover a period of about 1 million years. Within such periods, extreme climate changes may occur. At the national as well as at the international level, there is agreement that the occurrence of extreme climatic conditions, as for example ice ages, must not impair the integrity of a repository system /AKE 02/. Accordingly, the effects of climatic changes are already considered in some safety cases for repositories in deep geological formations (e.g. /SKB 06/, /NAG 02/, /OND 01/). So, for example, in Swedish and Belgian studies, scenarios were identified for the effects of climatic changes, respective conceptual models developed and consequence calculations performed.

The aim of this study is to assess, for the first time, the effects of climatic changes on a hypothetical repository in salt at a potential site in Northern Germany. For this purpose, the main factors influencing the climate and today's global distribution of climate zones are indentified in a first step. In a second step, data are gathered about ancient climates and their impacts on the reference site. Due to the numerous geological and hydrological studies at the Gorleben site, this area was chosen as reference site for this study.

In addition to the available paleoinformation, the capacity of climate models applied today is discussed and literature results of simulations over correspondingly long periods are presented. The climate model calculations are affected by large uncertainties due to the various factors influencing the climate and their extremely complex coupling. This is why special importance is attached to paleoclimatology. Due to the large uncertainties in parameter assignment of the climate models, this model study mainly aims at the understanding of the processes taking place during climate change at the reference site and their key factors as affecting radionuclide migration in the repository system.

For a normal evolution of a repository for heat generating waste, where a complete confinement of the waste is reached by closure of all void volumes and transport pathways,

the processes considered here are not relevant. However, in a safety case also altered scenarios with radionuclide mobilisation and release from the host rock need to be considered. The consequences of changed climate conditions on processes and effects in the overburden of the salt dome and the biosphere are expected to be highest and are investigated here.

At first, conceptual models describing the effects of potential climatic changes on processes in both parts of the repository system are developed. For flow and transport in the overburden, the conceptual models are implemented in the codes d^3f /BIR 04/, /FEI 99/ and r^3t /FEI 04/ and exploratory calculations performed for selected climate conditions. For the biosphere, dose conversion factors for potential climate conditions are determined by means of mathematical models. Finally, the results are interpreted regarding the effects of climatic changes on the long-term safety of a potential German repository.

2 The climate

2.1 Definition and classification

The term climate refers to the average conditions of the atmosphere over a long period time of some ten, typically 30 years. It is described by mean values and totals of selected parameters, such as average monthly or annual temperatures and annual precipitation totals. Their evaluation is performed for the place of their measurement in form of climate diagrams and, from a larger perspective, leads to the division of the Earth into climate zones. One possible way of describing different climates is the classification according to the so-called Köppen-Geiger scheme. Here, the climates are subdivided into climate zones, climate types and climate subtypes (see Tab. 1).

Tab. 1 Potential combinations of climate zone, climate type and climate subtype

Climate zone	A	B	C, D	E
Climate type	f, m, s, w	W, S	f, w, s	T, F
Climate subtype		h, k	a, b, c, d	

The climate zone refers to the fundamental properties of the climate and includes, in particular, information on temperature zones (see Tab. 2).

Tab. 2 The Köppen-Geiger climate zones

Climate zone	Climate	Parameter thresholds
A	tropical climates	all monthly means > 18°C
B	arid climates	precipitation below the humid/arid boundary for year-round precipitation: annual precipitation [cm] < $2\cdot(T_a+7)$ summer precipitation: annual precipitation [cm] = $2\cdot(T_a+14)$ winter precipitation: annual precipitation [cm] = $2\cdot T_a$
C	warm temperate climates	temperatures of the coldest month: -3°C to 18°C. temperature of the warmest month: > 10°C.
D	boreal or snow forest climates	temperature of the coldest month: < -3°C temperature of the warmest month: > 10°C.
E	snow and ice climates	average temperature of the warmest month: < 10°C
T_a average annual temperature		

The climate zones are further differentiated by climate types under consideration of amount and distribution of the precipitations (see Tab. 3). An important criterion is the number of the humid months, i.e. those in which the average monthly precipitation is higher than its

potential evaporation. The potential evaporation is the maximum possible evaporation under the given meteorological conditions. If the average precipitation in a month is less than its evaporation, these months are referred to as arid.

Tab. 3 Climate types according to Köppen-Geiger

Climate type	Parameter thresholds
S	semi-arid steppe climates > 2 humid months
W	desert climates 1 to 2 humid months = semi-desert not humid months = desert
f	moist year round all months > 60 mm precipitation
M	rain forest > 1 month < 60mm and $> \frac{100mm - annual\ precipitation}{25}$
s	summer dry summer precipitation < 40 mm and less than 1/3 of precipitation sum of the wettest month
w	winter dry climate zone C and D: average precipitation of the driest winter month $< \frac{1}{10}$ of the precipitation of the wettest month climate zone A: at least one month < 60mm precipitation
T	tundra: warmest month > 0°C
F	permafrost: warmest month < 0°C

Further division into climate subtypes is ensured by addition of a third letter. This letter refers to the average temperatures of the warmest but also coldest months (see Tab. 4). Fig. 1 shows today's world-wide distributions of the respective climates according to the Köppen-Geiger classification.

Tab. 4 Climate subtypes according to Köppen-Geiger

Climate subtype	Parameter thresholds
h	warmest month > 18°C
k	warmest month < 18°C
a	warmest month > 22°C and > 4 months > 10°C
b	warmest month < 22°C and > 4 months > 10°C
c	< 4 months > 10°C and coldest month > -38°C
d	< 4 months > 10°C and coldest month < -38°C

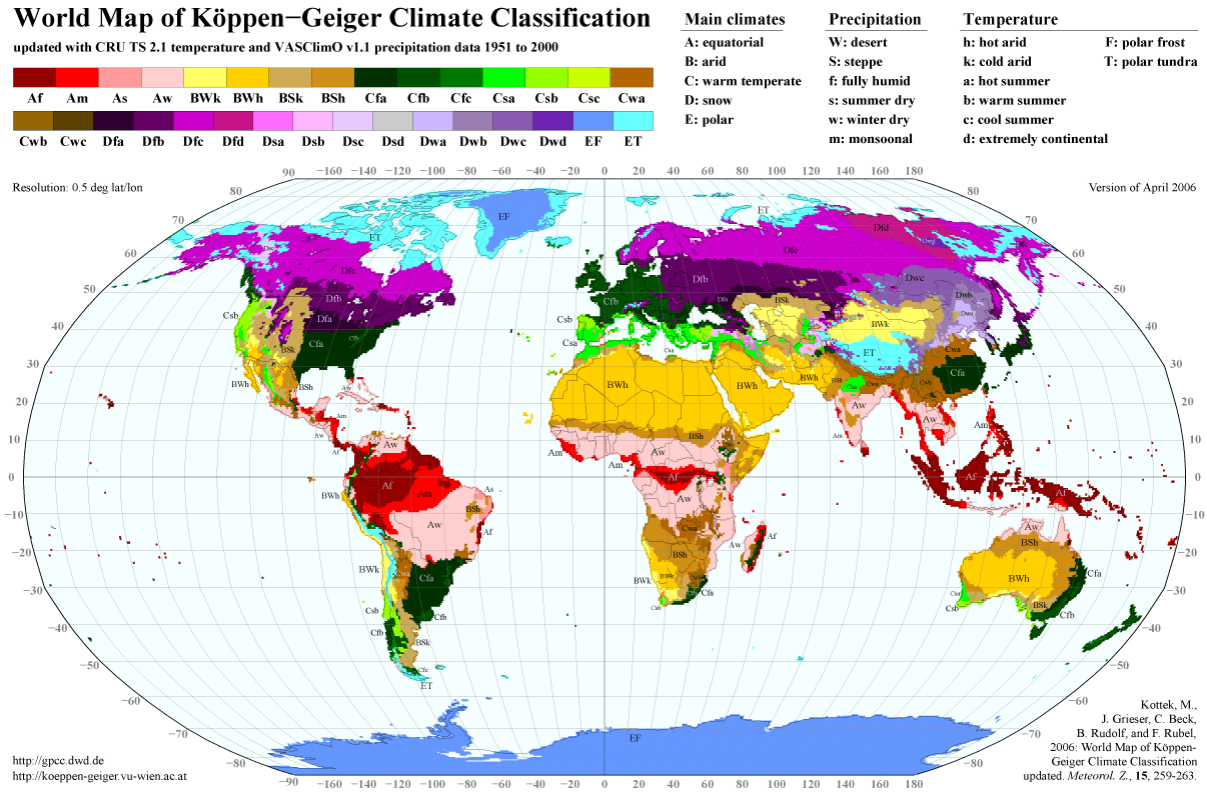

Fig. 1 Climate zone classification according to Köppen und Geiger /VUW 08/

2.2 Influence of the climate on the biosphere

Climate influences vegetation dynamics directly by the climatic parameters temperature, precipitation and evapotranspiration and also indirectly by the soil-forming processes and their intensity. Due to the positive feedback loops between biomass production and soil formation, the annual length of the vegetation period and the amount of air and soil moisture are key factors of soil and vegetation formation. A profile of the pole to the equator in

Fig. 2 gives a rough overview of the dependencies between the climate factors average annual temperature, evapotranspiration and the annual precipitation total, the depth and type of weathering processes and the existing natural vegetation.

Weathering of the igneous rock and thus soil depth increase with increasing soil moisture, which is highest in savannah and rain-forest regions. Lowest soil formation is found in steppe and desert areas with lowest amount of precipitation. The fertility of the soil can only be explained in part by its moisture, since the depth to groundwater as well as soil structure, type of igneous rock and depth and type of the humus layer are of influence.

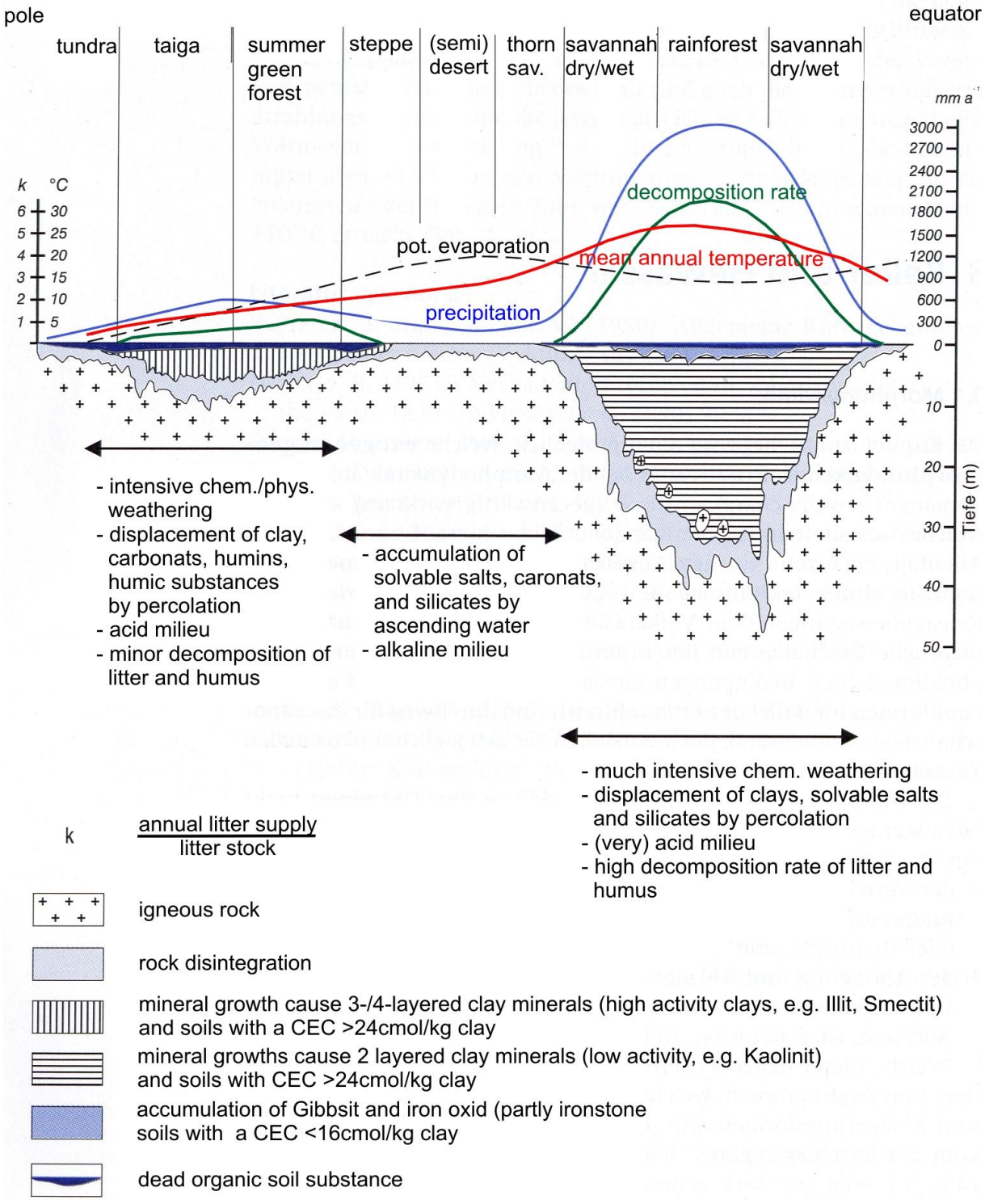

Fig. 2 Soil development and vegetation in relation to the climate /SCH 02/

2.3 Climate archives: witnesses of ancient climates

The basis of each climate prediction is the understanding of the processes and mechanisms regarding climatic changes in the geological past. Series of weather data measurements started only 250 years ago at the earliest. The characterisation of ancient climates is therefore based on so-called climate archives. Their evaluation with regard to long-ago environmental changes is the only way to obtain information about changes in the atmosphere, the ocean, the cryosphere, the biosphere, its dynamic and interaction older than any instrumental and historical records. For this purpose, the archives therefore have to allow the reconstruction of continuous time series of climate indicators which date back with high temporal resolution of years to centuries. In this respect, the following archives are of great importance:

- **Ice cores:** In particular, the ice cores from Greenland and the Antarctic form the basic framework of today's investigation of ancient climates due to their annual layers resulting from different ice crystal sizes in summer and in winter. Cores from Greenland cover a time window of up to about 100,000 years BP. Longer time scales are available with the cores from the Antarctic with time windows of 420,000 years for the Vostok core and 800,000 years for the Dome C core /JOU 07/. In addition to the ice cores from Greenland and the Antarctic reaching back into the past over an extremely long period of time, investigations also extend to inland glaciers and ice caps, e.g. in the Himalaya /DUA 07/, the Kilimanjaro /THO 03/ or the Andes /THO 03/. However, the information obtained by it, only date back to about 25,000 years at the earliest /SCH 07b/. From the thicknesses of the annual layers conclusions can be drawn on the past precipitation amounts. The content of greenhouse gases of air bubbles trapped in ice show their concentration in the past atmosphere. The ratio between the heavy and light oxygen isotope, $\delta^{18}O$, and hydrogen isotope, $\delta^{2}H$, in the H_2O gives information about the average air temperature at the time of the snowfall. Material blown into the ice layers, such as ashes and dust, give indications to wind direction and strength in the past, trapped seaweeds and their outgassing may be an indication to their changing living conditions /ALL 02/.

- **Tree rings:** The reconstruction of the Holocene climatic changes on the continents is mainly based on tree rings. They give information over a period of about 1,000 years. The data are obtained from the radial growth and the carbon isotopic composition, $\delta^{14}C$.

- **Coral reefs:** The information contained in them might be used for a period of up to several 100,000 years. Sea level changes can be determined by means of location and height of coral reefs if the land uplift rates of the region in the past are known. The age of

the corals is typically determined by means of the isotopic contents of the uranium decay series.

- **Ocean and lake sediments:** For the identification of climate changes for the different ocean basins in high temporal resolution, ocean sediment cores are the only archives. They serve the reconstruction of variations in ocean temperature, in salt content, the flow conditions and the biological production. The ocean sediments give information over a long period of about 1,000 to hundred million years. The temporal resolution depends, above all, on the annual accumulation rate of the sediments on the seabed. High sedimentation rates, partly with a temporal resolution in the range of years, are found in river deltas, fjords and deep basins in areas near the continents. There are layered sediments (varves) and non-layered sediments. Further, the ice volume of the glaciers can be determined from the abyssal sediments. Since the oxygen isotopic composition is a function of the temperature and the ice volume, the ice volume is determined by determination of $\delta^{18}O$ contents, in particular in calcareous organisms, such as foraminifera, ostracods and molluscs. The necessary information on the temperature of the deep ocean can be determined independently from this by means of the Mg/Ca ratio in the carbonates of the sediments. The sea level change derived from the ice volumes are calibrated by means of the height of coral banks (see above).
  Lake sediments are the most important archives of recent interglacials and give information for a period of 10 to 10,000 years BP. Special places of discovery are located in Bispingen and Quakenbrück /MEY 94/ in Lower Saxony.

Further, but less exploitable climate archives, are loess profiles and stalagmites. Loess is formed during cold periods by deposition of wind-transported very fine-grained material, mainly silt and fine sand. However, the profiles formed seldom reach a temporal resolution of years. From the stalagmites, in particular the oxygen isotope signals from the different stages of growth of the carbonate precipitated from the groundwater are used.

Thus, tree rings, ocean and lake sediments, ice cores and coral cores are archives allowing annual resolution. Due to the availability of climate archives always with high resolution, as e.g. the anoxic sediments and drift sediments from the North Atlantic in the Cariaco Basin and the Santa Barbara Basin, even shorter periods and also cyclic Holocene climate changes could be identified on time scales of few decades to centuries. The possible time spans of the climate archives are illustrated in Fig. 3.

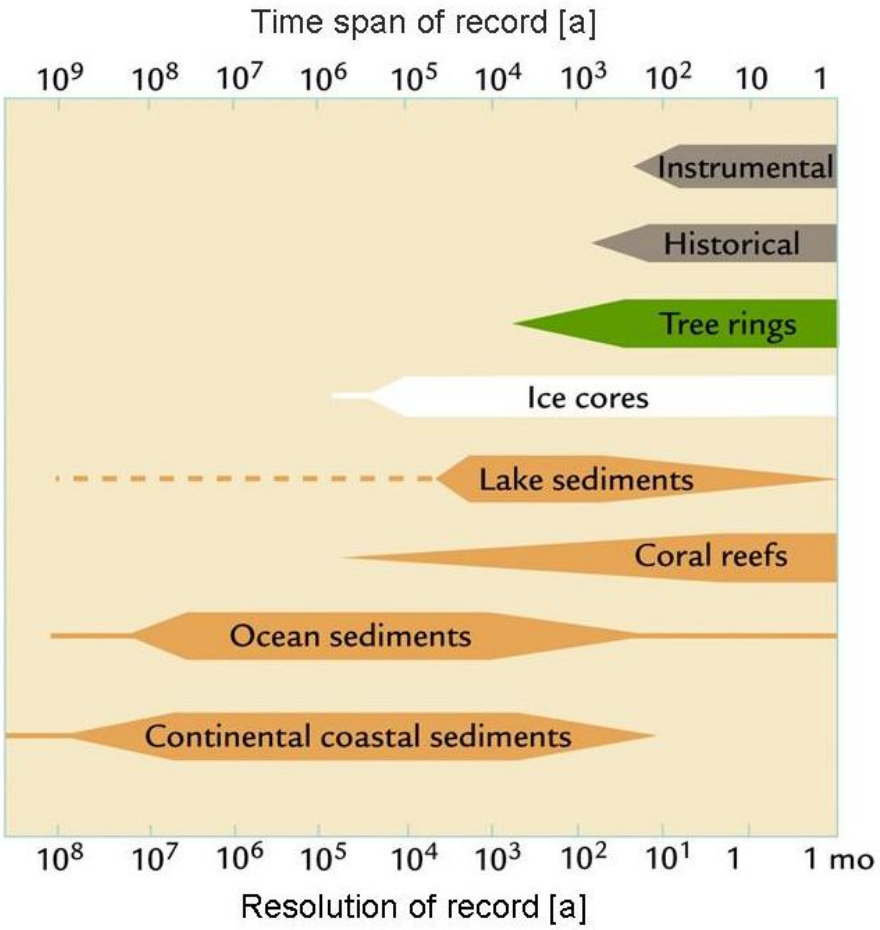

Fig. 3 Time spans of climate archives (according to /RUD 01/)

2.4 Factors influencing climate

Earth's climate is the expression of complex interactive effects between external and internal factors. The primary factors influencing the climate and its changes are known. The secondary factors, however, which intensify or weaken the primary ones, their interaction and mutual influence as well as their effects on the climate, in many cases are only clarified to a certain extent. In summary, it can be stated that one factor alone is not sufficient to explain the occurrence of ice ages. Only the interaction of the factors described may cause such a climate change. An overview of the main processes influencing the climate, the time span during which these processes are effective and their significance for the long-term safety analysis are presented in Tab. 5.

Tab. 5 Important factors of climate formation, time span during which they are effective and significance for the long-term safety analysis /BIO 01b/

Time [a]	10^{-1}	10^{0}	10^{1}	10^{2}	10^{3}	10^{4}	10^{5}	10^{6}	10^{7}	10^{8}	10^{9}	PA relevant
Galactic dust										■	■	No
Earth orbit parameter						■	■	■				Yes
Solar activity	■	■	■	■	■	■	■	■	■			No
Plate tectonics and polar								■	■	■	■	No
Isostasy						■	■	■	■	■	■	Yes
Atmospheric dust and aerosols		■	■	■	■							Yes
Ocean circulation					■	■	■	■	■	■		Yes
Atmosphere/ ocean/ice/land feedback loops	■	■	■	■	■	■						Yes

2.4.1 Primary factors

Those factors are referred to as primary ones which decisively determine the climate and its trend. Long-term effects, i.e. such effects whose influence mainly concern time spans > 10,000 years result from the orbital constellation, the distribution of the continents on Earth, the isostasy and the ocean circulation. In addition to solar phenomena, short-term changes are caused, for example, by dust and aerosols and also by feedback loops between atmosphere, ocean, ice and land.

2.4.1.1 Orbital constellation

This comprises all astronomical factors causing solar irradiance changes, thus influencing the climate by their effect on the character, length and differences of the seasons. At least the Quaternary climate cycles were mainly determined by astronomical factors /RAH 07/. These astronomical factors show typical periodicities by which their effect on the climate may be increased or reduced, thus becoming predictable with some degree of certainty. These factors are the **eccentricity of the Earth's orbit**, the **precession** and the **obliquity** of the

Earth. The changes of these orbital parameters, the resulting change of the solar energy flux density and the impact on the onset of ice ages were described for the first time by the Milankovitch theory. In the following, the different parameters and their effects on the climate are explained more detailed:

Eccentricity is a measure for the deviation of the elliptical and the circular orbit. Due to the elliptical movement of the Earth and the fact that the sun is not in the centre of this ellipse, the Sun-Earth distance currently varies between about 152.1 million km (aphelion, at the beginning of July) and 147.1 million km (perihelion, at the beginning of January) (see Fig. 4). The faster movement of the Earth at the closest point to the Sun (perihelion) currently leads to a shorter winter and a longer summer in the northern hemisphere. The influence on the climate also results from the solar irradiance which varies with the Sun-Earth distance. The eccentricity of the orbit may correspond to values between 0.054 and 0.001 /IMB 80/. The main period of eccentricity variations between these two extreme values is about 100,000 years. At present, the eccentricity of the orbit is 0.017 and slightly decreases due to the gravitational influences of the surrounding planets. In the next 25,000 years, this tendency will continue which will lead to an increasing equalisation of the lengths of the seasons on Earth /BER 02/.

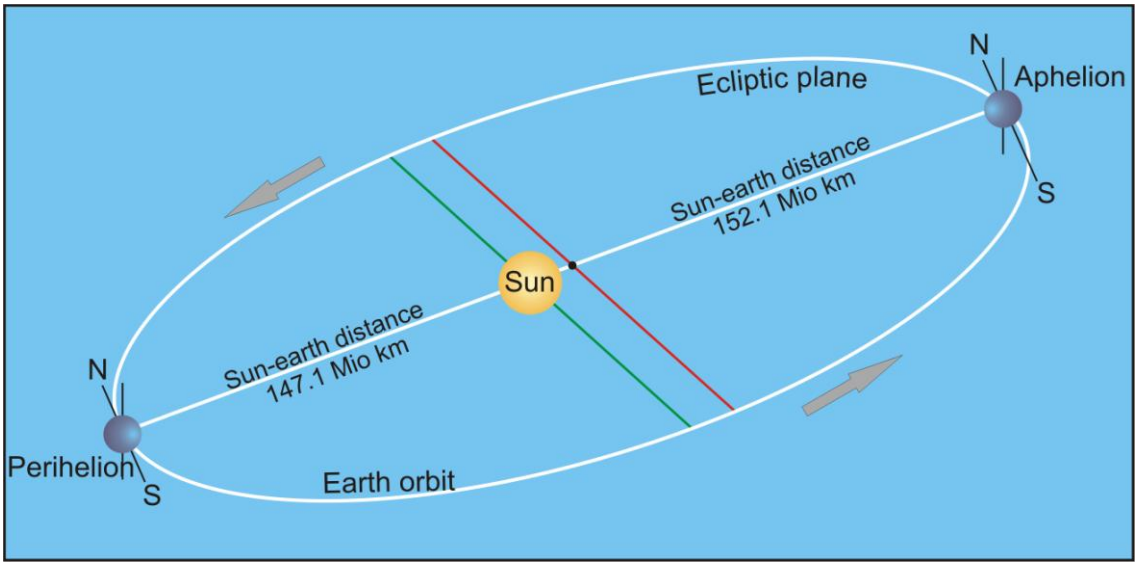

Fig. 4 Eccentricity of the Earth's orbit

Precession is defined as the compensating movement in form of a circular motion of the Earth caused by the torque resulting from the gravitational force of the Moon and the Sun (see Fig. 5). It takes about 26,000 years for the axis of the Earth to complete one full circle. It depends on the precession in which season perihelion and aphelion occur. At present, the

Earth is at perihelion around the winter solstice (see above), whereas it was at aphelion towards the end of the last ice age.

The fact that the Earth's axis is not perpendicular to its orbital plane is referred to as **obliquity of the ecliptic** and is the cause of the seasons. The obliquity of the ecliptic varies within a period of about 40,000 years and with an amplitude of about 1° around a mean value of about 23°. The obliquity of the Earth's axis relative to its orbital plane is about between 24°36' and 21°55' and has an influence on the strength of the seasons: the greater the angle, the greater the contrast between the seasons. Ice ages may occur if the angle is small since under these conditions the solar irradiance in summer in high northern latitudes is smaller (see below). At present, the tilt of the Earth's axis is 23°27' and decreases by about 0.47'' per year which leads to a decreasing contrast between the seasons. Fig. 5 illustrates the processes.

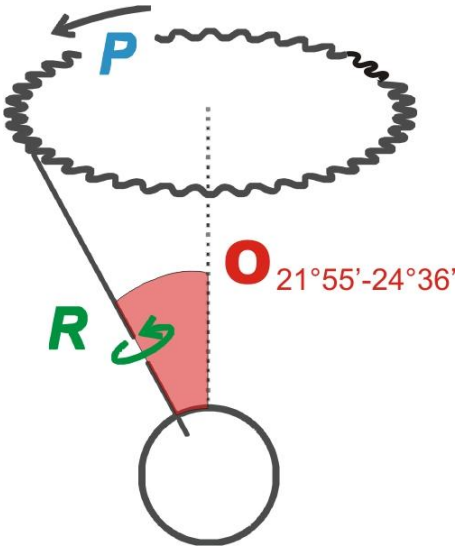

Fig. 5 Precession (P), spin (R) and obliquity (O) of the Earth

The **solar constant** is defined as radiation energy of the sun above the atmosphere per unit time and unit surface. The World Meteorological Organisation defined 1,367 W/m^2 as mean value of the solar constant. The solar constant varies, depending on the distance between the Sun and the Earth, between 1,325 W/m^2 and 1,420 W/m^2 as stated above. The changes due to astronomic factors are also referred to as Milankovitch cycles after their discoverer. Additionally short-term changes with cycles of 11 years occur due to the variation of the solar activity.

The Milankovitch theory includes the assumption that the insolation in the northern hemisphere in summer is a critical factor for the occurrence of ice ages. This assumption was based on the fact that below a certain temperature decreasing insolation does not melt the snow and ice formed during winter. Indeed, the Quaternary climate changes show, at least for the last 800,000 years, that the occurrence of ice ages closely correlate with minima of insolation in summer at 65° northern latitude (see e.g. /ARC 05a/, /RUD 01/). Fig. 6 shows the time evolution of the orbital parameters and the resulting variation of insolation in June at 65° northern latitude for the next one million years /BIO 01b/. Over the next 100,000 years, the amplitude of insolation will be relatively small with a variation of 25 W/m^2 for the next 50,000 years. Compared to this, the amplitude between 125,000 and 115,000 years BP (not shown) was about 100 W/m^2 /BER 02/. This small amplitude of insolation variation is exceptional and due, among others, to the small eccentricity in the next tens of thousands of years. It is only comparable with the interglacial that occurred between 420,000 and 400,000 years BP /BER 02/.

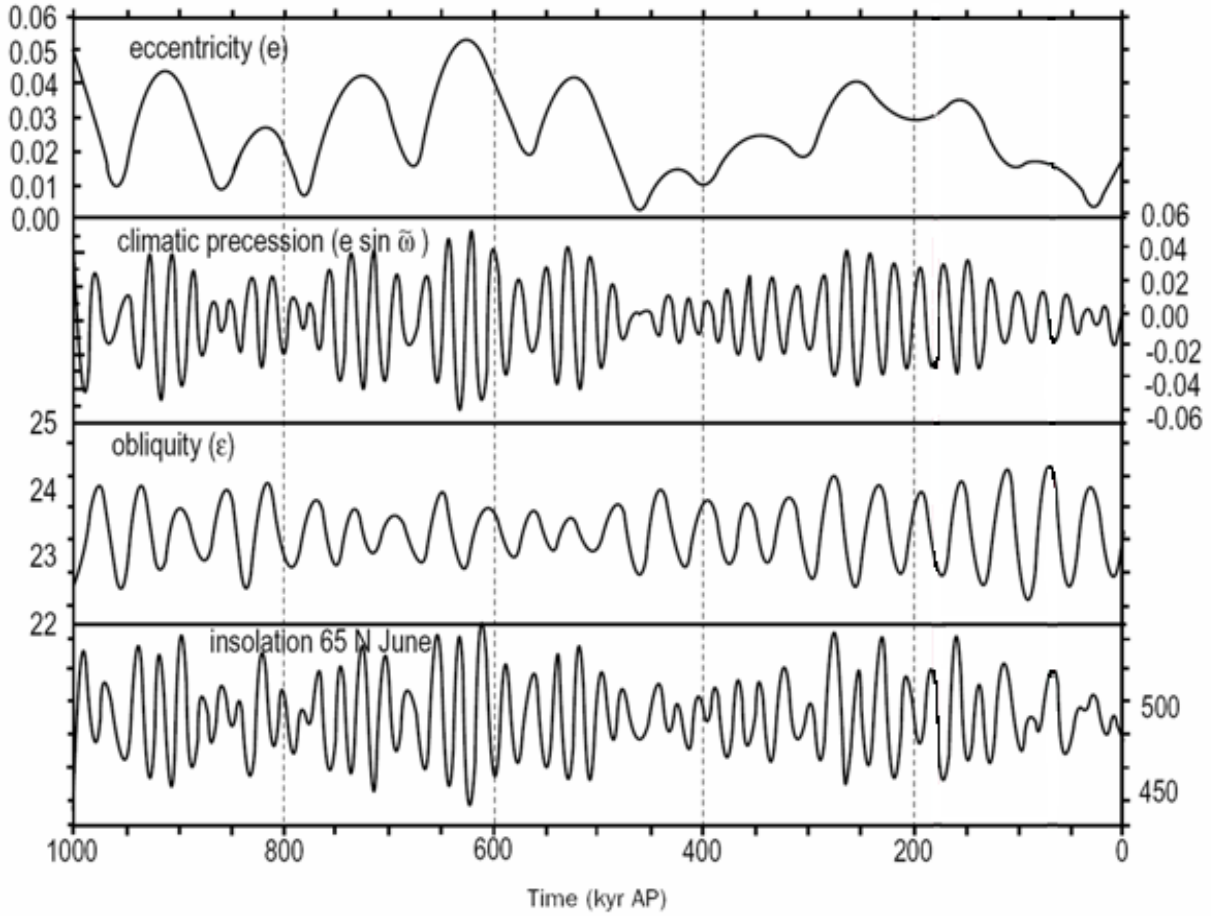

Fig. 6 Orbital parameters and insolation calculated from them in June at 65°N within the next 1 million years /BIO 01b/. The time axis is inverted (increasing to the left)

2.4.1.2 Plate tectonics

For the onset of ice ages, fundamental importance is attached to the continental drift. The past shows that a primary requirement for the onset of an ice age are land masses in at least one of the two polar regions, as well as land/ocean distribution and mountain location and height allowing the corresponding air and ocean currents and their intensities as moisture supply for the nourishment area of the ice sheet.

In contrast to the southern hemisphere, there is only evidence for glacial conditions in the northern hemisphere for the last one to two million years. It is assumed that the large-scale glaciation in the northern hemisphere was initiated by the final closure of the Panama Isthmus about 2.7 million years ago and its influence on the Gulf Stream /HAU 02/, /HAU 05/. Moreover, the formation of the ice sheet without a land mass at the North Pole took place over a longer period of time and was only possible because the North Pole is located since the Pleistocene in an ocean basin largely surrounded by continents which allows the existence of a closed pack ice sheet today existing for about 80,000 years. Today's Greenland ice forms the rest of the Laurentide ice sheet of the Weichselian glacial period.

2.4.2 Secondary factors

The influence on the climate by secondary factors is non-linear to a large degree and thus hard to analyse. This refers above all to the complex interactive effects between atmosphere, hydrosphere, cryosphere, lithosphere and biosphere. The cryosphere is the third largest component of the climate system in terms of volume after the atmosphere and the world ocean. Therefore, the water cycle plays a key role in climate development.

2.4.2.1 Radiation budget

The natural processes of the Earth's radiation budget are also decisively influenced by the components of the water cycle (see Fig. 7). The global average incoming solar radiation on Earth is 342 W m^{-2}. This insolation is weakened e.g. within the atmosphere by clouds in dependence of their water vapour concentration by absorbing or reflecting a part of the solar radiation. About 30 % of this shortwave radiation is reflected back into space by clouds, gases/particles and the Earth's surface /RUD 01/.

A change in the concentration of gases and particles in the atmosphere can change the incoming solar radiation significantly. A concentration increase of particles and gases may be due to natural processes but also by anthropogenic effects. A natural concentration increase of sulphurous gases and particulate matter in the atmosphere is caused, e.g., by explosive volcanic eruptions. Dust and gases are distributed around the Earth and reduce the global insolation by reflection significantly resulting in a large decrease of the summer temperatures /PAG 01/. The anthropogenic effects are addressed in Chapter 2.4.2.2.

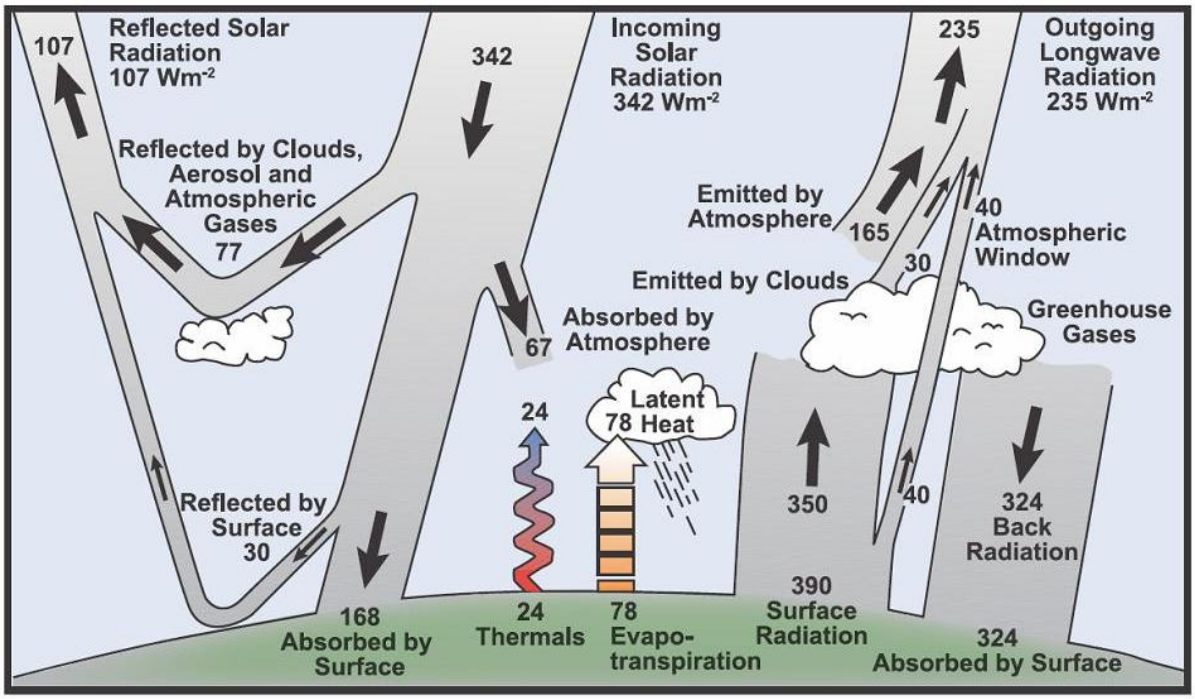

Fig. 7 Earth radiation budget /IPC 07/

The Earth's surface radiates longwave radiation back into the atmosphere. In the atmosphere, about 80% of this radiation is reflected again to the Earth as counterradiation. This downward radiation causes the so-called "greenhouse effect" and is positively correlated with the concentration of the so-called "greenhouse gases" (CO_2, CH_4, N_2O…) (see Chapter 2.4.2.2).

In Central Europe in summer under clear sky conditions, the radiation incident on the Earth's surface reaches about 1,000 W m^{-2}. For cloudy weather, the values descend below 100 W/m^2. In Germany, the annual average is between 100 W m^{-2} and 135 W m^{-2}.

The ratio of the amount of incident and reflected radiation is used as a measure of the reflectivity of a surface and referred to as albedo. It is dependent on the surface properties (see Tab. 6).

For the albedo, the water cycle again plays a key role since, with 30 % to 90 %, the snow and ice surfaces have the highest albedo. Due to the large surface areas they cover (in the northern hemisphere in winter, snow surfaces account for 50 % of the land surface, ice surfaces - with an area of 14.8 million km^2 – occupy about 10 % of today's land surface, and with 22.5 million km^2, sea ice covers about 6.5 % of the oceans on an annual average) their importance even increases /LEM 03/. Thus, the albedo intensity is of great significance for characteristics and change of glacial and interglacial periods.

Tab. 6 Albedo of various surfaces after Sellers /RUD 01/

Surface	Albedo range [%]	Surface	Albedo range [%]
Fresh snow or ice	60 - 90	Tundra	15 - 35
Old, melting snow	40 - 70	Grasslands	18 - 25
Clouds	40 - 90	Forest	5 - 20
Desert sand	30 - 50	Water	5 - 10
Soil	5 - 30		

The fraction of global radiation that is not reflected will be absorbed. At present this faction amounts to 47 % of global radiation on a global annual average /RUD 01/. Since the amount of the global radiation varies with the geographical latitude, the amount of absorbed radiation also varies. Areas near to the equator absorb more radiation energy than the polar regions. Ocean currents and winds partly compensate the differences by transporting tropical heat to the polar regions.

2.4.2.2 Anthropogenic influence

In addition to the processes and effects mentioned, anthropogenic factors also have an important influence on climate. Fig. 8 shows their influence as well as that of solar activity on the incoming solar radiation by the length of the bars. The black horizontal lines indicate the range of variation that is due to results of different analyses /IPC 07/, /CED 04/. Further, it is shown over which periods and spatial scales these factors are effective and how the degree of scientific understanding on the different factors is assessed.

At present, the long-lived greenhouse gases have the largest influence, and the scientific understanding of their influence on the climate is the only factor assessed to be high. The influence of the aerosols currently is subject to the largest uncertainties /IPC 01/.

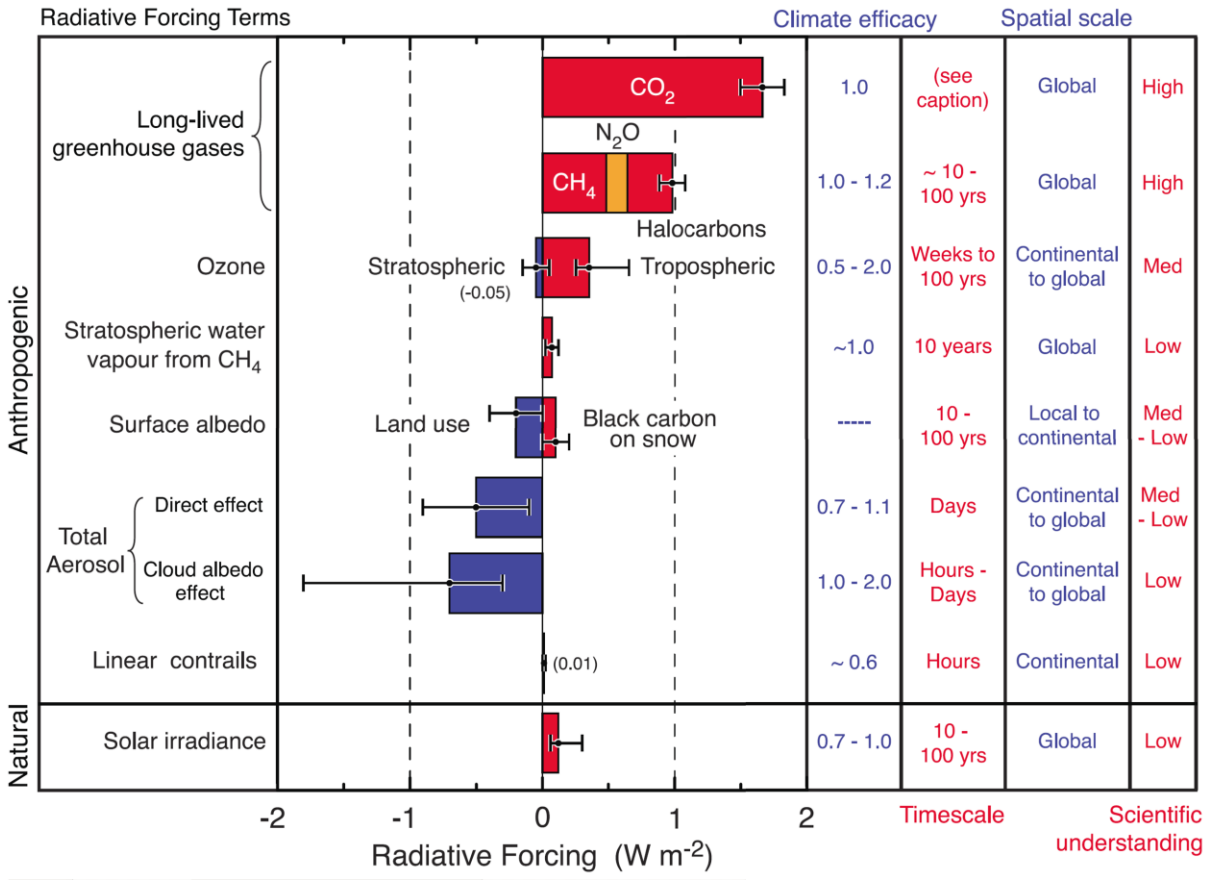

Fig. 8 Anthropogenic influence on the incoming solar radiation /IPC 07/

A continuous increase of CO_2 since industrialisation at the beginning of the 19th century has been verified. According to *Ruddiman*, man has already been influencing the climate since 5,000 years /RUD 03/. He is of the opinion that without this anthropogenic influence the conditions of the “small ice age” (1550-1850) would still prevail today. The influence is due to first agricultural activities and rice cultivation already 5,000 years ago. This would have caused a global temperature increase by about 0.8°C and an increase in northern latitudes by 2°C, enough to prevent a glaciation.

In general, a close correlation between CO_2 and CH_4 with the Antarctic temperature can be deduced from the Vostok ice core /PET 99/. *Petit et al.* suggest that the greenhouse gases are of great relevance due to the amplifying effect of the initial orbital forcing. It is assumed that they contribute to a global temperature increase during glacial-interglacial transition to

about a half (i.e. 2°C to 3°C). During such transitions in the past the concentrations of CO_2 increased from 180 ppmv to 280 - 300 ppmv and that of CH_4 from 320 - 350 to 650 - 770 ppbv. Such high concentrations of both gases of 360 ppmv and 1770 ppbv, as they prevail today, did not occur in the past 420,000 years.

According to Loutre, ice ages only occur if incoming solar radiation and the atmospheric CO_2 content decrease /LOU 03/. During the past 11,000 years, incoming solar radiation did indeed decrease but the CO_2 content in this period was always above 260 ppmv with increasing tendency since 8,000 years.

The behaviour of aerosols is still not well understood. They are small liquid or solid particles suspended in the air and comprise sulphates, nitrates, organic substances, dust and fly ash. Typical natural aerosols occur due to volcanic eruptions, sand storms, forest fires or at the sea. Their lifetime in the atmosphere is significantly shorter compared to greenhouse gases and is in the range of days to weeks. Contrary to the globally occurring greenhouse gases they often occur locally in increased concentrations in regions of anthropogenic sources, mainly in the northern hemisphere. It is generally assumed that aerosols contribute to cooling because they reflect sunlight, thus reducing the amount reaching the Earth's surface.

2.4.2.3 Ocean circulation

Due to its function of redistribution and storage of heat, moisture supply and the storage of gases – in particular CO_2 – and their exchange with the atmosphere, the world ocean is one of the main components of the climate system. The large-scale ocean circulation can be thought of as combination of water mass flows due to different causes. They are generated by winds, tides, the distribution of land masses and barriers on the ocean floor as well as by density differences resulting from temperature and salinity gradients. Due to the complex cause-and-effect relations, ocean circulation is a highly nonlinear factor in global and regional climate dynamics. For the climate in Northern Germany, the circulation of the North Atlantic Deep Water (NADW) is of particular significance (see Fig. 9). It is mainly caused by the density differences, is part and important driving force of the Gulf Stream waters and transports warm sea water northwards. In the North Atlantic there is one of the three key regions of the Gulf Stream where the water releases its heat into the atmosphere. Thus its density increases, it sinks down and contributes to the formation of deep water. Due to the evaporation of the warm sea water there is a significantly warmer climate with higher precipitation than to be expected for the geographical latitude.

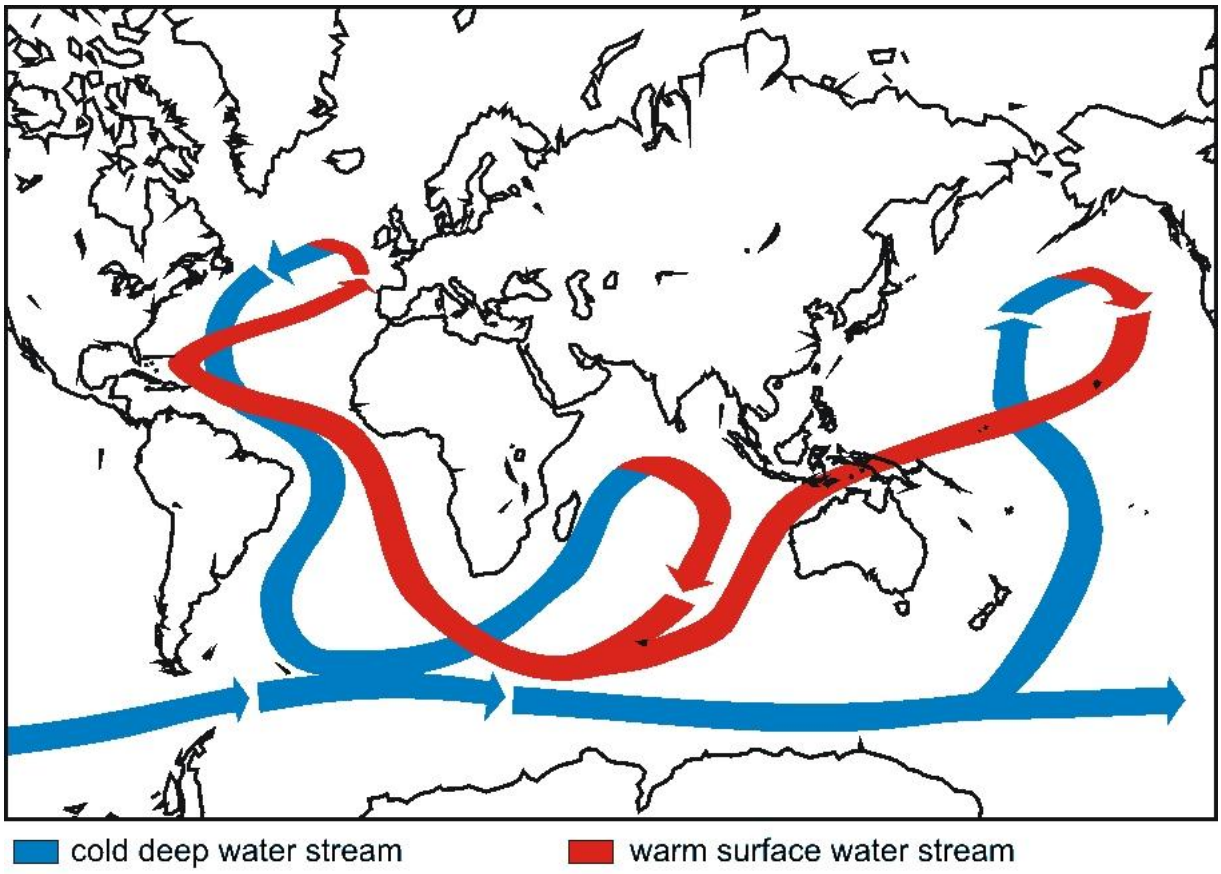

Fig. 9 Today's path of the Gulf Stream by Broecker et al 1985

However, the circulation of the NADW can be influenced by a change of amount and distribution of the freshwater input, the surface runoff and the location of the edge of the pack ice in the polar regions /LEM 03/. In the past, there were – dependent of the climatic situation – three different stable circulation types of the NADW /RAH 02b/:

- During interglacial periods, the stream extended into the North Sea,
- during the glacial period it extended in the subpolar open North Atlantic into the mid-latitudes, south of Iceland, and
- during the very fast temperature changes of less than 1,000 years – so-called Heinrich events – there was no NADW due to the melting of huge icebergs discharged from ice sheets whose water filled the deep Atlantic basin.

In the northern regions, the change of the circulation of the Gulf Stream became manifest in sudden and dramatic climate changes with regard to temperature but also to precipitation. According to current model calculations, a stop of the NADW results in a maximum cooling in the North Atlantic of up to 6°C, that of the air is 6°C to 11°C on an annual average /RAH 02/.

Further, due to its function of moisture supply, the Gulf Stream also plays an important role for precipitation formation and the growth and melting of glaciers in the northern hemisphere.

But also the glaciers in the southern hemisphere are influenced by NADW. The reaction is just the opposite of that in the northern hemisphere: if the north gets warmer, the south cools down and vice versa. This is due to the fact that the deep water stream flowing back from the north leads to an increased return flow of warm surface water in the southern hemisphere. If this driving force weakens or stops, there is less energy loss and the surface of the ocean around the Antarctic is getting warmer /ALL 02/.

2.5 The quaternary climate history of Northern Germany

The climate is integrated in long-term climate cycles (see Fig. 10). Within these long-term climate changes there were also short-term climate changes. Therefore, interglacial and glacial periods alternated more frequently than presented in Fig. 10.

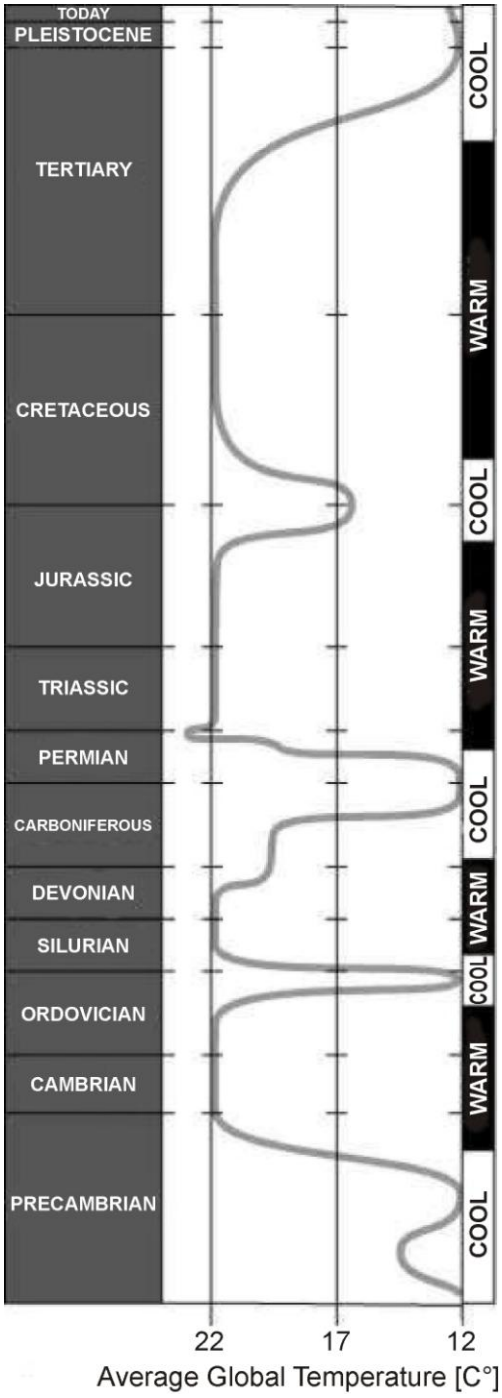

Fig. 10 Development of the average global temperature since the Precambrian /SCO 05/

The different climates also left marks in Northern Germany in form of changed underground structures, sediments and soils, topographies as well as floras and faunas. Since as period under consideration for the following modelling work the next 1 million years are of interest, only the climates of the younger quaternary past until the present situation were dealt with.

The last ice age began with the Pleistocene about 2.6 million years. According to *Herget*, the number of interglacial and glacial periods during this time amounts to about 50 /HER 00/. Fig. 11 illustrates by means of the average global temperature history those climate changes that have been occurring over the past 1 million years. The climate changed cyclical but was clearly dominated by cold conditions. The last two interglacials were, with periods of about 10,000 to 15,000 years significantly shorter than the glacials. The change between an interglacial temperature maximum and a glacial temperature minimum during this period shows a periodicity of about 100,000 to 120,000 years.

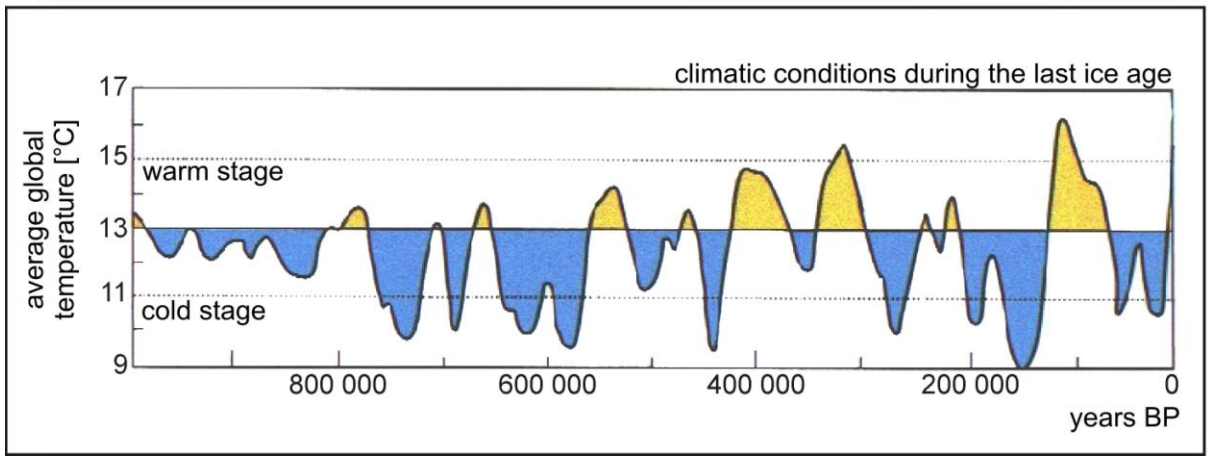

Fig. 11 Temperature history of the last 1 million years, according to Schönwiese et al. /EIS 08/

The glacials were characterised by increasing glacier and sea ice formation. Fig. 12 shows their maximum extension in the northern hemisphere during the Quaternary. Worldwide the glaciers covered about 32 % of the solid surface of the Earth.

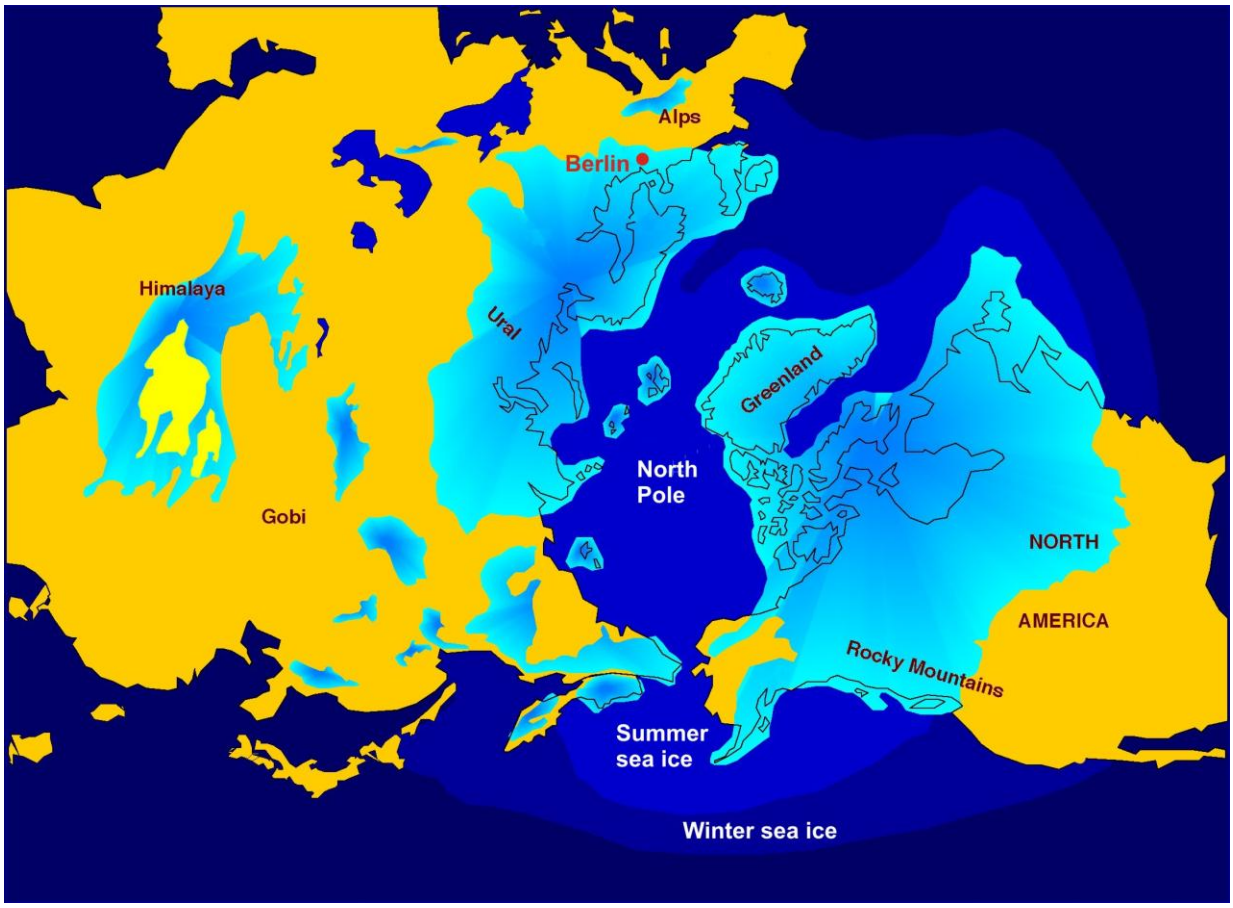

Fig. 12 Maximum extension of glaciers and sea ice in the northern hemisphere during the Quaternary, according to /GRO 06/

In Northern Germany, there were three large-scale glaciations during the Quaternary within the last 400,000 years. In addition to ice cover, permafrost soils with a thickness of about 40 m to 140 m were formed in the area in front of the glacier front /BGR 07/. The degree of overprinting of the underground decreases with the decreasing number of ice covers from north-east to south-west. Thus, north easterly of the maximum Weichselian ice advance (red line), there was a strong glacial overprint, southward to the maximum Elsterian and Saalian ice distribution (yellow line) there were only small periglacial overprints of the existing sedimentations. (see Fig. 13).

Fig. 13 Scheme of the maximum ice margin positions of the last three long ice ages according to Fischer on the basis of /WAL 92/

A large part of older sedimentations was replaced and/or overprinted by glacial processes so that in Germany there is evidence for sedimentation only since the Menapian in the late Pleistocene /KLI 02/. The most common sediments of the Elsterian glacial are the different moraines, as well as sands and gravels transported by meltwaters and the aeolian transported silts and sands sedimented as aeolian sand sheets, dunes or as loess. The interglacial periods were characterised by sporadic floods caused by sea transgressions and thus left marine sediments. Tab. 7 gives a survey of the climate-induced processes occurred during the different interglacial and glacial periods in Northern Germany since the Menapian as well as the glacial and interglacial sediments in the respective periods. The climate and the soils from sedimentation caused the formation of tundras, steppes or marshes.

Tab. 7 Time history of the Quaternary changes, the processes initiated and the sediments left in Northern Germany since the Elsterian glacial /BER 04/

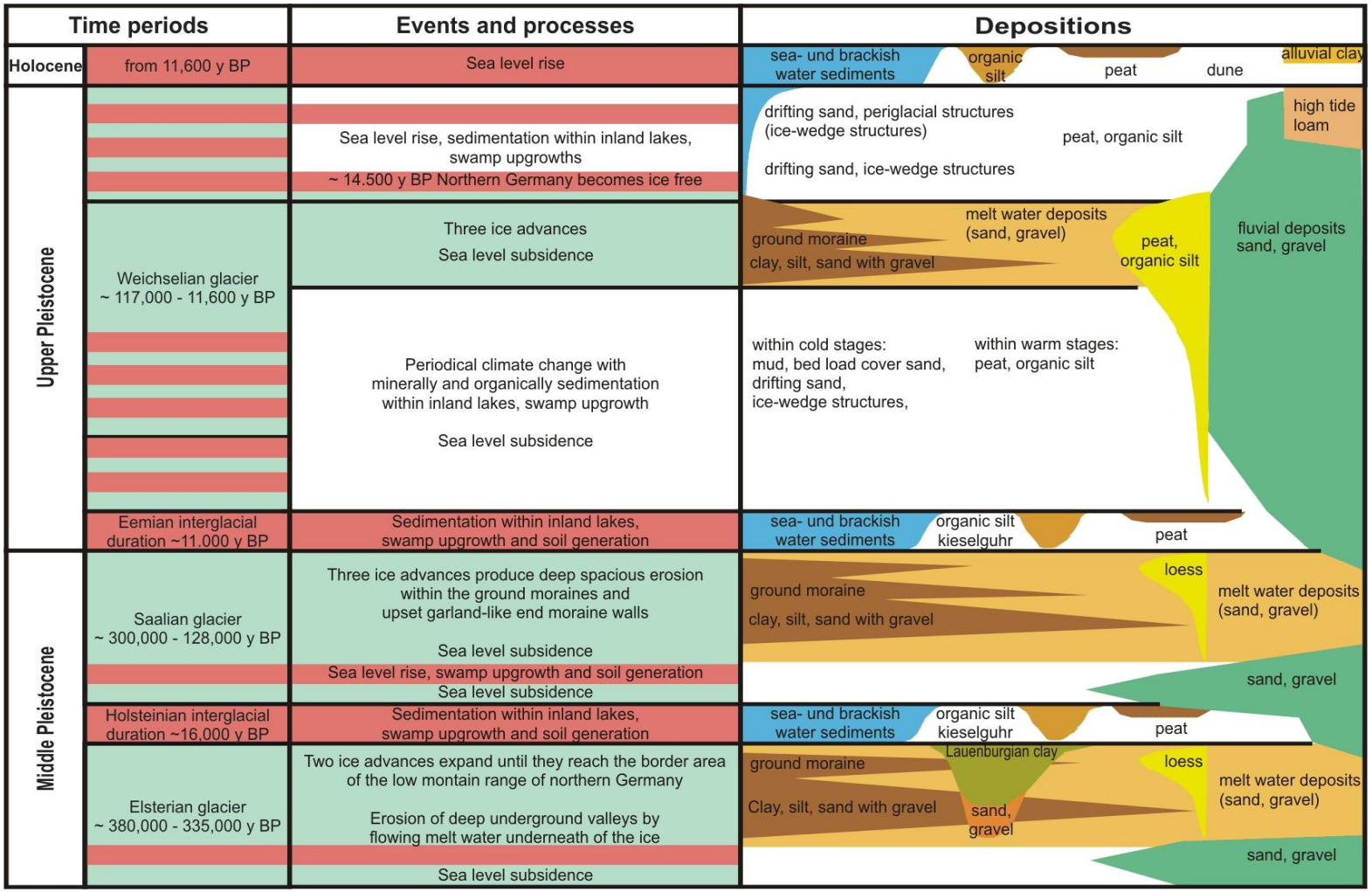

2.5.1.1 Elsterian glacial

The Elsterian glacial period was about between 385,000 and at least 335,000 years BP. At the beginning, the average global July temperature fell clearly below 10°C for several millennia, followed by two warmings during which the temperatures again rose up to 15°C /BER 04/.

The Scandinavian inland ice temporarily extended far into the northern German lowlands with velocities of 600 m a^{-1} to 900 m a^{-1} /BER 04/ (see Fig. 14). Only the following Saalian glacial showed a comparable large-scale glaciation in the Quaternary /DEL 91/.

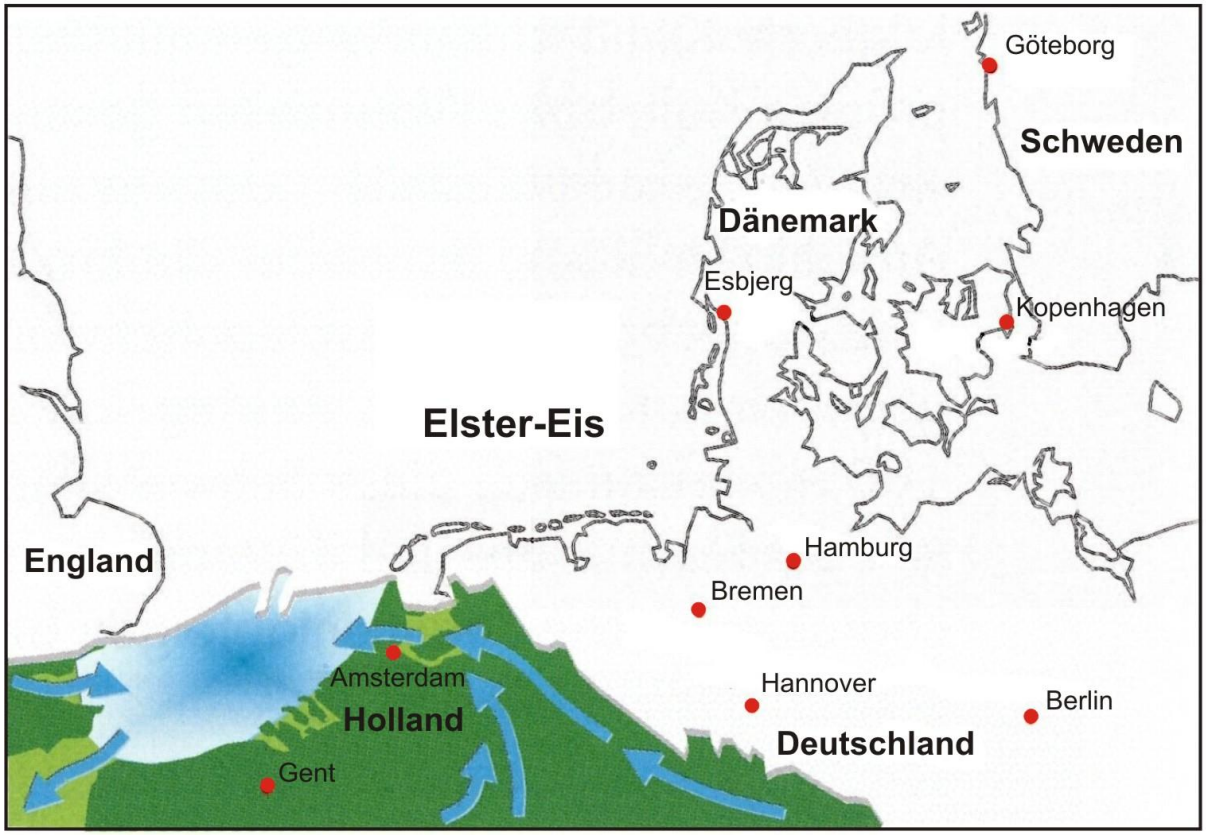

Fig. 14 Maximum ice margin position in Northern Germany during the Elsterian glacial /BER 04/

In front of the ice margin, a valley was formed that took up the meltwater and discharged it along the ice margin in northern direction. During the Elsterian glacial, deep channel systems were formed, presumably by meltwater (see Fig. 15). They have a depth of up to 500 m and are often cut into the underground over lengths of more than 100 km /KLI 02/. Channel formation only took place during the Elsterian glacial. The exact reason for it has not been

clarified yet. Most of the channels were almost completely re-filled with sediments already during the Elsterian glacial.

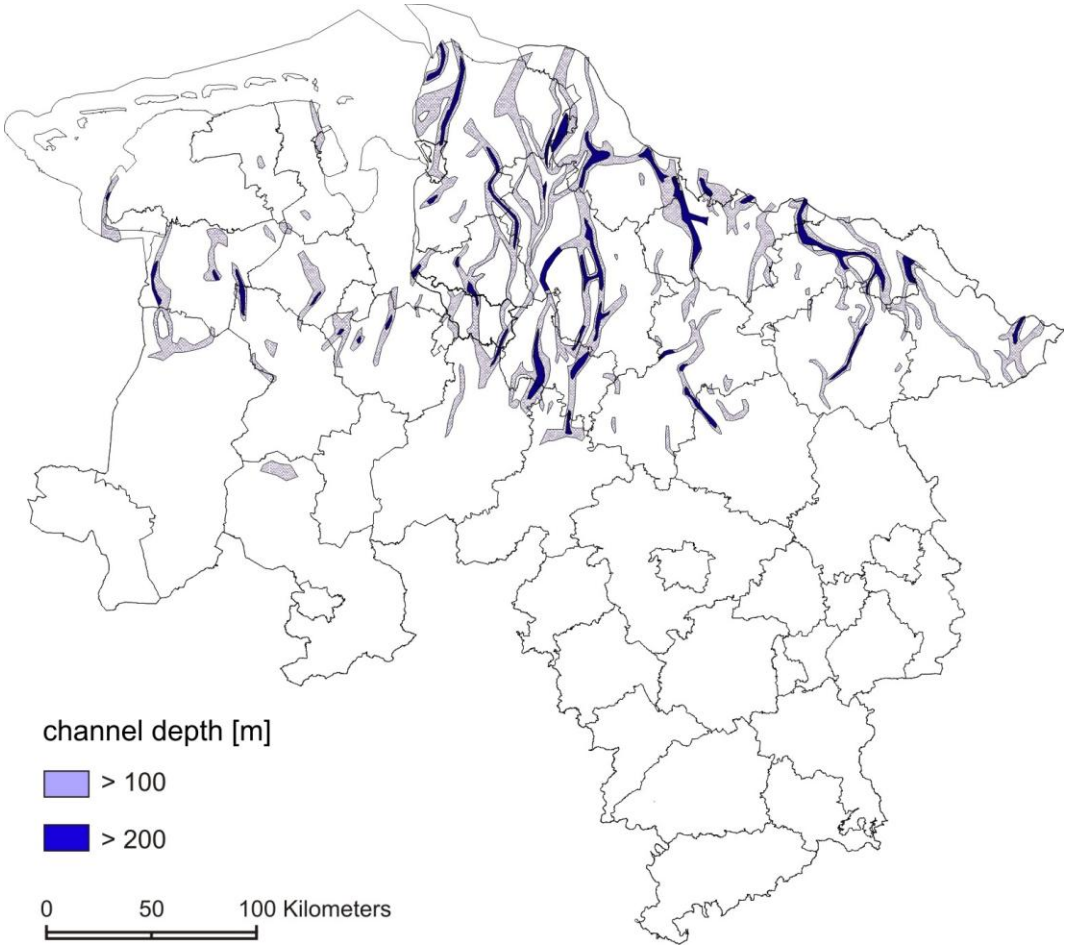

Fig. 15 Channel system of the Elsterian glacial period, Lower Saxony (Quaternary base 1:500.000 NLfB)

2.5.2 Holsteinian interglacial

The Holsteinian interglacial lasted about 16,000 years and was between 335,000 and 300,000 years BP /BER 04/. The average global July temperature during this period is presented in Fig. 16. First there was a rise of the temperature curve to values of 19°C. In between, however, there were two short-term climate ameliorations where the average global July temperature only reached values of about 12°C.

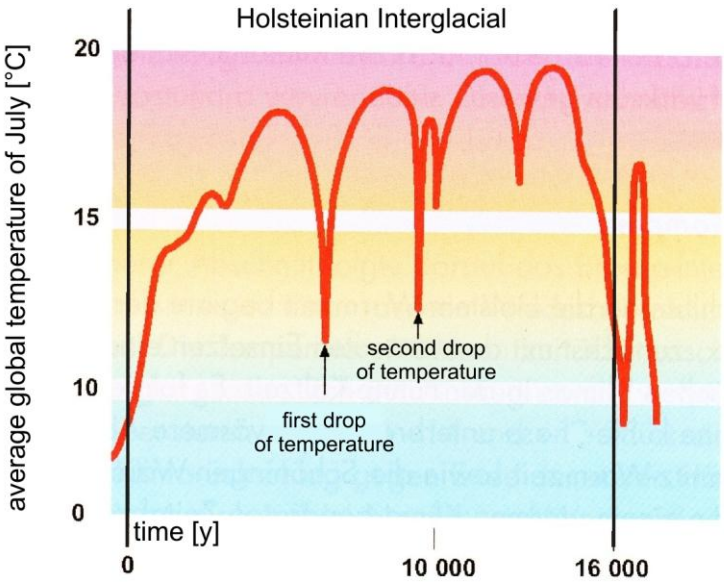

Fig. 16 Evolution of the average July temperature during the Holsteinian interglacial /BER 04/

The melting Elsterian glacial ice resulted in a sea level rise. At the time of maximum extension the Holstein Sea reached far into the Lower Elbe region (see Fig. 17). There, the maximum sea level rise was 55 m with a rate of at least 1 m per century.

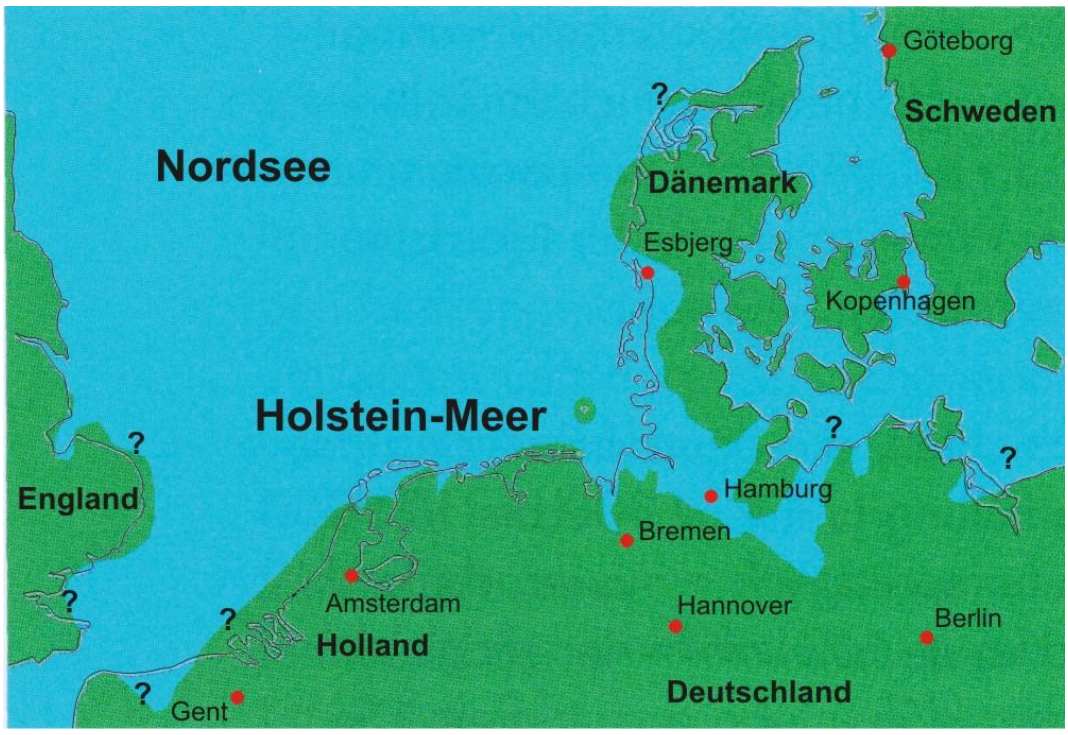

Fig. 17 Maximum extension of the Holstein Sea in Northern Germany /BER 04/

2.5.3 Saalian glacial

The Saalian glacial began, at the latest, about 300,000 years ago and ended about 128,000 years BP /BER 04/. During this glacial there were three ice advances, i.e. the Drenthe, the Warthe and the Fuhne. Fuhne and Drenthe are separated from each other by the Dömnitz interglacial /BER 04/. In Northern Germany, the eastern ice margin remained behind that of the Elsterian period. In the west, however, the extension of the Saalian ice was larger than that of the Elsterian glaciers (see Fig. 18).

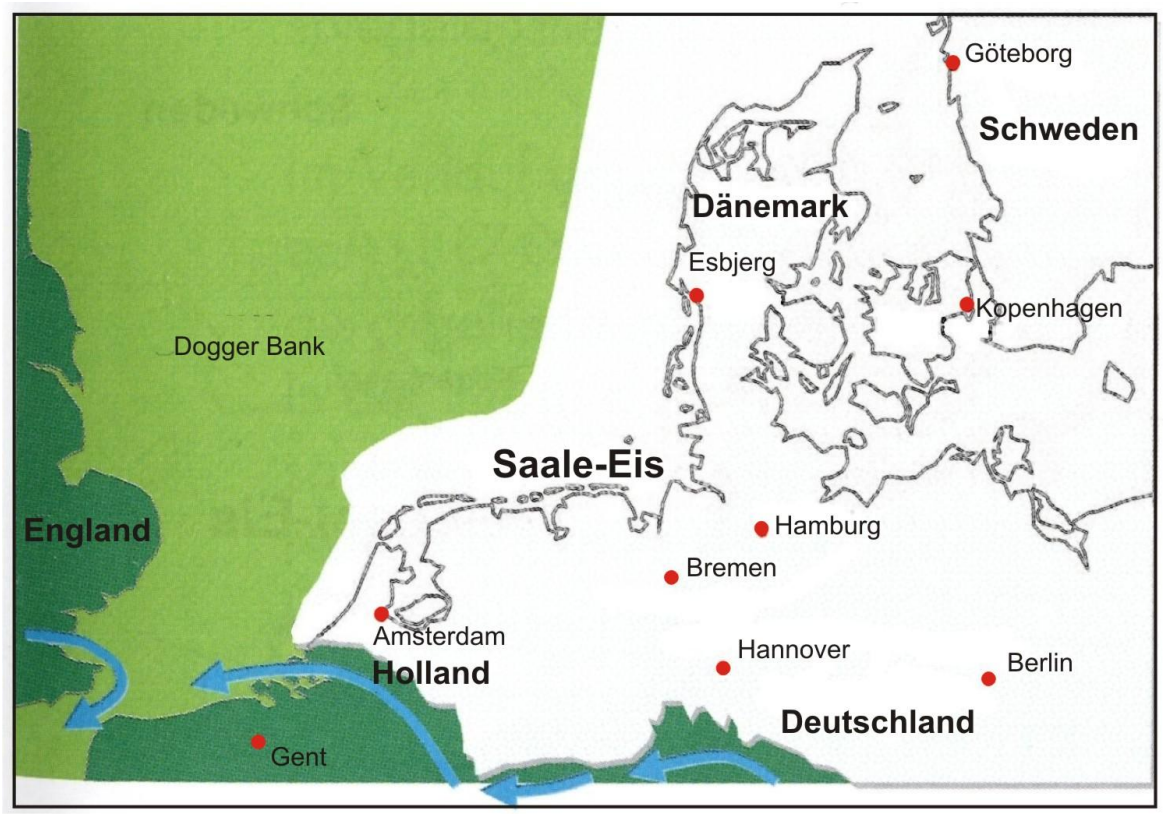

Fig. 18 Maximum extension of the Saalian ice /BER 04/

2.5.4 Eemian interglacial

The Eemian interglacial lasted about 11,000 years, between 128,000 years and 117,000 years BP /BER 04/ and was warmer than today's interglacial. Most of the terrestrial pollen records indicate, contrary to all other interglacials mentioned, a continuous warm period and a relatively constant climate /AAL 98/. As shown in Fig. 19, the glacial-interglacial transition took place within a few centuries with a rise of the average July temperature by10°C.

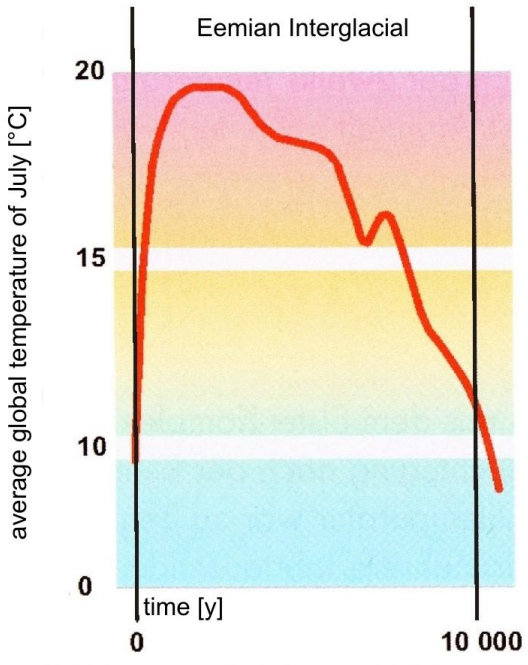

Fig. 19 Temperature evolution during the Eemian interglacial /BER 04/

On the basis of pollen analyses, Aalbersberg and Litt divided the Eemian into three periods /AAL 98/:

- Due to the extremely fast temperature rise there was a sea level rise during the first period by about 20 m in only 450 years which led to flooding of the coastal regions in Northern Germany. After this extremely high rate of more than 4 m per century, the sea level remained constant for about 4,000 years. Due to the near ocean, there was a subcontinental, maritime climate. The annual precipitation rate was about 600 mm. The minimum average July temperature in Northern Germany was about 18°C, the minimum average January temperature about 0°C to -2°C, equivalent to an annual temperature amplitude between 18°C and 20°C.

- Northern Germany was increasingly subject to maritime influence which led to a milder climate, in particular in winter. The annual precipitation rate was more than 600 mm. The minimum average July temperature in Northern Germany was about 15°C to 18°C, the minimum average January temperature about 0°C to 1°C, equivalent to an annual temperature amplitude of only 16°C to 18°C. During its largest extension, the coastline of the Eemian Sea was, except for some deviations, roughly comparable with today's coastline (see Fig. 20). The latest sediments of the Eemian sea flood are 5 m to 7 m below today's North Sea level, the oldest layers, dating back about 127,000 years, are at a depth of about 45 m /BER 04/.

- In this third period, the temperatures decreased rapidly and without significant variations until the beginning of the Weichselian glacial. The climate was still under maritime influence but increasingly changed to boreal conditions. The annual precipitation rate as well as the minimum average July and the minimum average January temperature remained unchanged. However, the annual average temperatures only reached values between 6.5°C and 9.5°C. The decrease in temperature led to the formation of ice caps ant thus to a subsidence of the North Sea level by at least 40 m.

Fig. 20 Maximum extension of the Eemian Sea /BER 04/

2.5.5 Weichselian glacial

This last glacial began about 117,000 years ago and ended about 11,600 years BP /BER 04/ and can, on the basis of the temperature evolution, be subdivided into the four phases pre-, middle-, main- and late-glacial (see Fig. 21). The dotted line illustrates the dating uncertainties until the middle of the Weichselian glacial. The climatic trend until the main phase of the Weichselian was clearly downwards even if it was interrupted by warmer phases so that in Northern Germany Arctic climate conditions did not prevail over the entire period /CHO 83/. During the pre-glacial period, climate cooled down rapidly within a few millennia. The middle glacial period was characterised by frequent alternations of cold and a

little bit warmer phases. During the main glacial period, there was another strong temperature decrease within a few millennia until the minimum values of this glacial were reached about 18,000 years ago /DEL 91/. The late glacial period lasted about 5,000 years and represents the transition to the Holocene. The transition period is characterised by very rapid and short-term climate variations /CHO 83/. The cause is assumed to be a deviating formation rate of the NADW which led to a change in the intensity of the atmospheric circulation over the northern hemisphere /SCH 03/.

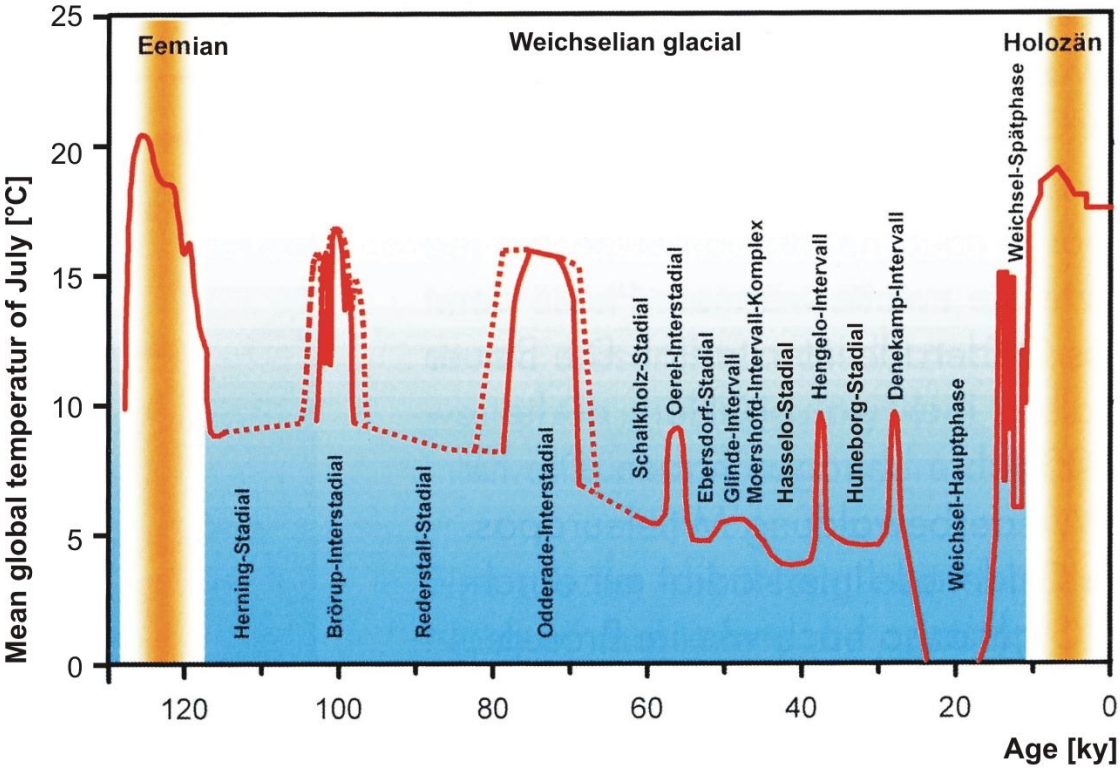

Fig. 21 Average July temperature during the Weichselian glacial /BER 04/

Since during the time following the sediments were only overprinted to a small degree, there is much more information available about this glacial than the preceding glacials so that these shall be addressed here more detailed. Tab. 8 summarises climate elements relevant for the different warmer and colder phases of the middle glacial period and the main period of the Weichselian glacial, as well as the resulting conditions for development of nature and landscape. The data were derived from the results of analyses on climate archives (cf. chapter 2.3), such as deep sea sediments, ice cores, pollen and from the variety of periglacial landforms in Northwest and Central Europe, in particular Central, Western and Northern Germany.

Tab. 8 Climate development in Germany during the Weichselian glacial and resulting sedimentations /HUI 98/, /HOH 05/, /CAS 01/, /BOS 01/

ka BP	Associat. phase	Annual average-T °C	Average July-T °C	Average January-T °C	Annual T amplitude °C	Sedimentation
117-105	Herning	< -1	8-12	-18- -12 (to -28?)	> 20	Sand, silty mud
105-93	Brörup	n.s.	15- ≥16	-10 - -8 -20 - -25	23 to 29	Kieselguhr
93-85	Reder-stall	n.s.	8-15	> -12 (-10)	< 10	Sands, sandy sedimentations, mineral/silty muds
85-74		0 to 1	15-16	app -12	26,5 to 28	Sands, sandy sedimentations, mineral/silty muds
74-59	Odde-rade Schalk-holz	-8 to -4	10-13	-26 to -20	30 to 39	Extensive sand surfaces, solifluction
59-55	Oerel	-8	< 10	-17	< 27	Turf, muds with high content of humin
55-52	Ebersdorf	n.s.	7	-26	around 33	n.s.
50-41	Glinde Moers-hoofd	≤ -4 to ≤ -1	≥7 to ≥10	≤ -13 to ≤ -20	23 to 27	Muds, huminic and silty sea sediments, sandy loess, silty loam, sand and silt
43-42		4-9	16 to 18	-7,5 to 0,5	15 to 26	
41-38	Hasselo Hengelo	-9 to -4	10 to 11	-27 to -20	30 to 37	
36-32	Huneborg Dene-kamp	-7 to -2	10	-20 to -16	26 to 30	Fine-grain sediments, in particular clay
27-20	main glacial	-8 to -4	4 to 8	-25 to -20	28 to 33	Aeolian sand sheets and loess belts
20-13		-9 to -4	7 to 11	-26 to -20	28 to 36	
15-11	late glacial	-6	11 to 12	around -23	around 35	Gravel, rubble, sand, till, aeolian sand sheets and loess belts

During the cold periods, there was generally much material displaced by erosion. On the one hand, there was no protective and no major vegetation cover due to the inhospitable conditions and, on the other hand, extreme forces were effective. The glaciers scraped the underground (exaration), their meltwaters transported, above all, the gravels and sands loosened by the glaciers, and the high glacial wind velocities spread the fine material deposited in front of the glaciers over large distances. During the Weichselian glacial, the permafrost soils had different thicknesses, different extensions and alternated between discontinuous permafrost, seasonally frozen ground and continuous permafrost.

In dependence of the amounts of water and the newly formed sediments, the discharge behaviour of the rivers alternated between an extensive meandering river system during the warmer periods and a braided river system during the cold periods. Here, the change between the flow systems was both subject to short-term seasonal temperature variations and the long-term temperature variations of the warmer and colder periods.

During the Weichselian glacial, the climate in Northwest and Central Europe was mainly influenced by three factors: the Fennoscandian ice sheet, the North Atlantic surface water and the climate on the continent /HUI 98/. The weighting of these factors changed within the course of the Weichselian glacial and thus led to climate changes.

- During the cold phases, the ice shield had the main influence on the climate. Due to the subsidence of the sea level and the fact that during this phase large parts of the North Atlantic and the North Sea were covered by ice, the land was too far from the sea so that the relatively warm temperatures of the North Atlantic could not reach Northwest and Central Europe.

- The cooling of the atmosphere reduced the evaporation rate of the seas and the moisture holding capacity of the air. This caused a change to a continental, cold/arid climate in Northern Germany, partly with extremely cold winters, high wind forces, dry summers, a high temperature amplitude, a low annual precipitation rate and, as a consequence, a short growth period.

- Only in longer warmer phases, during which the sea ice margin retreated northwards, the influence of the North Atlantic surface water on the climate in Northwest Europe increased. The maritime influence on the continent became stronger again which led to an overprint of the formerly strong north-south temperature gradient by a west-east gradient. By this, the influence of the Atlantic on the climate in the west of Germany increased whereas in the east a continental climate continued to prevail /CAS 01/. In the regions under maritime influence, the winter temperature increased causing a decrease of the temperature gradient. Due to the higher air humidity the precipitation rate increased again /HUI 98/.

- The inland ice development in Scandinavia began within the course of the first 5,000 years of the glacial with an increase of the ice mass volume by about 5,000 km^3 per year. Under the heavy weight of the ice the lower ice masses began to deform and to move outwards. The glacier temporarily reached an advance speed of 60 m a^{-1} to 120 m a^{-1} /CHO 83/. In the course of the glacial, the ice retreated again at least two times

due to the intermittent warmer periods /CHO 83/ and until the Huneborg Stadial the ice sheet margin did not yet extend over the Baltic Sea. The glacier reached Northern Germany as late as the last period of the Weichselian glacial during the main phase and there it is evidenced by the three glacier advances of the Brandenburgian (25,000-18,000 years BP), the Frankfurt (18,000-16,000 years BP) and the Pomeranian stage (16,000-14,500 years BP). Within 7,000 years, the ice advanced from Central Sweden to the Spree forest. The Weichselian glacier reached its maximum extension during the Brandenburgian stage with an average ice shield thickness of 1,500 m. The glaciers advanced from the Gulf of Bothnia, starting from north-east to south-west, into the north of Germany. On the North Sea, they joined with a smaller ice mass descending from the Scottish /CHO 83/. Terminal moraine walls up to a height of 50 m were heaped up and compressed /CHO 83/. Compared with the maximum glacier extension of the older Elsterian and Saalian glacials, the extension of the Weichselian glacier was significantly less and the Elbe was not crossed. Fig. 22 shows the maximum extension of the Weichselian glacier (BGR). The rapid warming at the end of the glacial led to a rapid disintegration of the ice shield which partly retreated northwards with velocities of 600 m a^{-1} /CHO 83/.

Due to the year-round low temperatures, there was a polar desert in front of the glacier front in which many periglacial structures had been formed. At the beginning of the glacial, large regions were still covered with snow which protected soil and vegetation so that despite low temperatures evidence for permafrost soil can only seldom be found /CAS 01/. For this time, there is evidence for solifluction sheets and cryoturbations in Northern Germany /CAS 01/ but already in the second cold phase there were largely discontinuous permafrost soils /CAS 01/ and since then periods with discontinuous permafrost alternated with sporadic permafrost /BOS 01/. In addition, there was the formation of large ice-wedge casts in Northern Germany. During the Hasselo Stadial, the permafrost extended into depths of up to 130 m /CHO 83/. The short-term warming during the Hengelo and Denekamp interstadials then initiated the degradation of the permafrost soil and the ice-wedge cast /HUI 98/. In the main phase of the Weichselian, there was again a formation of a large ice-wedge cast and largely continuous permafrost whose margin was close to the glacier front. In the regions from which the glacier later retreated there were again permafrost soils as the formation of ice and sand wedges show. Further warming then led to decreasing permafrost so that only frost-crack partings and small cryoturbations occurred. However, deeper permafrost of former times cannot be excluded /HUI 98/.

Fig. 22 Maximum extension of the Scandinavian Weichselian glacier /NAE 07/

The sea level is directly correlated with the ice mass. Towards the end of the Eemian interglacial, the sea level was about 20 m to 30 m lower than today and subsided during the first cold phase of the Weichselian glacial resulting in a shift of the coastline in the northwest direction /CAS 01/. Since the warmer periods only lasted a short time, the sea level hardly rose so that during the Rederstall and Hasselo stadials it was about 50 m lower than today and thus the coast line was 250 km further to the sea /CAS 01/. During the main phase of the Weichselian, more than 70 million km^3 of water was bound in form of ice /CHO 83/.

Tab. 9 shows the subsidence of the sea level at the time of the last glacial maximum compared to today's conditions and the contributions of the different ice covers /RUD 01/. The largest volume results from the Laurentide Ice Sheet in Canada. Altogether, the sea level was 109 to 129 m lower than today. The reduction of the sea level resulting from the stored amount of water would be more than 155 m. However, other forces, such as the isostatic movement of the Earth's crust, counteract this subsidence. The weight of the ice masses, for example, deformed the Earth's surface and depressed the Earth's crust to one third of the overlying ice thickness which also resulted in an elevation of the sea floor.

By this, the coastline shifted about 600 km northwards. The rapid sea level rise of about 75 m below today's level is the manifestation of the rapid warming and the associated reduction of the glacier ice volume at the end of the Weichselian glacial. Fig. 23 shows a sketch of the Elbe estuary region at the end of the Weichselian glacial. At that time, the North Sea advanced again between the glaciers from Scandinavia and the Scottish Highlands and through the English Channel. At that stage the Elbe estuary was about 200 km more to the north than today.

Tab. 9 Ice volumes, stored amounts of water and subsidence of the sea level at the time of the last glacial maximum compared to today /RUD 01**/**

Ice sheet	Location	Excess ice volume [Mio km^3]	Sea level	
			Amount [m]	Change [m]
Laurentide	East Central Canada	25 - 34	72 - 100	50 - 70
Cordilleran	Western North America	1.8	5	3.5
Greenland	Greenland	2.6	7	5
Britain	England, Scotland, Ireland	0.8	2	1.5
Scandinavian	Northern Europe	7.3	21	15
Barents / Kara	Shelf north of Eurasia	6.9	20	14
East Antarctic	Eastern Antarctica	3.3	9	6
West Antarctic	Western Antarctica	6.5	18	13
Others	Various	1.2	3	2
All ice sheets		55 - 64	155 - 183	109 - 129

The deposition of sediments was closely related to the climatic processes and led to a characteristic layering due to changes in sediment accumulation and way of transport which occurred along with climate development. In the dry and very windy stadials with scarce vegetation and open landscape, there was mainly glaciofluviatile and aeolian sediment transport. The meltwater removed large amounts of gravels and sands from the glacier. During passage through the glacier snout, directly at the glacier front, the flow velocity strongly decreased so that at the surfaces there, much glacial debris in form of gravels, rubble and sands was deposited. With increasing distance to the glacier, the melt water flow velocity decreased so that the grain size of the transported sediments also became smaller with the distance to the glacier. In the main phase of the Weichselian glacial, the rivers Ems, Weser, Elbe and Eider formed an interconnected river system with discharge into the North Atlantic. In parts, still today there is evidence for it in form of a channel on the North Sea floor with a width of 30 km to 40 km /CHO 83/. Hillside, solifluction processes took place due to softening of the soils /HUI 98/ /CAS 01/.

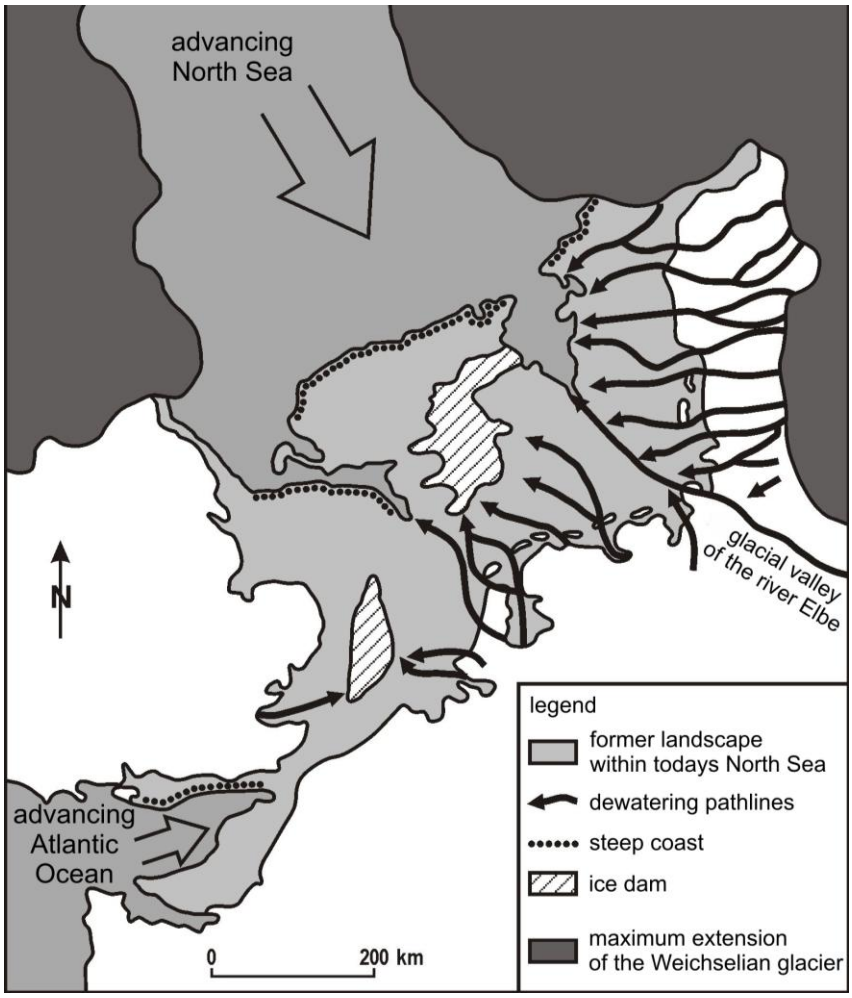

Fig. 23 Elbe estuary about 12,000 years ago /FOE 00/

Towards the end of the stadials, glaciofluviatile sediment transport decreased and aeolian sediment transport gained in importance due to the still low temperatures and small precipitation amounts. Therefore, the amount of fine-grain sediment deposits increased towards the end of the cold and in the beginning of the warmer periods. Fine-grain sediments were blown out of the 20 m to 50 m thick sandurs in front of the glacier which resulted in the formation of large-scale aeolian sand sheets with heights of up to 2 m and loess sediments with heights up to 6 m throughout Northwest Europe /MEY 07/. Due to the large seasonal surface discharge, in particular during spring melt and siltation of river beds caused by the high sediment load the rivers carry, extensive meandering river systems are formed /HUI 98/. Above all in former lakes, in which sedimentation of the fine-grain sediments could take place undisturbed, large amounts of mineral and silty muds deposited towards the end of the cold periods. Soil formation was characterised by clay enrichment. During the interstadials, however, typical sediments were kieselguhr (Brörup), turf and huminic (Oerel) or silty muds (Glinde, Moershoofd). The amount of organic material contained in the sediments indicates

the vegetation cover. So, in the warmer phases of the Glinde and the Moershoofd, mainly sandy loess, silty loam, sand and silt were deposited due to the high aridity.

2.5.6 Holocene

The Holocene climate evolution is also referred to as Flandrian interglacial and began about 11,000 years ago. The climate variations during this time are illustrated in Fig. 24 by means of the global temperatures. Within a few millennia, there was an abrupt temperature rise at the end of the Weichselian glacial which initiated the most recent geological epoch of Earth's history, the Holocene. During the time following the Weichselian glacial, relatively constant climate conditions prevailed.

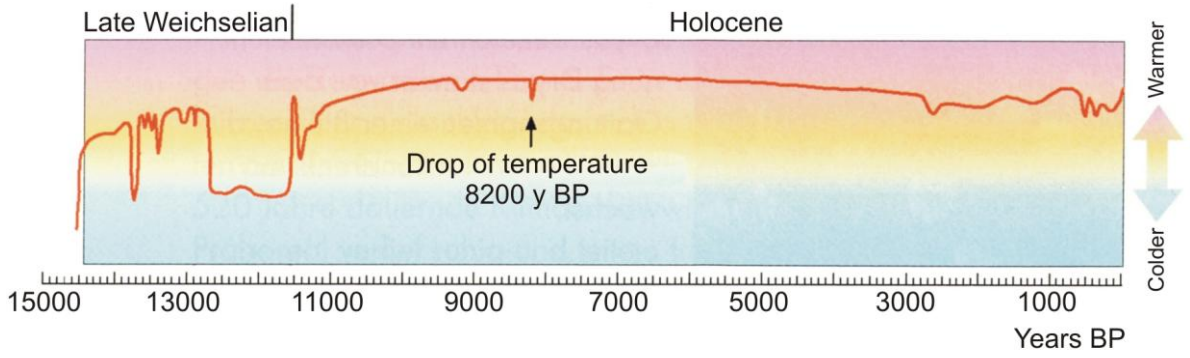

Fig. 24 Evolution of the average July temperature during the Holocene /BER 04/

However, the entire Holocene period was characterised by regular, rapid and less intense climate variations at short intervals of 1,500 to 3,000 years. These small variations seem to be directly related to deviations of the formation rate of the North Atlantic Deep Water and the intensity of the atmospheric circulation over the northern hemisphere /SCH 03/. *Bond et al.* /BON 02/ discovered that in North Atlantic sediment cores, variations in the content of iceberg-transported sand and silt correlate with Holocene variations of the ^{14}C production rate in the atmosphere and thus are subject to an external driving force. The short-term climate variations have therefore not been caused by orbitally induced periodic changes of the solar irradiation but by variations of the solar activity /SCH 03/.

The average annual temperature was in the range of that of today with a temperature deviation of 3°C. The highest temperatures so far occurred in the early Holocene about 8,000 to 6,000 years ago. This relatively warm period in the course of climate history is also

referred to as climate optimum. Since then, it is getting colder with short-term variations. Evidence for these variations is given by about ten smaller ice advances, each lasting for 600 to 900 years. The strongest cooling occurred about 8,200 years BP and it is assumed that it is related to the drainage of the meltwater lake “Lake Agassiz“ (North America) - which also occurred in the period 13,000 to 10,300 years BP /LEV 00/ - into the North Atlantic and the resulting weakening of the thermohaline circulation /RAH 02/, /PAG 01/, /SCH 03/. Between the 15th and 19th century, there was another cold period, also referred to as “Little Ice Age”. The cooling is attributed to volcanic activity and solar variability /PAG 01/. Today, most of the experts attribute the temperature rise since then to the concentration of the atmospheric greenhouse gases increasing since the industrialisation about 150 years ago /IPC 07/.

The sea level rise already beginning at the end of the Weichselian glacial by melting of glacier ice continued in the Holocene. Until the end of the so-called climate optimum about 6,000 years ago, the sea level rose by about 120 m compared to the lowest sea level during the Weichselian glacial and still rises today (see Fig. 25).

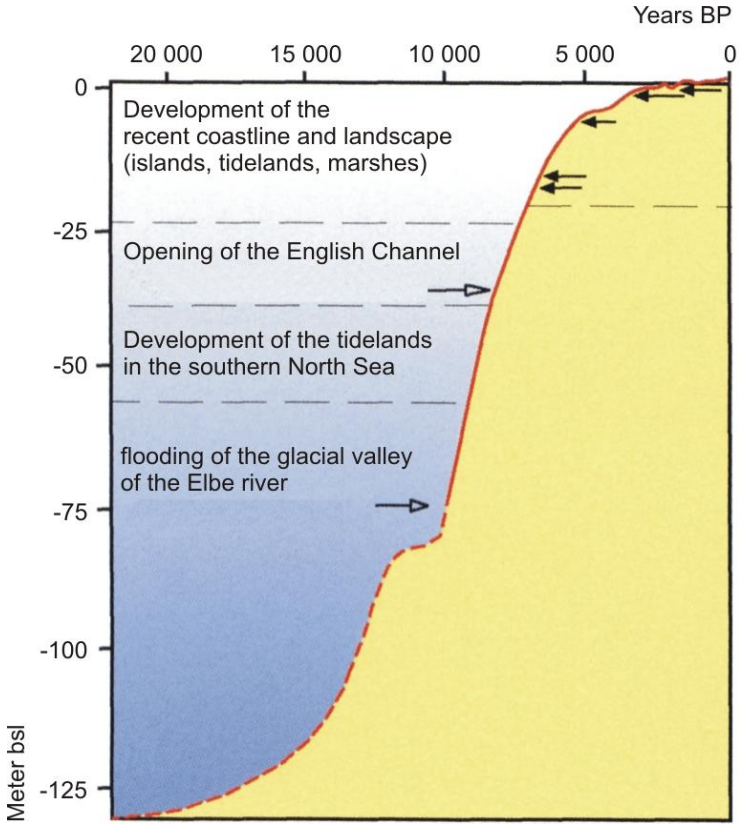

Fig. 25 Sea level change since about 20,000 years BP ago /BER 04/

Today's coastal regions of Northern Germany largely developed during the very steep sea level rise of the so-called Flandrian or Calais transgression which began about 9,000 years ago and between 5,000 years BP and 3,000 years BP was followed by a small regression. Then, the Dunkirk transgression followed which lasts until today. The sea level rise not only had an influence on the directly adjacent coastal regions but, due to backwater, also on the rivers discharging into the North Sea.

A new sea level curve was presented in /BEH 04/. In addition to the dates of the basal peats, previously only referred to regarding the development of the sea level, information from so-called "floating peats", i.e. peats intercalated in the marshes, as well as archaeological information now supplement the data base existing until then. Besides dating of the sea transgressions, this also enables the determination of sea regressions. So, a total of seven regressions was indentified for the Holocene so far. However, dates for a revision of the sea level curve are still not available, above all for the older periods.

In addition to the change of the sea level, the coastline of Northern Germany also depends on the uplift of the Earth's crust after removal of the ice load and subsidence of the surrounding area. While there had been an uplift of Scandinavia by about 300 m since the end of the Weichselian glacial and still today there is an uplift of parts by about 1 cm per year, there is a subsidence of almost the whole of Northern Germany by about 1 mm to 2 mm per year. Only in some regions, there is an uplift of about 1 mm per year (also see Fig. 26). According to Behre, today's isostatic influence on the coastline is, at least for the southern North Sea, that weak that it can be neglected /BEH 04/.

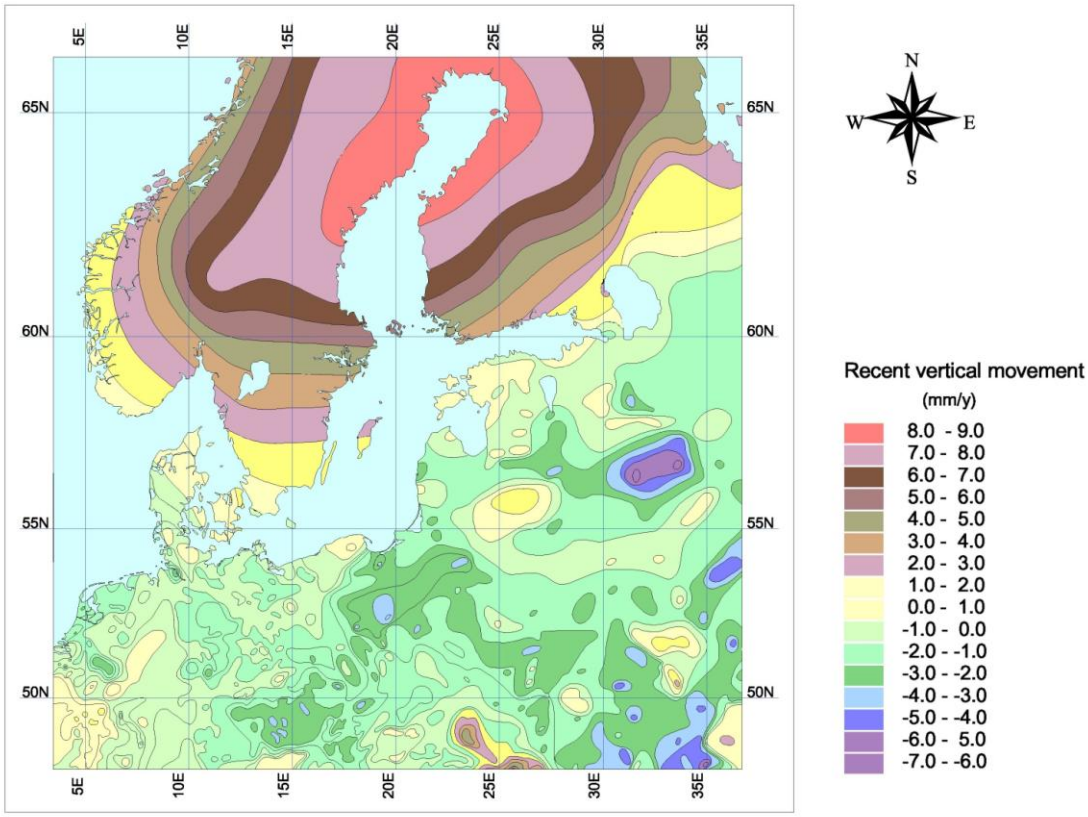

Fig. 26 Subsidence and uplift levels of the Baltic Sea region due to the postglacial isostatic movement /MEY 01/

Together with the development of the weathering processes and the vegetation cover, the ice ages, sea transgressions and regressions, the climatic conditions as well as the previously existing igneous rock and the deposited sediments in the course of the last 480,000 years led to the formation of the soils existing today in Germany (see Fig. 27). The largely warm climate and the existing sediments and soils led in Northern Germany to the growth, in particular, of beech and mixed beech forests and oak-hornbeam forests.

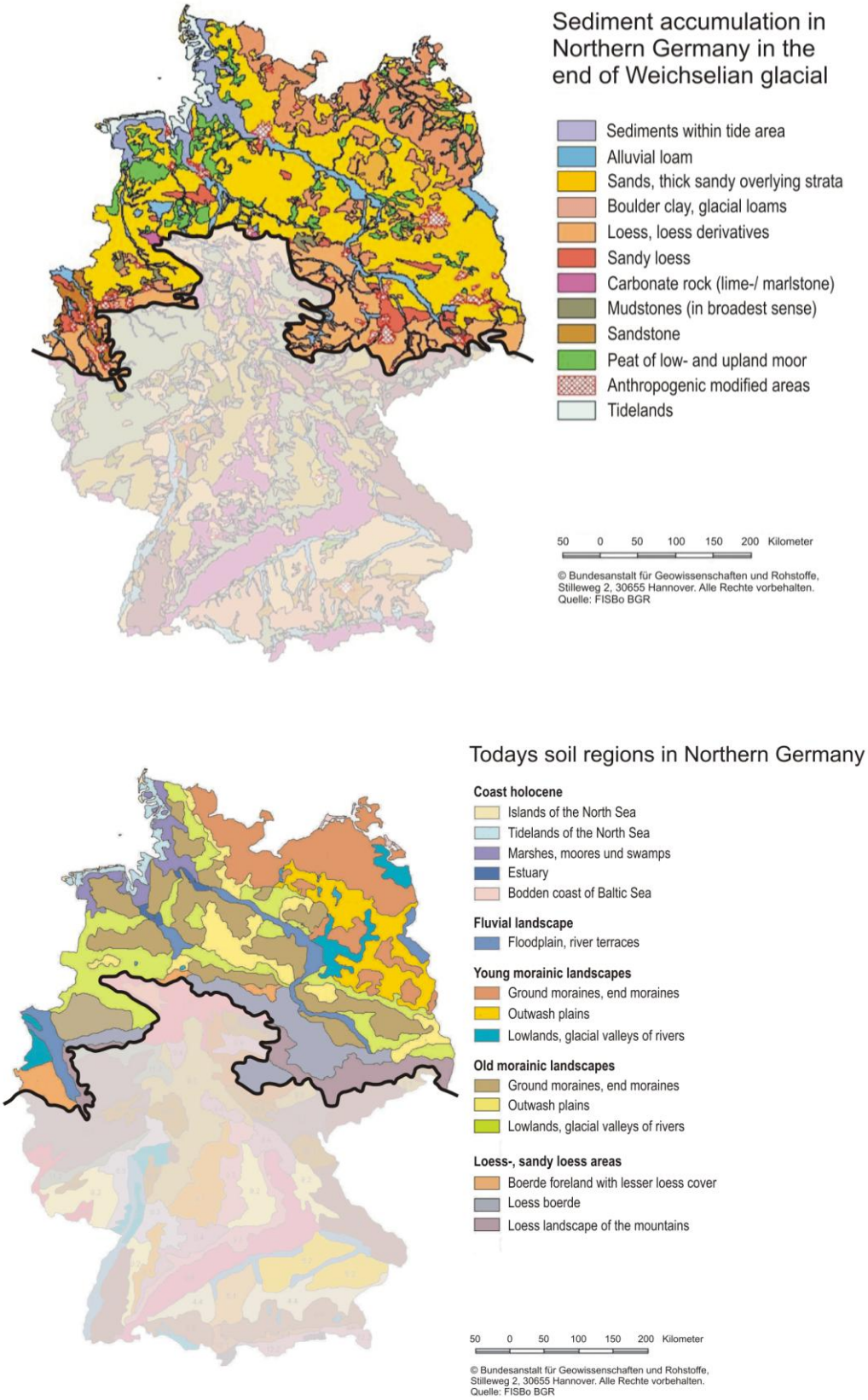

Fig. 27 Todays sediments (top) and soils (bottom) in Northern Germany formed by glacial and postglacial processes, on the basis of /BGR 07a and b/

2.5.7 Conclusions

The climates in the past described in the previous chapters and their impacts on Northern Germany indicate which consequences a continuation of the current interglacial and a future glacial could have on the area under consideration. The information gained from paleodata is therefore of decisive importance for the development of the models used later on (cf. chapters 0 and 8). Thus, the following summarises the information relevant for the later modelling at the site under consideration.

The last three glacials of the Elsterian, Saalian and Weichselian lasted about between 60,000 years and 180,000 years. The glaciers advanced from Scandinavia in south-west direction and covered the area under consideration during the first two glaciations whereas the Weichselian glacial remained free of ice. At the beginning of the glacials, the glaciers first had to reach a certain thickness that the lower ice layers could be deformed by their own weight and began to move. Finally, the Scandinavian glaciers reached the area under consideration with an average velocity of about 100 m a^{-1} to 125 m a^{-1} in the second half of the glacials and covered it for less than 10,000 years. During the past glacial maxima, the sea level was 110 m to 140 m lower than today /PAG 01/. The increasing distance to the sea led to an increasingly continental climate and further cooling in regions in front of the glacier. This led to deeper permafrost soil there for which there is evidence in Northern Germany down to a depth of 40 m to 140 m as a maximum. In dependence of duration and temperature development, sporadic, discontinuous and continuous permafrost alternated. At least during the Weichselian glacial, the Elbe was used as glacial valley for melt water and discharged the glacier water towards the North Sea. During the Elsterian glacial, the topography in the area under consideration changed considerably due to the formation of channels with a depth of more than 300 m. However, most of the channels were already largely filled up during the Elsterian glacial by ground moraine material, glaciofluviatile outwash gravels, sands and silt. During the Saalian glacial, two push moraines were formed in the direct vicinity of the area. Later, above all podsols, pseudogleys, gleys, grey-brown podsolic soils, non-calcic brown soils, alluvial soils and regosols were formed from the sediments.

The Holsteinian and Eemian interglacials approximately lasted about 11,000 years and 16,000 years, respectively. During these periods, the ice retreated from the area under consideration and also permafrost no longer occurred. The sea level rise of 120 m between the Late Weichselian and the Holocene with a minimum rate of 1 m per century and a maximum rate of 4 m per century led to the flooding of regions silted during the glacial and a

backflow of the Elbe. In the regions flooded by the sea, sea sediments deposited, and in the area of the rivers overflowing its banks there were deposits of alluvial loams. Due to the closeness to the sea, the area under consideration became increasingly subject to a maritime influence. During the Holsteinian interglacial the Sea reached far into the Lower Elbe region and caused a transgression of the reference site considered here. This transgression lasted over time frames of about 3,000 to 4,000 years.

With 3,000 to 4,000 years, the glacial-interglacial transitions were generally slower than the interglacial-glacial transitions with a maximum of 200 to 300 years.

3 Climate Models

In order to predict a climate in the long-term future, observations of past and present climate change must be correlated to the orbital variations described in chapter 2.4.1.1. The periodic orbital changes can be predicted over the next million years with comparably high accuracy. These external factors represent the basis for long-term climate modelling and are usually linked by the correlation between orbital perturbation and insolation, which is a direct input parameter for the climate calculation.

To understand the dynamics of the climate not only atmosphere processes but also processes occurring in the hydrosphere (oceans), the cryosphere (inland and sea ice, permafrost and snow cover) and the underlying lithosphere as well as interactions between these systems need to be considered in the climate models /CLA 02/. Fig. 28 illustrates the correlations and interactions of the factors and processes relevant for the description of climate changes /PET 00/. Due to the high complexity of the system with several nonlinear feedback mechanisms predictive climate calculations are covered with high uncertainties.

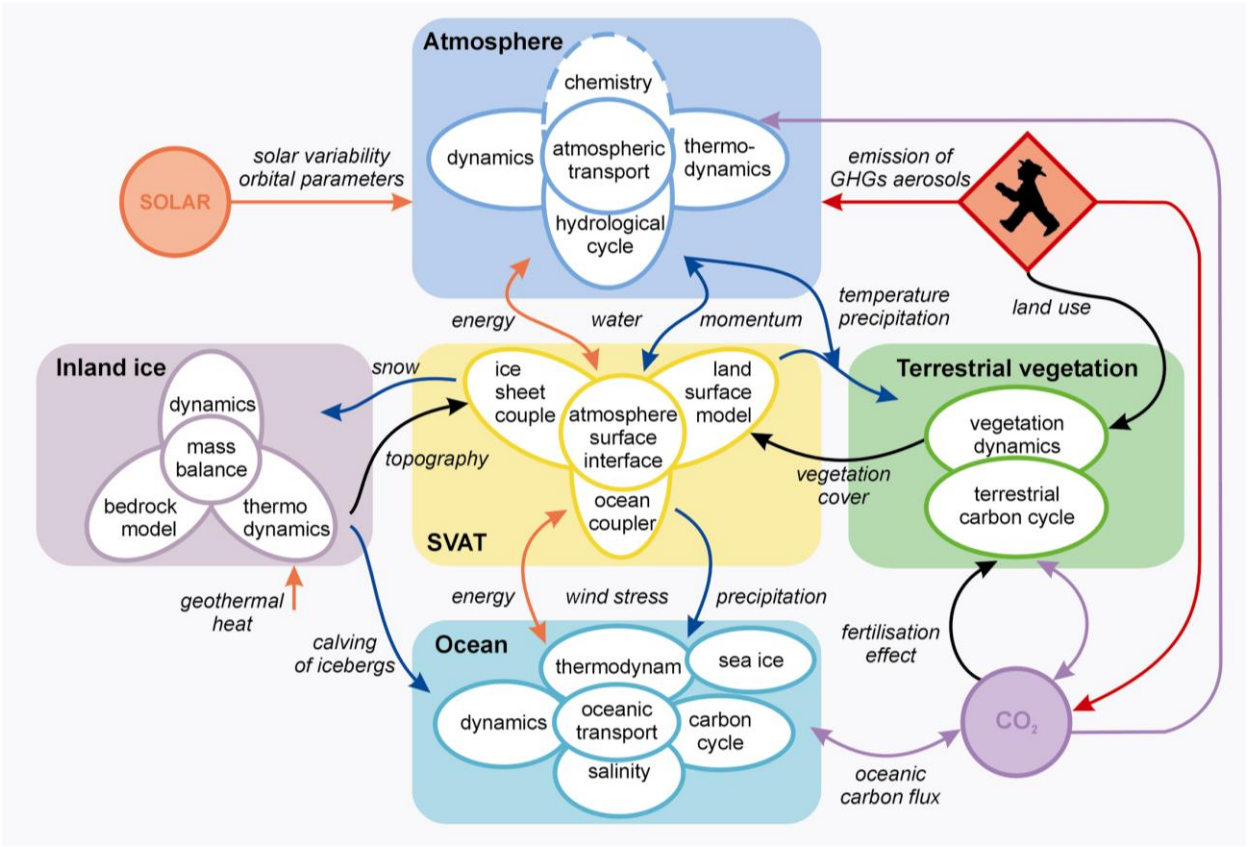

Fig. 28 Correlations and interactions of climatic factors and processes as realised in the climate system model CLIMBER /PET 00/

With respect to the different purpose of their application different kinds of climate models have been developed, which, generally, can be divided into three groups:

- Simple, conceptual models
- Complex, comprehensive models
- Models of intermediate complexity

In the group of simple models belong for example energy balance and radiation convection models. The spatial dissolution of these models is usually low, mostly they are one dimensional or so-called box models, i.e. different compartments like the ocean or the atmosphere are treated as a single box. Furthermore, the number of processes described is relatively low. They are simple mechanistic models usually applied to demonstrate the plausibility of processes /CLA 02/. Paillard presented two simple multi-state models that successfully simulated all glacial-interglacial cycles (of different temporal extension), over the

last one million years with correct time and approximately correct amplitude /PAI 98/. The model assumed different stages for the climate and a transition between each stage triggered, when the summer insolation in 65° northern latitude reaches a specific threshold value.

The so-called Coupled General Circulation Models (GCMs or CGCMs) for the atmosphere and the ocean including ice sheets are considered today as the most comprehensive type of climate models available. Typically, these models have spatial solutions with grid lengths of 100 - 200 km and consider a large spectrum of variables and processes in great detail /KUB 00/. They are based on conservation equations of mass, impulse, energy and water vapour. The complex models usually describe circulation in the atmosphere and the ocean three dimensional including specific flow patterns like regional currents in the ocean /CLA 02/. The coupling between ocean and atmosphere is dynamically, i.e. flow of impulse, heat and water is exchanged, ideally in each time step. More and more a detailed modelling of external forces like anthropogenic occurrence of aerosols and greenhouse gases are implemented. Some of them also include dynamic vegetation and atmosphere chemistry modules. These models are able to describe the climate processes in great detail and are especially applied for studies where high spatial dissolution is needed. However due to the high computing times they are usually restricted to shorter time scales of few tens of years.

In order to bridge the gap between the simple box models and the complex GCMs so-called Earth system Models of Intermediate Complexity (EMICs) have been developed. EMICs describe a similar number of processes as the complex GCMs, often not explicitly but in a simplified, parameterised form. Furthermore the description of the dynamics is mostly simpler than in GCMs. However, a large bandwidth of different EMICs exist /CLA 02/. The EMICs also consist of an atmosphere and an ocean module, but there is a large difference in the treatment of the atmosphere and ocean systems. The description of atmosphere and ocean in a number of models is reduced to two dimensions. For the atmosphere sometimes the 2D-systems distinguish between a limited number of layers. The ocean models are usually divided into two-dimensional boxes for the Pacific, Atlantic and Indian ocean. Only few describe a global vegetation dynamics /CLA 02/.

Additionally for the EMICS a reduced spatial resolution - typically grids of 500 to 1000 km length - is used for the calculations. As a consequence the computing time is significantly reduced compared to GCMs, which enables EMICs to perform long-term calculations up to time scales of several 100,000 years, or to explore the potential sensitivity of the climate to a

particular process over a wide range of parameters, e.g. /GAN 01/. Otherwise EMICs cannot be used for calculation of regional climates, where a high spatial dissolution is needed.

The different kinds of models are developed for different purposes and complement each other. As discussed above EMICs are applicable to very long timescales. Thus they can be used to screen the historical and future climates and to identify interesting points in time, which can then be analysed by complex general circulation models in detail. Such a strategy was chosen in the European project BIOCLIM /TEX 03/. Transient climate calculations for the next 200,000 years have been performed with EMICs. For the boundary conditions chosen in this study these calculations identified the occurrence of at least two quite extreme climate conditions, worth to investigate their regional impact:

- a “super-interglacial condition” 67,000 years from now, due to the simultaneous occurrence of an increased summer insolation, a high atmospheric CO_2 concentration and no ice sheets in the Northern hemisphere, and
- a widespread glaciation in the Northern Hemisphere 178,000 years from now characterised by a CO_2 concentration in the atmosphere of pre-industrial level and occurrence of large Laurentide and Fennoscandian ice sheets.

For both discrete future states calculations with complex GCMs have been performed to evaluate more detailed global or regional climatic patterns in Europe including the vegetation states for such extreme climate conditions.

Model verification and qualification is done by intercomparison of test case calculations with other models and by comparison with measured data. For the long timescales considered here, the information from paleodata, in particular the information received from ice cores are valuable to compare e.g. global temperature characteristics for the past several 100,000 years with the results from model calculations, e.g. /PAI 98/.

4 Potential future climate changes

The difficulty in coupling of the many parameters as well as in dealing with large areas and long periods of time is still topical and thus the object of research of many national and international projects. For their studies, climate researchers use data from so-called climate archives (see Chapter 2.3). First, the data were used to derive regularities and to project them into the future. Corresponding statements of important paleontologists are briefly described in the next chapter. Current climate predictions, however, are based on complex model calculations in which the paleodata are used as input data and for model calibration (see chapter 3). The following chapters summarise the results of current projects investigating potential future climate evolutions over very long time frames, in particular model calculations performed by national and international groups.

4.1 Conclusions from past climate cycles

In part, climate predictions made only on the basis of conclusions drawn from past climate cycles differ considerably from those made on the basis of model calculations for climate scenarios. *Emiliani* was the first to discover by means of oxygen-isotope analyses on foraminifera in deep sea cores an astonishing regularity between the previous interglacial maxima and glacial minima although it is known that intermittent short-term temperature changes caused by volcanic eruptions or sudden discharge of large glacial freshwater lakes often occurred /EMI 57/. Accordingly, the change between an interglacial maximum and a glacial minimum showed a periodicity of about 100,000 to 120,000 years per glacial cycle. In the past 500,000 years, the interglacial lasted about 10,000 to 15,000 years. Moreover, as discussed in chapter 3 the climate changed cyclical during the past 500,000 years but was dominated by cold conditions /PAG 01/. According to *Emiliani's* opinion, the current temperature increase caused by the elevated atmospheric CO_2 concentration will also not have a long-term influence on the climate. Consequently, he assumes that the maximum of the next glacial will occur in about 20,000 years. In 1972, a considerable number of hydrogeologists were also of the opinion that the present so-called Flandrian Interglacial – lasting for 11,500 years by now – is already in the late phase.

Other authors also assume that the cooling interrupted by the effect of the greenhouse gases CO_2, CH_4, N_2O, O_3 and chlorofluorocarbons (CFC) will already continue in less than 1,000 years. According to *Seiler*, an average annual temperature of -18°C would already have been reached by now, i.e. more than 33°C below today's value, without the existence of

the atmospheric greenhouse gases /SEI 03/. The view that the climate without further anthropogenic CO_2 emissions will develop towards a glacial of “medium intensity” in the next 3,000 to 4,000 years – corresponding to the typical periods of transition from interglacial to glacial - with maximum impacts as during the Weichselian glacial is also held in /EHR 86/, /SCH 74/ and /SIR 02 /.

4.2 Results from model calculations

Due to the complexity of the model calculations (see chapter 3) and the associated necessity of using mainframe computers, the number of research centres which are able to perform long-term climate calculations is low. The main institutions in Germany dealing with this topic are, above all, the Potsdam Institute for Climate Impact Research (PIK), the German Climate Computing Centre (DKRZ) as well as the Alfred Wegener Institute for Polar and Marine Research (AWI) and the Max Planck Institute for Meteorology (MPI-M). World-wide, model calculations over extremely long periods of some 100,000 years are only performed by a few working groups, e.g. of Paillard (CEA/DSM) and Ganopolski (PIK).

4.2.1 Global climate changes

The first climate predictions over long periods were based on statistical regularities derived from past climates, e.g. /TEX 03/. These predicted that the beginning of cooling about 6,000 years ago will continue and lead to a next cold interval in about 25,000 years with glaciation beginning in about 55,000 years /DAH 98/, /BER 02/.

The first climate model calculations in the eighties showed, under consideration of a constant, average CO_2 content of 230 ppm, similar results /BER 97/. Due to the fact that the climatic conditions closely correlate with the varying concentrations of the atmospheric CO_2 /PET 99/, /BER 02/, more recent climate models consider, in addition to the external factor insolation, also the change and the influence of the atmospheric CO_2 concentrations. These model calculations show a long-lasting influence of the currently increased CO_2 content on the climate so that, as a consequence, today’s interglacial climate is prolonged to at least 55,000 years. In scenarios with very high CO_2 emissions in the next decades/centuries, the onset of the next glacial event is not expected before 178,000 years, in an extreme scenario not before 500,000 years /BIO 01/, /ARC 05/.

Model calculations on long-term climate developments were performed, e.g., by Archer et al /ARC 05a/ and within the framework of the BIOCLIM study /BIO 01b/. The results of Archer et al, calculated with the CLIMBER-2 model on the influence of the anthropogenic CO_2 emissions, are presented in Fig. 29. The calculations consider four different scenarios on CO_2 emissions /ARC 05b/:

- Natural conditions without anthropogenic CO_2 emissions (280 ppmv CO_2; shown in green),
- emissions of 300 Gt CO_2, equivalent to the amounts already emitted today (shown in blue),
- emissions of 1,000 Gt CO_2 (shown in orange), and
- emissions of 5,000 Gt CO_2, equivalent to the estimated fossil resources still existing on Earth (shown in red).

The resulting curves of the CO_2 partial pressure are represented in of Fig. 29 a. In scenarios with very high CO_2 emissions, increased CO_2 concentrations in the atmosphere still occur over periods of several 100,000 years.

The evaluation of the paleoclimatic data and accompanying model calculations showed that the onset of ice ages in the northern hemisphere – at least within the past 800,000 years – was correlated with insolation minima in summer in 65°N and that there was a transition into an ice age when insolation fell below a critical value of about 480 W m^{-2}. An increase of CO_2 has the effect that a transition to an ice age only takes place if the value of insolation is even lower. Fig. 29 b therefore shows the solar minima in June in 65°N calculated from orbital parameters for the last and next 500,000 years (in units of the standard deviation σ; 1 σ equals 20 W m^{-2} /ARC 05a/). The green, blue, orange and red curves show for the different CO_2 emissions the values of the insolation minima which lead to a transition into an ice age. It can be seen that the present solar minimum of about 0.7 σ exceeds all curves and thus does not fall below the value of 480 W m^{-2} which will not occur before the next minimum in about 50,000 years. In scenarios with CO_2 emissions of 1,000 and 5,000 Gt, the critical value of insolation subsides to such an extent that also at this time there will be no transition to an ice age.

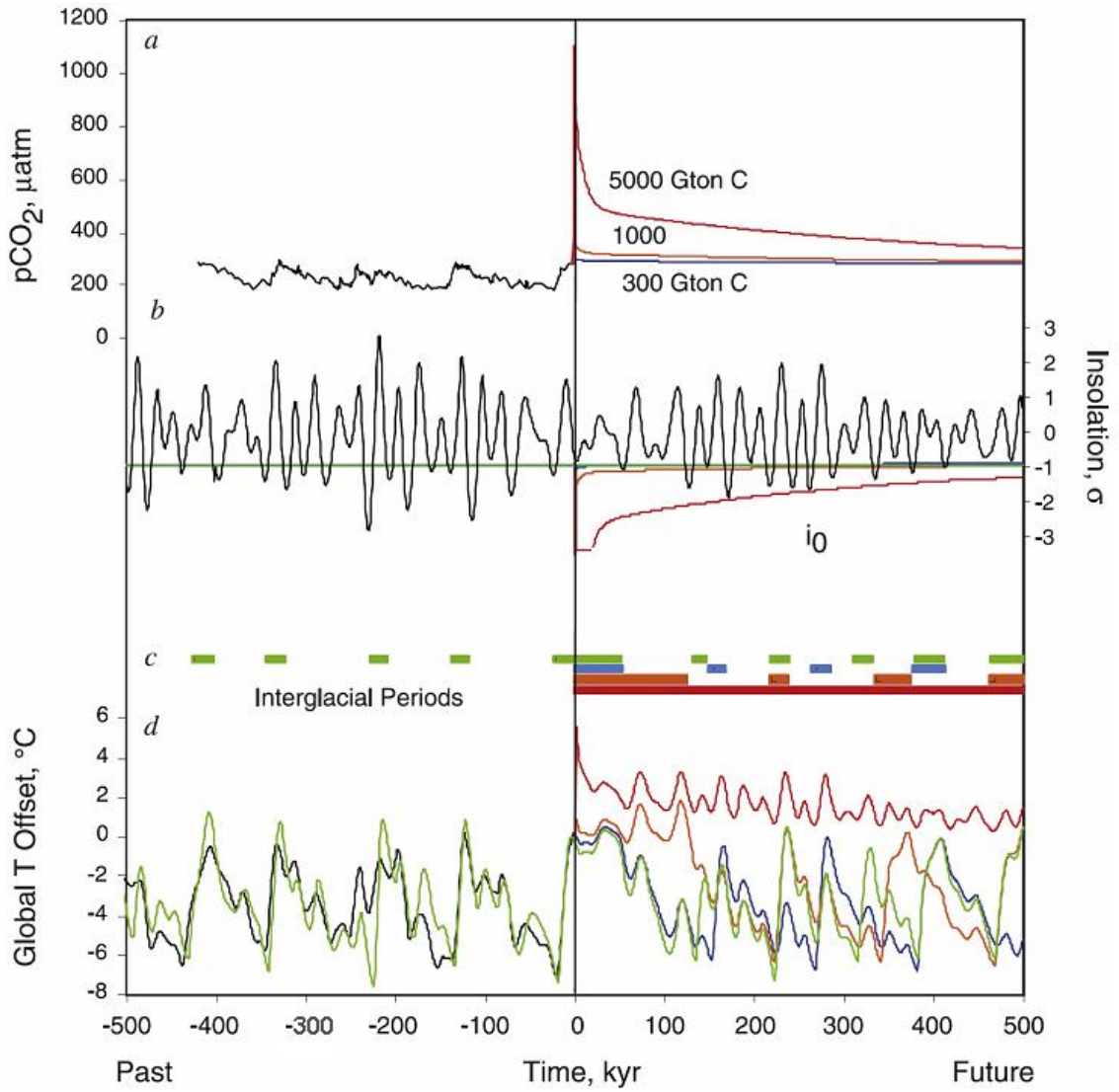

Fig. 29 Influence of fossil CO_2 emissions into the atmosphere of the long-term climate development. a) CO_2 partial pressure, b) insolation in June in 65°N and evolution of the values of the critical solar minimum, c) interglacial periods and d) average global temperature in dependence of the respective scenario. Further details are given in the text /ARC 05a/

The corresponding results are presented in Fig. 29 c and d in form of occurrence and duration of interglacial periods as well as the evolution of the average global temperature. They demonstrate the long-lasting influence of CO_2 on the climate. Accordingly, under natural conditions and in case of emissions up to 300 Gt C, no new glacial is to be expected in the next 50,000 years. According to the calculations, emissions of 1,000 Gt C would have the effect that the next glacial will not occur after about 170,000 years. Emissions of 5,000 Gt C would even prevent the beginning of the glacial over the next 500,000 years.

At least the results for the next 50,000 years are also supported by the works of other authors. As discussed in chapter 2 eccentricity within the next 50,000 years will be very low and, as a consequence, the impacts of changes in precession and obliquity of the ecliptic are not sufficient to generate a distinct solar minimum so that the onset of a new glacial during this period is not to be regarded as probable, e.g. /LOU 00/.

A study performed with the Canadian climate circulation model of Peltier and Vettoretti also shows that the climate system will need about 50,000 years to compensate the anthropogenic influence from the early third millennium /VET 04/. Under the conditions of today's insolation and the pre-industrial CO_2 concentration, the beginning of a new glacial during this period is also not possible according to their model. Only if assuming CO_2 concentrations below 220 ppmv, which are regarded as unrealistically low, there would be an earlier transition into the next glacial.

Almost all climate models predict a significant warming in Europe in the next centuries. According to the respective studies, an increase in the average global temperature will be between 1.5°C and 6°C. BIOCLIM calculates a global temperature increase between 2°C and 5.5°C, the IPCC study expects an average warming of 1.5°C to 6.0°C compared to today's value already in the next 100 years /IPC 07/. According to model calculations of the Royal Netherlands Meteorological Institute (KNMI), there will be a temperature increase of 3°C to 5°C by the end of the 21st century. The global temperatures will then rise by 3°C to 9°C in summer and by about 4.5°C in winter. For higher latitudes it is expected that the temperature increase will be larger by a factor of 2 than in the lower latitudes. Consequently, a temperature increase of at least 5°C on an annual average is expected for Germany.

4.2.2 Regional climate changes in Northern Germany

4.2.2.1 Results of the BIOCLIM project

The BIOCLIM project (Modelling sequential BIOsphere systems under CLIMate change for radioactive waste disposal) was performed within the 5th Framework Programme of the European Commission and had the objective to investigate regional climate changes and their impacts on the biosphere in potential European repository regions /BIO 04/. Central England, Northeast France and Central Spain were selected as main regions. For the regions Northern Germany and the Czech, less detailed studies were performed. The studies

comprise both specific climate sequences and continuous climate sequences over at least one glacial cycle.

For the climate simulations, the global climate change was predicted as a first step with less complex models over periods of some 100,000 years. As a next step, detailed model calculations were performed for the regions Central England, Northeast France and Central Spain with complex climate models for selected time spans.

Further, transient calculations were performed for scenarios with various amounts of anthropogenic CO_2 emissions over the next 200,000 years. Therefore the following developments of CO_2 were taken into consideration:

- Natural variations of the CO_2 content without post-industrial emissions by combustion of fossil energy carriers (BIOCLIM A4 scenario),
- natural variations of the CO_2 content, including a small contribution by combustion of fossil energy carriers (BIOCLIM B3 scenario), and
- natural variations of the CO_2 content, including a large contribution by combustion of fossil energy carriers (BIOCLIM B4 scenario).

The climate sequences constructed for Northern Germany over a period of 200,000 years, with indication of the resulting climate classification and, in particular, special characteristics with regard to precipitation and temperature, are presented in Tab. 10.

It becomes obvious that higher CO_2 contents result in a larger temperature rise in the first tens of thousands of years. As a consequence, a partial or complete melting of the Greenland glacier and a resulting sea level rise by up to 7 m is expected in the next centuries /BIO 04/. Due to its location, the German region will only be affected indirectly by the sea level rise. Should, however, the Elbe not have a dam as flood protection downstream, it could relatively easily reached by a flood wave /BIO 04/.

After about 20 ka AP, the scenario sequences are relatively similar although the year-round temperatures of the A4 scenario are 1°C to 2°C lower than in the B3 scenario. The model results show that in the course of the next 200,000 years, Northern Germany will be dominated by a Cfb climate. This will only be replaced temporarily by a Df climate which, according to the models, occurs around 100,000, 150,000, 170,000 and 190,000 years AP or in the B4 scenario also by a Cs climate until about 20,000 or possibly until 90,000 and

around 130,000 years AP. The potential climates and their impacts on biosphere and landscape can be summarised as follows:

- Cfb climate / Df climate: biosphere and landscape similar to today's conditions.
- Cfb- / Cs climate: biosphere and landscape similar to today's conditions, but with 3°C to 5°C higher July temperatures.
- Cfb climate: biosphere and landscape similar to today's conditions, but with colder winters and warmer summers due to the more continental climate.

The duration of transition between the various climate classes is very different. Between climate conditions 1) and 2), it is a few hundred years whereas those between 2) and 1) as well as between 3) and 4) or 4) and 3) are in the range of 10,000 years.

With the MoBidiC model /CRU 02/, lower winter temperatures were calculated over the entire period than with the CLIMBER model /PET 00/. These, however, led at no time, not even during the coldest period between 170,000 and 180,000 years AP, to glaciations or permafrost conditions in the site region. However, during the cold period around 170 ka AP, the growing ice shield results in an eustatic lowering of the global sea level by 60 m and retreat of the coastline of the North Sea. This will lead to a more continental climate in the site region.

The climate change predicted for Northern Germany has direct impacts, e.g. in form of the length of the vegetation period but also indirect impacts, e.g. by a change in the hydraulic situation and the soil water budget. In some of the scenarios of the BIOCLIM study, a water flow velocity in the Elbe is expected during some month that is more than twice as fast. Due to the low relief, it leads less to its deepening but rather to a broadening of the river bed. Due to the higher winter precipitations, the number of floods increases during this time while those in spring will decrease as a result of the smaller amount of snowmelt waters. The small amount of water carried in summer leads to meandering over the entire surface of the new river bed. The changed annual precipitation amount and distribution lead to a reduced groundwater recharge. Further, it is assumed that during the Cfb climate from May to August, there is a water deficit which is compensated over the year by excess water during the winter months while those of the Cs climates between April and September will not be compensated /BIO 04/.

Tab. 10 Potential climate sequences constructed for Northern Germany /BIO 04/

<table>
<tr><th>ka AP</th><th>A4</th><th>B3</th><th>B4</th></tr>
<tr><td rowspan="2">until ~20</td><td rowspan="2">Cfb climate:
temperatures and precipitation rate similar to those of today:
summer temperatures 13°C - 23°C
winter temperatures -1,5°C - 2°C</td><td colspan="2">rapid temperature rise => Cs climate
sea level rise by up to 7 m</td></tr>
<tr><td>summer and winter temperatures are 4°C - 5°C higher than those of today
dryer summers
wetter winters
annual precipitation increases by ~30%</td><td>average annual temperature rises from 10°C to 15°C - 17°C
annual temperature amplitude is, as today, 17°C - 18°C
annual precipitation remains the same but distribution changes:
(winter precipitation increases by 1 mm/d, summer precipitation decreases by 0.3 mm/d – 1.7 mm/d)
very small change in topography
more frequent floods, change of the river beds
reduced groundwater recharge</td></tr>
<tr><td rowspan="2">until ~90</td><td rowspan="2">Cfb climate</td><td colspan="2">temperature drop
=> Cfb or Cs climate
summer and winter temperatures higher than today, summers are getting dryer and the early winters wetter, the total precipitation increases up to 30%</td></tr>
<tr><td colspan="2">Cfb climate: cold summers</td></tr>
<tr><td>until ~100</td><td>Cfb climate ⇔ short phases Df climate cooling, above all in summer (temperature of the warmest month: 15°C - 16°C, winter temperature around 0°C), wetter summers</td><td colspan="2">Df climate</td></tr>
<tr><td>until ~120</td><td>Cfb climate: summer temperature 20-22°C</td><td colspan="2"></td></tr>
<tr><td>until ~130</td><td>Cfb climate: summer temperature 16°C</td><td colspan="2">temperature rise => Cfb climate ⇔ Cs climate</td></tr>
<tr><td>until ~137</td><td>Cfb climate: summer temperature > 20°C</td><td colspan="2" rowspan="5">cooling => Df climate (more continental)
=> vegetation period: 1 - 3 months
=> 3°C - 4°C lower summer temperatures
=> winter temperature around 0°C</td></tr>
<tr><td>until ~147</td><td>Cfb climate: summer temperature < 15°C</td></tr>
<tr><td>until ~150</td><td>Df climate</td></tr>
<tr><td>until ~160</td><td>Cfb climate: summer temperature ~23°C</td></tr>
<tr><td>until ~170</td><td>Df climate: summer temperature: ~13°C, winter temperature: 2°C</td></tr>
<tr><td></td><td colspan="3">formation of continental ice shields => sea level drop by about 60 m</td></tr>
<tr><td>> 182</td><td></td><td colspan="2">warming => app. today’s temperatures</td></tr>
<tr><td>> 190</td><td></td><td>Df climate</td><td></td></tr>
</table>

The climate predictions indicate that there will be no soils without vegetation during the period under consideration. Moreover, the soil properties will not change to that degree during the next 200,000 years as in the past 200,000 years if climate changes will be less extensive and, above all, there will almost be no cold climate conditions /BIO 04/.

The low relief in the site area as well as the year-round existence of vegetation ensure that there is only a low erosion and the soil is both protected against frost and heat which prevents large variations in the soil temperature. On most of the surfaces in the site area, however, the natural soil development to be expected leads to podsolisation /BIO 04/. This development is strongest in the course of cold climates, i.e. according to the BIOCLIM calculations around 170,000 years AP because the eluviation of nutrients from the sandy soil progresses particularly rapid then. The pH value of these soils decreases to about 4. In former times, they were enriched with peat, sods, river sediments or sludge from waste water to enable agriculture. The soil is then referred to as anthrosol. Its formation is rather expected during the warmer climates, i.e. in particular in the first millennia AP because during the transition to a colder climate animal husbandry would be preferred to agriculture. Besides podsol and anthrosol, gleys (e.g. histosols) are formed in the flood areas of the rivers due to the water impact /BIO 04/. Loamy luvisols or cambisols are found seldom /BIO 04/.

By anthropogenic influence on the soil water budgets, the growth phases of certain plants can, in dependence of the temperature, be improved, prolonged or made possible at all. In climate class Df, an improvement of the soil water budget is achieved by means of drainage activities and in climate class Cs by irrigation activities. To increase harvest of certain plants with better quality, irrigation measures are also performed in climate class Cf despite the balanced water budget over the year /BIO 04/.

4.2.2.2 Results of other studies

In addition to regional climate calculations, such on partial aspects of the climate, as e.g. the formation of a permafrost soil or of entire ice shields, and on changes of the Gulf Stream are also performed.

The **formation of the Scandinavian ice shield** and its movement were modelled, among others, by Delisle /DEL 91/. It is generally agreed that the development of a glacier to a great extent depends on the annual precipitation rate. Since a cold climate reduces the moisture

content in the air and thus precipitation, it counteracts the growth and the movement of a glacier. The calculations show that the Scandinavian glacier with only small lateral movement first has to reach a certain thickness for lateral extension. During the Weichselian glacial, the ice shield only extended laterally by about 200 km within 6,000 years after having reached a thickness of nearly 3 km in the centre. It is therefore to be expected that the glacier will reach Northern Germany only with considerable delay.

Further, Delisle performed calculations regarding the **development of permafrost** /DEL 08/. These calculations considered, on the one hand, the processes of heat transfer through the rock mass and, on the other hand, the release or absorption of latent heat at the freezing or melting front on the basis of paleotemperature curves. In 1998, the development of the permafrost soil in the past was investigated for the area under consideration. The frost depth of the soil is thus mainly influenced by the average surface temperature and the existence of lakes and rivers. For the past, five different permafrost phases with maximum depths between 40 m and 140 m were simulated (see Fig. 43, chapter 6.2).

A **sea level rise** by about 20 m to 30 m within the next 50,000 years as consequence of the temperature increase is also regarded as probable /GAN 07/. This comprises the sea level rise caused by the melting of all inland glaciers (about. 0.5 m), the Greenland glacier (5 - 7 m) and the West Antarctic (16 - 18 m) as well as by the temperature-induced water extension (some meters). The amount of waters released during melting of the entire Antarctic would correspond to a sea level rise of 60 m and would lead to an overall rise of more than 70 m. This scenario, however, is currently being regarded as somewhat unlikely. Moreover, the ice stability of the West Antarctic is an uncertain parameter. The West Antarctic consists of shelf ice. For this reason, its ice stability depends on the sea level. Due to the density difference of the sea water, the rise of the sea level is locally very different.

In the area influenced by the North Atlantic Deep Water flow as part of the **Gulf Stream**, the release of large amounts of freshwater by melting of the glaciers could lead to a dilution of the sea water and thus to a reduction of the surface water density. Since a high density of the surface water in the Northwest Atlantic is the prerequisite for the so-called thermohaline circulation, shutdown but at least a change of the thermohaline circulation in form of flow deflection can occur. According to model calculations, a noticeable weakening of the North Atlantic Current will only occur in the next decades and its interruption at the earliest in 2100 under the most conservative assumptions /RAH 07/. For this case, *Schiller et al.* in /GOO 99/ simulated a cooling of the water surface of the North Atlantic near to the European coast by 8.5°C as a maximum and temperature decreases in Northwest Europe by about 5°C.

According to *Ganopolski*, a maximum temperature decrease of 12°C could occur in large parts of Central and Northern Europe /GAN 07/. Due to the short duration of this event of about 1,000 years and the continuing temperature rise in all other parts of the Earth resulting from the greenhouse gases in the atmosphere, the temperature decrease does not lead to a new ice age again. But a small ice shield within Scandinavia would be possible /GAN 07/.

Another aspect is the modelling of **biosphere processes**. On the basis of the climate prediction for Northern Germany performed within the framework of the BIOCLIM study, GRS compiled resulting biosphere models /BEC 03/. In addition to the Cf, Cs and Df climates, the impacts of an ET and Dw climate were also investigated. The changing distance of the site to the sea resulting from the development of the sea level has not been taken into consideration.

4.3 Conclusions on future climate development

Due to the number of factors involved and their complex interactions, predictions on the climatic development over very long periods of time are subject to large uncertainties. Nevertheless, there are some working groups which perform model calculations on climate changes over periods of some 100,000 years. The most important parameters influencing climate evolution over such periods of time are the orbital parameters with their influence on insolation, ice or snow covers of land and their behaviour during a climate change as well as the CO_2 content which, in particular, plays an important role for glacier formation in times with insolation minima.

Formerly assumed maxima of the next ice age in 10,000 years or 20,000 years, mainly based on an analysis of paleodata and regularities derived from it, are not regarded as very likely and are even not expected within the next 50,000 years in view of the high CO_2 concentrations and the low amplitude of insolation. The statements of most of the more recent studies agree that the present interglacial will not be followed by the next glacial in the next tens of thousands of years. However, the intensity and length of the interglacial is closely related to CO_2 concentration in the atmosphere developing in the future. According to some studies, the consideration of anthropogenic CO_2 emissions into the atmosphere shows a very long-lasting effect of the CO_2 on the climate. If only assuming insolation conditions based on the orbital parameters – the Milankovitch cycles – and today's CO_2 concentrations, the present interglacial will last for further 50,000 years and will lead to further warming in Europe in the next centuries. For scenarios with high anthropogenic CO_2 emissions in the

next decades to centuries, model calculations show a time for transition into the next glacial only after 170,000 years, in case of extreme concentrations (combustions of all fossil energy carriers presently existing) even only after 500,000 years.

There is some agreement that the extent of the next glacial will be the same as or less than the Weichselian glacial. Due to the eustatic lowering of the sea level by about 60 m resulting from the formation of continental ice shields, the coastline will then retreat. It is not to be expected in this cases that there will be glaciations at the area under consideration. Permafrost conditions, however, are very likely.

There are only very few studies on climate changes beyond 200,000 years. As far as there will be no extremely high CO_2 emissions during the next centuries, it is plausible to assume that over such periods of time similar glacial-interglacial cycles as in the geological past of the Quaternary will occur, i.e. glacial periods of about 100,000 years and interglacial periods of about 10,000 years. Glaciations at the area considered, as they occurred during the Elsterian and Saalian glaciation, are of course possible.

The degree of the sea level rise during temperature increase depends on which glaciers melt. In case of melting of all inland glaciers, the Greenland glacier, the West Antarctic and of temperature-induced water extension, a sea level is to be expected that is 20 - 30 m higher than today. For the unlikely case of melting of the entire Antarctic glacier, the rise would be about 70 m.

The response to the rising global summer temperatures and rising winter temperatures until the end of the 21st century would be, on the one hand, the intensification of the hydrological cycle with an increased run-off and, on the other hand, an increased amount of freshwater due to the melting glaciers. The globally averaged precipitation amount could then increase by more than 10%. Precipitation events would not continue to be mainly characterised by front passages with long-lasting and widely distributed rain but increasingly by convective processes leading to locally limited thunderstorms with intensive rains and hail. As a consequence, the temperatures and precipitation amounts will be increasingly subject to a regional differentiation.

Several colder periods are expected within the warm period with a temperature decrease by 3°C to 4°C in summer which are due, e.g., to the weakening of the North Atlantic Current resulting from the lower density of the surface water caused by melt water and warming. However, such a shutdown of the thermohaline circulation is not to be expected during the

next decades and would not last more than 1,000 years. It could make the formation of a small ice shield in Scandinavia possible. In Germany, however, they neither lead to periglacial or even glacial conditions due to the duration of the cold periods and their small temperature decline.

5 The reference site Gorleben

5.1 Geographical position

The salt dome Gorleben is situated one half each in the federal states Lower Saxony and Brandenburg. It extends in southwest-northeast direction over a distance of about 14 km and is crossed in its course by both the river Elbe and its tributaries Löcknitz and Seege. About 2 km south of the Elbe, the pilot mine of the salt dome Gorleben is situated, see Fig. 30.

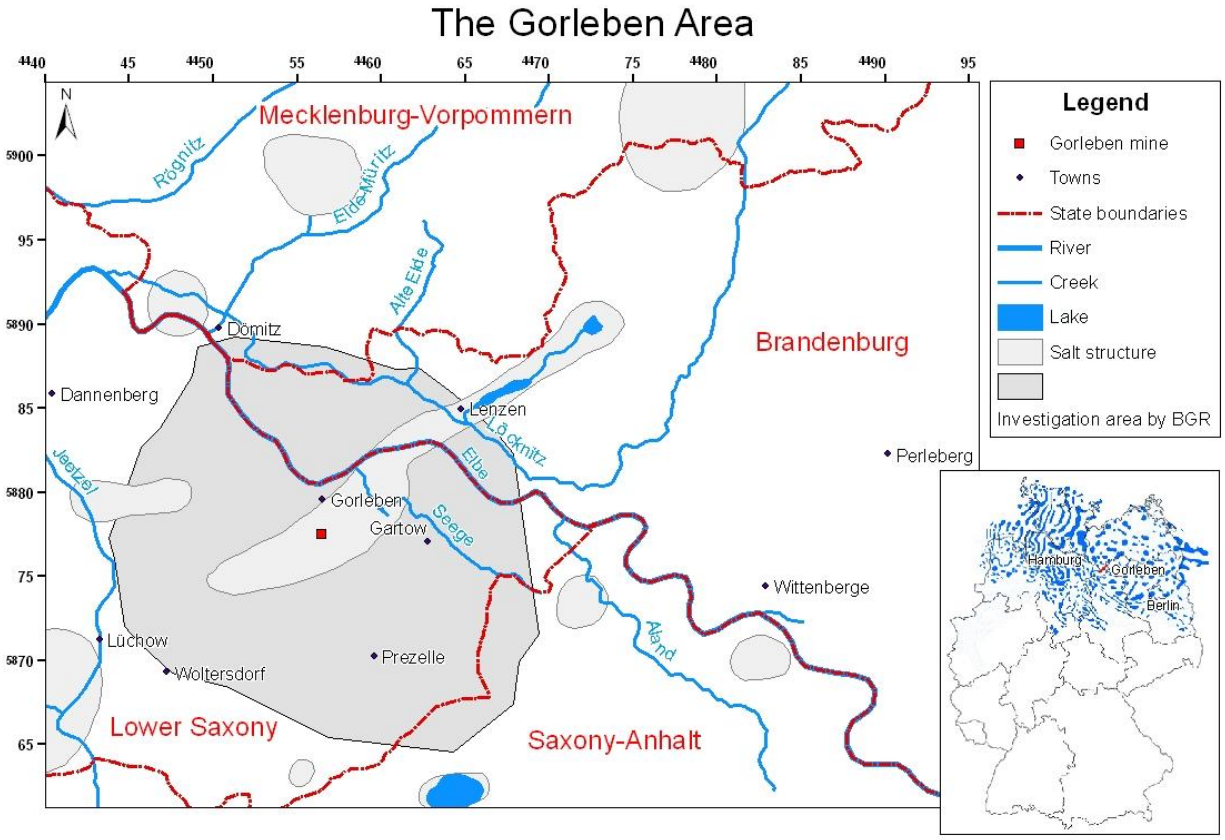

Fig. 30 Position of the salt dome Gorleben /FLU 09/

The area above the salt dome was severely superimposed by glacier advances of the Quaternary and can therefore be distinguished in different biogeographical units /DUP 83/. During the Saalian glaciation a landscape consisting of older moraines was formed first. The mountain range of the Drawehn, which reaches up to 142 m a.s.l., as well as the plateaus of Öring, Lemgow and Lagendorf, which are partly formed of push moraines and have a height of about 50 m a.s.l., and of the 76 m a.s.l. high Höhbeck are among them. During the following Weichselian glaciations, the Elbe river bed served as glacial valley. Today, the

lower terrace sands take up the greatest part of the Elbe lowland and are situated in a height of about 15 m a.s.l. to 20 m. a.s.l. Subsequent to the glaciation, the Elbe floodplain deepens into the lower terrace sands. In preferential locations up to 5 m high layers of drift sand were accumulated /KLI 02/.

The genesis of the different biogeographical units led to the deposition of several sediments, see Fig. 31. Characteristic soils developed depending on these sediments as well as on location factors. The soils again have influence on the actual land use in the region. In the Holocene lowlands, mainly alluvial clay and fluviatile sands are found out of which preferably gleys emerge. Formation of fens and peats occurred sporadically. Today, they are used as grassland where possible. Wetlands are found here otherwise. Mainly Luvisols (Grey forests soil/Albeluvisol) emerged out of the clayey ground moraine material of the Saalian glaciation, which consisted primarily of drift and boulder clay /BIO 01b/. In the area of the former glacial valley, gravels and sands deposited by melt water are preferentially found. These fluviatile sediments are partly covered by drift sands with a thickness of up to 2 m. Podsols emerged out of these sediments. These areas are used today for agricultural and forestry purposes depending on their topography and their nutrient content. The region is sparsely populated and no production plants worth mentioning exist here.

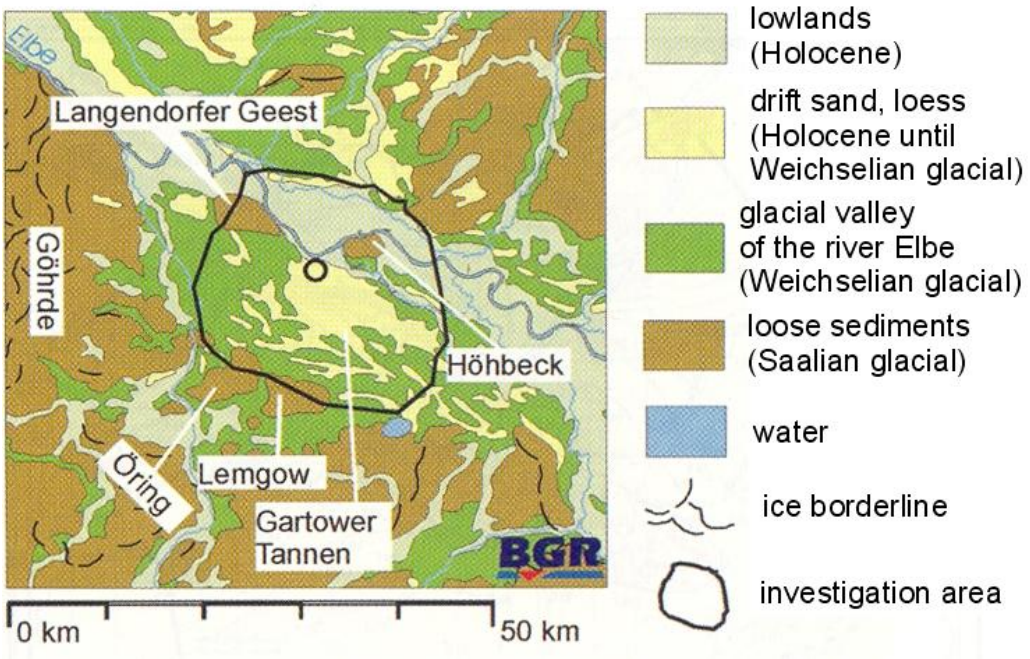

Fig. 31 Biogeographical units in the vicinity of the reference site based on /LUD 02/

5.2 Geology

The area is geologically characterised in essence by the salt dome Gorleben and the Gorleben Channel which was formed during the Elsterian glaciation. In no other channel in Northern Germany, as many exploration boreholes were drilled as in the Gorleben Channel which extends to a depth of 309 m b.s.l. Its evolution was determined by salt and glacier ice and its melt water /DUP 83/. The salt dome was also explicitly investigated. This was mainly done by measurements employing seismic reflection and seismic refraction as well as drillings /JAR 80/, /KOE 07/.

A simplified geological profile of the salt dome and its closer surroundings is shown in Fig. 32. Near the surface, Quaternary sediments of the about 300 m deep Elsterian glacial meltwater trough, of the Saalian end and push moraines, of the Weichselian Elbe glacial valley and of the Holocene Elbe floodplains are found. The deeper bedrock comprises the salt dome, which rises up to 100 m below the surface, and its rim syncline, in which Mesozoic sediments of the Triassic and the Cretaceous period with a thickness of 1,000 m to 2,500 m are deposited superposed by Tertiary sediments. The basement of the salt dome is situated on average in a depth of about 3,200 m /EHR 86/.

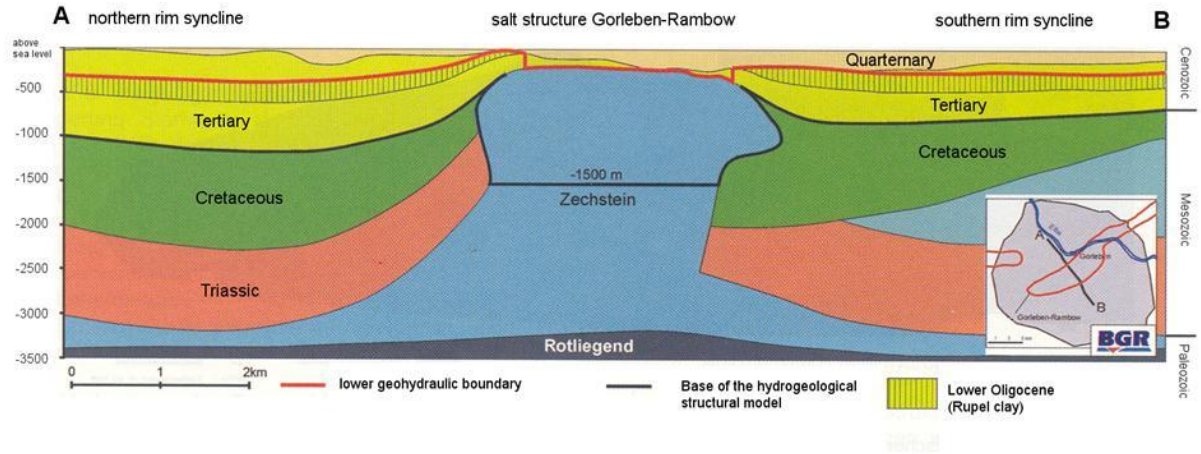

Fig. 32 Simplified geological profile of the salt dome Gorleben and its closer surroundings /LUD 02/

5.2.1 Zechstein to Cretaceous

The area is situated in the Pompeckj Block within a very old tectonic depression field, the so-called Northern German Depression, which was subjected to severe and frequent uplifts and subsidences in the course of geologic history. Due to the subsidence, sea transgressions of the Zechstein and Holstein Sea respectively, which took place again and again far on land, occurred via the Elbe Bay during the time between the Permian (about 250 million years BP) and the Quaternary (about 300,000 years BP). During the Permian, the inundated Northern German Depression was temporarily cut off from the ocean owing to the uplift of the area. Due to arid climatic conditions, sea water in the border sea was in this time subject to high evaporation, and the carbonates and salts contained in the water precipitated according to the magnitude of their solubility: after the deposition of clay, firstly lime and dolomite, then anhydrite or gypsum, then rock salt and lastly potash salts. This saliniferous cycle recurred four times in the Zechstein Sea. However, the cycles were not always completed. In the reference site, the Zechstein 2 (Stassfurt series) and the Zechstein 3 (Leine series) are developed the most completely.

The mass flow of the Zechstein salts, due to the plastic properties of rock salt occurred under the high pressure of the overlying rock. This process began during the Triassic and lead to the forming of the salt dome. Already in the Keuper, the Late Triassic, a great salt pillow was formed in the underground of Gorleben. A diapiric break-through of the Gorleben salt dome occurred in the Upper Jurassic and the Lower Cretaceous, more than 100 million years ago. Firstly, the salt came from the south-eastern flank. Since the Upper Cretaceous (about 65 - 100 million years before today) the influx of salt took place additionally from the north-western flank. The investigations concerning the elevation velocity of salt domes in North-Western Germany show that the maximal elevation rate during the diapir phase was between less than 0.1 and about 0.5 mm per year /JAR 80/. A mean movement of at most 0.02 mm per year /JAR 80/ to 0.04 mm per year /ZIR 91/, /KOE 07/ since the beginning of the Tertiary can be derived for the Gorleben salt dome. However, Duphorn holds that it is possible to show at the example of the high towering salt domes Gorleben, Dannenberg and Groß-Heide-Siemen that some salt domes were and are respectively still very active in the Quarternary /DUP 83/.

The diapiric break-through of the salt domes Wustrow, Dannenberg, Groß-Heide-Siemen and Rambow, which were connected with the Gorleben salt dome under the Elbe, also occurred in the time of the Upper Jurassic and the Lower Cretaceous. The salt domes Bockleben and Dömitz already broke through during the Triassic.

5.2.2 The Tertiary

At the beginning of the Tertiary, the salt dome Gorleben had generally the current form /KLI 02/. In the following time, the Tertiary sediments were largely eroded over the salt dome. However, they reached a thickness of up to 1,100 m in the rim synclines and are pulled up by its movement at the flanks of the salt dome, see Fig. 32. Hanging (clayey) silts of the Eochatt are superposed by the lower brown-coal sands, which consist of moderately permeable fine sands and silts. They are often summarised with the silts of the Eochatt. They can reach a thickness between 60 m and 130 m in the rim synclines, whereas they are about 25 m thick above the salt dome. The overlying Hamburg clay formed in the lower Miocene can reach a thickness of 60 m to 100 m in the rim synclines. Both the Hamburg clay and the lower brown-coal sands were eroded in the Quaternary and are today only distributed in the area of the north-western rim syncline and in the south-west of the salt dome. The Tertiary stratigraphic sequence is completed by the upper brown-coal sands. Erosion relicts of them are only found in the north-western rim syncline. Up to 50% of the Tertiary layers are non-calcareous /KLI 02/. A stratigraphic gap of 14 million years follows up to the Quarternary /KLI 02/.

5.2.2.1 The Quaternary

Sand, boulder clay and basin sediments dominate the stratigraphic sequence since the Elsterian glaciation. With more than 300 m the Quaternary is thickest in the Gorleben Channel. After the refilling of the remaining channel in the Holsteinian interglacial, the area was thrice crossed by inland ice but the erosion and sediment accumulation did not come up to the dimension of the Elsterian glaciation /KLI 02/. The sediments of the Holsteinian interglacial contain only one marine layer of the Quaternary sequence /JAR 93/. Holocene sediments crop out in the lowlands in form of thin low-permeable flood and meadow sediments.

The cap rock shows pre-Tertiary and early Tertiary karstification phenomena, Palaeogene refilling of the karst voids, Elsterian cap rock breccias and post-Elsterian layered gypsum /JAR 93/. Basically, it consists of anhydrite and gypsum, which were left over geological periods at the top of the salt dome due to the preferential solution of rock and potash salt by circulating ground water /EHR 86/. The strongest subrosion occurred in the diapir phase as a consequence of regional uplift. Afterwards the subrosion rate was at most some hundredth of millimetre per year. Subrosion happens in many salt domes still today /JAR 80/.

The salt level, which forms the interface between salt rock and cap rock, shows a relief and is situated in a mean depth of -250 m /EHR 86/. The cap rock breccia was formed along the salt level by injection of water and sediment penetrating under the overlying weight of the ice from the channel into the zone of weakness at the salt level /KOE 07/, /JAR 93/. The existence of crest faults at the top of the salt dome is regarded to be very unlikely /JAR 93/.

The mean rising velocity today is at most 0.01 mm a^{-1} /JAR 80/ to 0.02 mm a^{-1} /ZIR 91/, /KOE 07/, since the supply of salt from the south-eastern flank is largely exhausted.

5.3 Hydrogeology and hydrochemistry

The spacious hydrogeological situation of the location was and is shaped by its position in the area of the (glacial) valley of the river Elbe. During the Weichselian glaciation, huge amounts of melt water came out of the glacier snout in the north of Lenzen. Gravels and sands were eroded, transported, and deposited. A lake developed around Lüchow-Dannenberg and silted up slowly not until ca. 5,000 years BP.

Today, the near-surface groundwater flows from the heights of the Geestland with a small hydraulic gradient of 1 $^{o}/_{oo}$ to 5 $^{o}/_{oo}$ towards the lowlands, see Fig. 33 /KLI 02/. The altitude difference between the dune fields of the Gartower Tannen in the south of the salt dome and the lowlands of the Elbe in the north is about 15 m /KLI 02/. The altitude difference of the groundwater table is about 6 m /KLI 02/. The recharge of groundwater in the dune fields of the Gartower Tannen in the south of the salt dome is about 160 mm/a. In the lowlands the most part of the newly recharged groundwater is led into the Elbe.

The groundwater runoff in the Elbe-Löcknitz lowland is superimposed by anthropogenic activities. A widely ramified drainage system runs through the lowland and is dewatered into the Elbe by a pumping station. This causes a permanent lowering of the groundwater table, which is compensated by infiltration of surface-water from the Elbe into the aquifer. The withdrawal of groundwater is carried out from the near-surface aquifer and serves for the drinking water supply of households, small trades and for the water supply in the agriculture. The current withdrawals are low and have barely influence on the groundwater runoff and the total water balance /BUH 08b/. The hydrogeological conditions could be changed by water management measures. A significant change of the current situation has to be considered in case of a radically different anthropogenic use of the area with drastic water management measures like impoundment of the Elbe or highly increased groundwater withdrawal rates.

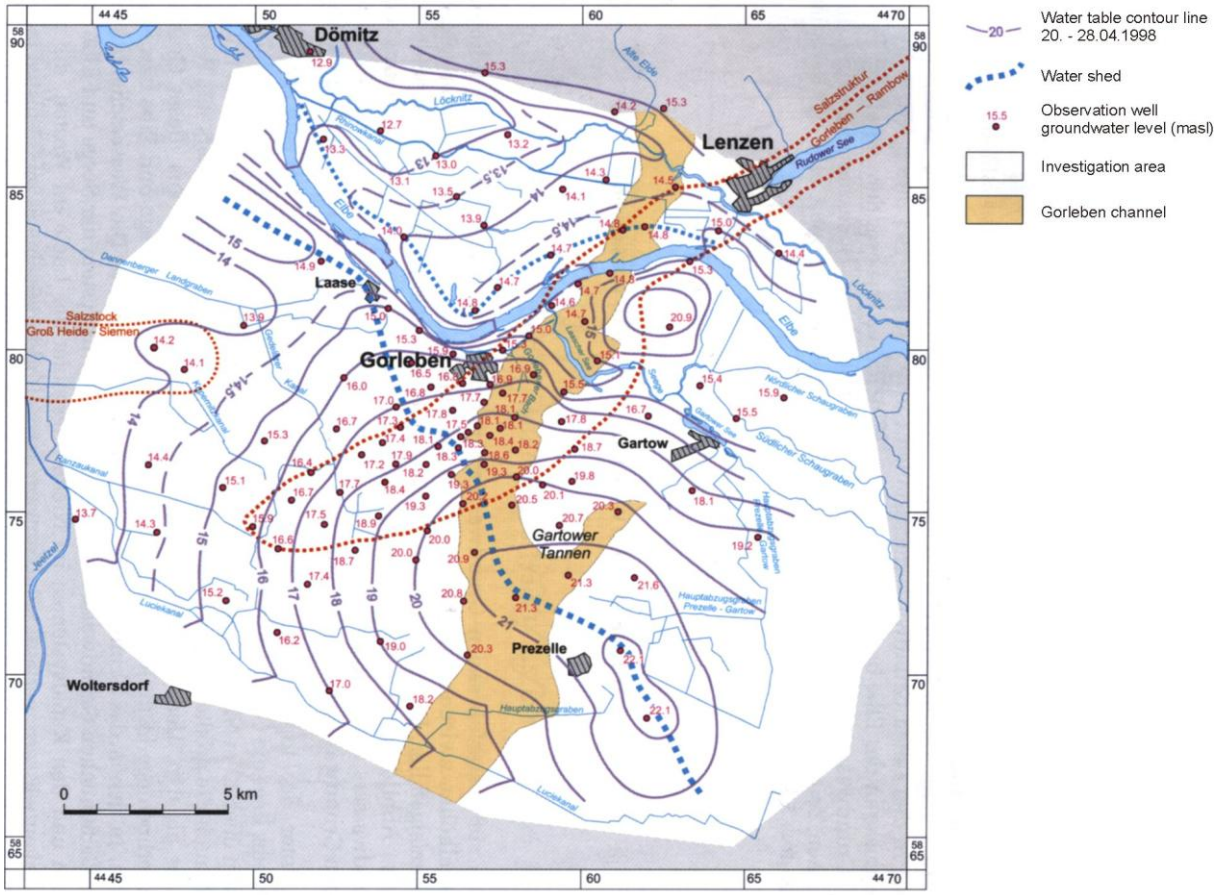

Fig. 33 Water table contour lines in the reference site Gorleben /KLI 07/

The Weichselian and Saalian overlying strata of the salt dome Gorleben with a thickness of up to 430 m form a very inhomogeneous set of aquifers and aquitards, see Fig. 34. Two groundwater storeys are distinguished:

The Elsterian Channel sands and the lower brown-coal sands in the south and in the north of the salt dome are summarised to one lower aquifer, the Weichselian and Saalian deposits form the upper aquifer.

The groundwater storeys are widely separated by Lauenburg and Hamburg clays but mainly in the south-east and the north-west they are assumed to be connected by hydraulic windows /KLI 02/. The surface of the Oligocene Rupel Clay forms the basement of the regional aquifer system.

The Gorleben Channel is a fundamental structure element in the overburden of the salt dome Gorleben. In the Gorleben Channel the Rupel Clay is to a high degree eroded. Over an area of several km² the layer of melt water sands at the basement is in direct contact to the cap

rock and locally to the Zechstein salts of the salt dome. In the north and the south of the salt dome, these sands are in hydraulic contact with the regionally active aquifer which is situated in the rim synclines under the lower brown-coal sands. Within the channel, the lower brown-coal sands and the Tertiary Hamburg clay were eroded during the Elsterian glaciation and were replaced by channel sands and the Lauenburg Clay Complex of silts and clays. The latter reaches a thickness of up to 90 m in the centre of the channel. Saalian sediments are widely distributed over the thin silts and muds of the Holsteinian interglacial. They consist mainly of sands deposited by melt water, boulder clay and glaciolimnic clays and silts.

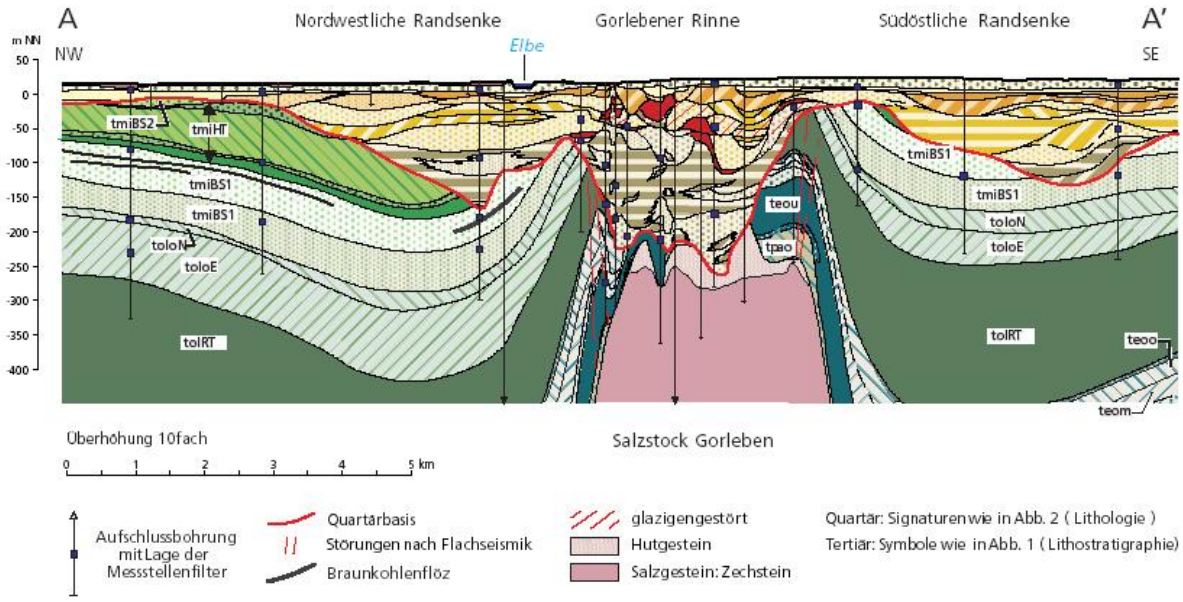

Fig. 34 Geologic cross section of the salt dome Gorleben, ten times exaggerated /KLI 02/

Due to the direct contact of the Zechstein salts and the Quaternary sediments in the centre of the Gorleben Channel a high mineralisation of the groundwater occurs in this area. The salt waters are very uniform in their chemical composition and correspond to halite subrosion waters. The deep salt water leaves the Gorleben Channel and follows the rim syncline according to the slope into north-western direction. There it accumulates at the aquifer basement due to its higher density. Therefore, the waters of the northern rim syncline contain highly saliniferous waters between 100 g l^{-1} und 320 g l^{-1} NaCl /KLI 02/.

Age classifications of the water by means of oxygen and hydrogen isotope compositions and measurements of the C-14 contents show that the brines in the north-western rim syncline were formed during the Pleistocene glaciations /KLI 07/. Apart from these brines of the Pleistocene glaciations also salt waters of the Holocene or mixed waters were detected

within the Gorleben Channel. The postglacial formation of the brines supports that the recent water movement includes the lower channel aquifer, whereby the Pleistocene waters are in part displaced or mixed.

High altitude areas of salt water with to some extend extraordinary high salt contents are found in different parts of the area. Partially the whole aquifer system up to the groundwater surface is filled with salt water /KLI 02/. At least the saltwater above the Gorleben Channel makes a connection of the two groundwater storeys probable, even if no increased vertical permeabilities or gaps in the distribution of the Lauenburg Clay could be detected by exploratory drillings up to now. It is likely that they stem from the channel aquifer, which flow through local hydraulic windows into the upper aquifer and reach in diluted form the groundwater surface in the Elbe lowlands /KLI 02/. In the south of this salinisation area, salt contents of at most 90 g l^{-1} were detected within the upper aquifer. The mineralisation of the salt waters decreases northwards up to values of 2 g l^{-1} to 10 g l^{-1} in the vicinity of the Elbe.

The greatest thicknesses of freshwater of 100 m to 170 m are found in the rim synclines in the north-west and the south-east of the salt dome, predominantly Ca-HCO_3 waters. Only in the near-surface groundwaters SO_4^{2-} dominates compared to HCO_3^- due to superficial decalcification of the sediments.

5.4 Actual climatic conditions

The area around Gorleben is today part of the temperate climatic zone which extends between the tropics and the arctic circles. This climatic zone does not show any excessive cold or warm periods. Precipitations occur during the whole year and the Gulf Stream forms a climate which is exceptionally mild for these latitudes. The maritime influence decreases from the north-west to the south-east, see Fig. 35. Spring, summer, autumn and winter form distinct seasons. The highest temperatures are registered in June, the lowest in January.

The mountain range Drawehn with a height of 100 m forces clouds advancing mainly from the west to release their moisture before they reach the reference site, see Fig. 36.

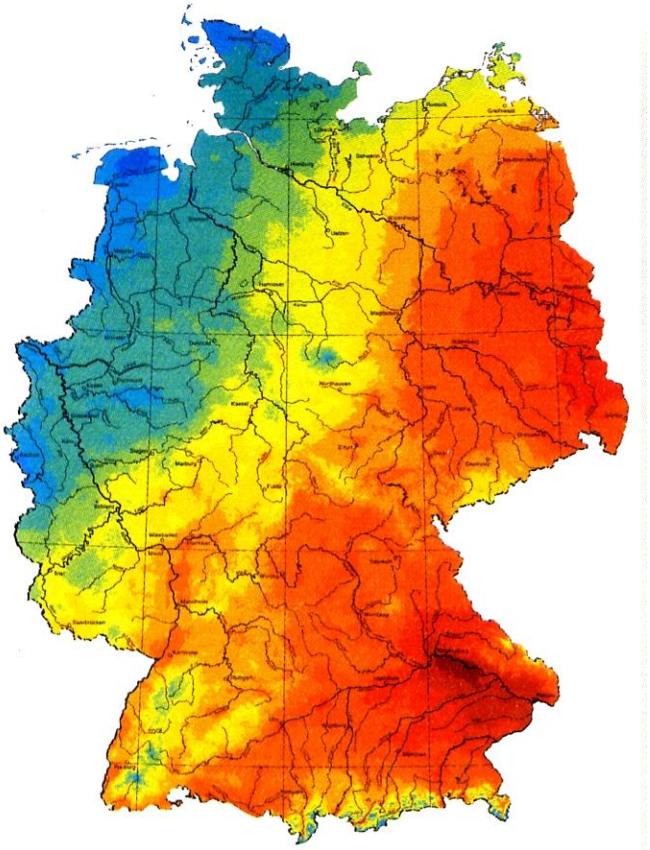

Fig. 35 Maritime influence of the climate in Germany, decreasing from blue to red /GEO 06/

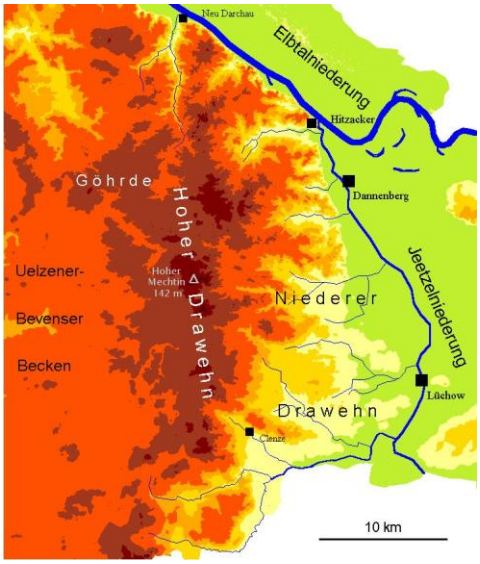

Fig. 36 Topography of the Drawehn (green areas < 20 mNN, orange/red between 50 and 75 mNN, dark brown areas > 100 mNN) /WIK 08/

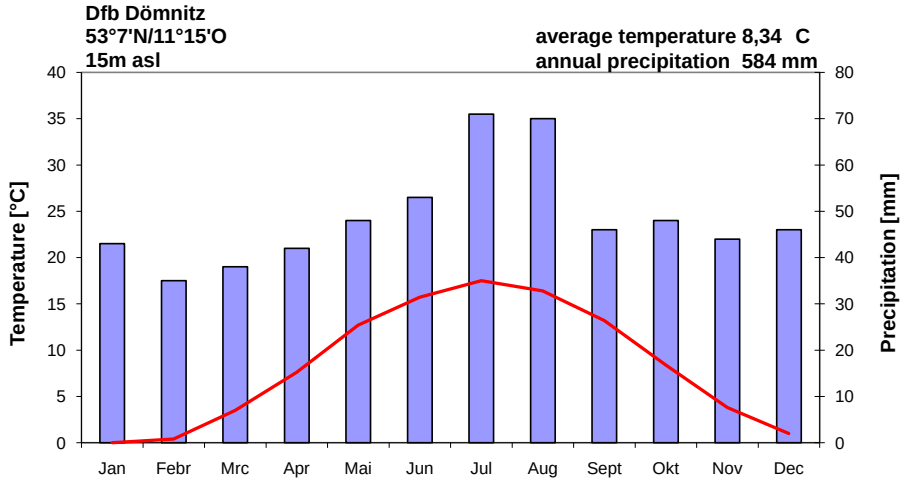

	1901-1950	
	°C	mm
Jan	-0,1	43
Febr	0,4	35
Mrc	3,5	38
Apr	7,6	42
Mai	12,7	48
Jun	15,7	53
Jul	17,5	71
Aug	16,4	70
Sept	13,2	46
Okt	8,4	48
Nov	3,8	44
Dec	1	46

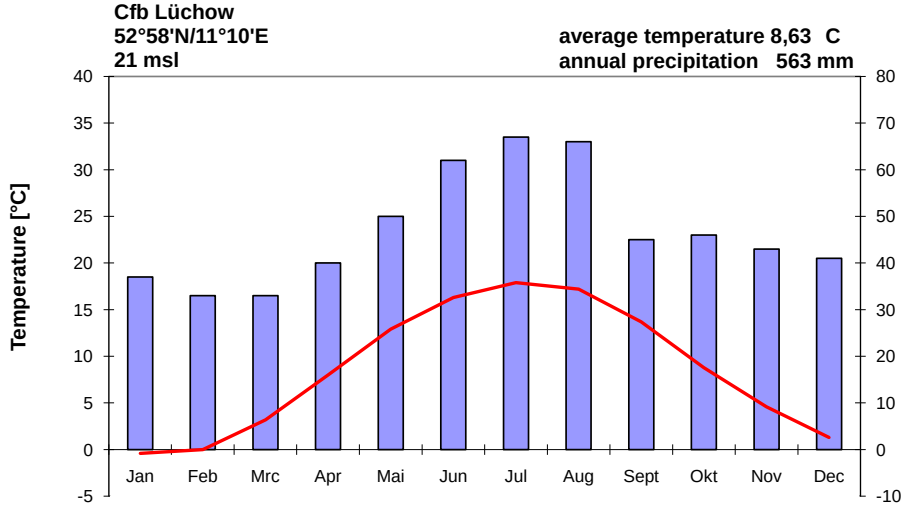

	°C	mm
Jan	-0,4	37
Feb	0	33
Mrc	3,2	33
Apr	8	40
Mai	12,9	50
Jun	16,3	62
Jul	17,9	67
Aug	17,2	66
Sept	13,7	45
Okt	8,8	46
Nov	4,6	43
Dec	1,3	41

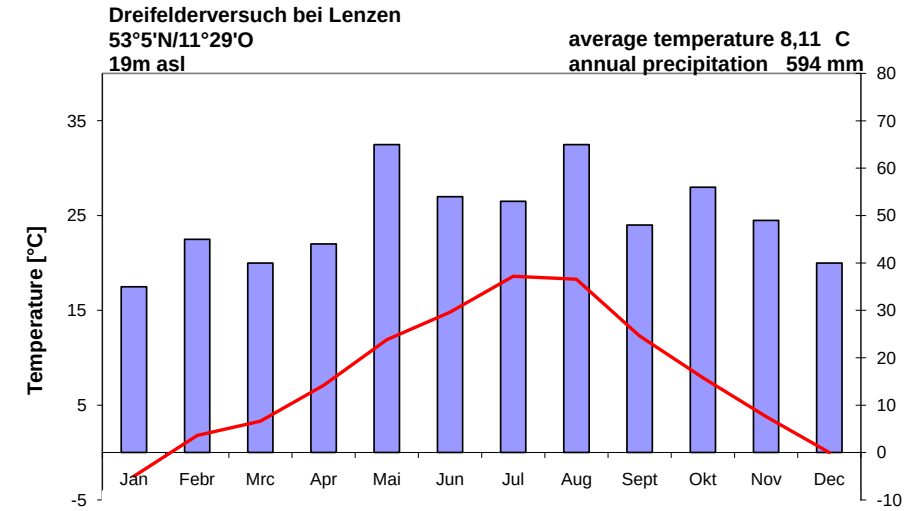

	1994-1999	
	°C	mm
Jan	-2,5	35
Febr	1,8	45
Mrc	3,3	40
Apr	7,1	44
Mai	11,9	65
Jun	14,8	54
Jul	18,6	53
Aug	18,3	65
Sept	12,3	48
Okt	7,9	56
Nov	3,8	49
Dec	0	40

Fig. 37 Climate charts of the three nearest climatological stations

For the further description of the actual climate at the Gorleben site, the climatological stations in Lüchow, Dömitz and Lenzen, barely 20 km away, are consulted see Fig. 37. The annual mean temperature at these stations is between ca. 8°C and 9°C. Maximum and minimum temperatures are reached between +18°C and -3°C, respectively. A mean temperature of more than 10°C applies for more than 4 months, but the warmest month reaches on average less than 22°C. The annual precipitation amounts to values between 545 mm and 594 mm. Humid conditions prevail the entire year. After Köppen and Geiger this is therefore a Cfb-climate. The vegetation period lasts about seven months.

Information about the most important climatic data, the possibly predominant fauna and flora, the residential density and the land use as well as the soil texture, the soil turnover and the sediment redeposition of the climate class Cf can be found in Fig. 38. Further information like for example the water deficit etc. can be found in Chapter 4.2.2.

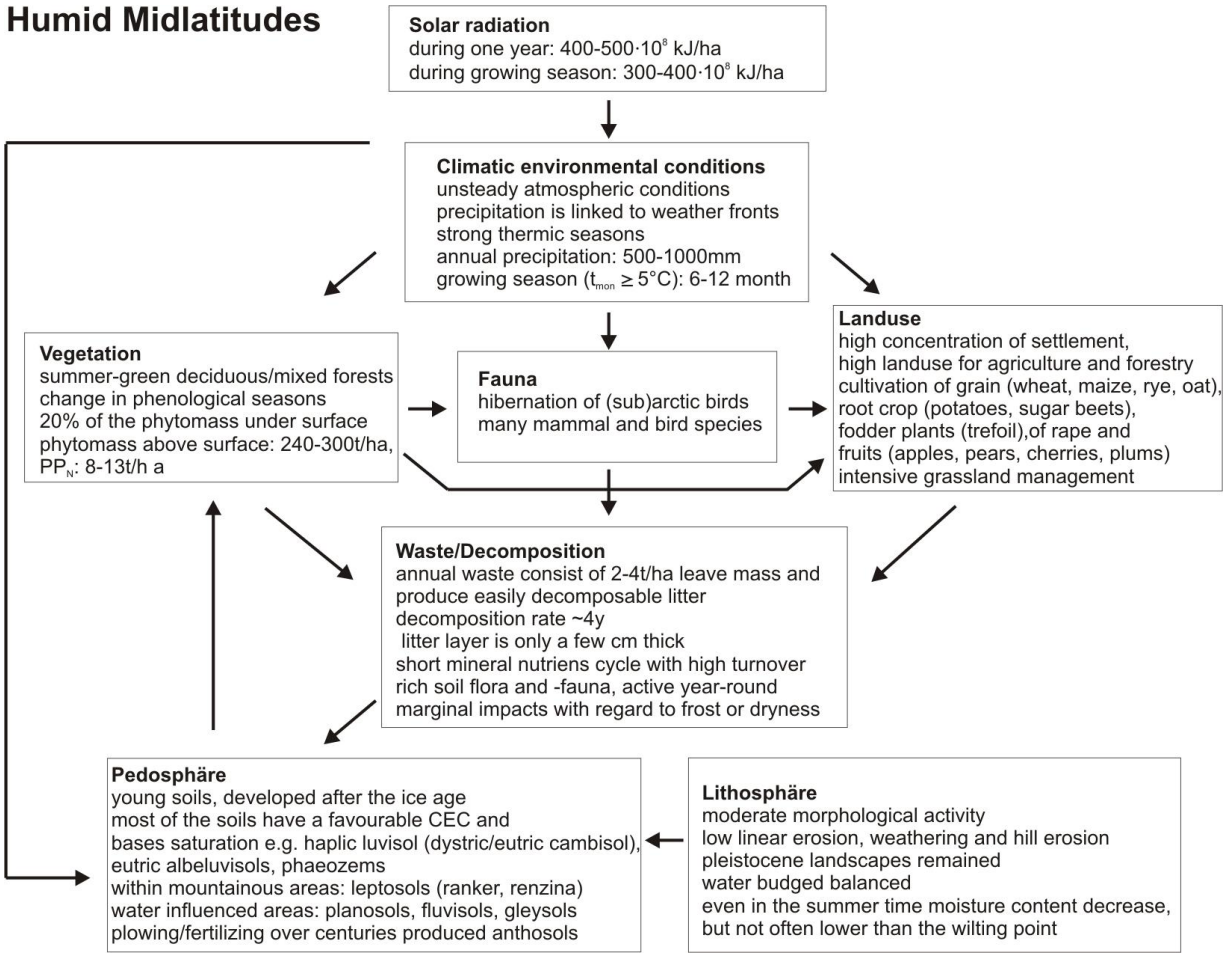

Fig. 38 Sketch of biosphere characteristic within the climate Cf /SCH 95/

6 Modelling of selected climate states

In case of a normal evolution all open voids in the salt dome will be closed after distinct time by convergence. Thereby all potential water pathways will be closed and no radionuclide release from the salt dome occurs, i.e. the waste is completely confined in the host rock formation. The considered investigation of the impact of different climate states on processes in the overburden and the biosphere are not of relevance for the case of this normal evolution. But it is of relevance for altered scenarios with radionuclide release from the host rock, which cannot fully be excluded and need to be considered in the safety case.

At this stage model calculations are restricted to discrete climate states; transient modelling of climate changes and its transitions are planned in a future project. The current modelling work can be divided into two major topics, i.e. the impact of different climate states

- on flow and radionuclide transport in the overburden and
- on biosphere processes.

Flow and transport modelling in the overburden of the salt dome requires a large effort for the development of models and in particular high computing costs for modelling of each climate state. Therefore this part was restricted to few selected models for extreme climate states, where significant differences are expected in the models and the simulation results. The aim is to define the relevant processes of the different climate states and to analyse their impact on flow and transport of selected radionuclides in the reference site. The following climate states are selected on the basis of the results concluded in chapters 2.5.7 and 4.3:

- continuation of the climate conditions occurring today,
- warming until a potential maximum sea level is reached, and
- cooling accompanied by the formation of a glacier similar to a Weichselian one with formation of permafrost situated in front of the glacier.

For biosphere modelling, also a selected number of climate states are considered. The choice of potentially occurring climates at the reference site is based on the results described in chapters 3, 4 and 6, in particular those from the BIOCLIM project /BIO 04/.

The effects for the following climate states are possible for the reference site were analysed: ET (Tundra), Dfa/Dfc (Boreal), Cs (Mediterranian), Cfb (Temperate), and BS (Steppe). In the following characteristics of warmer and cooler climates for the reference site are described.

6.1 Warming climates

An important aspect for **flow and transport modelling** is that a further climate warming leads to a sea level rise caused by the retreat of the today still existing glaciers. As discussed in chapter 4 a sea level rise between 20 m and 30 m is within the realms of possibility. To illustrate the consequences Fig. 39 shows which areas of the Elbe lowlands could be flooded by a sea level rise of 1 m, 7 m, 10 m and 14 m. According to this, the reference site is not directly affected by any scenario but that does not mean that it will remain uninfluenced. An extreme flash flood, for example, could easily reach the area /BIO 04/.

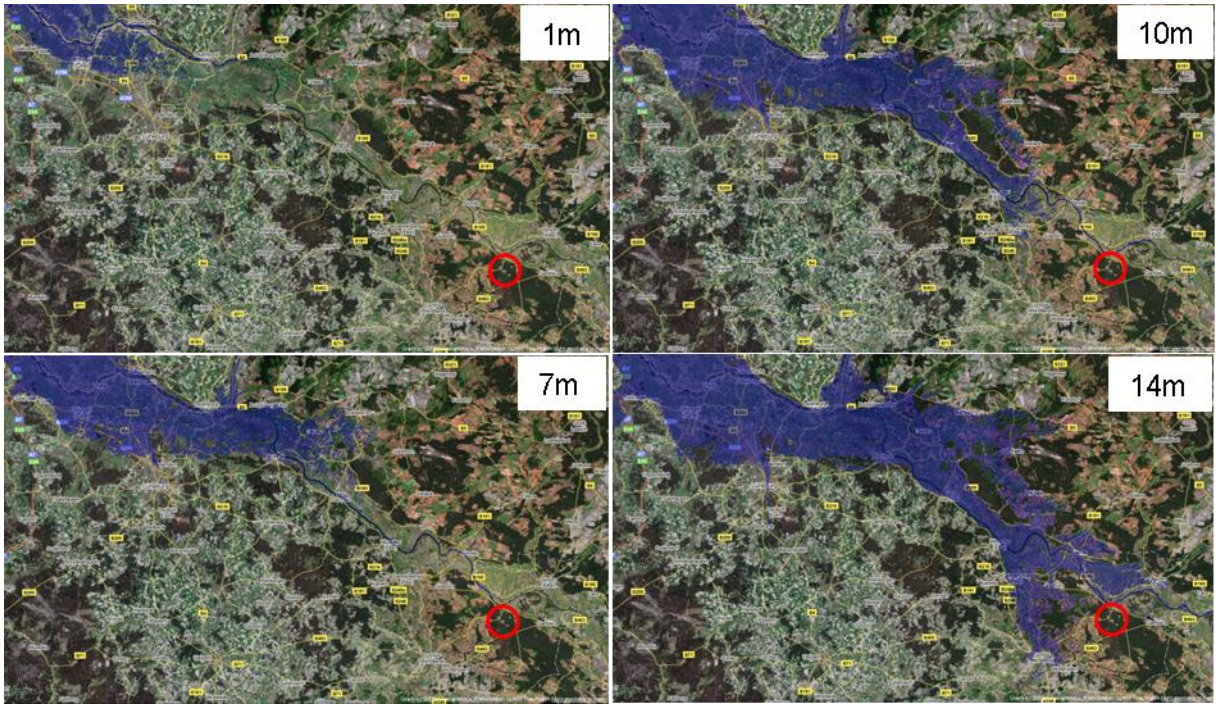

Fig. 39 Effects of sea level rise in the region of the Elbe lowlands in the vicinity of the reference site /GOO 08/

Furthermore, the predominant wind direction from north-west presses the water of the North Sea into the Elbe estuary, see Fig. 40. In consequence of this process, backwater

can occur in the river. This can additionally lead to a broadening of the riverbed as well as to a paludification of the Elbe lowlands and to a change of the course of the river.

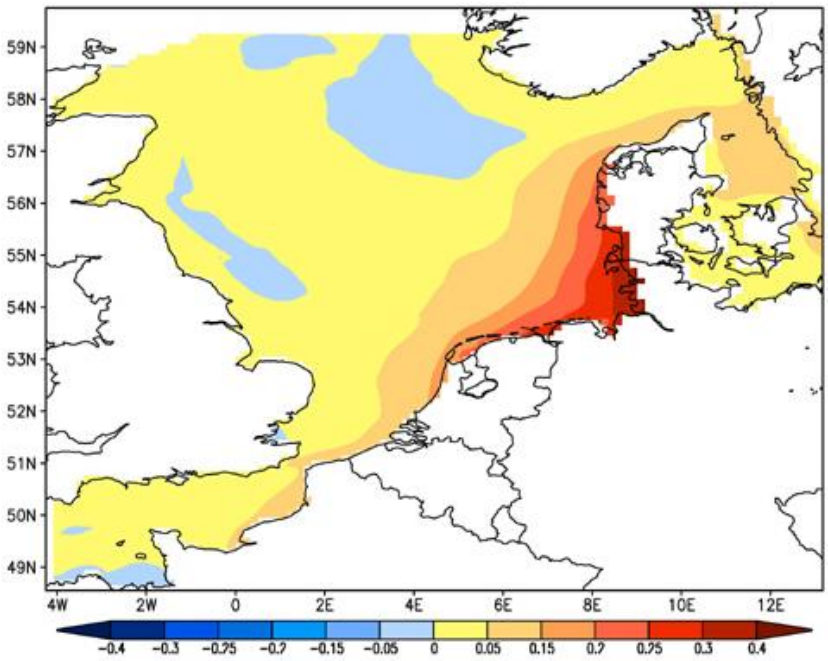

Fig. 40 Distribution of the sea level in the North Sea driven by predominant west winds /HAR 01/

Fig. 41 Sea transgression after retreat of all glaciers existing worldwide /KEL 02/

A retreat of all glaciers existing today, which may not be expected according to the actual state of knowledge but occurred in earlier times, would result in a sea level rise of about 60 m /KEL 02/ to 73 m /BER 04/. This would entail a nearly entire inundation of the North German lowlands /KEL 02/ as shown in Fig. 41. Only smaller areas in the Lüneburger Heide and in Brandenburg, which basically consist of end moraine tracts of the last glaciation, are excluded of the flooding /KEL 02/. Due to the low topography of the reference area between 15 m a.s.l. and 76 m a.s.l. /DUP 83/ and its proximity to the receiving stream Elbe with its direct connection to the sea, the maximum sea level in the region Gorleben will then be about 50 m above the today´s ground level /BUH 08b/.

With regard to **biosphere modelling** the potentially occurring climate states at the reference site need to be identified. This description is based on the climate scheme of Köppen and Geiger (see chapter 2.1).

The German location is currently situated in the climatic zone of humid midlatitudes, i.e. climate type Cfb, and borders northward and eastward on the boreal climatic zone, southward and westward on the Mediterranean climate zone. The continental influence of the climate is limited by the nearby sea and will be further reduced by sea-level rise. Therefore, the climates Cfb and Csa according to Köppen and Geiger would be most likely in the case of warming. However, in order to additionally investigate the impact of an even more extreme climate, the climate class Bs is included in the Biosphere modelling (see chapter 8). It is assumed that the groundwater table decreases with increasing continentally and associated missing winter precipitations but that the hydrological situation will persist in a similar form as today.

Information about the most important climatic data, the possibly predominant fauna and flora, the residential density and the land use as well as the soil texture, the soil turnover and the sediment redeposition of the climate classes Bs and Cs are found in Fig. 42. Further information like for example climate charts, water deficit etc. can be looked up in Chapter 8.

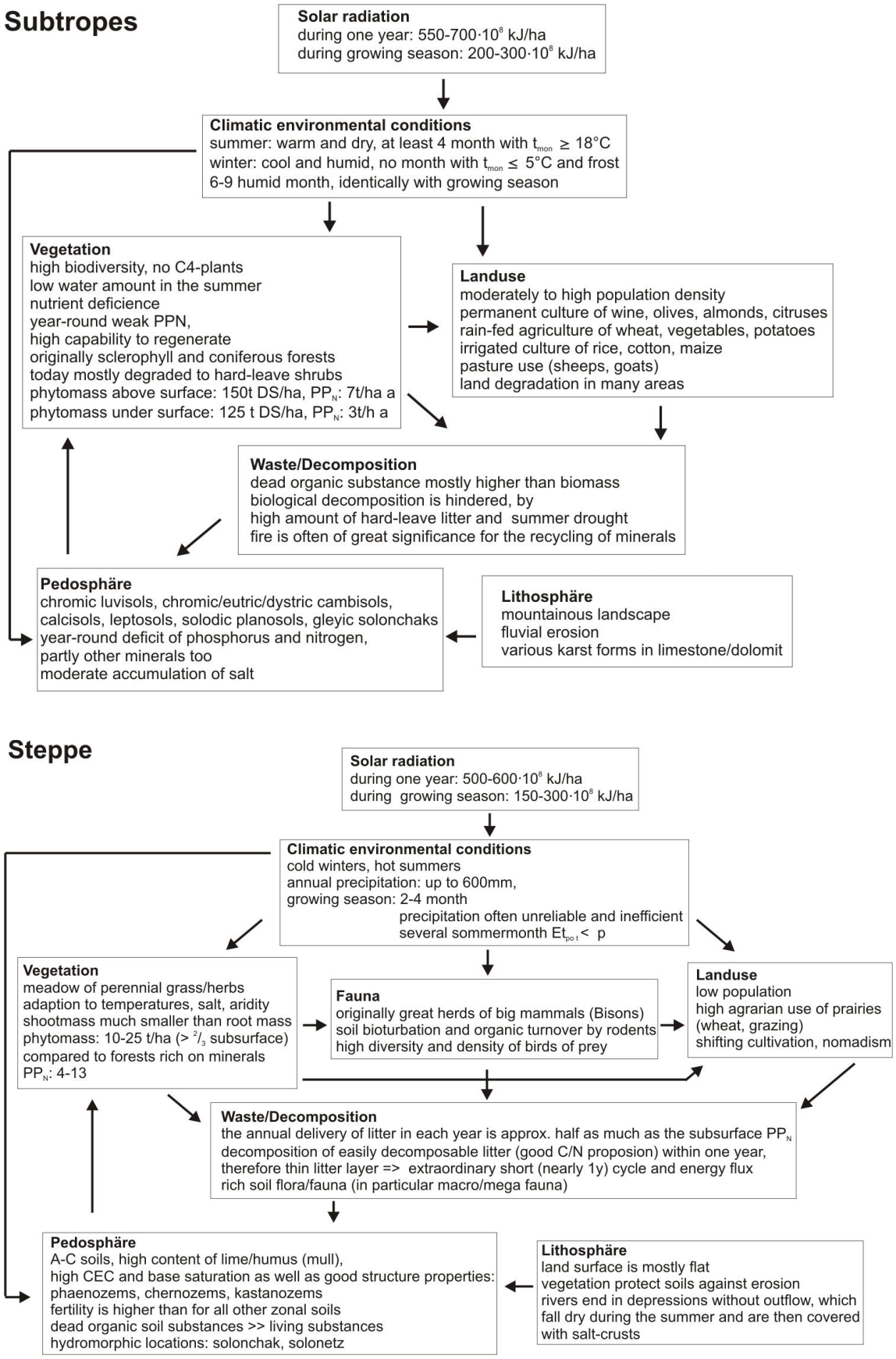

Fig. 42 Sketches of biosphere characteristics within climates Cs and BS /SCH 95/

6.2 Colder climates

According to the actual knowledge, a new glaciation period can be expected in 25,000 years at the earliest, but more likely in 100,000 years to 170,000 years. As discussed before in such a period great amounts of water will become fixed by the formation of glaciers, which causes a subsidence of the sea level. This results in an increase of the distance of the reference site to the coastline. It is assumed that the entire southern part of the contemporary North Sea is fold dry due to the flatness of the North Sea Basin and that the coastline displaces by about 600 km northwards (see chapter 2.5.5). The Elbe estuary is then situated several hundreds of kilometres further in the north, which results in a longer flow path of the river. By the subsidence of the sea level, the erosion level both at the coast and of the river is depressed. However, it is assumed that the present slope of the main conceiving stream Elbe will not be significantly elevated even with consideration of the longer flow distance.

With regard to **flow and transport modelling** the occurrence of glaciers and/or permafrost at the reference site are of highest importance. As discussed in chapter 2.5.5 a future glaciation is assumed to have an extension similar to the Weichselian glaciation. Thus the reference site would be affected only indirectly by the glacier which does not reach the Elbe river. However, it is likely that a glacier running parallel to the Elbe will use the Elbe lowlands as glacial valley for melt water. The amount of water to be drawn off by the Elbe increases due to the addition of glacier melt water, leading to increased flow velocities. A high groundwater recharge is given by melt waters in the vicinity of the glacial valley and below the glacier due to the missing permafrost in this area. As a result the chemism of the groundwater can be altered by the infiltrating, highly oxygen-containing, cold and low mineralised melt water. In addition, fluviatile and aeolic erosion and accumulation processes can change the regions topography.

A significant change of the hydraulic conditions can arise from the formation of permafrost. It is assumed that the permafrost in Northern Germany - depending on the sediment type - had reached a thickness between 40 m and 140 m /KLI 07/ during the last glaciation period (see Fig. 43). Similar conditions can also be expected during the next glaciation period, which is expected to be similar to the Weichselian. Groundfrost leads to the freezing of the soil water and by this limits its mobility nearly completely. That is why capillarity, infiltration and percolation are effective only to a small extent /MOE 02/. Therefore, just few or no groundwater recharge occurs in regions with permafrost /BAT 00/.

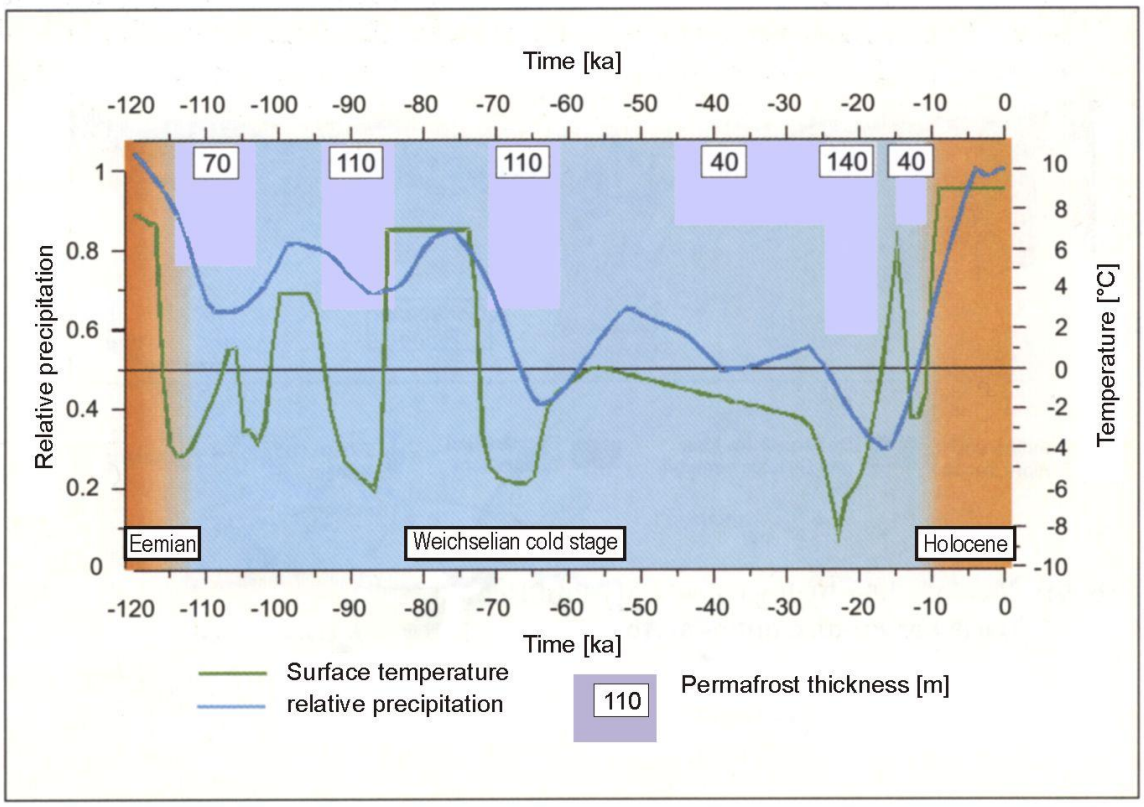

Fig. 43 Calculated penetration depth of the permafrost during the Weichselian /KLI 07/

Unlike in interglacial periods, in which the main part of the groundwater movement normally occurs in the near-surface layers, the groundwater runs in glaciation periods in deeper storeys beneath the permafrost /BER 04/. It is to assume that in this way more fresh water runs through the deeper storeys in glaciation periods than in interglacial periods /BER 04/. The groundwater flow below the permafrost could have therefore been higher than that, which is observed today in the same depth /DEL 98/. Keller, however, expects that the groundwater flow velocity will be low in times with a closed permafrost distribution (continuous permafrost) as a sealing of the groundwater recharge areas and connected with that a diminution of the “driving mechanism” for groundwater movements is to be assumed /KEL 02/.

However, it is unlikely that a growth of permafrost occurred in Northern Germany under lakes and rivers during the last glacial period /DEL 98/. Also model results show that at that time practically all zones under rivers and lakes exist as so-called taliks, i.e. were free of permafrost. It can therefore be assumed that during the next glaciation period as well rivers like the Elbe persist as taliks with unfrozen ground. Thereby they might form a hydraulic connection between surface water and deep groundwater.

The coastline retreats due to the eustatic subsidence of the sea level of about 60 m /BIO 04/ caused by the formation of continental ice sheets. Concerning the **biosphere models** the climate at the investigation site becomes more continental so that boreal climate conditions can be expected. In this case, the winter will probably comprise 5 months with temperatures about 0°C. Despite dryness in the late winter and spring as well as a wet autumn and early winter, temperatures in spring and autumn are sufficiently high for the formation of vegetation /BIO 04/.

Several studies and model calculations in the framework of BIOCLIM show that the occurrence of climate group D according to Köppen-Geiger will then be likely for Northern Germany. It is supposed that the reference site will not come under an extremely continental influence at any time and that the summers will become more humid and cooler. Therefore, the Dfb climate is the most likely climate state. However, in order to investigate the impact of even more extreme climate, the climate classes Dfa, Dfc are included in the Biosphere modelling (see chapter 8).

In case of a maximum extension of a glaciation similar to the Weichselian one the reference site would not be covered by a glacier but be under strong periglacial influence, as discussed above. In this case, an ET climate (Tundra) can be assumed. It is characterised by low winter temperatures, short summers and periods of high wind speed, which contribute to aeolian erosion.

Information about the most important climatic data, the possibly predominant fauna and flora, the residential density and the land use as well as about the soil textures, the soil turnover and the sediment redeposition of the climate groups Df and ET can be found in Fig. 44. Further information like for example climate charts, water deficit etc. can be looked up in Chapter 4.2.2.

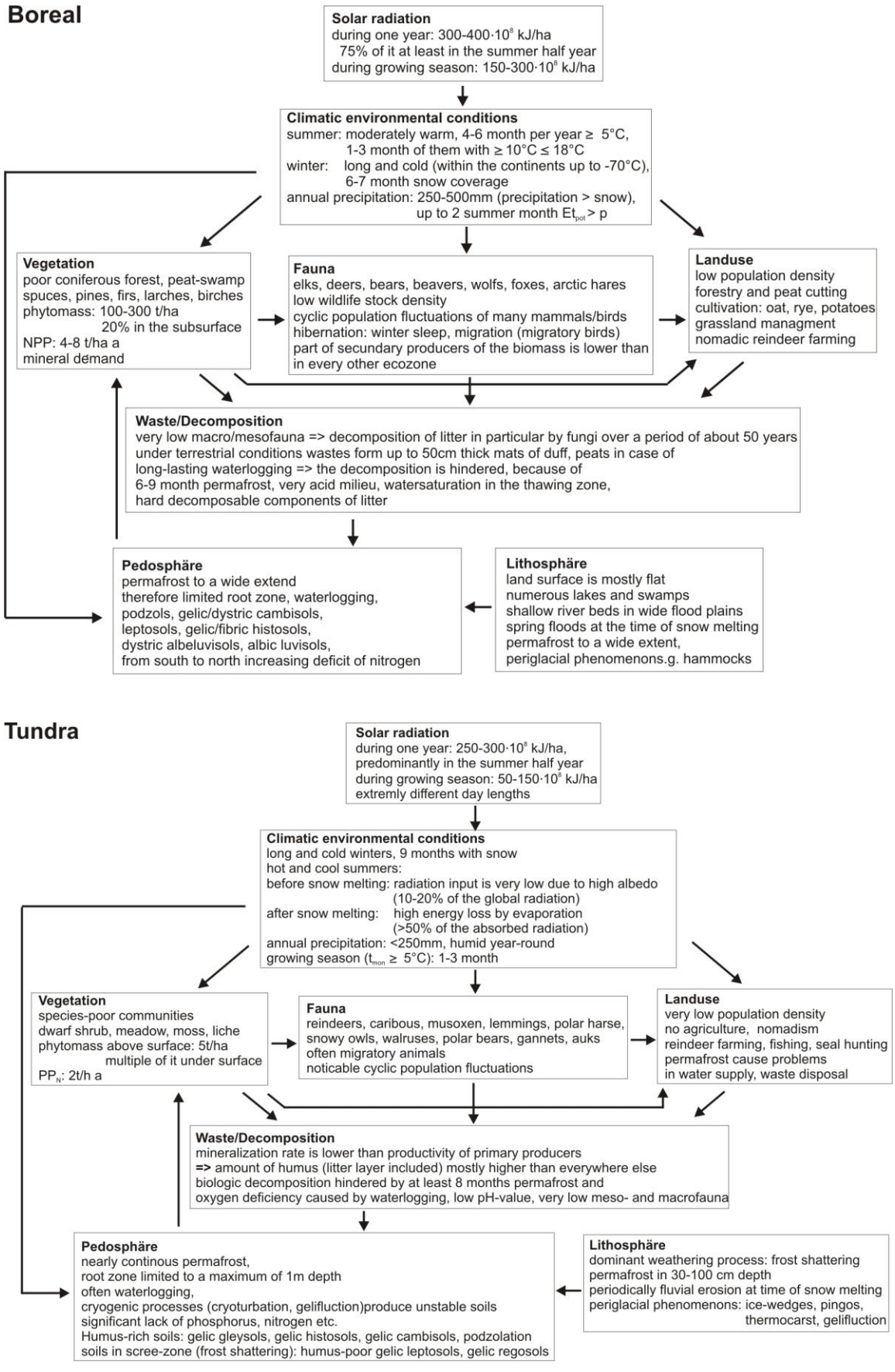

Fig. 44 Sketches of biosphere characteristics within climates Df and ET /SCH 95/

7 Modelling climate impact on flow and transport processes

As described in Chapter 6 the objective of flow and transport modelling is to identify climate induced changes in hydraulic conditions and distribution of salt concentrations and its impact on radionuclide transport in the overburden of a salt dome for altered evolution scenarios. In this first step, the major effects of climate changes are investigated using a model that is not too complex but contains the most significant characteristics of the overburden (see Chapter 7.1.1). For all calculations, it is assumed that the geological units of the model area will not change with time. This assumption is based on the restriction on climate states without glaciation like permafrost and sea water inundation. Under such conditions no essential changes of subsurface layers in the overburden are expected. Furthermore, the occurrence of strong changes of the geological structure in the overburden like deep erosion channels seem to be restricted to the Elsterian ice age and didn't occur during following glaciations. All results presented in this chapter are based on the dissertation of Judith Flügge /FLU 09/.

Flow and transport through the overburden of the salt dome for the selected reference site Gorleben for relevant climate states were modelled using the codes d³f (distributed density driven flow) and r³t (radionuclides, reaction, retardation, and transport) developed under the auspices of GRS /FEI 04/, /FEI 99/. Visualisation was realised on the basis of the software package GRAPE (GRAphics Programming Environment) of the Universities of Bonn and Freiburg /GRA 99/. d³f calculates flow fields under consideration of the varying salinity, considering, in particular, advection, diffusion and dispersion as transport processes. The salt concentration in the groundwater is expressed as relative mass fraction for salt. In this case, the maximum concentration is the mass fraction of saturated brine. The density and viscosity of the groundwater are functions of the salt content and temperature /FEI 99/. Transport calculations are based on the flow field calculated by d³f. Advection, dispersion and diffusion are taken into consideration. The most important feature of r³t is the possibility to simulate pollutant transport in very large model domains over long periods in time. In addition to radioactive decay, relevant interaction processes, such as sorption, precipitation and diffusion into immobile pore waters /FEI 04/.

Basic input data were taken from different publications of the BGR, among others on hydrogeology and geology of the Gorleben salt dome /KLI 07/, /KLI 02/, /LUD 02/. The code versions d³f_6.0 as well as r³t_10 and r³t_12 for two-dimensional models were used.

Unless indicated otherwise, all figures of the hydrogeological model are exaggerated by a factor of 10. All given flow velocities are Darcy velocities.

7.1 Present Climate

Modelling extreme climate states, the present groundwater flow has to be simulated first. Therefore the present transient groundwater flow and salt concentration was modelled in a first step to be able to verify the model results. In a second step, the future climate states were simulated starting with the present transient flow field until reaching the steady-state. A simplified, schematic cross-section (see Fig. 45) forms the basis of modelling. It includes the fundamental structures and describes the hydrogeological situation at the Gorleben site.

7.1.1 Geometry

A two-dimensional model (Fig. 46) is developed following the conceptual model in Fig. 45. The model area has a length of 16.4 km and a maximum thickness of 400 m. It consists of three different units representing a lower and an upper aquifer with an intercalated aquitard. The lower hydraulic boundary of the model is the Oligocene Rupel Clay as basis of the regional flow system /KLI 02/. This is overlain by the lower aquifer consisting of Eochattian and Neochattian strata (Upper Oligocene) and the Lower Brown Coal Sands (Lower Miocene). The overlying units Hamburg Clay (Lower Miocene) and Lauenburg Clay Complex (Pleistocene) form an aquitard. The upper aquifer of the model represents the relicts of the Upper Brown Coal Sands and the very inhomogeneous Quaternary sediments. In the model, both aquifers have a thickness of 100 m. During the uplift of the salt dome, there was a piling-up of sediments at the salt dome flanks and formation of lateral rim synclines in the north-west and south-east of the salt dome (see Fig. 34). The north-western rim syncline formed this way is realised in the model with an additional thickness of the lower aquifer of 150 m. The aquitard has a thickness of 50 m in the model. Both the Hamburg Clay and the Lauenburg Clay Complex are locally interrupted by “hydraulic windows”, i.e. local absence of the aquitard. These result from erosive processes during the advance of the Elsterian inland ice sheet up to the area of the Gorleben salt dome. Moreover, glacial-tectonic processes led to a strong local increase in the permeability of the Lauenburg Clay Complex. One hydraulic window with a width of 500 m is realised at a distance of 1,000 m to 1,500 m to the southern boundary of the

model. Since there is no clear evidence for a second hydraulic window, two model variants are realised. In contrast to model 1 with only one hydraulic window, model 2 has a second hydraulic window at the northern boundary of the north-western rim syncline at a distance of 12,250 m to 12,750 m to the southern boundary of the model domain (see Fig. 46). During the Elsterian period, melt water eroded the overlying sediments up to the cap rock of the salt dome and thus formed the Gorleben Channel. In Fig. 46, the contact of the lower aquifer to the cap rock of the Gorleben salt dome is marked in red. The structural elements are adopted in the model as most important characteristics of the hydrogeological system.

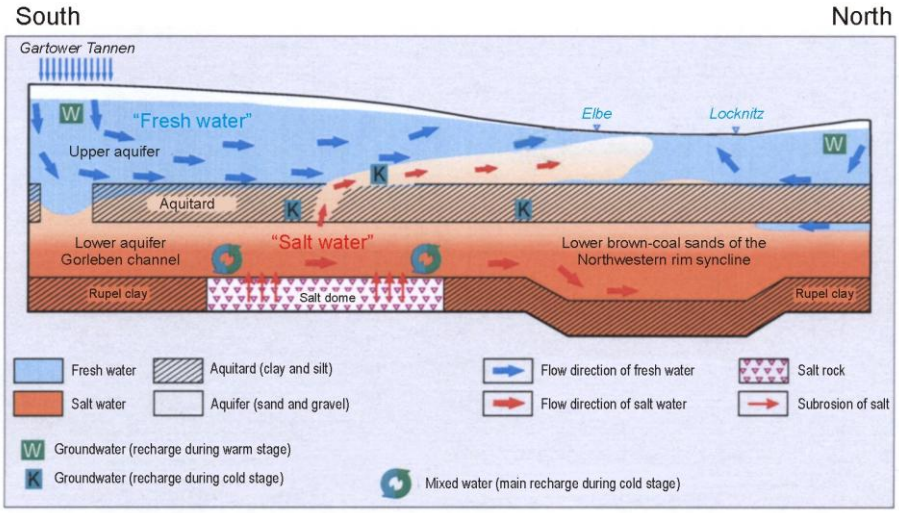

Fig. 45 Schematic cross-section through the model domain (according to /KLI 02/)

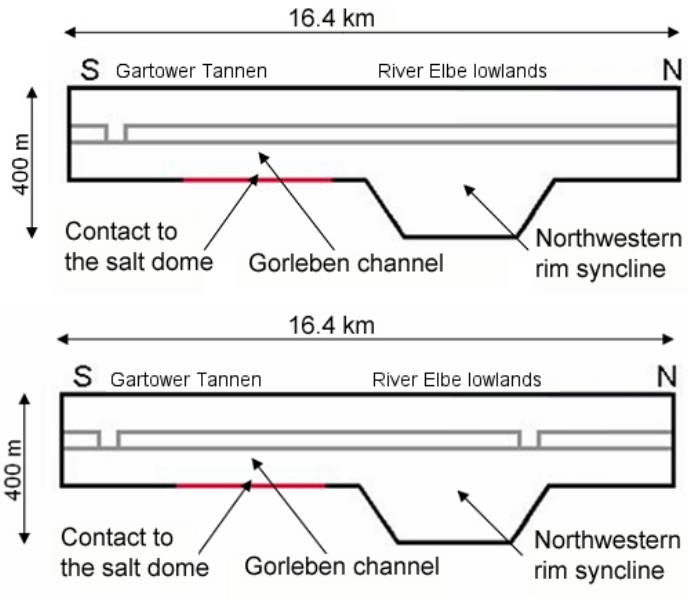

Fig. 46 Geometry of model 1 with one hydraulic window (above) and of model 2 with two hydraulic windows (below)

7.1.2 Hydrogeological parameters

Hydrogeological parameters for the modelling were taken from different publications, mainly of BGR and GRS /BIR 00/, /KES 07/, /KOE 00/, /LEI 89/, /VOG 91/ and are summarised in Tab. 11. Both aquifers have a permeability of $k = 1 \cdot 10^{-12}$ m², the aquitard has a permeability of $k = 1 \cdot 10^{-16}$ m². The porosity for the aquitard is defined with $\Phi = 0.05$, and for the aquifers with $\Phi = 0.2$. For all hydrogeological units, a longitudinal dispersion length of $\alpha_L = 10$ m and a transversal dispersion length of $\alpha_T = 1$ m as well as molecular diffusion coefficient of $D_m = 1 \cdot 10^{-9}$ m² s^{-1} are defined.

Tab. 11 Hydrogeological parameters for both models

Hydrogeological parameters	Aquifer	Aquitard
Permeability k [m²]	$1 \cdot 10^{-12}$	$1 \cdot 10^{-16}$
Porosity Φ [-]	0.2	0.05
Longitudinal dispersion length α_L [m]	10.0	10.0
Transversal dispersion length α_T [m]	1.0	1.0
Diffusion D_m [m² s^{-1}]	$1 \cdot 10^{-9}$	$1 \cdot 10^{-9}$

7.1.3 Initial and boundary conditions

Initial conditions are defined for the salt concentration and the temperature. The temperature at the model surface corresponds to an average temperature of the groundwater in northern Germany of 8°C /KAP 61/. On-site temperatures measured and calculated in the groundwater of observation wells are not taken into consideration due to the strong variation /KLI 07/. For simplification, a linear increase, of 8 °C at the ground surface up to 20 °C at the base of the north-western rim syncline is defined in the model, corresponding to the geothermal gradient of 0.03 °C m^{-1} in Northern Germany /LEG 04/. The code d³f indicates relative salt concentrations, so $c_{rel} = 0$ corresponds to a salt concentration of $c_{abs} = 0$ kg kg^{-1} and $c_{rel} = 1$ to a salt concentration of $c_{abs} = 0.264$ kg kg^{-1}, i.e. a saturated NaCl solution at 20 °C. For the upper 70 m of the upper aquifer, freshwater conditions are defined ($c_{rel} = 0$). Within the lower 30 m, the concentration increases linearly from $c_{rel} = 0$ to $c_{rel} = 1$. Salt water conditions with $c_{rel} = 1$ are defined for the entire aquitard and the lower aquifer.

North of the Elbe lowlands and in the area of the Gartower Tannen in the south there are areas with groundwater recharge /KLI 07/. The groundwater recharge rate for the Gartower Tannen (southern area of the surface, see

Fig. **45**) is indicated with 160 mm a^{-1} /KLI 02/. In the model, an inflow condition was selected for the southern 1.5 km and the northern 3.4 km of the surface corresponding to this recharge rate. For the inflow of freshwater a Dirichlet condition for the salt concentration with c_{rel} = 0 was assigned to these boundaries (see Fig. 47). At the central area of the model surface hydrostatic pressure is defined (Dirichlet boundary condition: p = 0 Pa). Here, a Dirichlet condition for the salt concentration of c_{rel} = 0 is defined for the inflow of freshwater, for the outflow, the salt concentration is specified by the actual concentration of the outflowing groundwater. From the north, about 10^6 m³ of groundwater per year flow into the lower aquifer in the investigation area over a width of about 5 km /LUD 02/ which corresponds to 200 m³ a^{-1} for the model section. This inflow was also realised in the model with a boundary condition for freshwater. For model 1, this value was reduced to 10% of the given value to obtain realistic flow fields and, above all, realistic salt concentrations (see 7.1.4). All other boundaries are considered to be impermeable for diffusive-dispersive transport. Subrosion takes place at the contact to the salt dome (see Fig. 47). There, a Dirichlet condition with c_{rel} = 1 is defined.

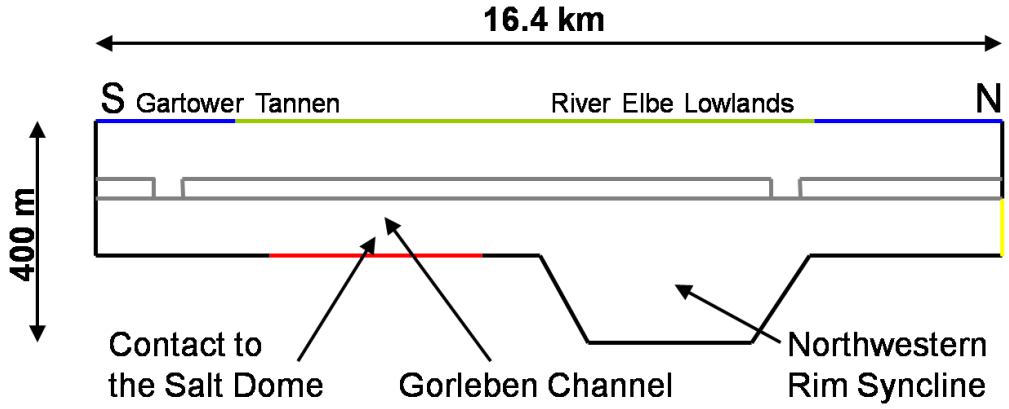

Fig. 47 Boundary conditions of models 1 and 2 exemplarily for model 2. Red: Contact to the salt dome, blue: Groundwater recharge rate = 160 mm a^{-1}, green: Hydrostatic pressure, yellow: Inflow of freshwater (model 1: 20 m³ a^{-1}, model 2: 200 m³ a^{-1}), black: Impermeable boundary

From a simplified point of view, today's flow field could develop since the end of the Weichselian Ice Age /KLI 07/, /KOE 00/ so that the present flow and salt concentration

field should be reached after a model time of 11,500 years. The start time for the modelling is therefore approx. 11,500 years BP, which represents the end of the Weichsel Cold Stage and the beginning of the Holocene /STR 07/. Therefore, the model was not run until reaching the steady-state, but it was stopped after 11,500 years model time. This corresponds to the fact that the present hydrogeological system is not in a steady-state

7.1.4 Results of flow modelling for the Present Climate

The main characteristics of the present hydrogeological system /KLI 07/, /LUD 02/, /KLI 02/ are reflected by both models (Fig. 48) after 11,500 years model time. These are

- two groundwater outflow areas at the surface,
- the southward groundwater flow in the upper part of the lower aquifer between the contact to the salt dome and the northern boundary of the model, and
- the northward groundwater flow in the lower part of the lower aquifer between contact to the salt dome and the north-western rim syncline.

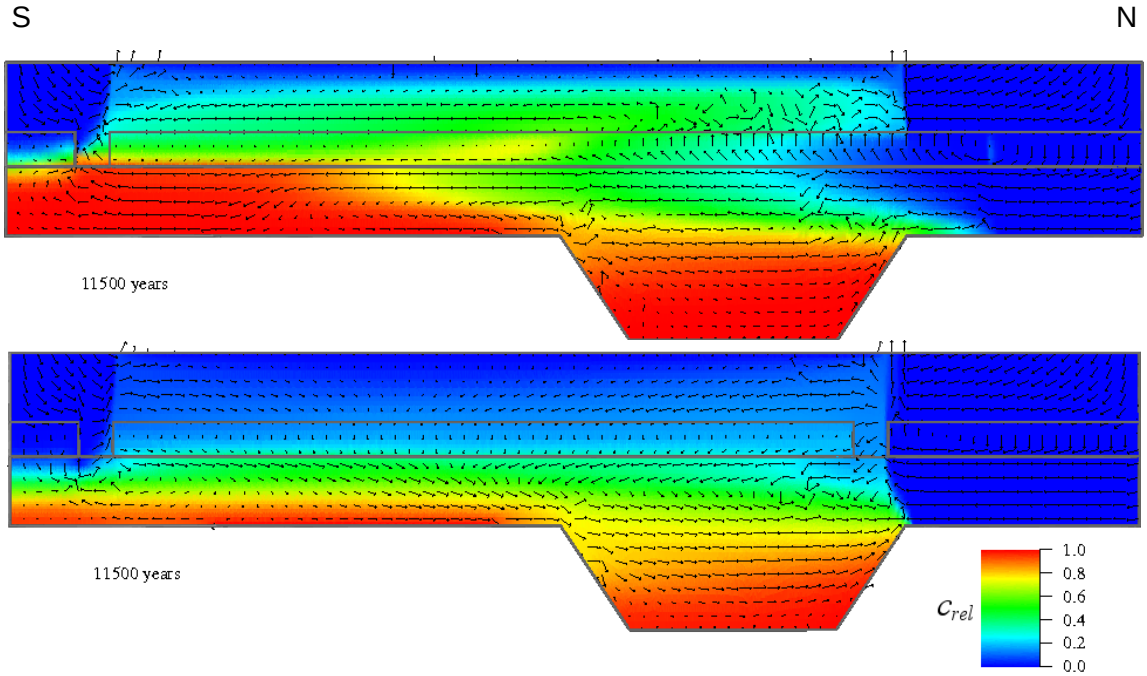

Fig. 48 *Present Climate*: Relative Salt concentrations and velocity fields for model 1 (top) and 2 (bottom). Colours: Relative salt concentrations. Arrows: Velocity vectors, vector length proportional to velocity between $1.2 \cdot 10^{-5}$ m a^{-1} and 13.1 m a^{-1} (model 1), and $1.9 \cdot 10^{-5}$ m a^{-1} and 10.6 m a^{-1} (model 2), above 0.036 m a^{-1} the arrows are cut off

South of the salt dome in the lower aquifer and above the contact to the salt dome in the upper part of the lower aquifer, the models show opposite flow directions. At the contact to the salt dome, salt is dissolved and transported into the rim syncline according to the flow direction in both models. There, the saline groundwater descends due to its higher density. Both models show a density stratification of the groundwater (Fig. 49). Fresh water areas with less than 1 g l^{-1} of total dissolved solids (TDS) (classification after /DAV 67/) are located in the central area. In model 1, the brackish water zone (1 - 10 g l^{-1} TDS) is located at a depth of less than 10 m, in the second model it reaches a depth of 34 m maximum. After a model time of 11,500 years, both models are filled with salt water (> 10 g l^{-1} TDS) except for the direct inflow areas of fresh water and the upper 10 m (model 1) and 50 m (model 2) below surface. In both cases, salt water reaches the model surface in the area of the Elbe lowlands and north of the Gartower Tannen. In model 1, the surface of the brine (> 100 g l^{-1} TDS) body shows a distinct morphology. Values of more than 100 g l^{-1} TDS are also reached in the upper aquifer, and in the area of the Elbe lowlands even extend to about 44 m below the upper model edge. In model 2, the surface of the brine body largely corresponds to the stratum boundary between aquitard and lower aquifer.

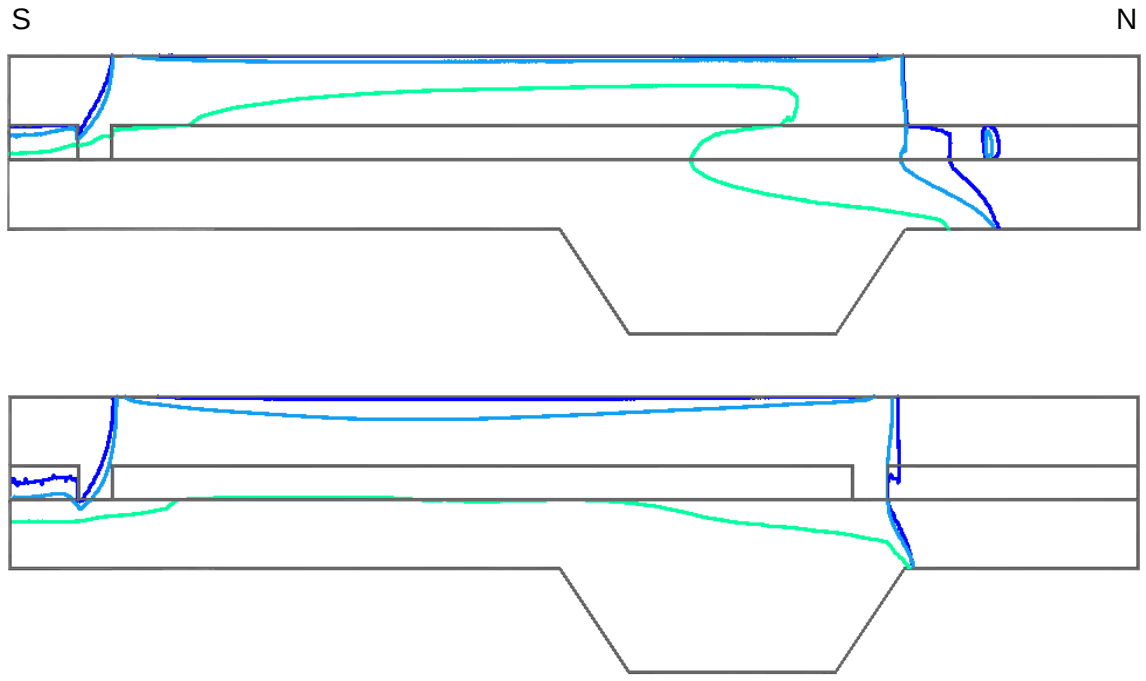

Fig. 49 Isolines of the salt water concentration for model 1 (top) and 2 (bottom) after 11,500 a. Dark blue line = 1 g l^{-1} NaCl (c_{rel} = 0.00378), blue line = 10 g l^{-1} NaCl (c_{rel} = 0.0375), green line = 100 g l^{-1} NaCl (c_{rel} = 0.344)

For a comparison of the salt concentrations with the real, present concentrations in the groundwater, density profiles of three observation wells GoHy 193, GoHy 483 and GoHy 674 of the BGR were referred to (Fig. 50). Projected into the cross section, the observation well GoHy 193 is located centrally between the southern hydraulic window and the salt dome, GoHy 483 in the centre of the salt dome and GoHy 674 centrally between the salt dome and the north-western rim syncline. The depth of the aquitards in the three observation wells varies between 20 m and 170 m b.s.l., whereas in the models, the aquitard is located at a depth between 50 m and 100 m b.s.l.

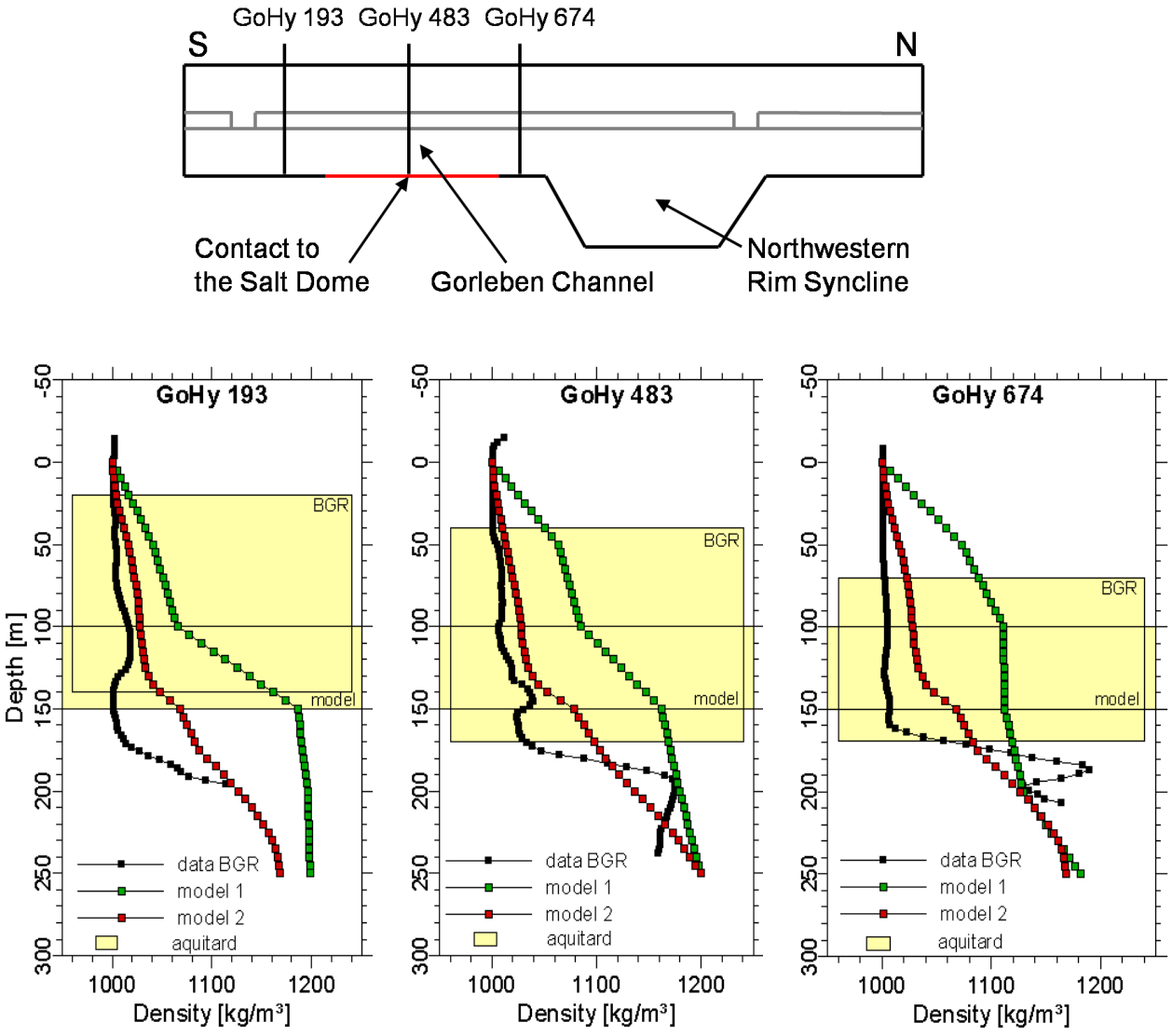

Fig. 50 Locations (above) and density profiles (below) of the observation wells GoHy 193, GoHy 483 and GoHy 674 (black) compared to the calculated density distributions for model 1 (green) and 2 (red). Aquitards are presented in yellow

In all three observation wells, there was a density increase only in the lower part of the aquitard and the upper area of the lower aquifer. This trend could be simulated in model 2. Model 1, however, already shows increased salt concentrations in the upper aquifer corresponding to a density of about 1,100 kg m^{-3} (GoHy 483, GoHy 674). Here, the density increases linearly up to 1,180 kg m^{-3} (GoHy 193) within the aquitard so that there is nearly salt saturation in the lower aquifer except at the border to the rim syncline.

Locally elevated layers of saltwater underlain by less saline water are observed at the base of the aquitard (GoHy 193, GoHy 483) and in the lower aquifer (GoHy 674). Their intensity decreases from north to south and shows the saltwater plume indicated in Fig. 45 up to the upper aquifers. Altogether, important features of the present hydraulic system can be reconstructed with both models (Fig. 50). Model 1 reflects the qualitative distribution of the salt concentrations including the elevated saltwater layers whereas they could be modelled in model 2 quantitatively. Drastic differences in the flow field of the two models are to be observed in the area of the contact to the salt dome in the lower aquifer with reverse flow directions. Since it is a process study, both models are used to model the three climate states.

With respect to the development of the salt water plume in the Elbe lowlands (see Ch. 5.3) the model hardly allows conclusions to be drawn. The salt water plume could be simulated in this work (Fig. 48, Fig. 49). In the model, the groundwater inflow from the north into the lower aquifer may be regarded as one of the decisive factors for ascending saline groundwater. This fresh water inflow is directed southward. Where it meets the salt water, a mixing and dilution takes place. Therefore, the ascending groundwater is a mixture of fresh water and salt water. It passes the aquitard and reaches the surface in the Elbe lowlands. In model 1, where almost the whole water volume passes the lower aquifer, the salt water plume is developed even more clearly than in model 2 (Fig. 49). Nevertheless, the development of a flow field and salt concentrations in the groundwater always is the product of all boundary conditions. Here, the impermeability of the southern border as well as the recharge rate and its location are assumed to influence the development of the salt water plume, too. According to /KLI 07/ the geological threshold at the salt structure causes the groundwater to ascend and reach the upper aquifer through the hydraulic window at the western boundary of the Gorleben Channel. Both characteristics are not implemented in the model geometry. A three-dimensional more complex model would better simulate the actual flow system and the origin of the salt water plume.

7.2 Selection of relevant climate states

Relevant states for the modelling of future climate changes at the reference site are derived from the geological past (see ch. 6). Three climate states were selected for this process study:

- *Constant Climate*,
- *Sea Water Inundation* during an interglacial, and
- development of *Permafrost* caused by a near-by inland ice sheet.

In order to analyse the impact of the different hydrogeological conditions caused by the climate changes, the calculation of each state was performed for one million years. Therefore, for each state the most important features can be identified. Modelling climate states with realistic periods of time and the combination of these different climate states is planned in a follow-up project.

7.3 Constant Climate

During the Quaternary, there were major climate fluctuations with periodicities between 20,000 and about 100,000 years (see chapter 2.5). Thus, it is very unlikely that the climate will remain as it is today over more than 100,000 years (until reaching the steady-state flow field and steady-state salt concentrations). On the other hand, correspondingly long periods with similar climate states already occurred in the geological past, and model calculations on climate development over the next 200,000 years indicate that, due to the low eccentricity of the Earth's orbit at that time, relatively *Constant Climate* states are possible for the next 50,000 years (see Chapter 4). Some model calculations, assuming very high anthropogenic CO_2 emissions, even show that a new ice age will occur again only after 170,000 years. For this reason, but in particular to provide a reference model, the development of the system under constant climatic conditions is investigated.

This process study aims to identify the basic processes of extreme climate changes. Therefore, marginal variations in precipitation or groundwater recharge will not be regarded. For this climate state, it is assumed that the climate prevailing today will not change significantly and thus all boundary conditions of the model for the *Present Climate* can be adopted without changes.

7.3.1 Derivation of the flow model

For the *Constant Climate*, all input parameters as well as boundary conditions were adopted from the flow model for the *Present Climate* (see Chapter 7.1, Fig. 47). The initial conditions for the modelling also correspond to the initial conditions for the *Present Climate*. The models were run until reaching the steady-state, disregarding the time scales model calculations predict for a *Constant Climate* state to prevail (see above).

7.3.2 Results

In both models, steady-state conditions are reached at the latest after 200,000 years. The two models clearly show the decrease in salt concentrations compared to the climate state *Present Climate* in particular in the north-western rim syncline (see Fig. 51, here after 300,000 years). While after a model time of 11,500 years there still are salt concentrations ranging from c_{rel} = 0.7 to c_{rel} = 1.0 in both models, they are reduced to about c_{rel} = 0.2 in model 1 and to about c_{rel} = 0.4 in model 2 after 200.000 a. This reduction mainly results from the inflow of freshwater into the lower aquifer which dilutes the saltwater in the rim syncline and transports it up to the surface. The saltwater plume from model 1, yet reaching up to the upper aquifer in the *Present Climate* state, is still present qualitatively but also with much lower concentrations of only about c_{rel} = 0.1. The flow fields scarcely change until reaching the steady-state. Relevant flow directions and velocities were already developed in the *Present Climate* state. In model 2, the areas of groundwater discharge at the surface also do not change their dimensions. Simultaneously, the area of outflow into the Elbe lowlands in the centre of the surface in model 1 is extended to a length of about 4 km to 4.5 km (*Present Climate* state: Approx. 500 m). The southbound groundwater flow in the upper part of the lower aquifer is maintained in both models. Due to the absence of the second hydraulic window in model 1, the entire groundwater inflow from the north is directed through the lower aquifer to the south of the model. This does only result in reduced salt concentrations in the north-western rim syncline but also in a partial reversion of the groundwater flow direction in the lower area of the lower aquifer from north to south. The groundwater flow from the contact to the salt dome into the north-western rim syncline resulting from the density difference is clearly reduced.

For the conditions of *Constant Climate*, steady-state flow fields and salt concentrations are only reached after 150,000 to 200,000 years for both models. The dominant process

for the distribution of the salt concentration is, as for the *Present Climate*, advection due to the high flow velocities. Also in this case, the presence of a second hydraulic window in the north of the area is of great importance for the salt concentrations in the north-western rim syncline as well as for the flow direction in the area of the Elbe lowlands and the area between the contact to the salt dome and the north-western rim syncline.

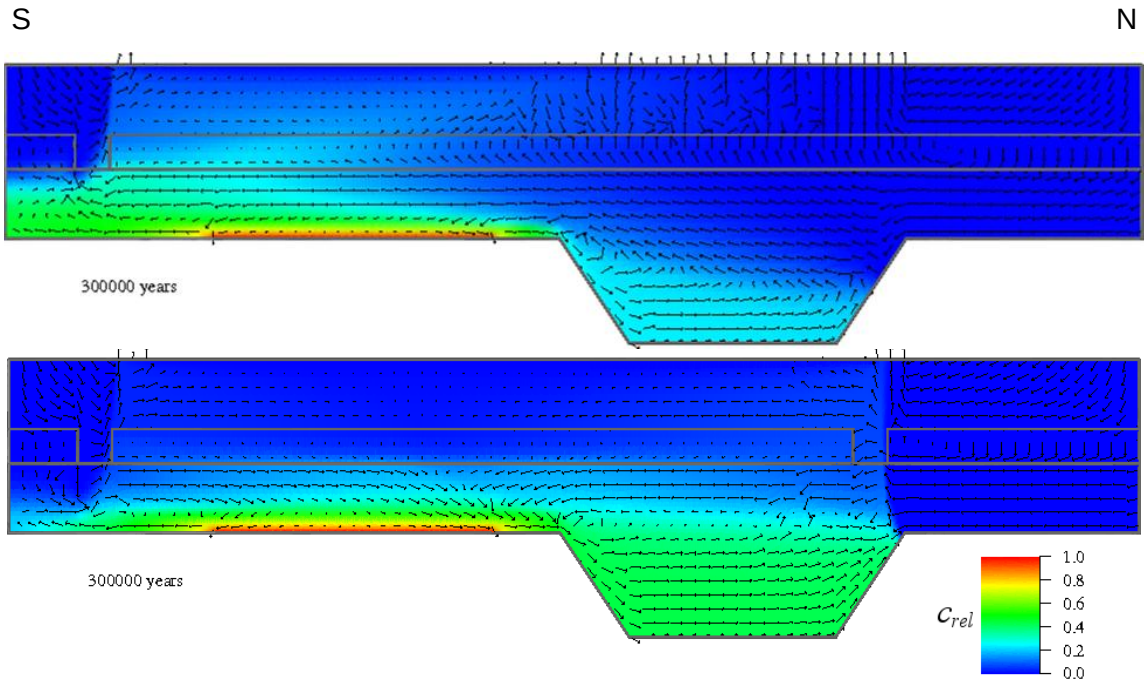

Fig. 51 *Constant Climate:* Relative Salt concentrations and velocity fields for model 1 (top) and 2 (bottom). Colours: relative salt concentrations. Arrows: Velocity vectors, vector length proportional to velocity between $6.2 \cdot 10^{-6}$ m a^{-1} and 10.0 m a^{-1} (model 1), and $6.2 \cdot 10^{-6}$ m a^{-1} and 10.1 m a^{-1} (model 2), above 0.036 m a^{-1} the arrows are cut off

7.4 Sea Water Inundation

For the *Sea Water Inundation*, different model simulations can be referred to (see Chapter 6.1) which result in different inundation levels under different assumptions on the natural climate development and on the consequences of the anthropogenic climate change. Of interest for this process study are the impacts of a maximum inundation height in the area of the reference site Gorleben. Assuming the melting of the entire Antarctic and Greenland ice volume, a sea level rise by about 67 m /GAN 07/ up to 75 m /BER 04/ is estimated. For the Gorleben area with heights between 12 and 76 m a. s. l. /KLI 07/, there could be an overlying water column of 50 – 60 m in maximum. Correspondingly, an

average 50 m water column was assumed for the simulation. The North Sea can be expected to transgress the area from northwest through the Elbe lowlands as a natural pathway like it did in the past (see Chapter 2.5.2). Thus the salt concentration of the inundating water can be simplified by the salt concentration of today's North Sea with approx. 3.5 % /LEE 01/. A melting of large volumes of the Antarctic and Greenland ice sheets would cause a dilution of the sea water and may lead to changes in the ocean circulation patterns /TEL 02/. Predicting the mixing processes of sea water and melt water, the influence of the lower temperature of the melt water on the ocean circulation and hence the possible future salt concentration of the North Sea is a complex task /RAH 02/ and not aim of this work. However, this dilution would only have a marginal consequence on the salinity of the transgressing sea water, because the volume of the melting ice is small compared to the global sea water volume /RUD 01/. By marine ostracode studies, *Ingram* showed that faunal assemblages from Holsteinian North Sea sites in Denmark, Northern Germany, and eastern Britain indicate a cold-temperate, boreal climate with marine salinities comparable to the present salinity of 3.35 % to 3.55 % /ING 98/. Therefore, the reduction of the salinity was not regarded in the simulations.

In the geological past, periods of sea water inundation persisted for about a few thousand years /SCH 06/.

7.4.1 Derivation of the flow model

Former areas of groundwater recharge and central areas with hydrostatic pressure at the model surface now are covered with an overlying water column. Here, a cover by a 50 m water column with a salt concentration equal to that of the North Sea water (c_{rel} = 0.13 - equivalent to 0.034 kg kg^{-1}) was implemented in form of a Dirichlet condition for the pressure (see Fig. 52). Moreover, the inflow into the lower aquifer does not apply anymore, since a sea water inundation can also be assumed for the recharge areas further north. All other boundaries are regarded as impermeable for diffusive-dispersive transport. The subrosion at the contact to the salt dome is described – as for the *Present Climate* – with a Dirichlet condition with c_{rel} = 1. The more likely case of hydrostatic pressure at the lateral model boundaries could not be performed due to technical reasons and the resulting long lasting computing times. Both model calculations were performed with the *Present Climate* state and the *Constant Climate* state as initial conditions. The

simulations were run until reaching the steady-state in order to illustrate processes and impacts for longer periods of time.

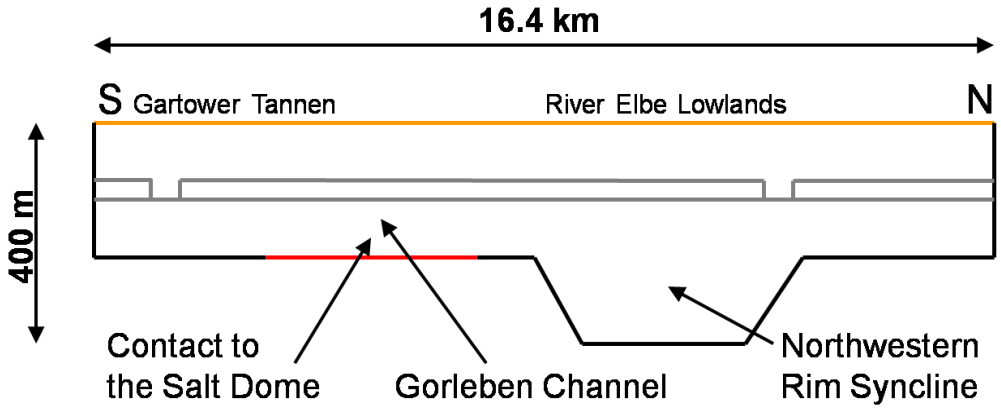

Fig. 52 *Sea Water Inundation:* Boundary conditions for the two models 1 and 2, exemplarily for model 2. Red: Contact to salt dome, orange: Overlying water column of 50 m and of c_{rel} = 0.13, black: Impermeable boundary

7.4.2 Results

The model calculations show similar results for both models and for both initial conditions (Fig. 54). In the following, the values of model 2 are given exemplarily with the initial conditions of the *Constant Climate* state (Fig. 54b). A clear change in the flow field can already be seen in both models after a model time of less than 1,000 years. Slight formation of fingering structures occur in the upper aquifer which result from infiltration of sea water with higher salt concentration (c_{rel} = 0.13) into the upper aquifer (Fig. 53).

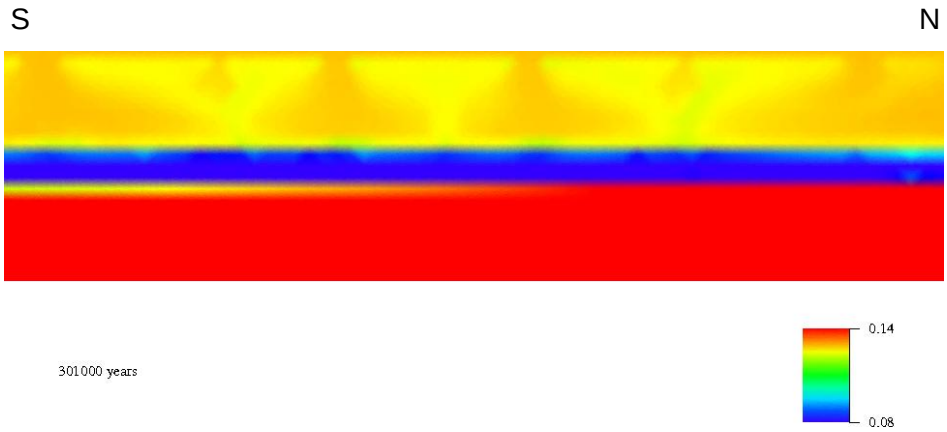

Fig. 53 Fingering structures in the upper aquifer: Relative salt concentrations between 0.08 and 0.14 for the area above the contact to the salt dome (approx. 1 km length, not exaggerated) of model 2 after 1,000 years

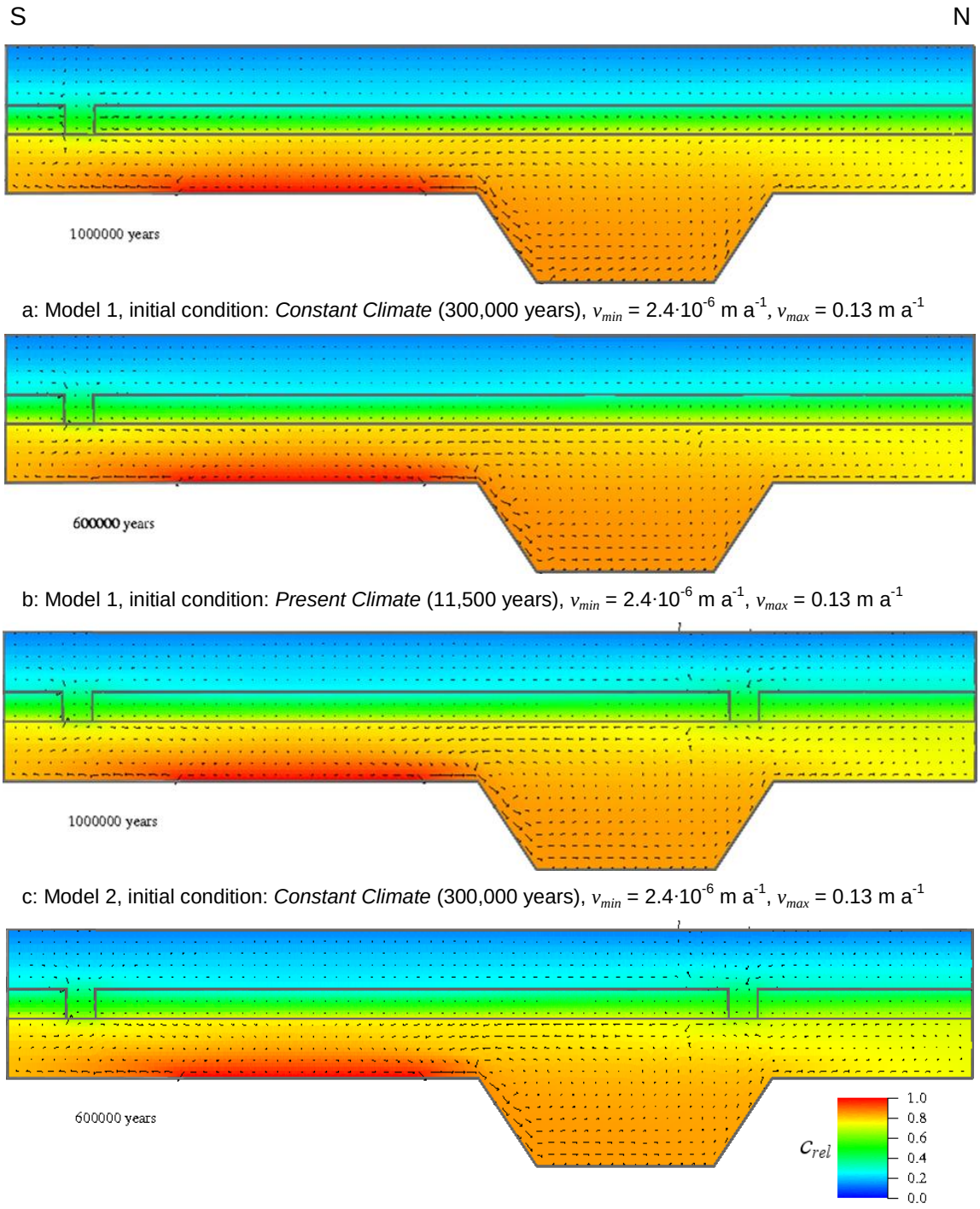

a: Model 1, initial condition: *Constant Climate* (300,000 years), v_{min} = 2.4·10^{-6} m a^{-1}, v_{max} = 0.13 m a^{-1}

b: Model 1, initial condition: *Present Climate* (11,500 years), v_{min} = 2.4·10^{-6} m a^{-1}, v_{max} = 0.13 m a^{-1}

c: Model 2, initial condition: *Constant Climate* (300,000 years), v_{min} = 2.4·10^{-6} m a^{-1}, v_{max} = 0.13 m a^{-1}

d: Model 2, initial condition: *Present Climate* (11,500 years), v_{min} = 1.4·10^{-6} m a^{-1}, v_{max} = 0.12 m a^{-1}

Fig. 54 Sea Water Inundation: Salt concentrations and velocity fields for model 1 (a, b) and 2 (c, d). Initial conditions: 300,000 years (a, c) and 11,500 years (b, d). Colours: Relative salt concentrations. Arrows: Velocity vectors, vector length proportional to velocity, above 0.036 m a^{-1} arrows are cut off

Since there is no inflow into the lower aquifer, the flow is driven by mixing processes between the groundwater with higher salt concentration above the contact to the salt dome and the groundwater with lower salt concentrations in the central and northern area of the lower aquifer. The entire upper aquifer already shows a salt concentration equal to the sea water of c_{rel} = 0.13 after less than 1,000 years.

After 50,000 years, steady-state conditions are not yet reached (not depicted) but nevertheless the models hardly differ in the salt concentration (Fig. 55) as well as in the flow field. Altogether, the models with initial conditions of the *Constant Climate* state show lower salt concentrations and groundwater densities over the entire depth due to the lower initial concentrations (Fig. 51). Density stratification of the groundwater occurs with increasing density with depth and an abrupt increase of salt concentrations within the aquitard from c_{rel} = 0.17 to c_{rel} = 0.39. In the upper aquifer and, in particular, in the aquitard, the flow velocities strongly decrease ranging from 0.2 to $1.4 \cdot 10^{-6}$ m a^{-1}. In the area between contact to the salt dome and the north-western rim syncline as well as at the base of the rim syncline, there are higher velocities of up to 0.42 m a^{-1}.

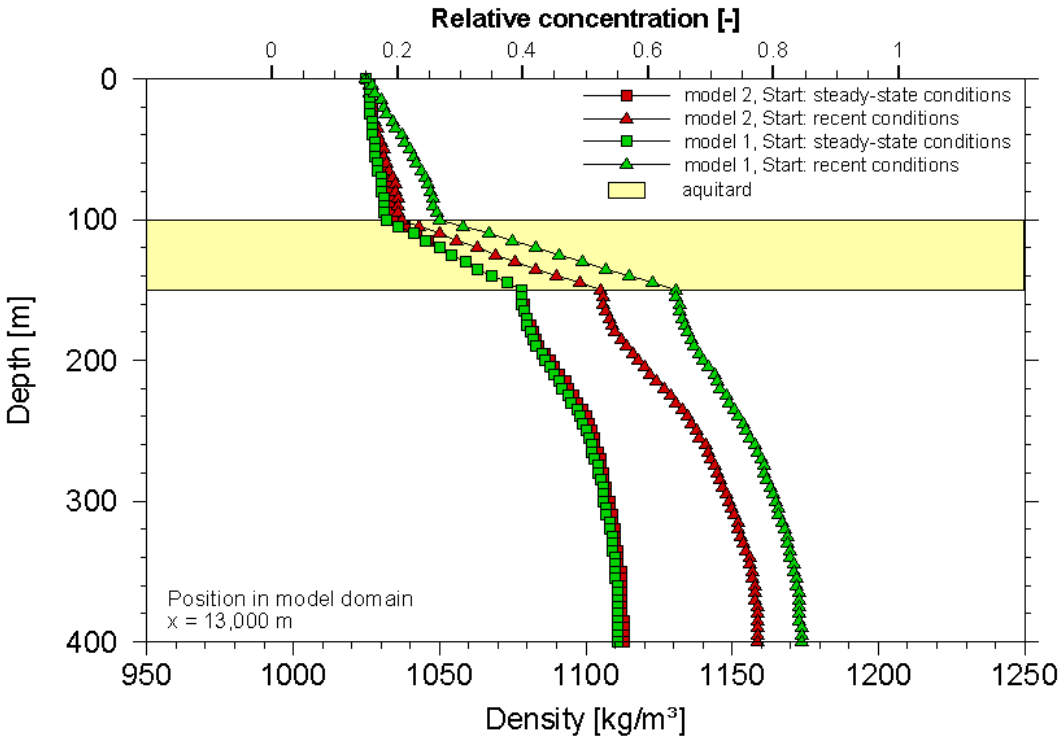

Fig. 55 *Sea Water Inundation:* Density and relative salt concentrations for the initial conditions *Present Climate* (11,500 a) and *Constant Climate* (300,000 a) after 50,000 a located 13 km from the southern boundary in the NW rim syncline. Yellow: Model Aquitard

Until the end of the calculations, salinity increases, in particular in the lower aquifer, resulting from the dissolution of salt and diffusion processes. After 700,000 years of sea water inundation, almost steady-state salt concentrations are reached. These range from c_{rel} = 0.13 at the surface to c_{rel} = 0.85 at the basis of the north-western rim syncline with maximum concentrations of c_{rel} = 1.0 at the contact to the salt dome (see Fig. 54). An abrupt increase of the concentration within the aquitard is further to be observed now with higher values between c_{rel} = 0.29 and c_{rel} = 0.74.

For the climate state of *Sea Water Inundation*, the presence of a second hydraulic window in the north is not important for large periods of time; the same applies to the initial conditions of the model calculations. Advection as dominant process regarding *Constant Climate* states is replaced by diffusion here. The steady-state flow field is reached after less than 50,000 years whereas the steady-state horizontal density stratification in the models is not yet reached after a model time of 700,000 years.

However, as already discussed, sea water inundation in the Gorleben area is not expected to last for several hundreds of thousands years but only for some thousand years. An inundation time of only a few thousand years has a clear influence on the salt concentrations in the upper aquifer and in the aquitard (model 2) which approximate the concentration of the sea water. During this period, the salt concentrations of the lower aquifer are hardly affected by the changed boundary conditions. Due to the absence of freshwater inflow into the lower aquifer, the velocity fields of models 1 and 2 are already very similar after 1,000 years. In the lower aquifer, the flow in the southern part is directed to the north towards the contact to the salt dome and the rim syncline. After the passage of the rim syncline, the groundwater partly flows further in northward direction and then partly flows back to the contact to the salt dome due to the formation of a convection cell above the rim syncline. Different flow directions in the two models are no longer to be observed.

7.5 Permafrost

In the geological past, *Permafrost* states occurred periodically at the Gorleben site. According to model calculations, permafrost during the Weichselian Glacial in the Gorleben area reached thicknesses between 40 m and 140 m /KLI 07/. Here, periods with and without permafrost alternated with a periodicity of 10,000 to 30,000 years (see Fig. 43, chapter 6.2). Completely unfrozen zones - so-called taliks - may be formed in the area

beneath rivers and lakes due to their thermal influence /KEL 98/, /DEL 98/. During the temperature development of the past 50,000 to 8,000 years, a talik with a width of 500 m could have been formed beneath a river with a width of 25 m /DEL 98/. For the Elbe, having a width of about 250 m in the Gorleben area, a talik of 5 km can be assumed. Another talik could have been formed beneath the River Seege farther south. With less than 50 m, the Seege has a smaller width than the Elbe, therefore a talik of 500 m is assumed. During rainfall or flood events, the unfrozen zones could serve as infiltration areas for groundwater recharge. At the same time, groundwater could be discharged during high inflow from the lateral boundaries into the lower aquifer through these unfrozen zones of the upper aquifer up to the surface.

In the case of a future glacial it is to be assumed that there will be, like in the past, an inland ice sheet north or north-east of the Gorleben area. The permafrost regions melt due to the load of the inland ice sheet. Assuming that the inland ice sheet, similar to the inland ice sheet of the last glacial (Weichselian) will be located directly north of the investigation area (see chapter 2.5.5), large volumes of meltwater could infiltrate into the underground and from there flow into the lower aquifer of the model domain. In this case, the southern boundary of the model domain is no longer defined as a subterranean water divide. While the southern boundary of the upper aquifer becomes impermeable for groundwater due to permafrost, the groundwater from the lower aquifer can discharge to the south or flow into the model area.

7.5.1 Derivation of the flow model

In the model, permafrost regions in the upper aquifer are realised by reduction of the permeability of $k = 1 \cdot 10^{-12}$ m² to $k = 1 \cdot 10^{-20}$ m². The permafrost thickness extends over the entire thickness of the upper aquifer of 100 m (Fig. 56). Unfrozen zones (taliks) maintain their original permeability of $k = 1 \cdot 10^{-12}$ m². A large talik has a width of 5 km and is located in the area of the Elbe lowlands above the north-western rim syncline (8,000 to 13,000 m north of the southern boundary of the model). At the boundaries, transition zones with a width of 500 m are defined in which the permeability decreases linearly to the reduced value of $k = 1 \cdot 10^{-20}$ m². Another small talik is located between 450 m and 550 m north of the southern boundary with lateral transitions to the frozen zones with a width of 50 m. A major difference between the models is that in model 1 the northern talik is located above the aquitard whereas in model 2 the hydraulic window is situated in the talik area and creates a path between the lower aquifer and the model surface. All other hydrogeological

parameters remain unchanged. At the model surface, a Dirichlet condition is defined for the pressure (p = 0 Pa). Similar to the *Present Climate* state, here a salt concentration of c_{rel} = 0 is defined at the entire surface for the inflow while for the outflow the concentration is set to the actual concentration of the outflowing groundwater. The southern boundary of the lower aquifer is modelled with the same hydrostatic pressure as the surface and the same implicit boundary condition for the salt concentration.

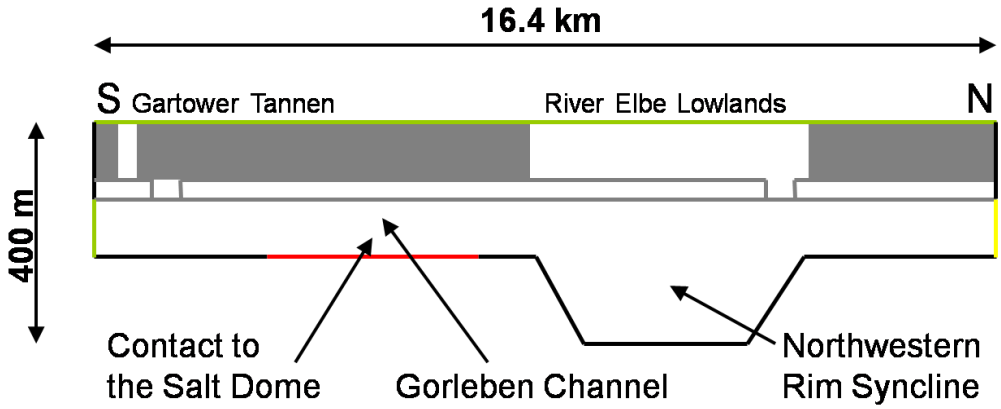

Fig. 56 *Permafrost:* Boundary conditions for the two models 1 and 2, exemplarily for model 2. Red: Contact to the salt dome, green: Hydrostatic pressure, yellow: Inflow of freshwater in form of a gradient of i = 0.1, grey: Permafrost region with k = $1 \cdot 10^{-20}$ m², black: Impermeable boundary

At the northern boundary of the lower aquifer, an inflow of meltwater is assumed which is given in form of a gradient of i = 0.1 /KOE 00/ and is indicated as a velocity boundary condition with v = $1 \cdot 10^{-6}$ m s^{-1}.

As for the state of *Sea Water Inundation*, the calculations were performed for the models 1 and 2 with the initial conditions of the *Present Climate* state and the *Constant Climate* state until reaching steady-state conditions.

7.5.2 Results

Models 1 and 2 differ essentially regarding the assumption of *Permafrost* conditions. However, the different initial conditions have almost no influence on the results of the simulations. For this reason, only the results of the model calculations of models 1 and 2 for the initial conditions of the *Constant Climate* are discussed exemplarily in the following (Fig. 57).

After 10,000 years already, both models show quasi-steady-state flow fields. The inflow of freshwater from the north into the lower aquifer is 160 times larger in model 1 and 16 times larger in model 2 than for the *Present Climate*. At the end of the simulations, the flow velocities in the permafrost regions in model 2 range between 10^{-10} and 10^{-6} m a^{-1} (Fig. 57). In the inflow area into the lower aquifer, there is a flow velocity in southward direction of 31.5 m a^{-1} which is reduced insignificantly at the hydraulic window and at the northern talik due to the additional upward flow path. There, velocities with the highest vertical components occur and the velocity vectors reach values of up to 30 m a^{-1}. The southbound groundwater flow is partly reversed at the contact area to the salt dome. Despite the high inflow from the north there is a back flow due to the dissolution of salt and the higher density of the groundwater and the groundwater sinks down into the north-western rim syncline. South of the salt dome, the flow is solely directed southward but with clearly reduced values of up to 0.2 m a^{-1}.

Due to the absence of a second hydraulic window in model 1, only a smaller groundwater volume can discharge through the northern talik. The major part of the groundwater flows out of the model area directly through the lower aquifer in southward direction. At the end of the simulations, the flow velocities in the northern talik only reach 0.3 m a^{-1} maximum. In model 1, the southern talik is also used as a flowpath for the groundwater. Here maximum velocities of 0.08 m a^{-1} are found. With the groundwater, dissolved salt also reaches the surface through the southern talik. Concentration reaches values up to c_{rel} = 0.36. In contrast to model 2, the flow direction in model 1 is not reversed between the rim syncline and the contact to the salt dome. The southbound flow direction to the southern boundary of the model is maintained with maximum velocities of 5.6 to 15.4 m a^{-1}.

In model 2, the large inflow into the lower aquifer results in a significant reduction of the salt content in the north-western rim syncline. In model 1, it even leads to a “wash out” of the rim syncline with reduction of the salt concentration to c_{rel} = 0. The salt concentration also decreases in all other areas of the model domain. In the permafrost regions, diffusion processes prevail so that steady-state salt concentrations are only reached very slowly and in dependence on the initial conditions. The higher the initial concentrations, the later the stationary salt concentrations are reached. In model 2, freshwater conditions dominated in the north and south of the upper aquifer at the beginning of the climate state *Permafrost* with higher salt concentrations up to c_{rel} = 0.07 in the centre. Steady-state salt concentrations are reached in the unfrozen zones after about 40,000 years. Although the permeability in the permafrost regions is very low, steady-state conditions are already

reached after 10,000 to 40,000 years due to the low initial concentrations. As an initial condition, model 1 has a larger saltwater plume in the upper aquifer (see chapter 7.1.4). In the frozen zones, the maximum salt concentration at the beginning of the simulation was c_{rel} = 0.17. Due to this higher concentration, the steady-state of the salt concentration by diffusion processes is not yet reached after 400,000 years in model 1. In the unfrozen zones, however, it is reached after about 2,000 years.

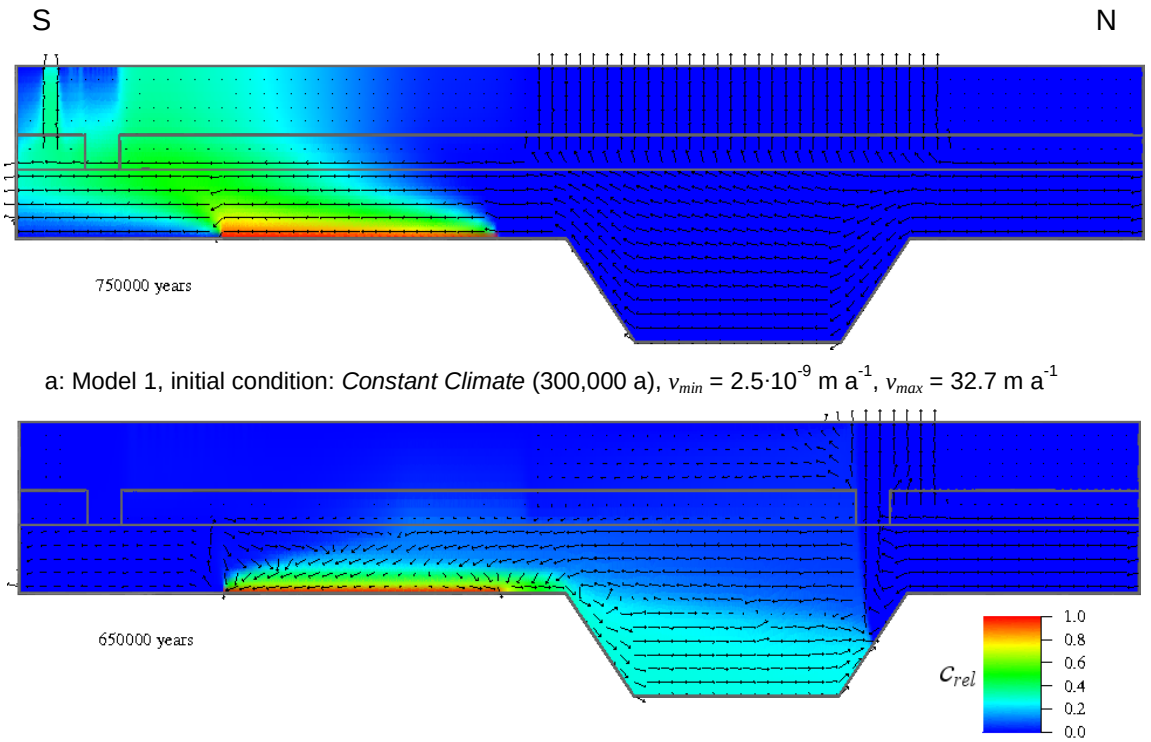

a: Model 1, initial condition: *Constant Climate* (300,000 a), v_{min} = 2.5·10^{-9} m a^{-1}, v_{max} = 32.7 m a^{-1}

b: Model 2, initial condition: *Constant Climate* (300,000 a), v_{min} = 1.1·10^{-10} m a^{-1}, v_{max} = 34.5 m a^{-1}

Fig. 57 *Permafrost:* Relative salt concentrations and velocity fields for model 1 (a) and 2 (b). Initial conditions: 300,000 years. Colours: relative salt concentrations. Arrows: Velocity vectors, vector length proportional to velocity, above 0.036 m a^{-1} arrows are cut off

Main features of the climate state *Permafrost* are the high velocities in the lower aquifer, the slow transport processes by diffusion in the frozen zones of the upper aquifer and the strongly reduced salt concentrations in the entire model domain, in particular in the north-western rim syncline. Main differences of the two models for the climate state *Permafrost* are the contrary flow directions above the salt dome in the lower aquifer, the remaining residual salt concentration in the north-western rim syncline in model 2 and the higher salt concentrations in the southern permafrost regions of model 1.

7.5.3 Subrosion rate

Subrosion rates at the contact to the salt dome are of special interest regarding the *Permafrost* state. *Zirngast* /ZIR 91/ reconstructed the primary thickness of the Zechstein for the salt structure Gorleben after the methods given by *Rühberg* /RUE 76/ in order to balance the salt volumes. He added the thicknesses of the rim synclines to the present Zechstein salt thickness below the synclines. The result allows conclusions to be drawn about the shape of the salt pillow before reaching the diapir stadium and the primary Zechstein thickness. Knowing the duration of the different geologic units and the epirogenetic uplift rate, it is possible to calculate the uplift of the salt dome and the velocity of salt flow. Additionally, the salt volumes can be balanced obtaining the total subrosion at the salt dome over time. *Zwirner et al.* /ZWI 04/ and *Klinge et al.* /KLI 07/ distinguished the subrosion rates for the different time frames in the Quaternary. Thus, post-Elsterian subrosion rates amount to an average 0.1 mm a^{-1} to 0.2 mm a^{-1}, with a maximum of 0.4 mm a^{-1} during the Saalian Glacial and a minimum of approx. 0.01 mm a^{-1} to 0.05 mm a^{-1} in the post-Saalian. Of special interest is the subrosion rate during a *Permafrost* state, because the highest water inflow is expected to occur due to a close-by inland ice sheet. Subrosion rates can therefore be estimated to be smaller than 0.05 mm a^{-1} commensurate to the post-Saalian (see above).

For the given models, the subrosion rate can be calculated analytically using the transport equation for a permanent source. Therefore, the model system is simplified according to Fig. 58.

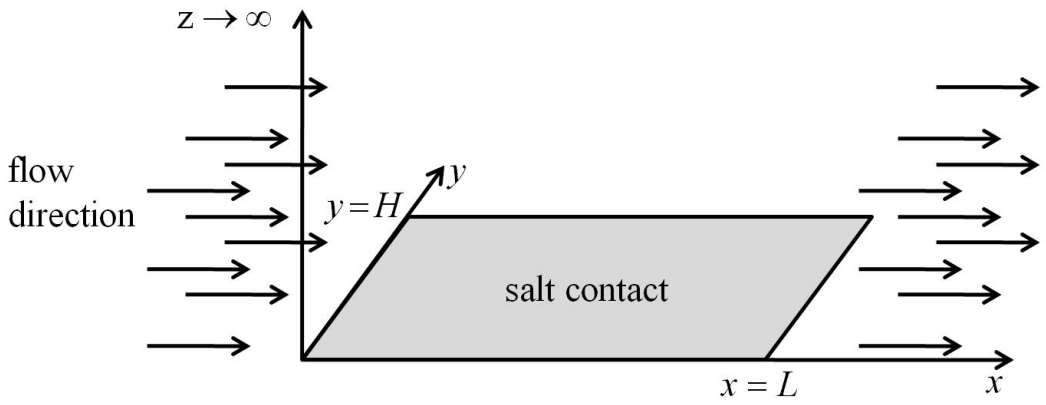

Fig. 58 Simplified scheme for the calculation of the subrosion rate

Postulating a uniform flow along the contact to the salt dome and considering the salt dome as a permanent source of salt, the salt concentration depends on the time t and the path z covered by the groundwater.

The salt mass leached from the salt contact then amounts to

$$m_{NaCl} = \int_0^{x=L} \int_0^{y=H} \int_0^{z=\infty} C(x,y,z)dxdydz$$

with m_{NaCl} = salt mass subroded from the salt dome contact and

$C(x,y,z,t) = C_{eq} \cdot erfc(\frac{z}{2\sqrt{D_m \cdot t}})$ = salt concentration (Fig. 59).

This analytical solution considers the salt dissolution by diffusion, while C_{eq} equals the equilibrium solubility of rock salt at the salt dome contact and C is set to zero for $z \to \infty$.

The subrosion rate SR [m s^{-1}] is then given by

$$SR = \frac{4 \cdot C_{eq}}{3 \cdot \rho_{NaCl}} \sqrt{\frac{D_m}{L}} \qquad (7.1)$$

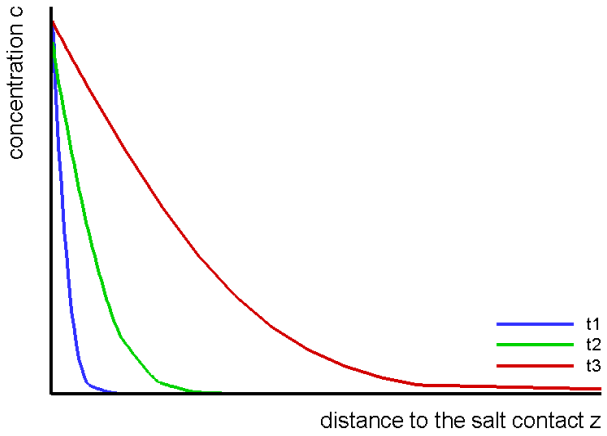

Fig. 59 Salt concentration by diffusion depending on the distance z to the salt dome for different time steps t

The subrosion rate for even flow along the salt dome according to Eq. (7.1) equals 1.87 mm a^{-1} for model 1 and 0.27 mm a^{-1} for model 2.

An easier but viable approach is balancing the salt mass flows over the boundaries of the model. According to

$$m_{out} = q_{out} \cdot \rho_f \cdot \Gamma$$

with m_{out} = total mass flow perpendicular to Γ,

q_{out} = groundwater velocity scalar perpendicular to Γ,

ρ_f = fluid density, and

Γ = area of the considered outflow model boundary,

the salt mass flow can be calculated based on the primary variables using $c_{rel} = \frac{c_{abs}}{c_{abs,\max}}$ by

$$m_{out,NaCl} = c_{abs,\max} \cdot c_{rel} \cdot q_{out} \cdot (\rho_0 + c_{rel} \cdot (\rho_{\max} - \rho_0)) \cdot \Gamma \qquad (7.2)$$

with $m_{out,NaCl}$ = total salt mass flow through the considered model boundary and

q_{out} = groundwater velocity component perpendicular to the considered model boundary.

Regarding the steady-state flow and salt concentration field of the *Permafrost* state, the salt, which is transported out of the model domain, can only originate from salt dissolution at the contact to the salt dome. Transport of salt over the boundaries of the model in the steady-state therefore only results from subrosion. The different model calculations for the *Permafrost* state result in the subrosion rates given in Tab. 12.

Tab. 12 Modelled subrosion rates at the contact to the salt dome for the climate state *Permafrost*, calculated by the salt mass flow out of the model domain (cf. Eq. (7.2))

	Initial condition	Salt mass flow [$m^3\ a^{-1}$] over		Total subrosion rate [$mm\ a^{-1}$]
		southern boundary	surface	
Model 1	*Constant Climate* (300,000 a)	$3.19 \cdot 10^{1}$	$4.36 \cdot 10^{-2}$	6.4
Model 1	*Present Climate* (11,500 a)	$3.19 \cdot 10^{1}$	$6.80 \cdot 10^{-2}$	6.4
Model 2	*Constant Climate* (300,000 a)	$8.62 \cdot 10^{-6}$	$1.68 \cdot 10^{-1}$	$3.4 \cdot 10^{-2}$
Model 2	*Present Climate* (11,500 a)	$1.13 \cdot 10^{-5}$	$1.69 \cdot 10^{-1}$	$3.4 \cdot 10^{-2}$

The subrosion rate of 6.4 mm a^{-1} resulting from model 1 is approx. 3.4 times higher than the 1.87 mm a^{-1} given above. The modelled subrosion rate of $3.4 \cdot 10^{-2}$ mm a^{-1} in model 2 is lower than the calculated 0.27 mm a^{-1}, but still close the given $1 \cdot 10^{-1}$ mm a^{-1} to $2 \cdot 10^{-1}$ mm a^{-1} for the post-Elsterian time [Klinge et al., 2007; Zwirner et al., 2004]. Extrapolated to past duration times of approx. 10,000 years with permafrost with a depth of more than 100 m (see Fig. 43), 64 m of the salt thickness would be subroded in model 1, while in model 2 the subrosion would be limited to approx. 0.34 m. Compared with the very low subrosion during the Weichselian [Klinge et al., 2007], the subrosion in model 1 can be regarded as too high.

The salt mass transport out of the model area occurs mainly over the southern model boundary in model 1 and over the model surface in model 2. The differences between the two salt mass flows are drastically higher in model 2 than in model 1.

Once again, model 2 is meeting the estimations better than model 1. Nevertheless model 1 still represents a possible future climate state. Therefore it is regarded in the transport calculations even though not as detailed as model 2 (see ch. 7.7).

7.6 Summary and conclusions

Tab. 13 gives an overview of the modelled climate states and their characteristics. With the present two-dimensional flow model, the present conditions of the hydrogeological system in the Gorleben area could be described in sufficient detail. Both models show the main characteristics of the salt concentrations and the flow field. Here, the existence of a second hydraulic window north of the north-western rim syncline in combination with the different inflow has obvious impacts on the groundwater flow in the lower aquifer, resulting in different flow directions and salt concentrations. It could be demonstrated that the present hydrogeological system is not in a steady-state. In the present state, the dominant process is advection.

The model calculations for the *Constant Climate* serve, among other things, as a reference case for the two extreme climate states. In this case, the existence of the second window and the inflow rate into the lower aquifer is of less influence than for the *Present Climate*. The dominant process remains the advection. Steady-states are reached after about 150,000 to 200,000 years.

Tab. 13 Summary of modelled climate states and their main characteristics. Influence of the number of hydraulic windows from very large (+++) to no influence (-)

	Present Climate	*Constant Climate*	*Sea Water Inundation*	*Permafrost*
Influence of hydraulic windows	++	+	-	+++
Dominant process	advection	advection	diffusion	Advection (diffusion in frozen zones)
Steady-state velocity field [a]	no steady-state	150,000 - 200,000	< 50,000	~ 10,000
Steady-state distribution of salt concentrations [a]	no steady-state	150,000 - 200,000	> 700,000	2,000 - 40,000 unfrozen zones 10,000 - > 400,00 frozen zones

Sea Water Inundation of the area already leads to changed salt concentrations and flow velocities in the upper aquifer after less than 1,000 years. Diffusion processes dominate so that more than 700,000 years are required to reach steady-state salt concentrations in the whole model area. A steady-state flow field, however, is reached after less than 50,000 years. In order to have clear impacts on the lower aquifer and the aquitard, *Sea Water Inundation* has therefore to last longer than several tens of thousands of years. Since expected periods of *Sea Water Inundation* will not last longer than a few thousand years, it can be assumed that *Sea Water Inundation* will have nosignificant impact on the entire hydraulic system except for the upper aquifer.

The second hydraulic window is of great relevance for the climate state *Permafrost*. Together with the dimension and position of the taliks zones in the upper aquifer, it determines the flow direction in the lower aquifer and the salt concentration in the north-western rim syncline. The hydraulic system reacts to the changed boundary conditions within a few thousand years. In the unfrozen zones, advection dominates due to the large inflow. Steady-state flow velocities are reached after about 5,000 to 10,000 years. Steady-state salt concentrations are reached in the unfrozen zones after about 2,000 to 40,000 years, in the permafrost regions, however, only after 10,000 or even more than 400,000 years. In this climate state, the highest flow velocities occur which are reflected in the transport models. The period in time until reaching steady-state salt concentrations do not only depend on the presence of a second hydraulic window but, to a large degree, also on the initial conditions of this appropriate climate state. The subrosion rates at the contact to the salt dome were calculated for the *Permafrost* state. In model 1, the

subrosion rate is much higher than during the past. Model 2 shows a realistic subrosion rate of $3.4 \cdot 10^{-2}$ mm a^{-1}. It is assumed that model 2 is a more reliable model for future *Permafrost* states.

7.7 Transport model

In the case of a disturbed evolution of the repository, radionuclides could be released from the near field into the far field and could be transported through the overburden and reach the biosphere. On the basis of their different half-lives and sorption properties, eight radionuclides were selected for transport modelling through the hydrogeological system of the overburden under varying climate conditions. These radionuclides are relevant for performance assessments for high level waste (HLW) /BUH 08a/. Within this study, no effective radiation exposures will be calculated. This is, like for the flow modelling, a process study. This is why an amount of reference substance was assumed for the radionuclides instead of a released amount of substance calculated for a disturbed evolution. The sediment characteristics and the geological structure of a location intended for a repository should ensure the isolation of the waste for a period in the range of one million years /AKE 02/. Therefore, all transport models were simulated over a model period of one million years.

7.7.1 Derivation of the transport model

Transport calculations were performed for the *Present Climate* state, the *Constant Climate* state and the climate states *Sea Water Inundation* and *Permafrost* (see Tab. 14). Selected radionuclides are Cs-135, I-129, C-14, Zr-93 and the radionuclides of the uranium decay series U-238, U-234, Th-230 and Ra-226. In addition to that, the transport of an inert tracer was simulated in each model calculation. This conservative tracer will be referred to as “tracer” in the following. The radionuclides and the tracer are released into the model area from a point source in the centre of the salt dome contact. The location corresponds approximately to that of the two shafts of the pilot mine Gorleben, which were projected into the cross section (see Fig. 30, chapter 5.1). An inflow of the examined radionuclides and of the tracer was defined over a period of one year (delta pulse) or one million years (continuous inflow) both with an amount of mass of n = 1 mol. In the case of the uranium decay series only an inflow of 1 mol of the parent nuclide U-238 was assumed. The daughter nuclides result from radioactive decay.

For the *Constant Climate* state, all combinations of transport calculations (model 1 and 2, all radionuclides, delta pulse and continuous inflow, Tab. 14) were performed. The simulation of all combinations of the transport models for Cs-135 (model 1 and 2, delta pulse and continuous inflow, all climate states) were accomplished as well. For the *Present Climate* state, the *Sea Water Inundation* state and the *Permafrost* state only the calculations for model 2 and the delta pulse were performed.

Tab. 14 List of the transport calculations performed (x: calculation performed). „U-Th-Ra“: Radionuclides of uranium decay series U-238, U-234, Th-230 and Ra-226. Inflow time: 1 a = delta pulse, 10^6 a = continuous inflow

		Cs-135		I-129		C-14		Zr-93		U-Th-Ra	
Inflow time [a]		1	10^6	1	10^6	1	10^6	1	10^6	1	10^6
Present Climate	Model 1	x	x								
	Model 2	x	x	x		x		x		x	
Constant Climate	Model 1	x	x	x	x	x	x	x	x	x	X
	Model 2	x	x	x	x	x	x	x	x	x	X
Sea Water Inundation	Model 1	x	x								
	Model 2	x	x	x		x		x		x	
Permafrost	Model 1	x	x								
	Model 2	x	x	x		x		x		x	

7.7.1.1 Boundary conditions

The boundary conditions were defined for the preceeding flow models. Thus, the boundary conditions for the transport calculations result in the boundary conditions described below.

For the *Present Climate* state a Dirichlet condition for the inflow in the lower aquifer with c = 0 mol m^{-3} is assigned. An inflow and outflow boundary condition is stated for the model surface. This depends on the flow direction, which was determined in the d³f calculations. The concentration in the case of inflow is assumed to be c = 0 mol m^{-3}. In case of outflow, the radionuclide concentrations are set equal to the concentrations in the outflowing groundwater.

The same boundary conditions are applied to the state of *Constant Climate*.

The boundary conditions for the surface are also adopted for state of *Sea Water Inundation* but in this case the northern boundary of the lower aquifer is assumed to be impermeable, as no inflow from the north exists.

For the *Permafrost* state, the inflow and outflow boundary conditions at the model surface are maintained. Here again an inflow of fresh water into the lower aquifer can be observed, this is realised like for the *Present Climate* state by a Dirichlet condition with c = 0 mol m^{-3}. On the southern boundary of the lower aquifer a hydrostatic pressure is implemented with the inflow and outflow boundary condition as described above.

7.7.1.2 Hydrogeological and hydrogeochemical characteristics

Hydrogeological parameters of the three sedimentary units are taken from the flow calculations (Tab. 11). The Darcy-velocity field and the salt concentration field of the flow calculations are transferred to the program r³t for the transport calculations. For every radionuclide the half-lives /MAG 06/ and K_d values /SUT 98/ which depend on the groundwater salinity and the sediment type are stated (Tab. 15). In comparison to one million years of model time, the half-lives of the selected radionuclides are very long with the exception of C-14. Therefore, it was expected that the influence of the radioactive decay on the transport calculations is smaller than the influence of the various flow fields and sorption coefficients.

The dependence of the sorption on the groundwater salinity is considered in r³t by means of different uniform sorption coefficients (K_d values) assigned for the different geological units. The sorption coefficients used were gained from a study evaluating sediment and groundwater samples from the Gorleben region. Here, the K_d values were differentiated with respect to the two states “fresh water” and “saline water” only. Saline water is defined by a content of total dissolved solids (TDS) higher than 10 g l^{-1}, hence the limit between fresh and saline water is given by a relative salt concentration of c_{rel} = 0.0375. As in this case flow fields with constant distribution of the salt content are applied, time-independent K_d values were defined for each hydrogeological unit to simplify the model. The K_d values were determined regarding the isolines of the salt concentration and of flow fields (Fig. 60). For zones with salt concentrations of c_{rel} > 0.0375, the K_d value for saline groundwater is assumed. However, mainly in the upper aquifer this cannot always be clearly

determined and has to be based on personal judgement, e.g. for the *Permafrost* state in model 1 (Fig. 60 d). Here the assignment depends on the flow direction. In this case, the flow in the lower aquifer is directed to the south with a high velocity. Although in the central part of the model area salt concentrations c_{rel} < 0.0375 exist, K_d values for saline water are assumed for all three sedimentary layers. The advective transport of the radionuclides from the source into the overburden is expected to match the flow direction out of the model area. In this area the salt concentrations are c_{rel} > 0.0375.

Tab. 15 Half-lives (HWZ) and K_d values of the radionuclides selected for the transport modelling. Limit between fresh water and saline water at TDS = 10 g l^{-1} (HWZ from /MAG06/; K_d values from /SUT98/)

Radionuclide	HWZ [a]	K_d, sand (aquifer) [ml g^{-1}]		K_d, silt, clay (aquitard) [ml g^{-1}]	
		Fresh water	Saline water	Fresh water	Saline water
C-14	$5.73 \cdot 10^3$	0.2	0.2	2	2
I-129	$1.57 \cdot 10^7$	2	0.1	2	2
Cs-135	$2.00 \cdot 10^6$	70	2	400	70
Zr-93	$1.50 \cdot 10^6$	40	40	100	40
U-238	$4.47 \cdot 10^9$	2	0.6	80	20
U-234	$2.46 \cdot 10^5$				
Th-230	$7.54 \cdot 10^4$	200	200	2000	200
Ra-226	$1.60 \cdot 10^3$	40	2	300	40

In almost all calculations K_d values for saline water are used. Exceptions are the calculations for model 2 for the state of *Constant Climate* and for the *Permafrost* state. In these cases, fresh water conditions predominate in the upper aquifer (*Constant Climate*), and in the upper aquifer and in the aquitard (*Permafrost*), respectively. For the calculations of the *Sea Water Inundation*, the salt concentration of the entire model area is above c_{rel} = 0.13, hence no isoline for c_{rel} = 0.0375 can be shown. The values of the sorption coefficients for hydrogeological units and for the different climate states are listed in Tab. 16.

It was not the aim of this work to derive sorption data from experimental results. Therefore, the most recent published data set with average values for argillaceous and sandy material was used /SUT 98/. The data for uranium in clay are quite low compared

to a value of 700 ml g^{-1} derived from a natural analogue site in Southern Germany /SCH 07a/ or values used in other safety assessments. However, the speciation and the sorption value of uranium is dependent on various parameters as redox potential, pH and ligands like carbonate. In particular, the assumption that uranium exists in its oxidised form might explain quite low sorption values in the Gorleben overburden.

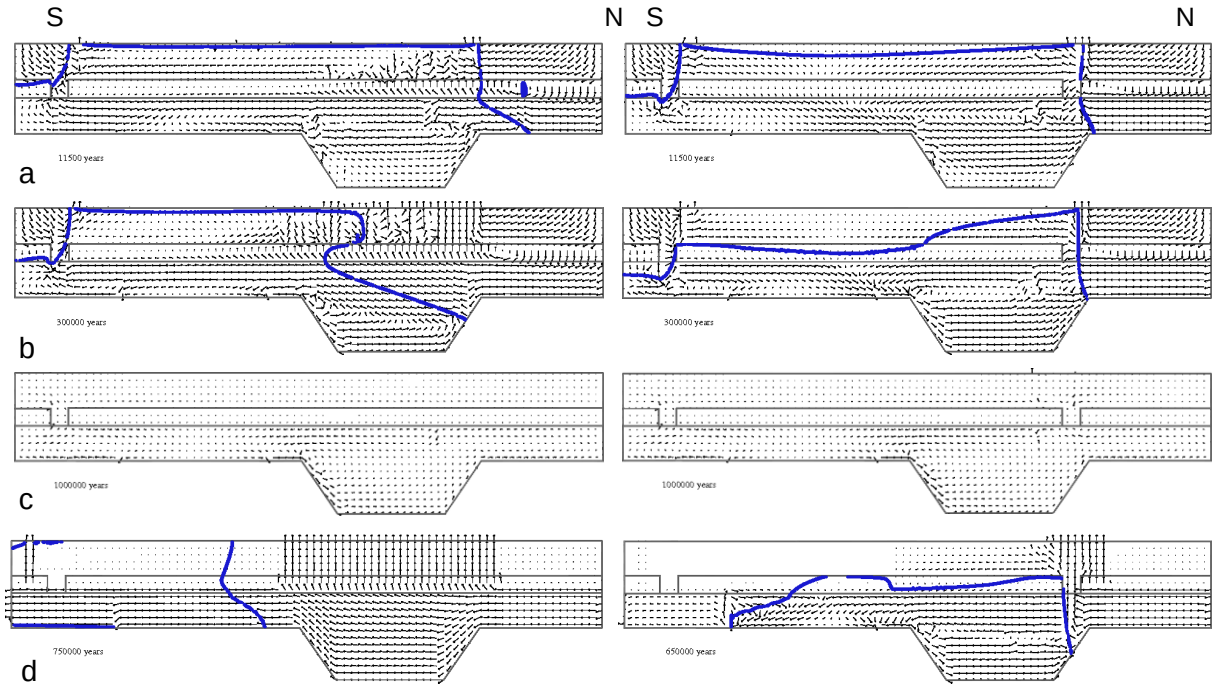

Fig. 60 Isolines for c_{rel} = 0.0375 and 10 g l^{-1}, respectively. c_{rel} and flow fields from the flow models as a basis for the transport models for a) *Present Climate* b) *Constant Climate* c) *Sea Water Inundation* and d) *Permafrost*. For the *Sea Water Inundation*, the isoline c_{rel} = 0.0375 does not exist (see text)

Tab. 16 Matrix derived from the flow fields and salt concentrations of the flow calculations (see Fig. 60) for the K_d values applied in the transport calculations; saline water with TDS > 10 g l^{-1}, freshwater with TDS < 10 g l^{-1}

		Upper aquifer	Aquitard	Lower aquifer
Present climate	Model 1	saline	saline	saline
	Model 2	saline	saline	saline
Constant Climate	Model 1	saline	saline	saline
	Model 2	fresh	saline	saline
Sea Water Inundation	Model 1	saline	saline	saline
	Model 2	saline	saline	saline
Permafrost	Model 1	saline	saline	saline
	Model 2	fresh	fresh	saline

7.7.2 Results

7.7.2.1 Transport of Cs-135

Constant Climate

Model 2, delta pulse

Cs-135 has a half-life of $2.00 \cdot 10^6$ years. The sorption coefficients of 2 ml g^{-1} (lower aquifer) and of 70 ml g^{-1} (upper aquifer and aquitard) differ significantly. After 1,000 years, Cs-135 reaches only the lower limit of the aquitard due to the retardation (Fig. 61a), whereas the non-sorbing tracer is already transported to the model surface and to the boundary of the north-western rim syncline (see Fig. 61c). After one million years, Cs-135 can be observed in almost the entire lower aquifer. It reaches the surface by passing the two hydraulic windows, whereby the transport through the northern window is significantly larger since the groundwater flow is directed northward. The southward transport is dominated by dispersion and diffusion against the flow direction. In this climate state, the upper aquifer contains fresh water, thus Cs-135 is sorbed more strongly than in the lower aquifer. Therefore, it does not spread horizontally within the entire upper aquifer but it is

mainly distributed vertically up to the surface above the hydraulic windows. It reaches the highest concentration above the northern window in the area of the rim syncline.

After one million years, a large amount of tracer has already left the model area. Since it is not sorbed, it can be transported by advection through the aquitard into the upper aquifer and to the model surface. The highest tracer concentration is located in the upper aquifer above the salt dome. After one million years $1.8 \cdot 10^{-1}$ mol of C-135 and $3.0 \cdot 10^{-6}$ mol of the tracer can be found in the model domain.

Model 2, continuous inflow

In this case 1 mol Cs-135 enters the model area over one million years (Fig. 62). A similar distribution is attained as after a delta pulse (Fig. 61). After 1,000 years model time the results of the model calculations differ only slightly. Cs-135 has reached the lower surface of the aquitard, whereas the tracer is already detectable at the model surface and in the north-western rim syncline. After continuous inflow of Cs-135, an amount of $6.4 \cdot 10^{-1}$ mol stays in the model area after one million years. This corresponds approximately to 3.5 times the amount of Cs-135 after the delta pulse. The remaining amount of the tracer of $3.6 \cdot 10^{-2}$ mol after one million years strongly exceeds the amount of the tracer of $3.0 \cdot 10^{-6}$ mol after a delta pulse. A strong impact of the different inflow can be observed in the lower aquifer south of the salt dome. After a delta pulse, the tracer is not detectable in this region at the end of the model simulation (Fig. 61d), while after a constant inflow, a tracer concentration of a approx. $1 \cdot 10^{-18}$ mol m^{-3} still can be found here (Fig. 62d). This difference is based on the fact that after a delta pulse, the tracer is transported out of the model domain and is not found south of the salt dome any longer after less than 400,000 years. In contrast to that, the continuous inflow takes places over the entire one million years. Therefore the tracer is still present in the southern region at the end of the model simulation. The tracer is not retarded by sorption. Therefore, the transport out of the model domain is faster than the transport of Cs-135. The greater amounts of substance remaining in the model domain after a continuous inflow are attributed to the decelerated inflow of the radionuclides and the tracer.

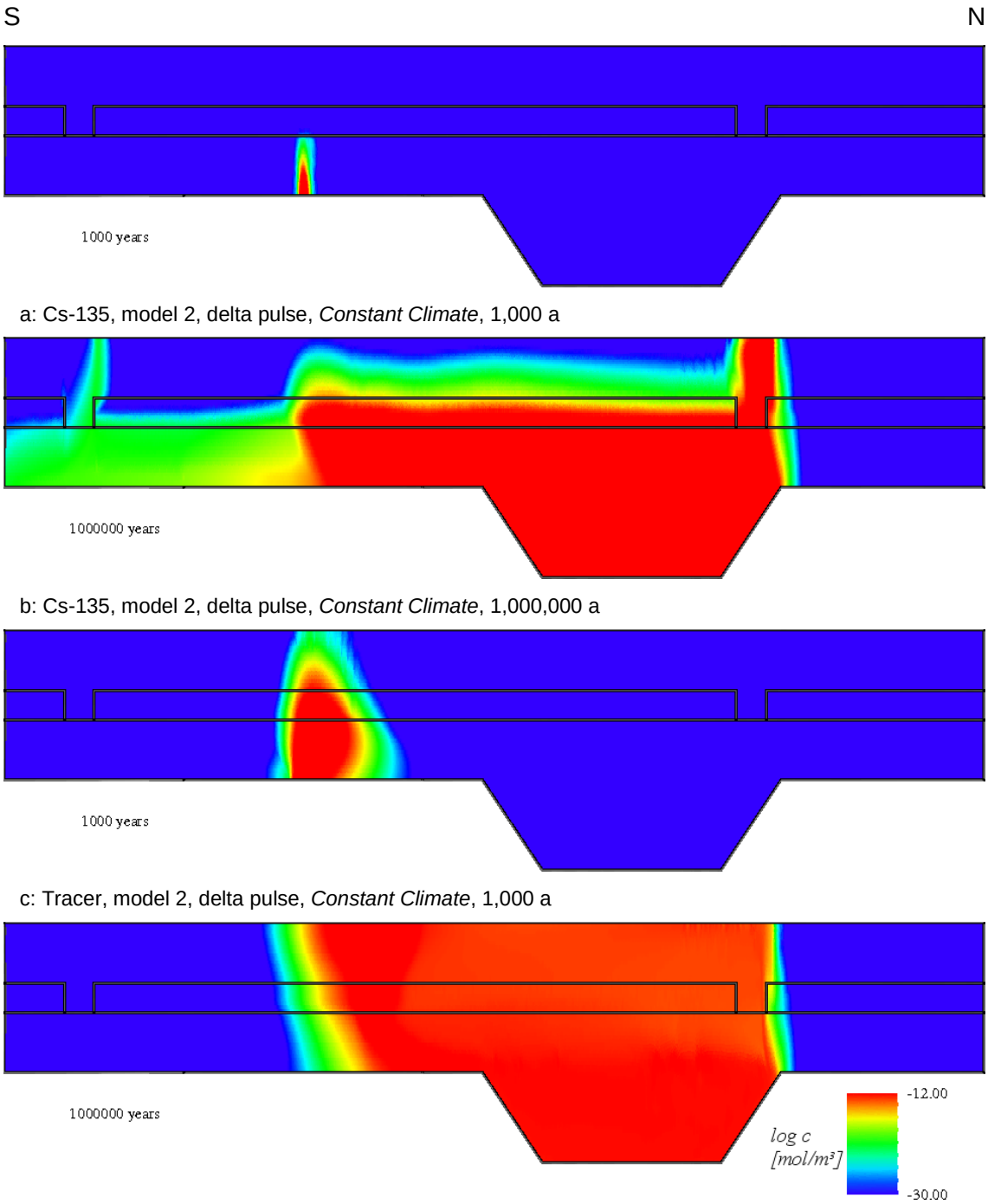

a: Cs-135, model 2, delta pulse, *Constant Climate*, 1,000 a

b: Cs-135, model 2, delta pulse, *Constant Climate*, 1,000,000 a

c: Tracer, model 2, delta pulse, *Constant Climate*, 1,000 a

d: Tracer, model 2, delta pulse, *Constant Climate*, 1,000,000 a

Fig. 61 Transport of Cs-135: *Constant Climate*, model 2, Cs-135 and tracer, delta pulse

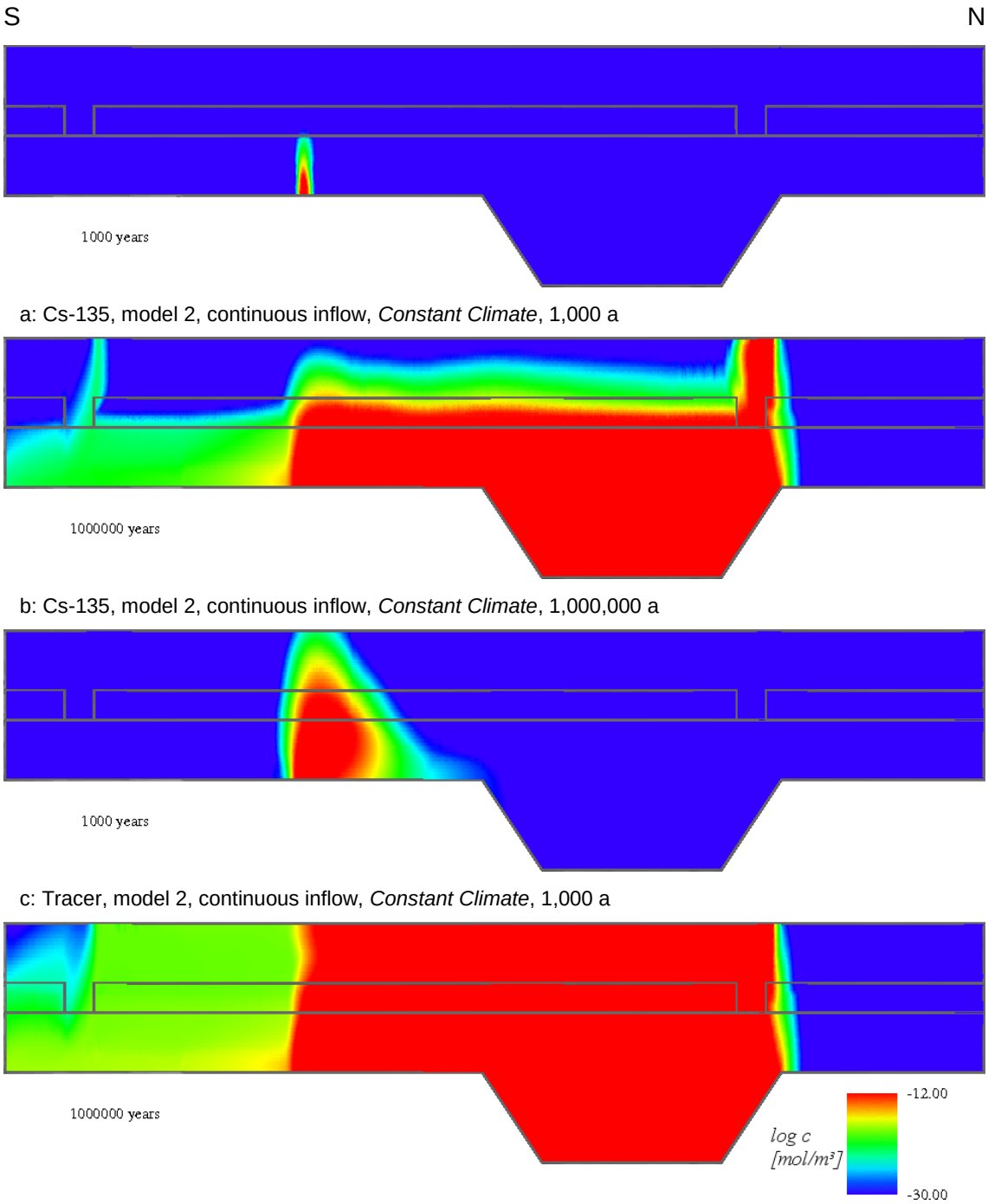

a: Cs-135, model 2, continuous inflow, *Constant Climate*, 1,000 a

b: Cs-135, model 2, continuous inflow, *Constant Climate*, 1,000,000 a

c: Tracer, model 2, continuous inflow, *Constant Climate*, 1,000 a

d: Tracer, model 2, continuous inflow, *Constant Climate*, 1,000,000 a

Fig. 62 Transport of Cs-135: *Constant Climate*, model 2, Cs-135 and tracer, continuous inflow

Model 1 and model 2, delta pulse

The results for model 1 are presented in Fig. 63, for model 2 in Fig. 61. The different flow fields of models 1 and 2 have distinct effects on the results of the transport calculations. The flow direction in the area of the salt dome contact in the lower aquifer is directed southward in model 1 and northward in model 2. Accordingly, the transport of the radionuclides is targeted in opposite directions. Furthermore, the higher flow velocities in model 1 cause a faster transport of the radionuclides so that a significantly broader pollutant plume can be observed already after the first 1,000 years (Fig. 63 a). After one million years of model time, the impacts of a second hydraulic window and the varying inflow rate become particularly apparent. In model 2, Cs 135 is mainly transported by advection through the northern hydraulic window up to the model surface. In model 1, Cs-135 reaches the northwestern rim syncline in the northern direction but the transport up to the model surface occurs mainly through the southern hydraulic window and subordinately through the aquitard. After one million years, $4.1 \cdot 10^{-1}$ mol of Cs-135 and $6.3 \cdot 10^{-10}$ mol of tracer still exist in the model area. Due to the high velocities and the shorter flow distance to the model surface through the aquitard and the southern hydraulic window, the so far smallest amounts of tracer occur in model 1. In contrast to that, an approximately 2.3 times larger amount of Cs-135 exists in model 1 compared to model 2. An important difference between the two models is the salinity of the upper aquifer. Unlike in model 2, the groundwater in the upper aquifer of model 1 is saline. Thus the sorption coefficient of Cs-135 is reduced from K_d = 70 ml g^{-1} (model 2) to K_d= 2 ml g^{-1} (model 1). Accordingly, in model 1 Cs-135 can be transported within the upper aquifer southward to the southern boundary and northward to the transition zone of the groundwater recharge area to the Elbe lowlands (Fig. 63 a and b). It is no longer discharged solely at the surface above the two hydraulic windows. Thus, the concentrations of Cs-135 in model 1, which are significantly higher in spite of the higher flow velocities and the lower sorption coefficients, can only be explained by the more extensive transport and therefore wide-spread Cs-135 concentrations.

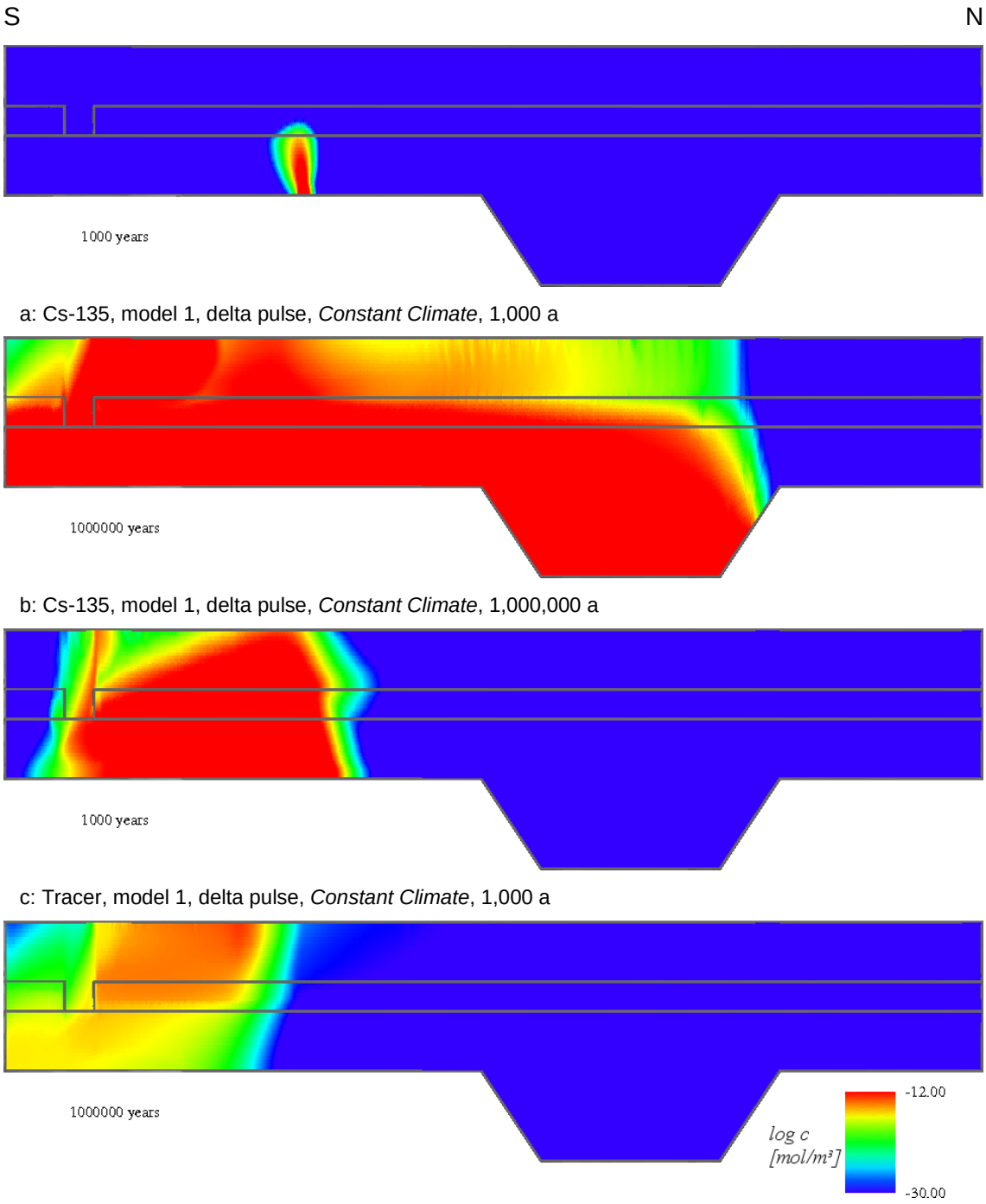

a: Cs-135, model 1, delta pulse, *Constant Climate*, 1,000 a

b: Cs-135, model 1, delta pulse, *Constant Climate*, 1,000,000 a

c: Tracer, model 1, delta pulse, *Constant Climate*, 1,000 a

d: Tracer, model 1, delta pulse, *Constant Climate*, 1,000,000 a

Fig. 63 Transport of Cs-135: *Constant Climate*, model 1, Cs-135 and tracer, delta pulse

Present Climate

Model 1 and model 2, delta pulse

As in the state of *Constant Climate*, Cs-135 reaches the lower border of the aquitard after 1,000 years in both models. The opposite flow directions in the lower aquifer of the two models become clearly noticeable in the *Present Climate* state like in the *Constant Climate* state as well. In model 1 (Fig. 64), the transport is directed from the source to the south, in model 2 (Fig. 65) to the north. In model 1, the transport of the tracer is limited to the area between the southern hydraulic window and the northwestern rim syncline, whereas in model 2 the tracer is distributed to the north and to some extent into the northwestern rim syncline. It is noticeable that the tracer is not only spread by advection through the northern hydraulic window but also, as indicated in

Fig. 45, through the aquitard up to the surface. In model 1, Cs-135 is detectable in almost the whole model area after one million years, even in very low concentrations in the zones of recharge and inflow. In contrast, the transport in model 2 is limited to the central area between the salt dome contact and the northern margin of the rim syncline. At that point of time, model 1 contains $5.6 \cdot 10^{-1}$ mol of Cs-135 and model 2 contains $7.1 \cdot 10^{-2}$ mol Cs-135. The distribution of the tracer in model 1 is similar to the distribution of Cs-135, except for the lower concentration of the tracer with $7.8 \cdot 10^{-13}$ mol. In model 2, almost the entire amount of tracer substance has left the model area after one million years (remaining substance amount: $7.2 \cdot 10^{-23}$ mol). In contrast to the state of *Constant Climate*, not only the different flow fields but also the higher salinity of the upper aquifer of model 2 affects the distribution of Cs-135 in the *Present Climate* state. The K_d value is reduced from $K_d = 70$ ml g^{-1} to $K_d = 2$ ml g^{-1} compared to the state of *Constant Climate* in model 2. Hence, Cs-135 can be spread more widely by advection in the upper aquifer in the *Present Climate* state than in the *Constant Climate* state. Nevertheless, a higher residual concentration of Cs-135 remains in the model area for the *Constant Climate* state.

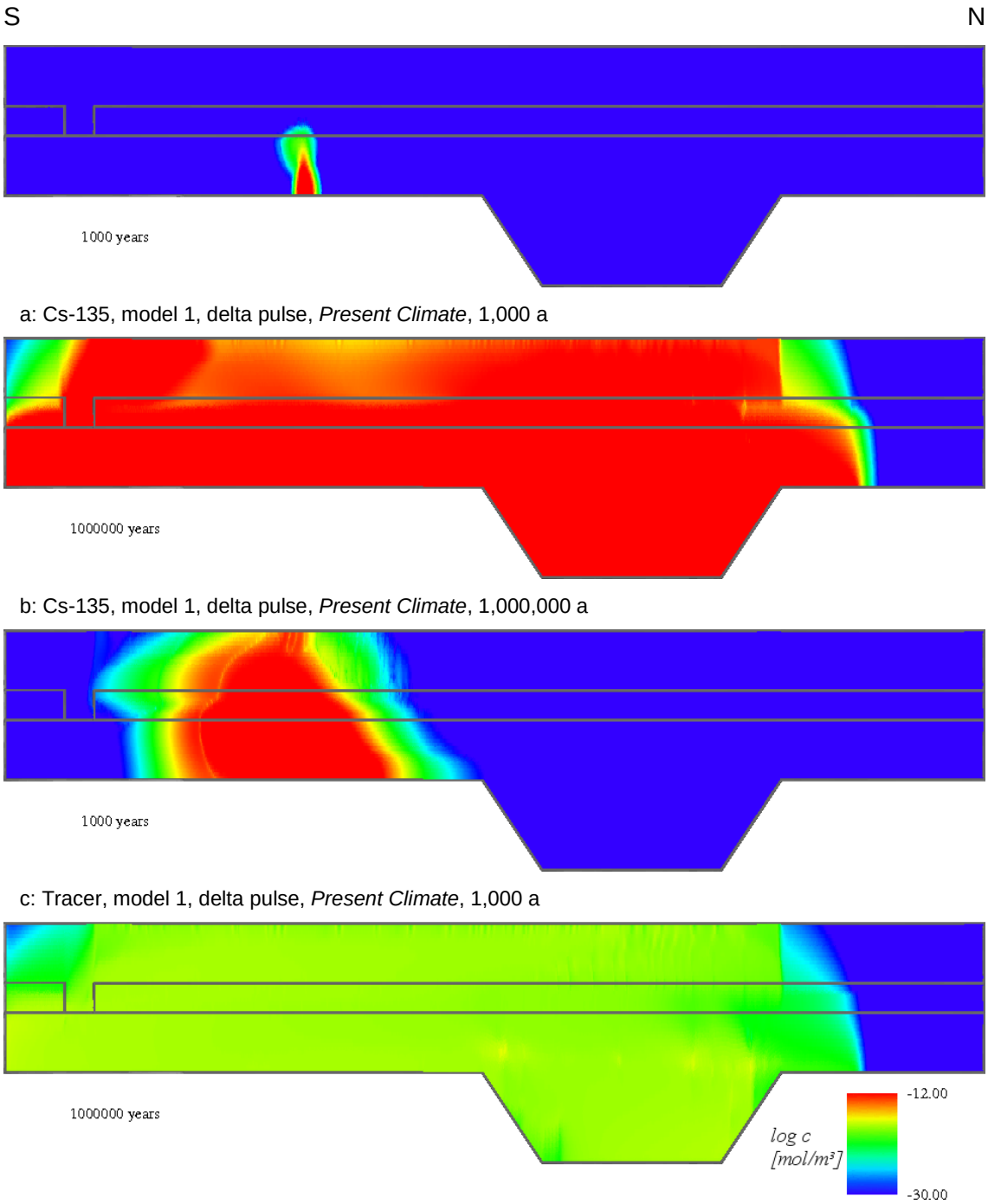

a: Cs-135, model 1, delta pulse, *Present Climate*, 1,000 a

b: Cs-135, model 1, delta pulse, *Present Climate*, 1,000,000 a

c: Tracer, model 1, delta pulse, *Present Climate*, 1,000 a

d: Tracer, model 1, delta pulse, *Present Climate*, 1,000,000 a

Fig. 64 Transport of Cs-135: *Present Climate*, model 1, Cs-135 and tracer, delta pulse

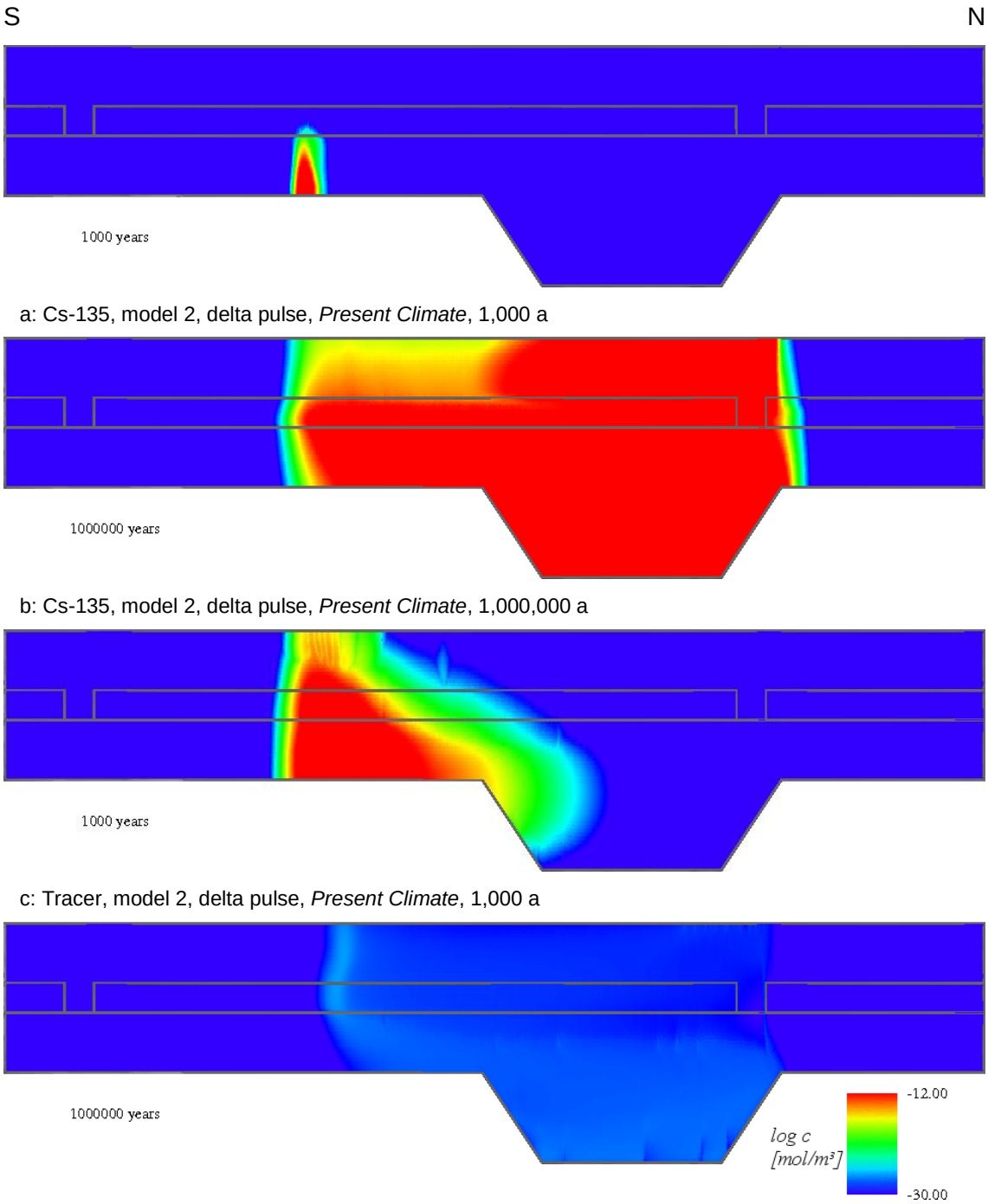

a: Cs-135, model 2, delta pulse, *Present Climate*, 1,000 a

b: Cs-135, model 2, delta pulse, *Present Climate*, 1,000,000 a

c: Tracer, model 2, delta pulse, *Present Climate*, 1,000 a

d: Tracer, model 2, delta pulse, *Present Climate*, 1,000,000 a

Fig. 65 Transport of Cs-135: *Present Climate*, model 2, Cs-135 and tracer, delta pulse

Sea Water Inundation

Model 1 and model 2, delta pulse

For the *Sea Water Inundation* state, the flow velocity is considerably reduced and diffusion dominates both the mixing processes between fresh water and saline water and the migration of radionuclides. After a model time of 1,000 years in both models, Cs-135 reaches the smallest distribution so far in comparison to the other climate states (Fig. 66 and Fig. 67). The contaminant plumes reach the basis of the aquitard but with a smaller lateral extent. After one million years, the shape of the contaminant plume and even the concentrations of Cs-135 and of the tracer are almost identical for both models. In both models $7.1 \cdot 10^{-1}$ mol of Cs-135 remain in the model area, while the remaining tracer mass amounts to $3.3 \cdot 10^{-1}$ mol in model 1 and to $3.8 \cdot 10^{-1}$ mol in model 2. It is remarkable that in this climate state the transport of Cs-135 by diffusion proceeds almost isotropically to all directions due to the low groundwater flow velocities. The tracer and Cs-135 leave the model area approximately vertically above the salt dome contact at the surface. After one million years, the presence of Cs-135 can be observed at the surface of both models within a small width of only 1 – 1.5 km, while the tracer is spread almost evenly in the entire model domain.

Permafrost

Model 1 and model 2, delta pulse

After a model time of 1,000 years the simulation for the *Permafrost* state in model 2 show a similar Cs-135 distribution as in the models described so far. The contaminant plume in model 2 (Fig. 68) reaches the basis of the aquitard and the transport is directed southward. The Cs-135 distribution in model 1 (Fig. 79) is different. Cs-135 already reaches the southern boundary of the lower aquifer after 1,000 years due to the very high flow velocity in the lower aquifer. Further, in this climate state, the southern talik serves as pathway for the transport of Cs-135, thus it can be observed at the model surface in the south above it after 1,000 years already. After a model time of one million years, the two models show distributions which are very different from the climate states discussed so far. This is caused by the high flow velocities in the unfrozen zones and the transport by diffusion in the frozen zones. In these permafrost regions within the upper aquifer, the transport by advection is slowed down drastically.

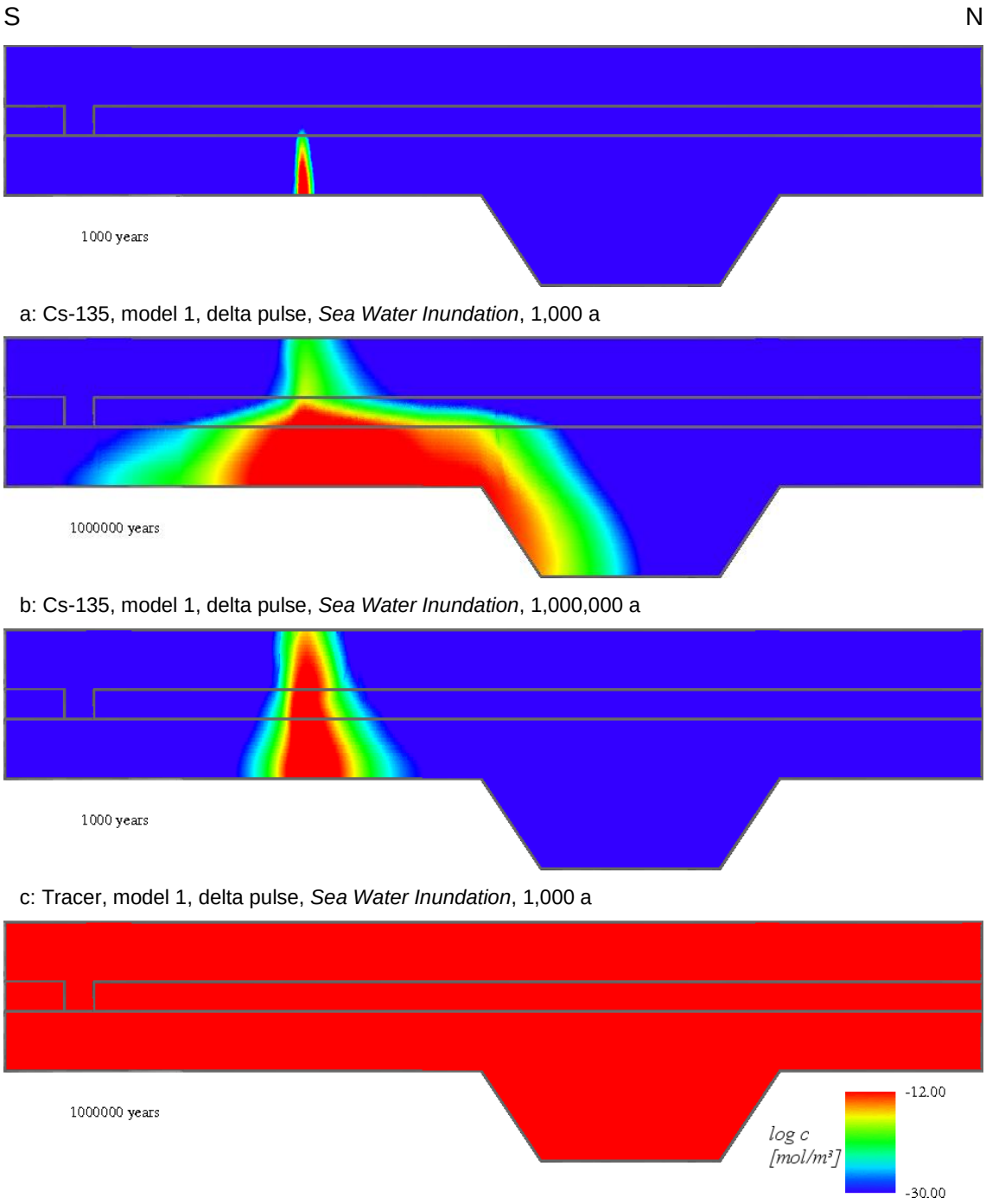

a: Cs-135, model 1, delta pulse, *Sea Water Inundation*, 1,000 a

b: Cs-135, model 1, delta pulse, *Sea Water Inundation*, 1,000,000 a

c: Tracer, model 1, delta pulse, *Sea Water Inundation*, 1,000 a

d: Tracer, model 1, delta pulse, *Sea Water Inundation*, 1,000,000 a

Fig. 66 Transport of Cs-135: *Sea Water Inundation*, model 1, Cs-135 and tracer, delta pulse

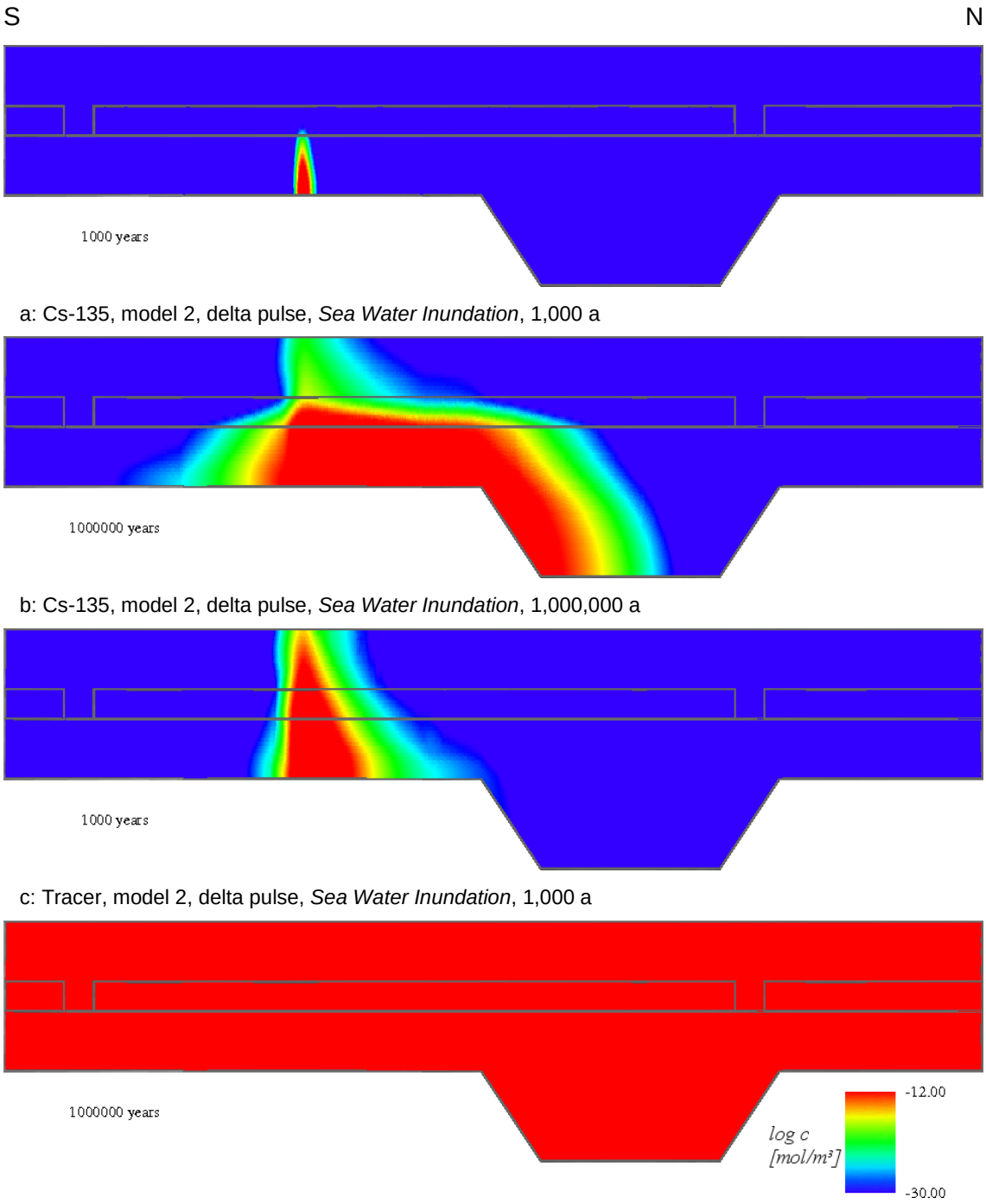

a: Cs-135, model 2, delta pulse, *Sea Water Inundation*, 1,000 a

b: Cs-135, model 2, delta pulse, *Sea Water Inundation*, 1,000,000 a

c: Tracer, model 2, delta pulse, *Sea Water Inundation*, 1,000 a

d: Tracer, model 2, delta pulse, *Sea Water Inundation*, 1,000,000 a

Fig. 67 Transport of Cs-135: *Sea Water Inundation*, model 2, Cs-135 and tracer, delta pulse

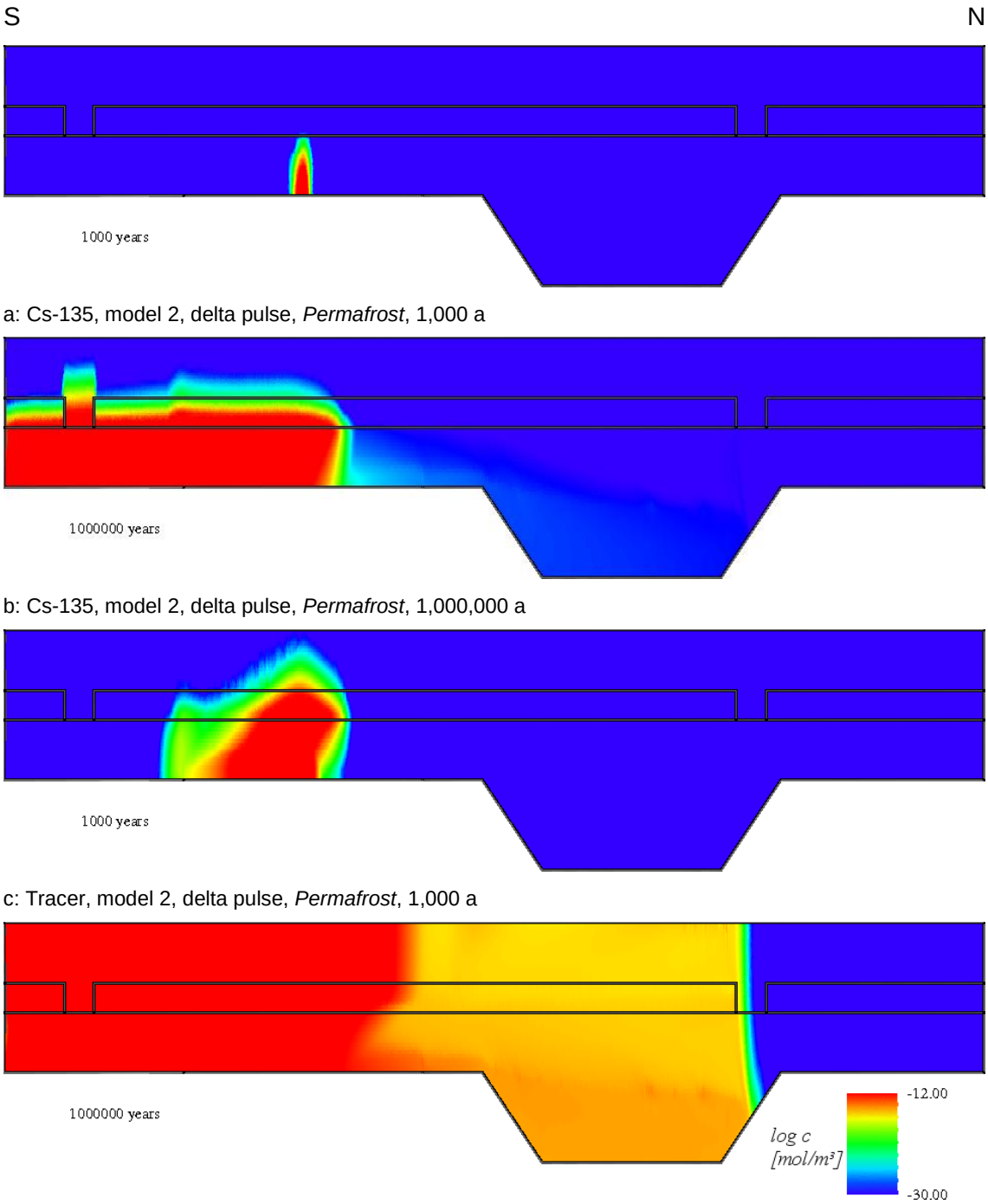

a: Cs-135, model 2, delta pulse, *Permafrost*, 1,000 a

b: Cs-135, model 2, delta pulse, *Permafrost*, 1,000,000 a

c: Tracer, model 2, delta pulse, *Permafrost*, 1,000 a

d: Tracer, model 2, delta pulse, *Permafrost*, 1,000,000 a

Fig. 68 Transport of Cs-135: *Permafrost*, model 2, Cs-135 and tracer, delta pulse

Moreover, due to the increased sorption in the aquitard (K_d = 400 ml g^{-1}, fresh water conditions) the upward transport is strongly retarded. Cs-135 is not transported into the north-western rim syncline in both models. In model 2, Cs-135 does not even reach the model surface. After one million years, $7.3 \cdot 10^{-4}$ mol of Cs-135 remain in the domain of model 1 and $4.8 \cdot 10^{-2}$ mol in the domain of model 2. The tracer, however, reaches both, the surface of the model and the southern model boundary after one million years. At this time, the concentrations clearly differ between the area to which the tracer is transported by advection (south) and the area to which it is transported by diffusion and dispersion, i. e. the centre (Fig. 68 d). In the northernmost part of the model, the tracer is not detectable. $5.5 \cdot 10^{-6}$ mol and $3.5 \cdot 10^{-4}$ mol of the tracer remain in the domain of model 1 and model 2, respectively.

7.7.2.2 Present Climate

In the following, the simulation results for the *Present Climate* state and different radionuclides are described. Besides the calculations for Cs-135, which were already discussed in chapter 7.7.2, simulations for the radionuclides I-129, C-14, Zr-93 and the uranium decay series were only performed for model 2 and the delta pulse.

I-129

In contrast to the K_d values of Cs-135, the K_d values for I-129 are very low, amounting to 2 ml g^{-1} for the aquitard and 0.1 ml g^{-1} for the aquifers. Due to the low sorption, the distribution of I-129 after 1,000 years (Fig. 69 a) is comparable to that of the tracer (Fig. 38 c). At that time I-129 almost reaches the northwestern rim syncline and can be found at the model surface. The concentration maximum at the surface is located above the location of the radionuclide source. After one million years, the presence of I-129 can be observed in the entire central area of the model domain (Fig. 69 b), comparable to the distribution of Cs-135 (Fig. 65 b), whereas the tracer almost does not occur any longer in the model domain (remaining tracer mass is $7.2 \cdot 10^{-23}$ mol). Similar to the distribution of Cs-135, the areas of I-129 distribution are delimited sharply. There is a transition zone ranging from 0 mol m^{-3} m^{-1} to more than $1 \cdot 10^{-12}$ mol m^{-3} (max. concentration: $1 \cdot 10^{-9}$ mol m^{-3}) between the inflow areas for fresh water in the north and the south where no I-129 is found and the central area. A half-life of Cs-135 of $2.00 \cdot 10^{6}$ years leads to a decay of about 30 % of the initial mass, while only about 4.3 % of the initial mass of I-129 with a half-life of $1.57 \cdot 10^{7}$ years will decay within one million years. Under identical boundary and initial conditions there is approx. 550 times the amount of Cs-135 left in the model domain

after a simulation time of one million years compared to I-129 ($1.3 \cdot 10^{-4}$ mol). This is caused by the lower sorption of I-129.

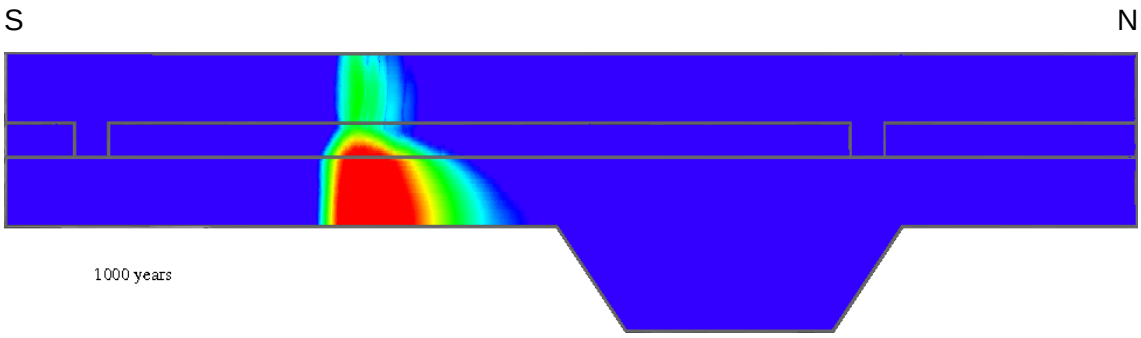

a: I-129, model 2, delta pulse, *Present Climate*, 1,000 a

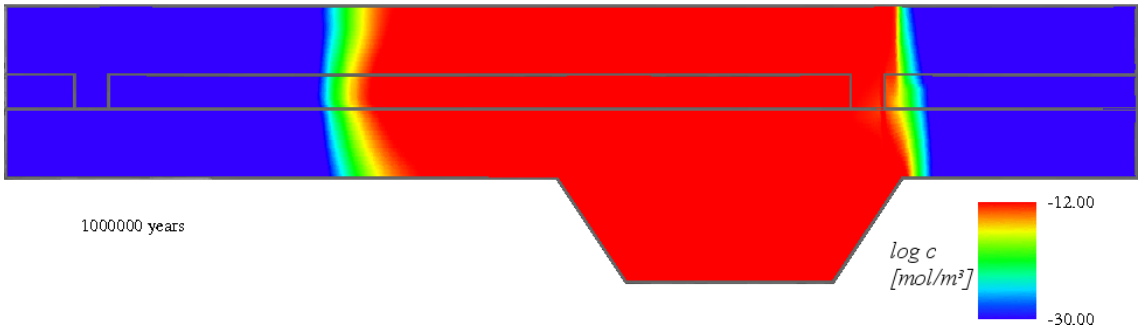

b: I-129, model 2, delta pulse, *Present Climate*, 1,000,000 a

Fig. 69 *Present Climate*: Model 2, I-129, delta pulse

Zr-93

Compared to the radionuclides considered so far, Zr-93 has relatively high sorption coefficients of $K_d = 40$ ml g^{-1} for all hydrogeological units. This is reflected in the low distribution of Zr-93 after 1,000 years (Fig. 70 a). In contrast to Cs-135 and I-129, Zr-93 does not reach the aquitard after 1,000 years. After one million years, it only extends into the lower aquifer without discharging at any model boundary. Here, the influence of the radioactive decay can be observed very well. Although no radionuclides are transported out of the model domain, only $6.3 \cdot 10^{-1}$ mol of Zr-93 remain in the model area after one million years. This amount equals the residual amount of Zr-93 as a result of the radioactive decay. In this model it is noticeable that the prefered transport pathway of Zr-93 is through the aquitard due to the equal sorption coefficients of the aquitard and of the aquifers.

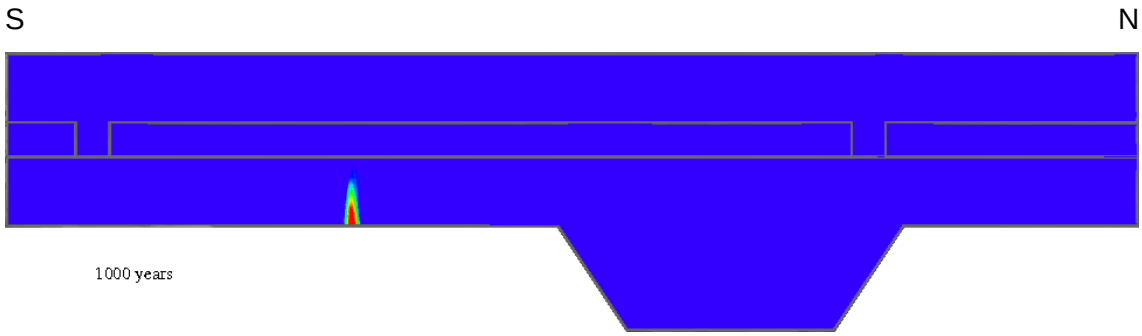

a: Zr-93, model 2, delta pulse, *Present Climate*, 1,000 a

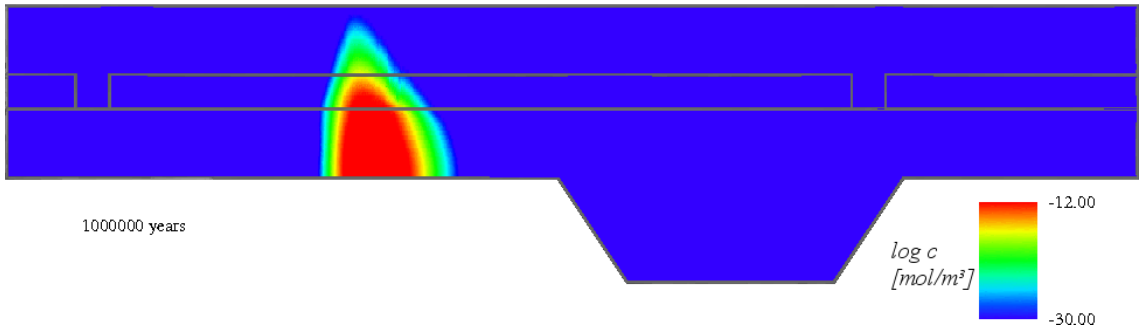

b: Zr-93, model 2, delta pulse, *Present Climate*, 1,000,000 a

Fig. 70 *Present Climate*: Model 2, Zr-93, delta pulse

C-14

With $5.73 \cdot 10^3$ years, C-14 has the shortest half-life of the radionuclides considered here and small sorption coefficients of $K_d = 0.2$ ml g^{-1} for the aquifers and $K_d = 2$ ml g^{-1} for the aquitard. After 1,000 years, the distribution and concentration of C-14 (not depicted) in the model area are similar to the results for I-129 due to the low sorption of both radionuclides. After 100,000 years, the highest concentrations occur in the northwestern rim syncline and – due to the transport through the northern hydraulic window – in the northern part of the upper aquifer. Already after 100,000 years, a similar picture is obtained as for Cs-135 after one million years (see Fig. 65 b). C-14 can no longer be observed in the model domain after one million years due to its short half-life. In comparison, I-129 is still present in the model area (Fig. 69) despite its low sorption coefficients.

Uranium decay series

The sorption coefficients for U-238/U-234 for the aquifers are $K_d = 0.6$ ml g^{-1} and for the aquitard $K_d = 20$ ml g^{-1}. After 1,000 years, U-238 has reached the aquitard – like Cs-135 – and extends in northward direction (Fig. 71 a). Since only the inflow of U-238 into the model domain is assumed but not an inflow of the daughter nuclides, the distribution of the radionuclides U-234, Th-230 and Ra-226 are mainly determined by the distribution of

U-238. Thus, a contaminant plume develops which extends to the aquitard, e.g. for Th-230 despite its very high sorption coefficients of K_d = 200 ml g^{-1} for the aquifers and the aquitard. In case of a finite inflow of Th-230 instead of the occurrence only due to radioactive decay, a distribution of less extent than for Zr-93 would be expected due to its stronger retardation (see Fig. 70 a). The contaminant plumes of the three daughter nuclides are comparable with the one of U-238 with decreasing concentrations. After one million years, the highest concentration of U-238 occurs in the centre of the model domain (Fig. 72 a), and the remaining amount U-238 is $2.1 \cdot 10^{-2}$ mol. The amounts of the daughter nuclides are $n_{U\text{-}234} = 1.1 \cdot 10^{-6}$ mol, $n_{Th\text{-}230} = 4.0 \cdot 10^{-7}$ mol and $n_{Ra\text{-}226} = 7.9 \cdot 10^{-9}$ mol. The increasing concentration of the daughter nuclides Th-230 and Ra-226 in the aquitard is remarkable compared to the other hydrogeological units. In the aquitard, the sorption of uranium is stronger than in the aquifers and accordingly this results in higher total concentrations. Although the K_d values for Th-230 remain constant for all sediments (K_d = 200 ml g^{-1}), the highest concentrations of Th-230 occur in the aquitard due to the decay of the increased amount of uranium there. The highest concentrations of Ra-226 occur at the interfaces between the aquifers and the aquitard.

7.7.2.3 Constant Climate

For the state of *Constant Climate*, all model calculations were performed, i.e. for all models, the delta pulse and continuous inflow and all radionuclides. The results for the model calculation for Cs-135 were already discussed in chapter 7.7.2.1 (see Fig. 62, Fig. 63, Fig. 64).

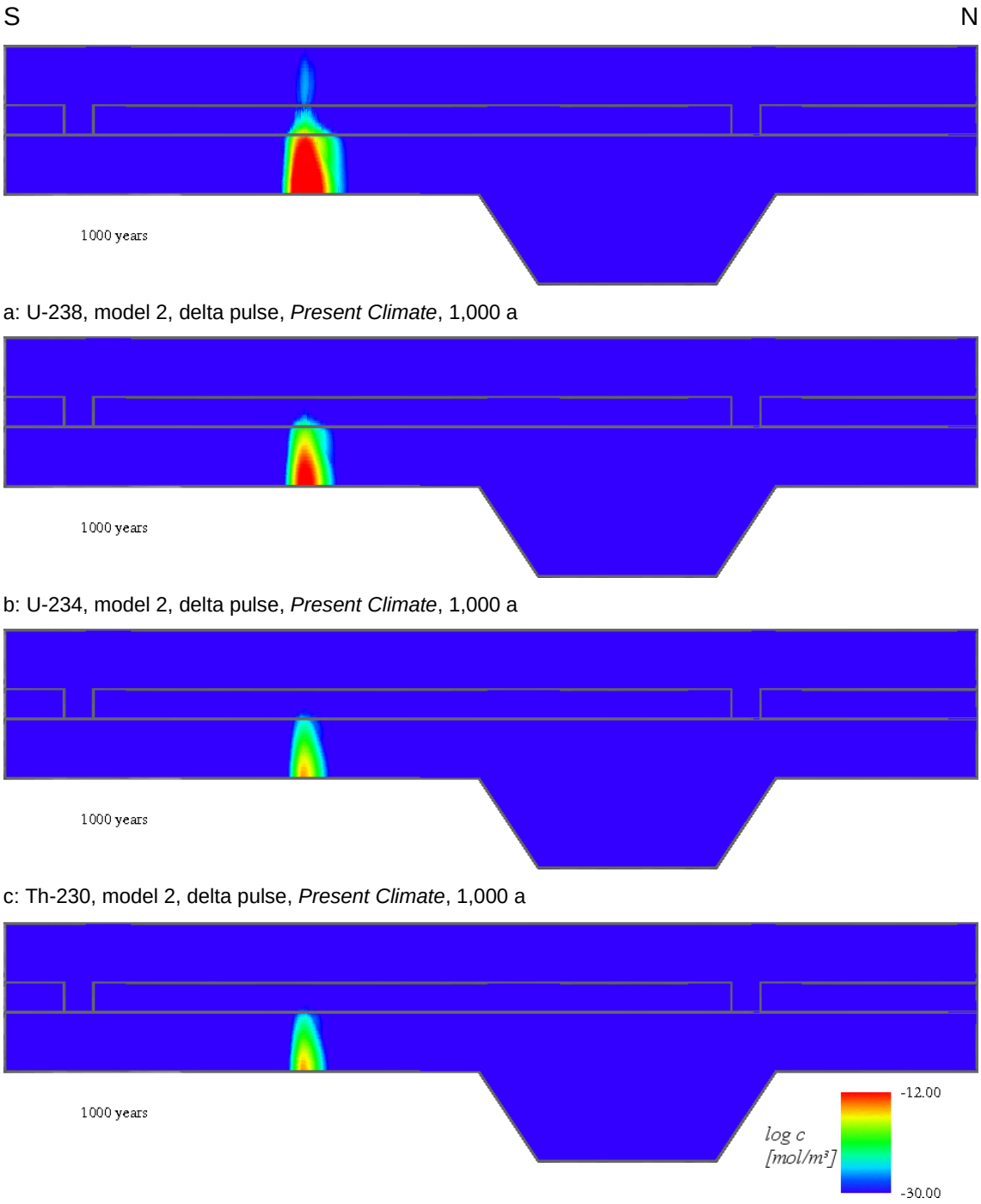

a: U-238, model 2, delta pulse, *Present Climate*, 1,000 a

b: U-234, model 2, delta pulse, *Present Climate*, 1,000 a

c: Th-230, model 2, delta pulse, *Present Climate*, 1,000 a

d: Ra-226, model 2, delta pulse, *Present Climate*, 1,000 a

Fig. 71 *Present Climate*: Model 2, U decay series, delta pulse

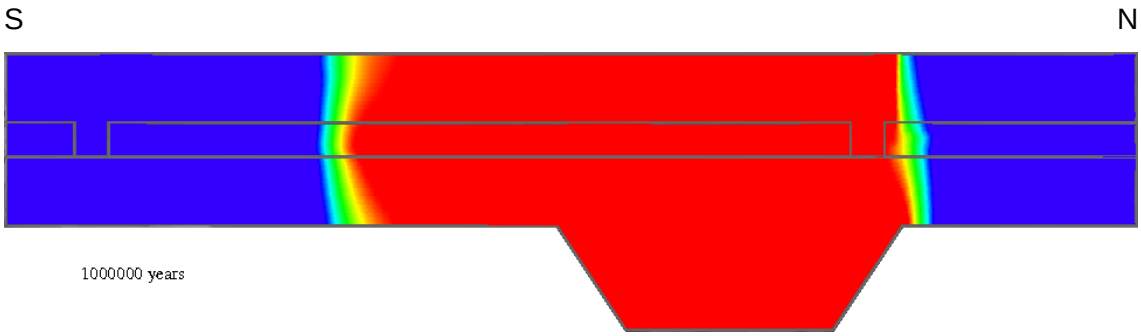

a: U-238, model 2, delta pulse, *Present Climate*, 1,000,000 a

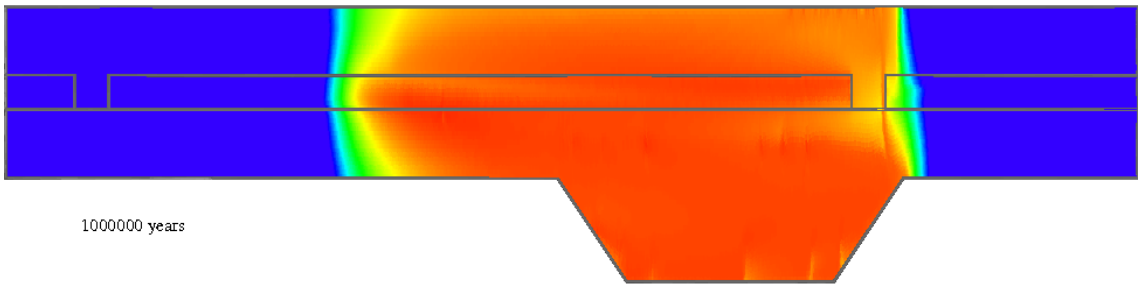

b: U-234, model 2, delta pulse, *Present Climate*, 1,000,000 a

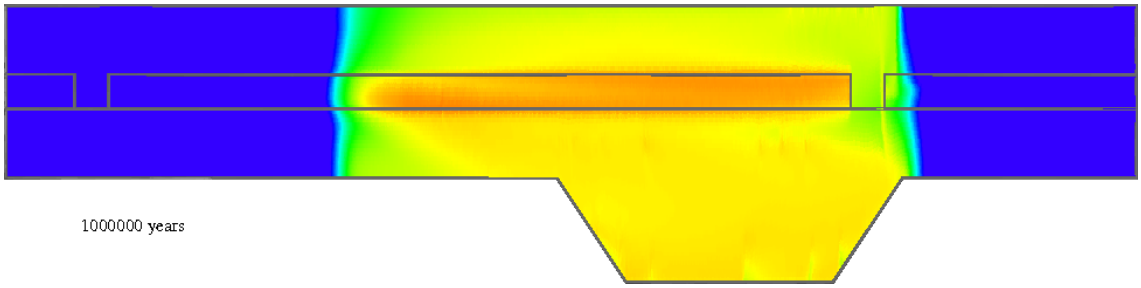

c: Th-230, model 2, delta pulse, *Present Climate*, 1,000,000 a

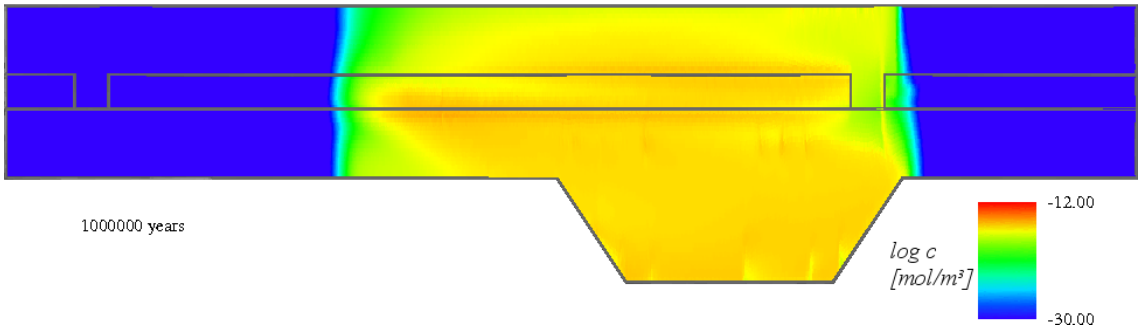

d: Ra-226, model 2, delta pulse, *Present Climate*, 1,000,000 a

Fig. 72 *Present Climate*: Model 2, U decay series, delta pulse

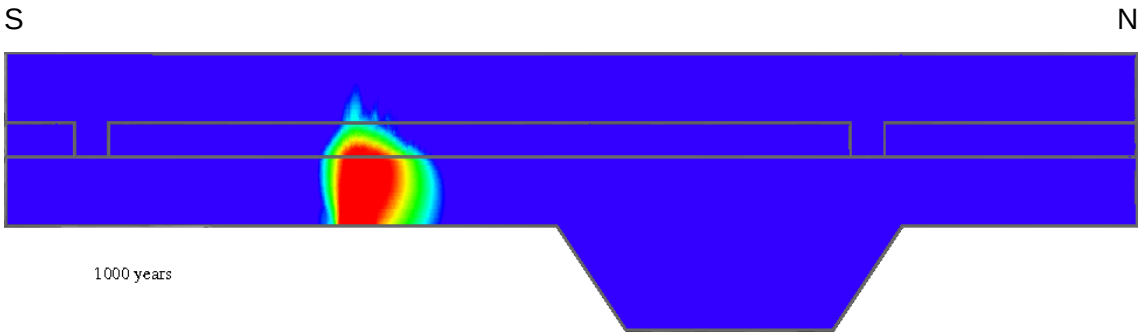

a: I-129, model 2, delta pulse, *Constant Climate*, 1,000 a

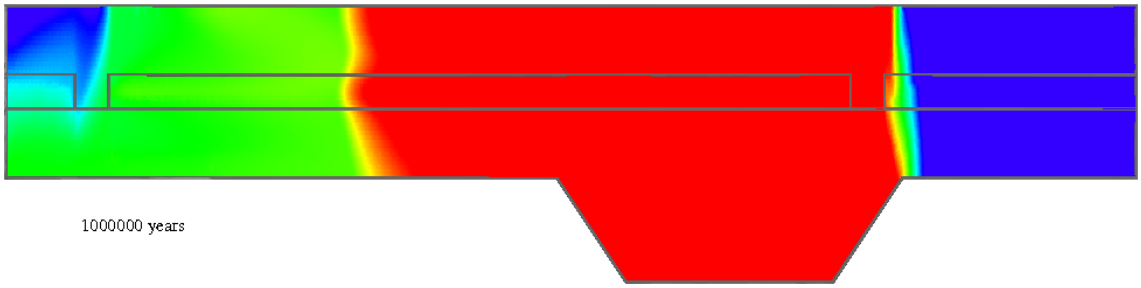

b: I-129, model 2, delta pulse, *Constant Climate*, 1,000,000 a

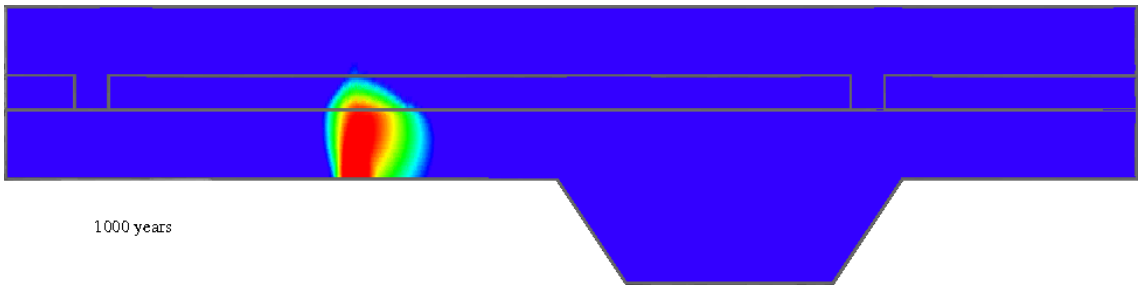

c: I-129, model 2, continuous inflow, *Constant Climate*, 1,000 a

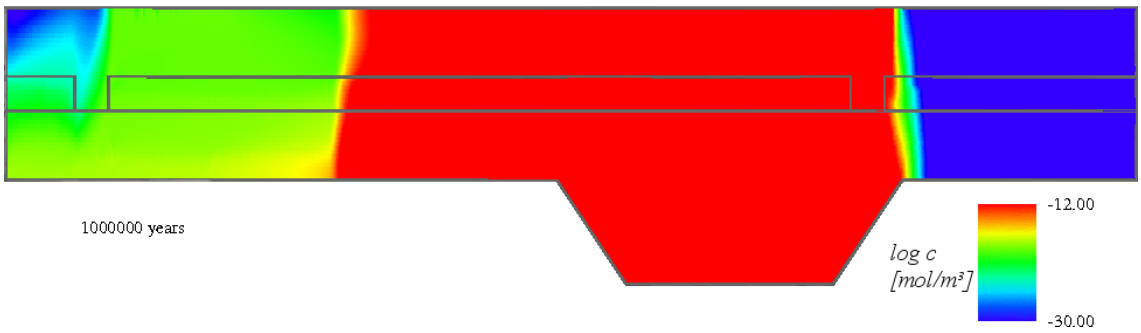

d: I-129, model 2, continuous inflow, *Constant Climate*, 1,000,000 a

Fig. 73 *Constant Climate*: Model 2, I-129, delta pulse and continuous inflow

I-129

Due to the low sorption coefficients, similar results of I-129 for the delta pulse and the continuous inflow occur after a model time of 1,000 years for model 2 (Fig. 73 a, c). No matter, which type of inflow is defined, I-129 reaches the upper boundary of the aquitard after 1,000 years. After one million years, $1.3 \cdot 10^{-2}$ mol of I-129 is left in the model domain after a delta pulse and $9.5 \cdot 10^{-2}$ mol after continuous inflow. By then, the highest I-129 concentrations at the surface can be found above the central area in both models. The reduced distribution in the upper aquifer is caused by the higher sorption under fresh water conditions. I-129 can be found at the entire model surface except for the inflow areas in both models with the highest I-129 concentrations in the central area.

In model 1, I-129 occurs after a delta pulse at the model surface above the hydraulic window after approx. 100,000 years (not depicted). I-129 reaches the model surface by another pathway through the aquitard after approx. 140,000 years to 150,000 years. After approx. 300,000 years, it can be identified in the north-western rim syncline. I-129 is found in the whole model area with the same mass of $1.3 \cdot 10^{-2}$ mol as in model 2 after one million years, while the distribution is comparable to the distribution of Cs-135 (cf. Fig. 63). After a delta pulse (not depicted) I-129 can be observed at the model surface after 5,000 years to 6,000 years. Here, both pathways - through the aquitard and through the southern hydraulic window – are used by I-129 leading to its occurrence at the surface approx. at the same time. After approx. 300,000 years the distribution of I-129 reaches the steady-state, showing a similar distribution as Cs-135 (Fig. 63), with a remaining mass of $1.2 \cdot 10^{-1}$ mol in the model area.

Zr-93

With relatively high K_d values of 40 ml g^{-1} for all geological units, Zr-93 is strongly sorbed. Thus it shows, as in the case of *Present Climate,* the slowest migration through the model domain (Fig. 74 a, b). For a delta pulse and for a continuous inflow, Zr-93 is distributed isotropically from the source to about half of the thickness of the lower aquifer after a model time of 1,000 years. For longer model times, the prefered migration pathway again is directed through the aquitard instead of through the hydraulic windows. After one million years, there is $6.3 \cdot 10^{-1}$ mol of Zr-93 left after a delta pulse and still $8.0 \cdot 10^{-1}$ mol after continuous inflow. Since no transport out of the model domain takes place, the concentration of Zr-93 only decreases by radioactive decay which explains the higher concentration after the continuous inflow. Compared to the *Present Climate* state, the flow

velocities in this state are slower so that the extension of the contaminant plume in this state is smaller (see Fig. 70 b and Fig. 74 b).

The results for model 1 (not depicted) are similar to the results for model 2. According to the different flow directions, the contaminant plume is directed southward in model 1. Due to the high sorption, no radionuclide transport out of the model area takes place here either. A reduction of the radionuclide concentration can only be traced back to the radioactive decay. Saline water occurs within the upper aquifer in model 1, so Zr-93 is less retarded than in model 2 but still doesn't reach the model surface. Likewise in model 2, after a delta pulse, $6.3 \cdot 10^{-1}$ mol of Zr-93 remain within the model area after one million years and $8.0 \cdot 10^{-1}$ mol after a continous inflow.

C-14

For the delta pulse and for the continuous inflow, similar results are obtained for model 2 after a model time of 1,000 years (not depicted). In both model variants, C-14 migrates into the aquitard and even reaches the upper aquifer. After 420,000 years model time, C-14 is no more detectable in the model area any longer in case of a delta pulse. In case of a continuous inflow, the steady-state is reached after approx. 240,000 years. A similar distribution of C-14 like in the steady-state in case of a continuous inflow can be observed for the delta pulse after approx. 100,000 years. The first occurance of C-14 at the model surface after a delta pulse is observed directly above the salt dome after approx. 20,000 years to 30,000 years. So again, the most rapid transport takes place through the aquitard. The second pathway is directed to the north through the northern hydraulic window, where C-14 reaches the model surface after approx. 40,000 years to 50,000 years. Transport through the southern hydraulic window is driven by diffusion, therefore C-14 is observed at the surface above the southern hydraulic window the latest, taking more than 100,000 years regarding either variant. After one million years, C-14 cannot be detected in the model area any longer after a delta pulse due to the short half-life, whereas after a continuous inflow, it is distributed in the entire central model area with the highest concentrations along the pathway from the source through the northern hydraulic window up to the surface.

In model 1, the distribution of C-14 is comparable to its distribution in model 2 (not depicted). After 1,000 years, C-14 can be observed in the aquitard and the upper aquifer, and it does even reach the model surface. This time, the transport through the aquitard is the fastest, although it only takes approx. 12,000 years of model time for C-14 to be transported through the southern hydraulic window to the surface as well. After approx.

40,000 years, C-14 reaches the rim syncline and shows the highest distribution within the model area between 100,000 years and 150,000 years. C-14 has completely left the model area after approx. 440,000, so after one million years, it cannot be found in the model area any longer. After a contiuous inflow, C-14 reaches the surface after more than 10,000 years and a steady-state distribution after less than 200,000 years. C-14 is then found in almost the complete model area, except for the sector north of the rim syncline. The highest concentrations are found above the salt dome in the lower aquifer and along the pathway through the southern hydraulic window up to the surface. Average C-14 concentrations range between $1 \cdot 10^{-15}$ mol m^3 to $1 \cdot 10^{-20}$ mol m^3 in the upper aquifer and in the central part of the model.

After continuous inflow, C-14 amounts to $7.2 \cdot 10^{-3}$ mol in model 1 and to $6.8 \cdot 10^{-3}$ mol in model 2 after one million years.

Uranium decay series

Compared to the *Present Climate* state, the contaminant plumes of U-238 and the daughter nuclides for *Constant Climate* are smaller after 1,000 years (see Fig. 71) due to the lower flow velocity in the lower aquifer. In model 2, an important difference to the *Present Climate* state besides the different flow field is the assumption of fresh water conditions in the upper aquifer with the correspondingly higher sorption coefficients of K_d (uranium) = 2 ml g^{-1}, K_d (Th-230) = 200 ml g^{-1} and K_d (Ra-226) = 40 ml g^{-1}. After a delta pulse, the nuclides are transported to the north according to the flow field. After passing the northern hydraulic window, the radionuclides can be distributed to the south within the upper aquifer. A second transport path is directed through the aquitard up to the surface. A transport path of nearly no significance is directed from the source to the south. Corresponding to the flow field, they can reach the upper aquifer by advection and are transported from there to the north. The influence of the reduced sorption in the upper aquifer becomes obviuous by the larger distribution of the radionuclides. The highest radionuclide concentrations at the model surface occur in the central area, mainly above the north-western rim syncline. Likewise in the *Present Climate* state, increased radionuclide concentrations of the daughter nuclides Th-230 and Ra-226 are found in the aquitard after one million years as a result of the very high sorption of Th-230 (see ch. 7.7.2.2). Remaining radionuclide masses in the model domain amount to $n_{U\text{-}238} = 5.8 \cdot 10^{-2}$ mol, $n_{U\text{-}234} = 3.0 \cdot 10^{-6}$ mol, $n_{Th\text{-}230} = 1.1 \cdot 10^{-6}$ mol and $n_{Ra\text{-}226} = 2.2 \cdot 10^{-8}$ mol.

After continuous inflow of U-238 into the model domain, similar contaminant plumes of the radionuclides occur after a model time of one million years as after a delta pulse (not

depicted). The highest radionuclide concentrations at the model surface occur above the northern hydraulic window and above the source after approx. 110,000 years to 120,000 years (U-238). After approx. 230,000 years, U-238 is observed at the surface above the southern hydraulic window as well. Due to the slower inflow, there are higher amounts of all nuclides in the model domain of $n_{U\text{-}238} = 3.1 \cdot 10^{-1}$ mol, $n_{U\text{-}234} = 6.7 \cdot 10^{-6}$ mol, $n_{Th\text{-}230} = 2.1 \cdot 10^{-6}$ mol and $n_{Ra\text{-}226} = 4.2 \cdot 10^{-8}$ mol.

In contrast to model 2 with the most important pathways through the northern hydraulic window and through the aquitard, in model 1, the transport takes place mainly through the southern hydraulic window and the aquitard. In the case of a delta pulse U-238 reaches the surface after approx. 30,000 years. At approx. 600,000 years U-238 shows its maximum distribution. After one million years, the highest concentrations of U-238 and U-234 are found in the central area, especially in the upper aquifer. Th-230 and Ra-226 are found to have the highest concentrations in the lower aquifer south of the salt dome and in the aquitard above that area. After a continuous inflow, the pathways of radionuclide transport remain the same. It takes more than 800,000 years until the simulation reaches a steady-state for the distribution of U-238. Remaining radionuclide masses amount to $n_{U\text{-}238} = 1.7 \cdot 10^{-1}$ mol, $n_{U\text{-}234} = 8.9 \cdot 10^{-6}$ mol, $n_{Th\text{-}230} = 2.9 \cdot 10^{-6}$ mol and $n_{Ra\text{-}226} = 8.3 \cdot 10^{-8}$ mol in model 2 and to $n_{U\text{-}238} = 4.8 \cdot 10^{-1}$ mol, $n_{U\text{-}234} = 1.5 \cdot 10^{-5}$ mol, $n_{Th\text{-}230} = 3.5 \cdot 10^{-6}$ mol and $n_{Ra\text{-}226} = 1.1 \cdot 10^{-7}$ mol in model 1.

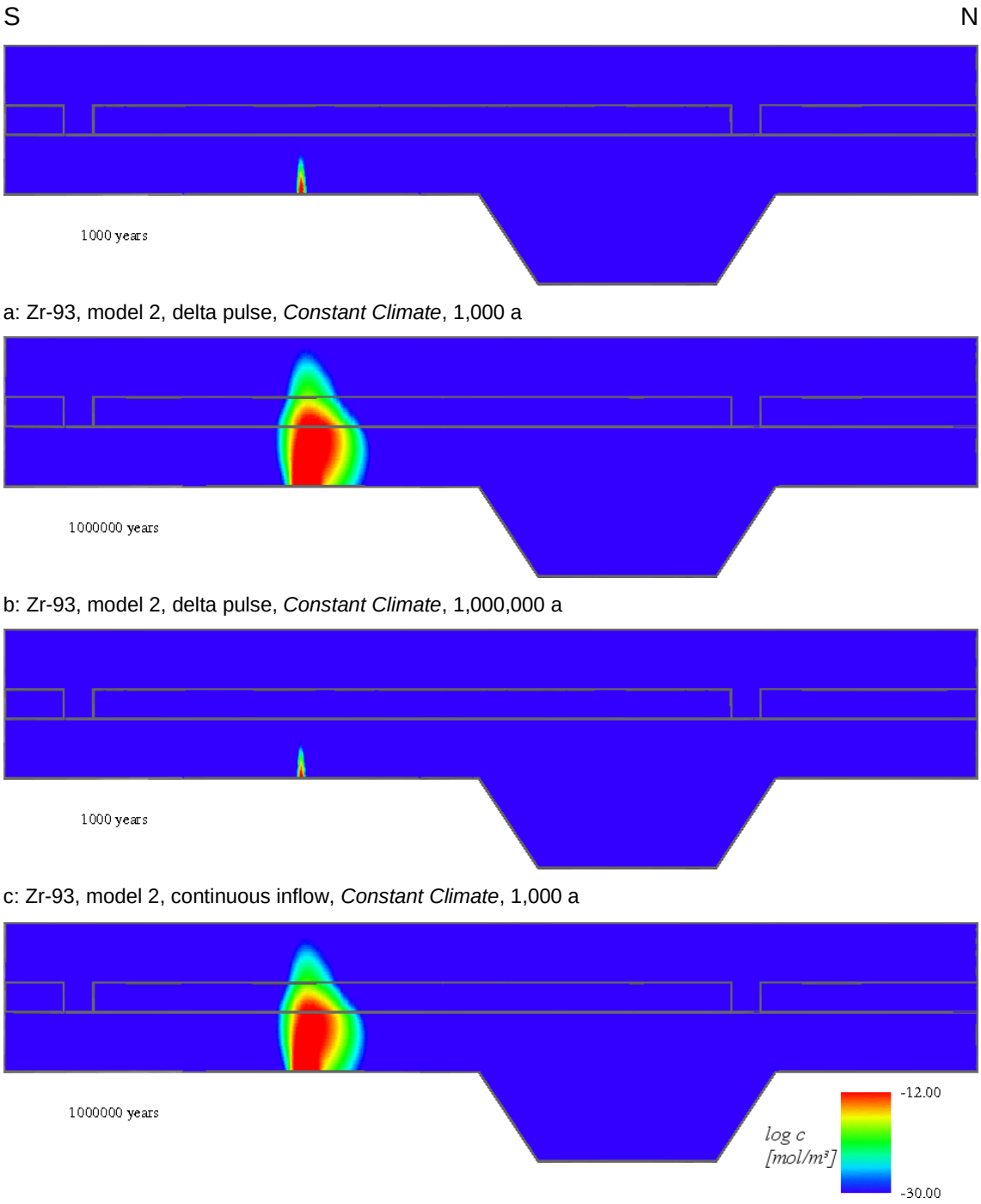

a: Zr-93, model 2, delta pulse, *Constant Climate*, 1,000 a

b: Zr-93, model 2, delta pulse, *Constant Climate*, 1,000,000 a

c: Zr-93, model 2, continuous inflow, *Constant Climate*, 1,000 a

d: Zr-93, model 2, continuous inflow, *Constant Climate*, 1,000,000 a

Fig. 74 *Constant Climate*: Model 2, Zr-93, delta pulse and continuous inflow

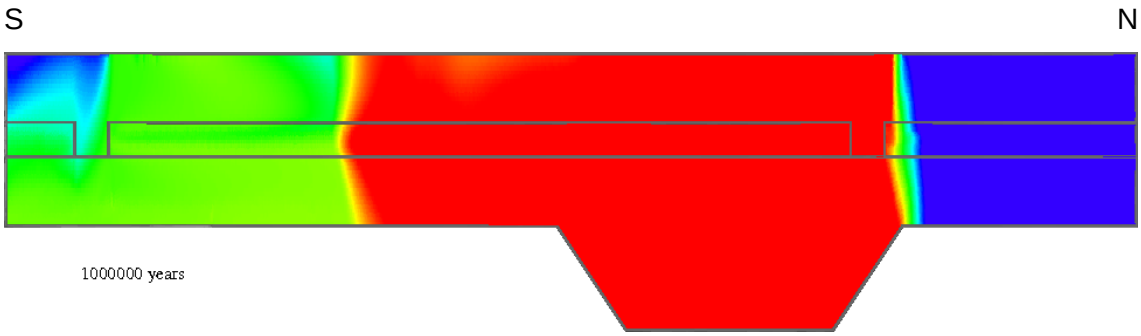

a: U-238, model 2, delta pulse, *Constant Climate*, 1,000,000 a

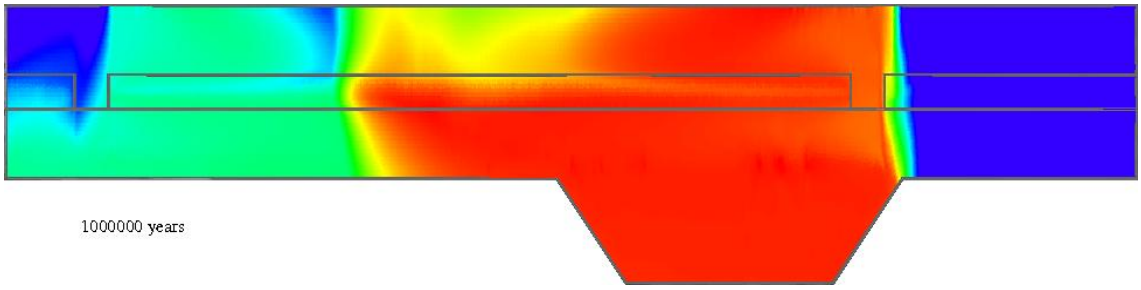

b: U-234, model 2, delta pulse, *Constant Climate*, 1,000,000 a

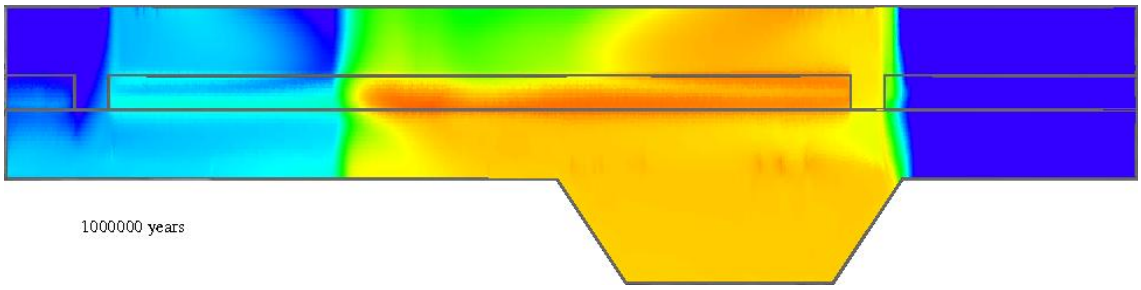

c: Th-230, model 2, delta pulse, *Constant Climate*, 1,000,000 a

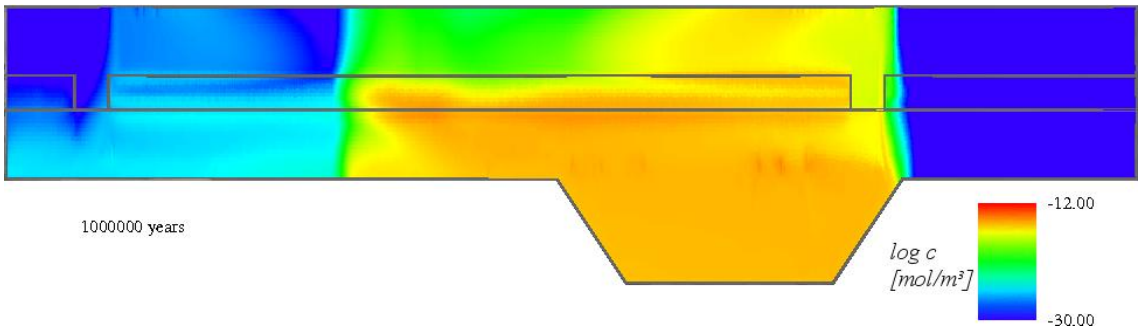

d: Ra-226, model 2, delta pulse, *Constant Climate*, 1,000,000 a

Fig. 75 *Constant Climate*: Model 2, U decay series, delta pulse

7.7.2.4 Sea Water Inundation

For the climate state *Sea Water Inundation*, all combinations of transport calculations for Cs-135 (model 1 and model 2, delta impuls and continuous inflow) were performed and, exemplarily, the calculations for the other radionuclides for model 2 and a delta pulse.

Cs-135

The results for the transport of Cs-135 after a delta pulse for model 1 and model 2 were already discussed in chapter 7.7.2.1 (see Fig. 66 and Fig. 67). The results for continuous inflow are very similar to those after a delta pulse. After one million years, Cs-135 amounts to $8.4 \cdot 10^{-1}$ mol in both models, while $5.8 \cdot 10^{-1}$ mol of the tracer are contained by model 1 and $5.3 \cdot 10^{-1}$ mol by model 2. The duration of inflow and the number of hydraulic windows have no significant influence on the migration of Cs-135.

I-129

Like the tracer (see Fig. 66 c), I-129 is initially distributed in the model domain isotropically from the source by diffusion (Fig. 76 a, note the exaggeration factor of 10). After 1,000 years, it has reached the model surface vertically above the salt dome as well as the southern boundary of the north-western rim syncline. After approx. 200,000 years, I-129 can be observed in the entire lower aquifer. In the upper aquifer, the highest radionuclide concentrations occur in the area vertically above the contact to the salt dome and the southern boundary of the rim syncline. Since the two hydraulic windows serve as a pathway for the radionuclide transport, high concentrations of I-129 are found above the hydraulic windows as well. At this point in time, it can clearly be seen that there is a reduced radionuclide concentration south of the salt dome contact in the lower aquifer compared to the northern area. Larger concentration differences occur than for Cs-135. This is due to the formation of convection cells with very low velocities above the contact to the salt dome. These convection cells in the northern area extend into the north-western rim syncline and can transport the radionuclides into the entire northern part of the lower aquifer. The southern convection cell has a smaller extension so that - in the long term - the transport to the south is smaller than to the north. Even after one million years these impacts are still to be observed by lower concentrations in the southernmost area (Fig. 76 b). At this point in time, there is still $5.7 \cdot 10^{-1}$ mol of I-129 in the model domain.

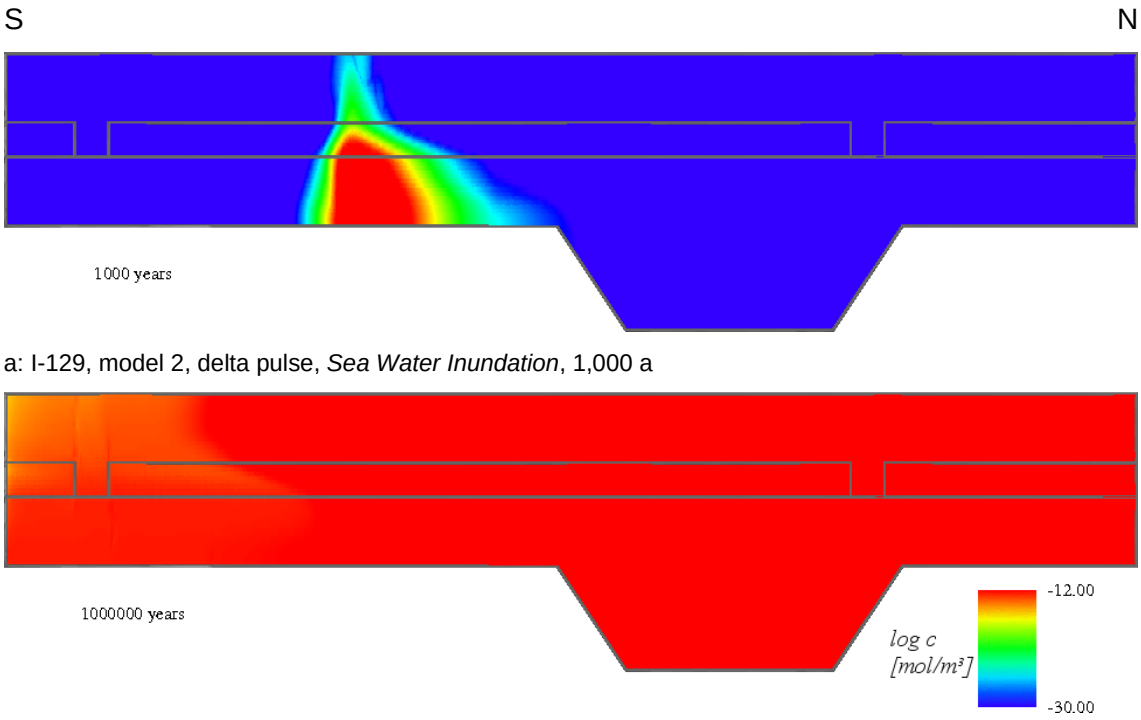

a: I-129, model 2, delta pulse, *Sea Water Inundation*, 1,000 a

b: I-129, model 2, delta pulse, *Sea Water Inundation*, 1,000,000 a

Fig. 76 *Sea Water Inundation*: Model 2, I-129, delta pulse

Zr-93

Likewise in the other climate states Zr-93 does not reach the aquitard after 1,000 years (Fig. 77 a) due the strong sorption. After one million years Zr-93 migrates to the upper edge of the aquitard. At the contact to the salt dome, where the width of the contaminant plume is the largest, Zr-93 can only be observed at a length of about 600 m to 700 m. As in the case of *Constant Climate*, only radioactive decay is responsible for the decrease of the substance amount in the model domain. There is still $6.3 \cdot 10^{-1}$ mol of Zr-93 in the model domain after one million years.

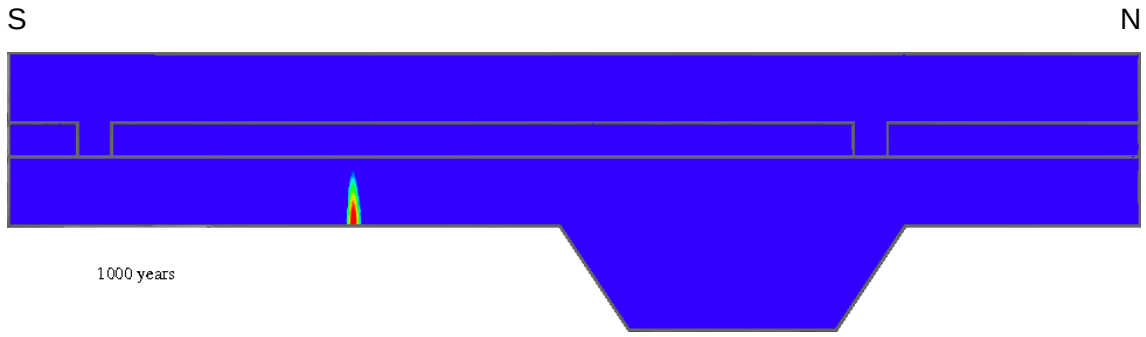

a: Zr-93, model 2, delta pulse, *Sea Water Inundation*, 1,000 a

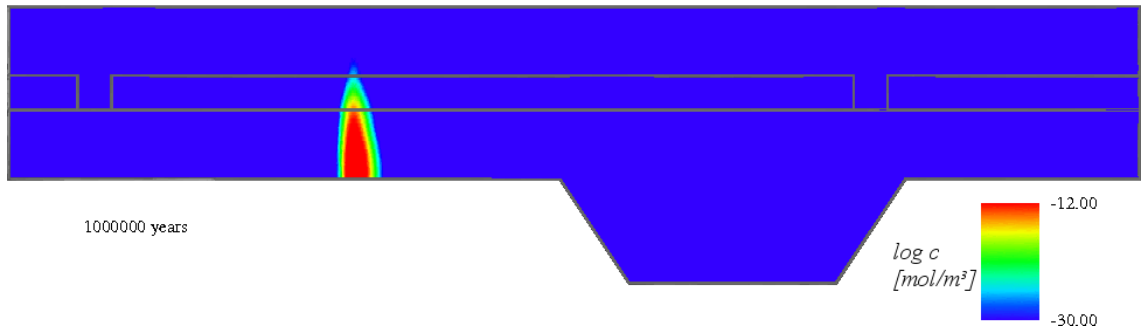

b: Zr-93, model 2, delta pulse, *Sea Water Inundation*, 1,000,000 a

Fig. 77 *Sea Water Inundation*: Model 2, Zr-93, delta pulse

C-14

Due to the low sorption, the propagation of C-14 after 1,000 years is similar to the propagation of I-129 (not depicted). C-14 has reached the model surface after 1,000 years already and is transported isotropically from the source into all directions. In contrast to the other radionuclides, C-14 does not spread all over the model area. The half-life of C-14 is too short to allow a wide-ranging distribution at these low flow velocities. After approx. 460,000 years, virtually any C-14 is found in the model area anymore.

Uranium decay series

U-238 reaches the aquitard after 1,000 years. The same applies to the daughter nuclides

but with lower concentrations. In the aquitard, the K_d value of 20 ml g^{-1} for U-238 and U-234 is increased compared to the aquifers (K_d (uranium) = 2 ml g^{-1}). Thus, the upward transport decreases and the northward and southward migration in the lower aquifer becomes more important. After approx. 120,000 years U-238 has just about reached the model surface in the area vertically above the source. At this point in time, the tracer is already distributed in the entire model domain. After about 600,000 years, U-238 has passed the southern hydraulic window and is transported up to the model surface. After 700,000 years, it can be observed in the entire lower aquifer as well as at the surface above the northern hydraulic window. The outflow area in the centre of the surface has a width of about 6 km. After one million years (Fig. 78), the highest concentrations in the lower aquifer occur in the rim syncline and in the upper aquifer above the hydraulic windows and in the centre. The distribution of U-234 is similar to that of U-238 with lower concentrations. Regarding the highest concentrations of Th-230, the concentration maximum in the aquitard is located above the source and is higher than that of Ra-226, although both radionuclides show similar distributions. The most important factor for the transport of U-238 is diffusion whereas the distribution of the daughter nuclides is determined by the distribution of the U-238. Very high substance amounts of $n_{U\text{-}238} = 7.7 \cdot 10^{-1}$ mol, $n_{U\text{-}234} = 4.0 \cdot 10^{-5}$ mol, $n_{Th\text{-}230} = 1.3 \cdot 10^{-5}$ mol and $n_{Ra\text{-}226} = 2.6 \cdot 10^{-7}$ mol remain in the model domain due to the low flow velocities.

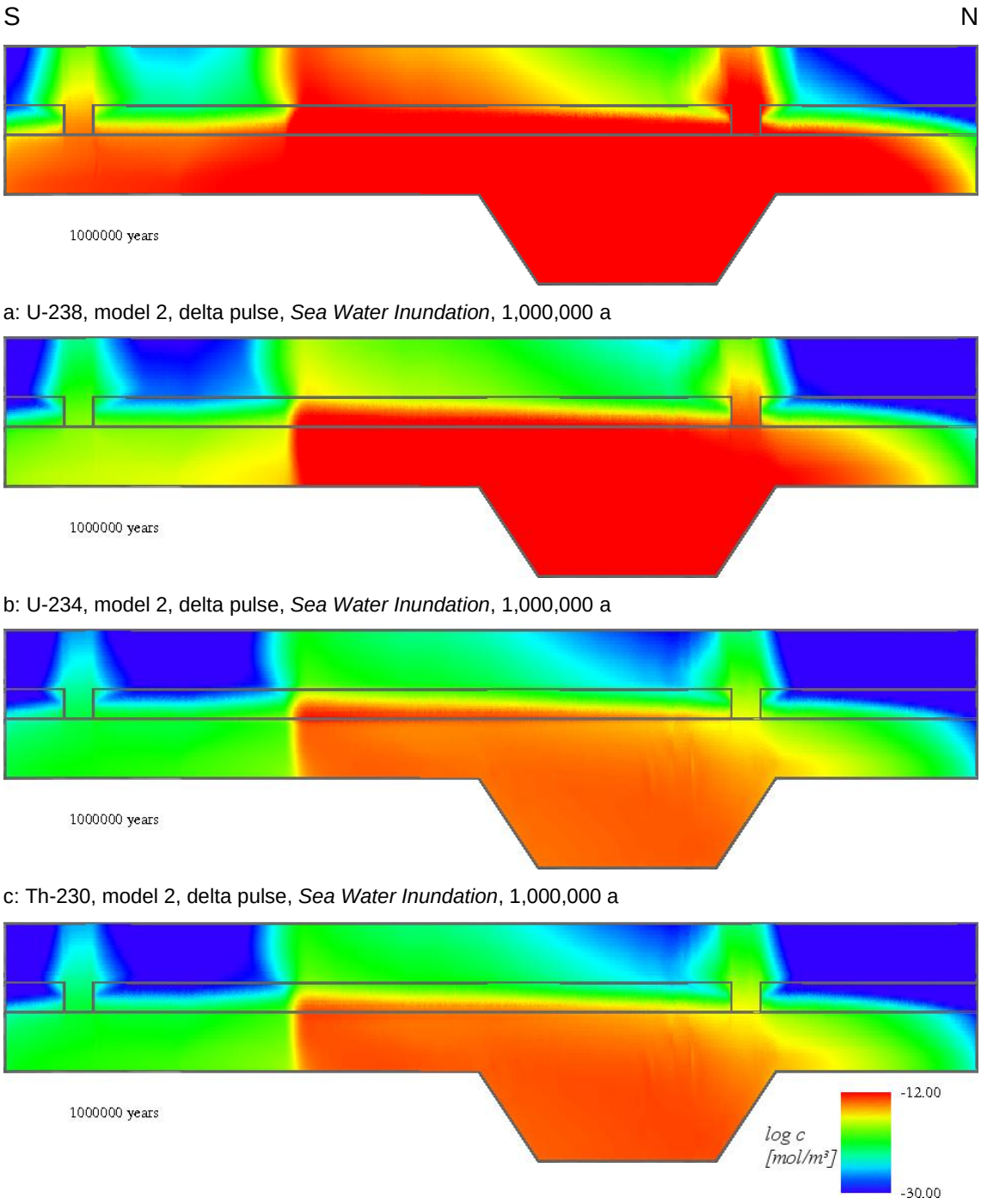

a: U-238, model 2, delta pulse, *Sea Water Inundation*, 1,000,000 a

b: U-234, model 2, delta pulse, *Sea Water Inundation*, 1,000,000 a

c: Th-230, model 2, delta pulse, *Sea Water Inundation*, 1,000,000 a

d: Ra-226, model 2, delta pulse, *Sea Water Inundation*, 1,000,000 a

Fig. 78 *Sea Water Inundation*: Model 2, U decay series, delta pulse

7.7.2.5 Permafrost

For the climate state *Permafrost*, all transport calculations were performed for Cs-135 (model 1 and model 2, delta pulse and continuous inflow). Simulations for the transport of the other radionuclides are restricted to model 2 and a delta pulse. An important difference to the other climate states is the occurrence of fresh water conditions and thus correspondingly higher K_d values in the upper aquifer as well as in the aquitard in model 2. In model 1, saline water occurs in all three hydrogeological units.

Cs-135

The results for model 2 and a delta pulse were already discussed in chapter 7.7.2.1 (see Fig. 68). After one million years, the distribution of Cs-135 is almost identical with that after continuous inflow. Solely the concentrations remaining in the model domain for continuous inflow ($n_{Cs\text{-}135} = 1.8 \cdot 10^{-1}$ mol and $n_{Tracer} = 6.4 \cdot 10^{-3}$ mol) are higher than after a delta pulse ($n_{Cs\text{-}135} = 4.8 \cdot 10^{-2}$ mol and $n_{Tracer} = 3.5 \cdot 10^{-4}$ mol). Due to the high flow velocities and the relatively low sorption in the lower aquifer, Cs-135 is transported out of the model domain through the lower aquifer to the south. Cs-135 does not reach the model surface and is only distributed in a restricted area of the upper aquifer.

In the lower aquifer, model 1 shows much higher flow velocities than model 2. After a delta pulse, Cs-135 reaches the southern boundary of the model domain already after 1,000 years (Fig. 79 a). After one million years, the highest concentrations in the aquitard and in the upper aquifer occur in the area of the southern talik and the hydraulic window. Since in model 1, saline water is present in all three units, the sorption of Cs-135 in the aquitard and the upper aquifer is lower than in model 2. Thus, Cs-135 is not only discharged via the southern boundary but also via the surface of the model.

For continuous inflow, a similar picture is obtained as for the delta pulse (not depicted). In this case, Cs-135 shows quasi-steady-state concentrations in the lower aquifer of approx. $1 \cdot 10^{-9}$ mol m^{-3} to $1 \cdot 10^{-10}$ mol m^{-3} between the salt dome contact and the southern boundary of the model. After one million years, there are still $4.8 \cdot 10^{-2}$ mol of Cs-135 in the model domain in case of a delta pulse and $1.77 \cdot 10^{-1}$ mol of Cs-135 for continuous inflow.

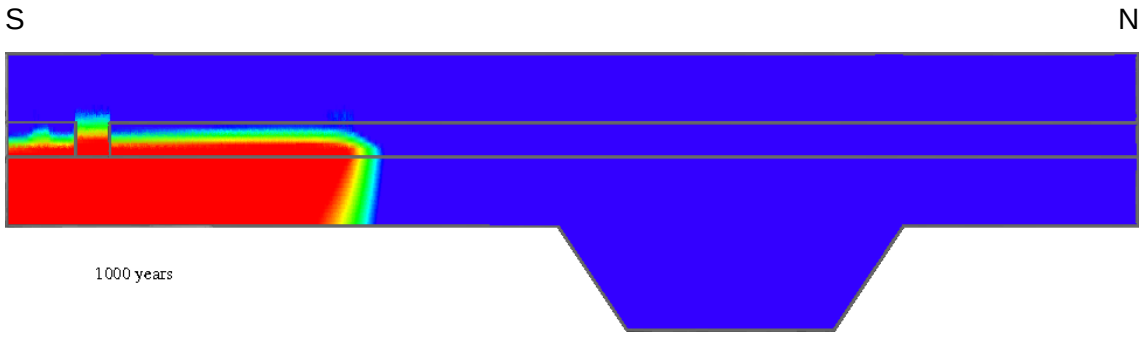

a: Cs-135, model 1, delta pulse, *Permafrost*, 1,000 a

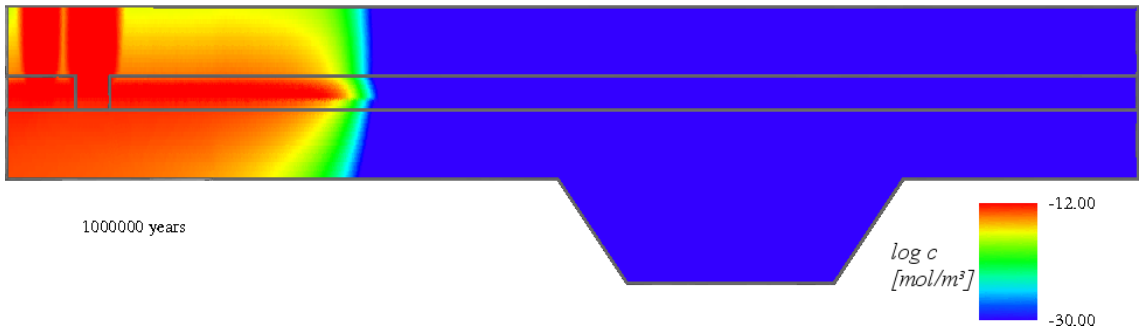

b: Cs-135, model 1, delta pulse, *Permafrost*, 1,000,000 a

Fig. 79 *Permafrost*: Model 1, Cs-135, delta pulse

I-129

Already after a model time of 1,000 years, the simluation results for I-129 (not depicted) differ significantly from the results for Cs-135 (see Fig. 68 a). Due to the lower sorption of I-129 in the aquitard (K_d (I-129) = 2 ml g^{-1}, compared to K_d (Cs-135) = 70 ml g^{-1}), I-129 can be observed in the frozen regions of the upper aquifer already after 1,000 years. The contaminant plume of I-129 reaches up to half of the thickness of the aquitard above the source. After about 20,000 years, I-129 reaches the southern hydraulic window. After another 20,000 years, I-129 can be detected at the southern boundary of the model. I-129 is not found at the top of the model until 50,000 years at least. The distribution of I-129 from the source to the south takes place by advection in the unfrozen regions and by diffusion in the frozen regions. To the north, I-129 also disperses by diffusion against the flow direction to the northern hydraulic window and up to the model surface, where it is observed after approx. 75,000 years. After about 600,000 years, I-129 occurs along the entire model surface except for the area north of the northern hydraulic window. Despite the low permeability of the permafrost regions, it is more difficult to distinguish by I-129 concentrations between the frozen and unfrozen regions or between the different hydrogeological units after one million years than in the simulations for the other radionuclides. After one million years, the mass of I-129 left in the model domain amounts to $2.8 \cdot 10^{-3}$ mol.

Zr-93

As for the climate states described above, Zr-93 is the only radionuclide that does not reach the aquitard after 1,000 years (Fig. 80 a). In this state, the sorption in the aquitard is increased to K_d = 100 ml g^{-1} due to the fresh water conditions. After one million years, the contaminant plume has a width of only about 3 km. It reaches the lower part of the upper aquifer with a width of about one kilometre. At the southern border of the contact to the salt dome, a convection cell formes in the lower aquifer of the flow model (Fig. 81).

At this point in time, the influence of the flow field on radionuclide transport becomes particularly obvious. First Zr-93 is only transported by advection from the source to the south. At the southern boundary of the salt dome, the groundwater flow is directed upwards, then northwards and finally down to the salt dome contact. Thus Zr-93 (as well as the other radionuclides) is transported upwards with the advection up to the aquitard and back to the north. For the transport calculations of the other radionuclides, the existence of this convection cell is of minor significance due to the lower sorption and therefore the faster transport. In the aquitard and in the upper aquifer, however, Zr-93 can only be transported by diffusion and therefore does not reach the model surface. After one million years, Zr-93 has a mass amount of $6.3 \cdot 10^{-1}$ mol in the model domain which again is only reduced by radioactive decay.

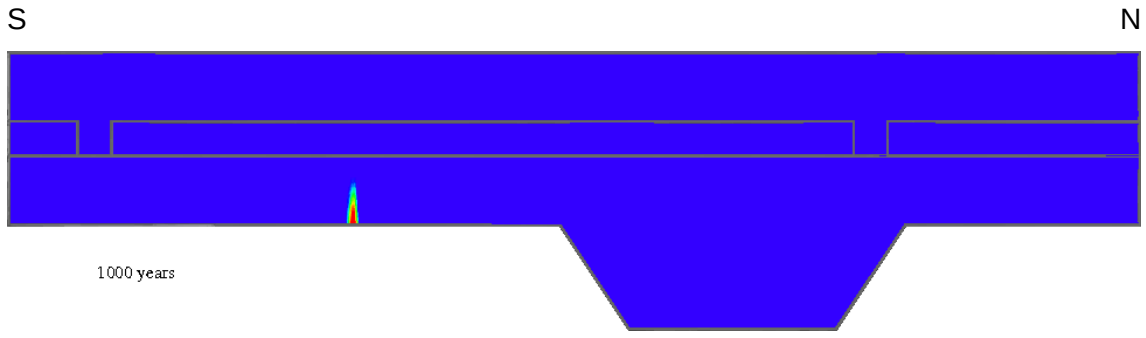

a: Zr-93, model 2, delta pulse, *Permafrost*, 1,000 a

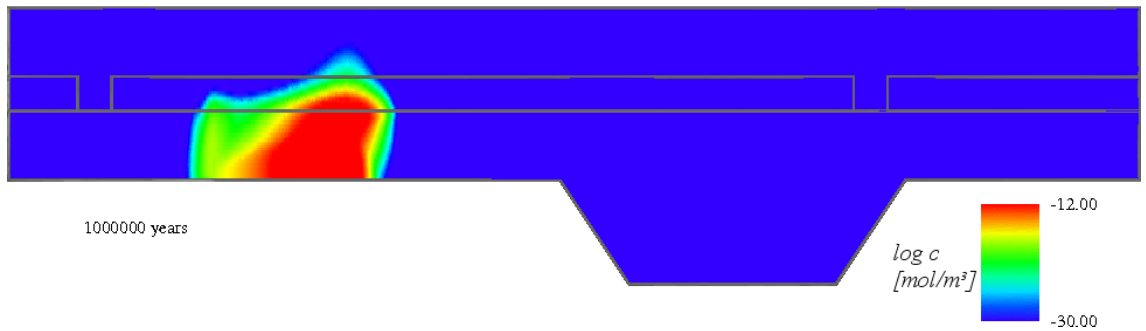

b: Zr-93, model 2, delta pulse, *Permafrost*, 1,000,000 a

Fig. 80 *Permafrost*: Model 2, Zr-93, delta pulse

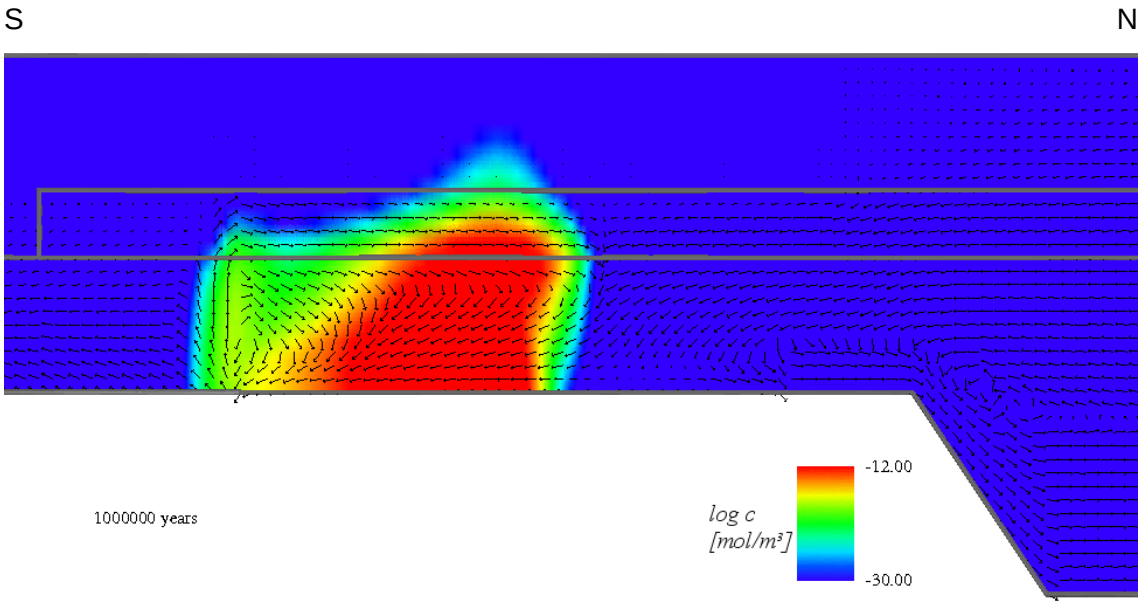

Fig. 81 *Permafrost*: Model 2 (section), Zr-93, delta pulse; radionuclide concentrations after $1 \cdot 10^6$ a. Arrows: Flow vectors, vector length proportional to velocity (in the entire model domain: v_{min} = 1.1·10-10 m a^{-1}, v_{max} = 34.5 m a^{-1}). Section with a width of about 8 km

C-14

After 1,000 years, C-14 can be detected at the top of the model (Fig. 82 a). C-14 has completely left the model area after one million years (not depicted). It occurs at the model surface vertically above the source after less than 25,000 years, while the highest C-14 concentrations occur in the area of the southern hydraulic window with approx. $1 \cdot 10^{-18}$ mol m^{-3} after approx. 100,000 years model time. After less than 450,000 years, it no longer occurs in the model domain. After 250,000 years the C-14 concentration in the model area is already very low (Fig. 82 b).

Uranium decay series

The sorption coefficient for uranium in the lower aquifer, which contains saline water, is K_d (uranium) = 0.6 ml g^{-1}. As a result of this low K_d value, the contaminant plume of U-238 (Fig. 83 a) is similar to that of C-14 after 1,000 years. For U-238 and the daughter nuclide U-234, the impact of the convection cell at the southern boundary of the salt dome contact again becomes particularly obvious within the first few thousand years. In the southern direction of the source, the concentration decreases rapidly. In parts of the convection cell, increased concentrations of U-234 occur in form of a contaminant plume with a steep vertical gradient which is not as distinct for Th-230 and Ra-226. The sorption of the radionuclides on the particles of the aquitard is very high, thus, after one million years, the

concentration maximum of all nuclides is localised in the aquitard. Highest radionuclide concentrations at the model surface occur above the southern hydraulic window (Fig. 84). Here, U-238 shows concentrations of up to approx. $c_{U\text{-}238} = 1 \cdot 10^{-9}$ mol m^{-3}. Despite the high flow velocities of the groundwater, transport takes place into the north-western rim syncline and through the northern hydraulic window into the upper aquifer (Fig. 84 a). There, however, it only reaches marginal concentrations. After one million years, U-234 shows lower concentrations in the rim syncline (Fig. 84 b) and Th-230 and Ra-226 are only present south of the rim syncline. The highest concentrations of the daughter nuclides occur – as in the other climate states – in the aquitard. Due to the large amount of nuclides discharged at the surface and to the south, there are relatively small substance amounts of $n_{U\text{-}238} = 4.0 \cdot 10^{-2}$ mol, $n_{U\text{-}234} = 2.1 \cdot 10^{-6}$ mol, $n_{Th\text{-}230} = 6.6 \cdot 10^{-7}$ mol and $n_{Ra\text{-}226} = 1.4 \cdot 10^{-8}$ mol in the model domain after one million years.

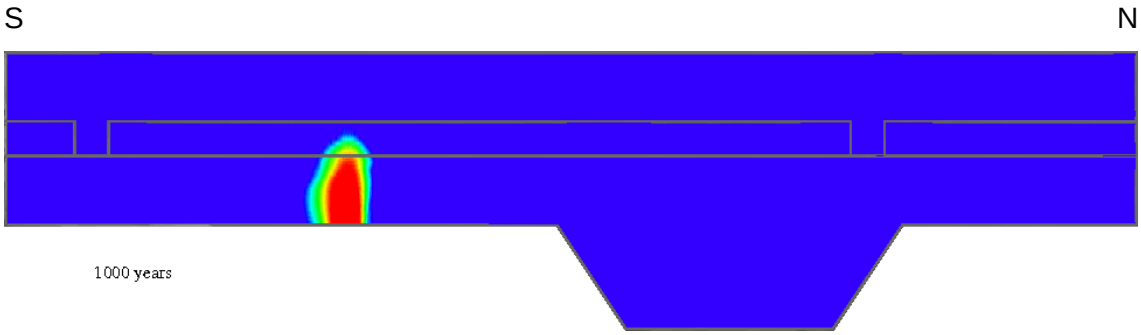

a: C-14, model 2, delta pulse, *Permafrost*, 1,000 a

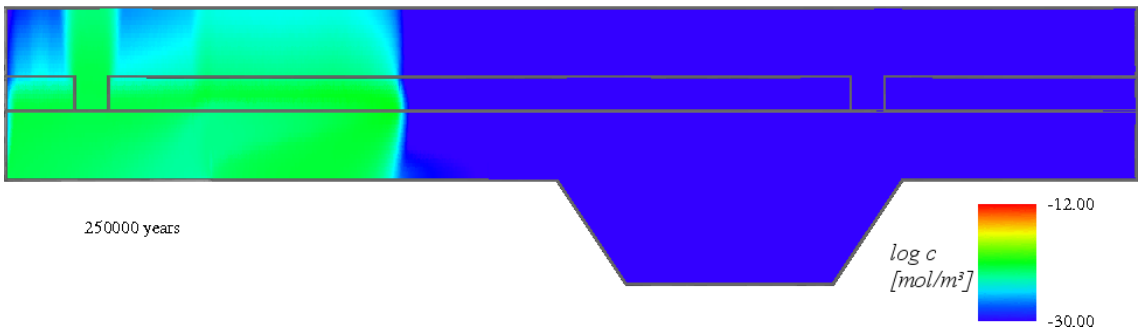

b: C-14, model 2, delta pulse, *Permafrost*, 250,000 a

Fig. 82 *Permafrost*: Model 2, C-14, delta pulse

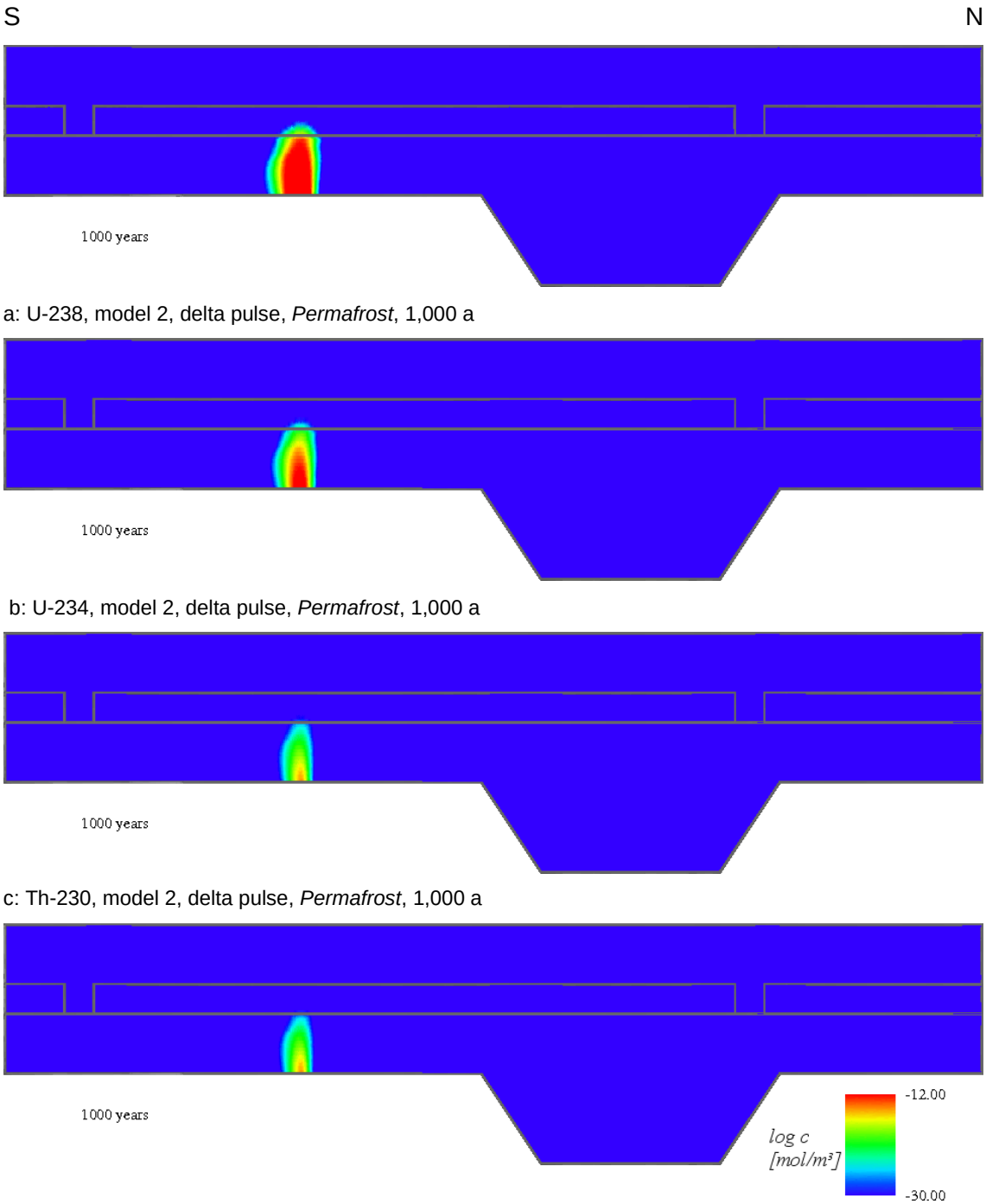

a: U-238, model 2, delta pulse, *Permafrost*, 1,000 a

b: U-234, model 2, delta pulse, *Permafrost*, 1,000 a

c: Th-230, model 2, delta pulse, *Permafrost*, 1,000 a

d: Ra-226, model 2, delta pulse, *Permafrost*, 1,000 a

Fig. 83 *Permafrost*: Model 2, U decay series, delta pulse

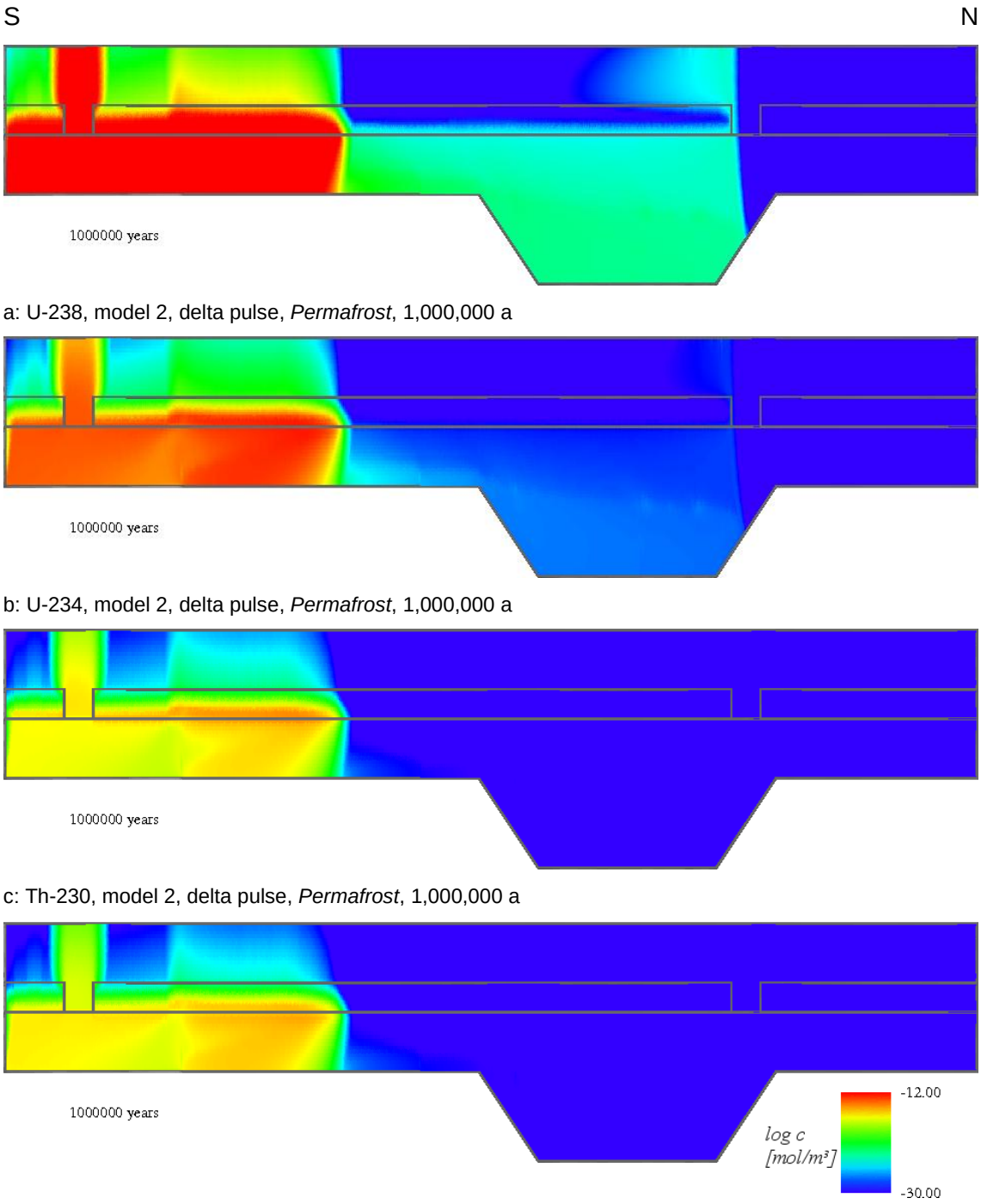

a: U-238, model 2, delta pulse, *Permafrost*, 1,000,000 a

b: U-234, model 2, delta pulse, *Permafrost*, 1,000,000 a

c: Th-230, model 2, delta pulse, *Permafrost*, 1,000,000 a

d: Ra-226, model 2, delta pulse, *Permafrost*, 1,000,000 a

Fig. 84 *Permafrost*: Model 2, U decay series, delta pulse

7.8 Summary and conclusions

For the climate states considered, significant differences were determined for the radionuclide transport. All transport calculations were performed on a constant flow field for a period of one million years. The radionuclide masses remaining in the model area at the end of the simulations are listed in Tab. 17.

Tab. 17 Residual masses [mol] in the model area after a model time of one million years. "n.c." = not calculated (see Tab. 14). Masses smaller than $n = 10^{-20}$ mol are represented by "-"

	Model	Tracer	Cs-135	I-129	C-14	Zr-93	U-238
Inflow	Delta pulse: 1 a						
Present climate	1	$7.8 \cdot 10^{-13}$	$5.6 \cdot 10^{-1}$	n.c.	n.c.	n.c.	n.c.
	2	-	$7.1 \cdot 10^{-2}$	$1.3 \cdot 10^{-4}$	-	$6.3 \cdot 10^{-1}$	$2.1 \cdot 10^{-2}$
Constant Climate	1	$6.3 \cdot 10^{-10}$	$4.1 \cdot 10^{-1}$	$1.3 \cdot 10^{-2}$	-	$6.3 \cdot 10^{-1}$	$1.7 \cdot 10^{-1}$
	2	$3.0 \cdot 10^{-6}$	$1.8 \cdot 10^{-1}$	$1.3 \cdot 10^{-2}$	-	$6.3 \cdot 10^{-1}$	$5.8 \cdot 10^{-2}$
Sea Water Inundation	1	$3.8 \cdot 10^{-1}$	$7.1 \cdot 10^{-1}$	n.c.	n.c.	n.c.	n.c.
	2	$3.3 \cdot 10^{-1}$	$7.1 \cdot 10^{-1}$	$3.3 \cdot 10^{-1}$	-	$6.3 \cdot 10^{-1}$	$7.7 \cdot 10^{-1}$
Permafrost	1	$5.5 \cdot 10^{-6}$	$7.3 \cdot 10^{-4}$	n.c.	n.c.	n.c.	n.c.
	2	$3.5 \cdot 10^{-4}$	$4.8 \cdot 10^{-2}$	$2.8 \cdot 10^{-3}$	-	$6.3 \cdot 10^{-1}$	$4.0 \cdot 10^{-2}$
Inflow	Continuous inflow: 10^6 a						
Present climate	1	$5.6 \cdot 10^{-2}$	$7.5 \cdot 10^{-1}$	n.c.	n.c.	n.c.	n.c.
	2	$2.5 \cdot 10^{-2}$	$5.1 \cdot 10^{-1}$	n.c.	n.c.	n.c.	n.c.
Constant Climate	1	$2.8 \cdot 10^{-2}$	$7.3 \cdot 10^{-1}$	$1.2 \cdot 10^{-1}$	$7.2 \cdot 10^{-3}$	$8.0 \cdot 10^{-1}$	$4.8 \cdot 10^{-1}$
	2	$3.6 \cdot 10^{-2}$	$6.4 \cdot 10^{-1}$	$9.4 \cdot 10^{-2}$	$7.2 \cdot 10^{-3}$	$8.0 \cdot 10^{-1}$	$3.1 \cdot 10^{-1}$
Sea Water Inundation	1	$5.8 \cdot 10^{-1}$	$8.4 \cdot 10^{-1}$	n.c.	n.c.	n.c.	n.c.
	2	$5.3 \cdot 10^{-1}$	$8.4 \cdot 10^{-1}$	n.c.	n.c.	n.c.	n.c.
Permafrost	1	$4.8 \cdot 10^{-5}$	$8.2 \cdot 10^{-3}$	n.c.	n.c.	n.c.	n.c.
	2	$6.4 \cdot 10^{-3}$	$1.8 \cdot 10^{-1}$	n.c.	n.c.	n.c.	n.c.

After a continuous inflow, the remaining mass amounts are generally higher than after a delta pulse. In case of a delta pulse, the complete mass amount of 1 mol of each substance is released into the model area at the start. Therefore, the radionuclides are subject to radioactive decay from the start. In addition to that, they may cover a longer transport distance and may be discharged out of the model area. In case of a continuous inflow, the radionuclides are released into the model area over the entire model time. Thus, they are less subject to radioactive decay and transport out of the model area.

Comparing the different climate states, the highest remaining mass amounts are found for the *Sea Water Inundation*. Here, the lowest flow velocities occur and the radionuclide transport is dominated by diffusion. The lowest mass amounts remain in the model area for the *Permafrost* state. Due to the short transport path to the south out of the model domain and the very high flow velocities, the radionuclides are rapidly removed from the model domain. The climate states *Present Climate* and *Constant Climate* show comparable residual mass amounts of the radionuclides. They range between $1.3 \cdot 10^{-2}$ mol $8.0 \cdot 10^{-1}$ mol. Only for the *Present Climate* in model 2, I-129 with its low sorption shows a lower remaining mass of $1.3 \cdot 10^{-4}$ mol. The tracer, which is not retarded by sorption is not detectable anymore as well as C-14 with its short half-life.

The different climate states almost have no influence on the remaining masses of the strong sorbing radionuclides. For example, the mass amounts of Zr-93 are only differentiated by their different inflow time. After a delta pulse, $6.3 \cdot 10^{-1}$ mol for Zr-93 remain in the model area for each climate state, while after a continuous inflow, there is $8.0 \cdot 10^{-1}$ mol left for each climate state. In contrast to that, the different half-lives of the radionuclides have a strong impact on the remaining amount of mass. C-14 with the shortest half-life cannot be detected in the model domain after one million years model time for any of the climate states. It is only found after a continuous inflow.

Comparing the results for the two different models 1 and 2, the remaining masses are generally lower in model 2. Here, the second hydraulic window is an additional pathway to the surface. For the *Present Climate* and the *Constant Climate* state, the advective flow to the south is remarkable higher in model 1 than in model 2. Therefore, the main transport in model 1 takes places to the south, while in model 2 the radionuclides are distributed to the north as well as to the south. Equal mass amounts in the two models occur for example for the strong sorbing radionuclide Zr-93 and for the diffusion dominated climate state *Sea Water Inundation*. Smaller residual mass amounts for model 1 are only found for the *Permafrost* climate state (Cs-135 and the tracer). A slightly higher amount of the tracer in model 2 than in model 1 is also found for the *Constant Climate* state (continuous inflow). The values differ by 0.6 % only, so the remaining mass amounts can be regarded as approximately equal.

In order to be able to better compare the results for the transport simulations given in Tab. 17, the values were corrected using the data for radioactive decay. Therefore, the amount of mass loss due to the decay was added to the mass amount resulting from the model

calculations for the delta pulse. The resulting values indicate the mass loss by transport out of the model area and are given in Tab. 18.

Tab. 18 Residual masses [%] in the model area after a model time of one million years, decay corrected by the amount of mass reduction by radioactive decay. "n.c." = not calculated (see Tab. 14). Masses smaller than $n = 10^{-20}$ mol are represented by "-"

	Model	Tracer	Cs-135	I-129	C-14	Zr-93	U-238
Inflow	Delta pulse: 1 a						
Present climate	1	$7.8 \cdot 10^{-11}$	85	n.c.	n.c.	n.c.	n.c.
	2	-	36	43	-	100	2.1
Constant Climate	1	$6.3 \cdot 10^{-8}$	70	44	-	100	17
	2	$3.0 \cdot 10^{-4}$	47	44	-	100	5.8
Sea Water Inundation	1	38	100	n.c.	n.c.	n.c.	n.c.
	2	33	100	76	-	100	77
Permafrost	1	55	29	n.c.	n.c.	n.c.	n.c.
	2	35	34	43	-	100	4.0

Neglecting the radioactive decay, the strong sorbing radionuclide Zr-93 completely remains within the model domain. U-238 features a very long half-life of $4.47 \cdot 10^{9}$ years, so the radioactive decay has almost no influence on the remaining mass. The mass reduction due to the decay only amounts to $1.6 \cdot 10^{-2}$ %. As for the tracer, the values resulting from the model calculations and the corrected values are identical. The impact of the radioactive decay on the transport of C-14 is hard to identify due to its very short half-life. Thus, it is not found in the model domain after one million years anymore and the corrected values are not given in Tab. 18.

Both, for I-129 and Cs-135, the corrected values are much higher than the original results. Approx. 43 % of I-129 and 29 % of Cs-135 decay within one million years. For example, in the *Sea Water Inundation* state, the complete amount of Cs-135 would be retarded. Due to the lower sorption, I-129 would still be transported out of the model domain.

Generally, the climate states determine the groundwater flow field and thus the flow direction and respectively the dominant transport processes (advection or diffusion). Accordingly, the results for the radionuclide transport show large differences. The existence of a second hydraulic window together with the different inflow rate is of high importance for the *Present Climate* and the *Constant Climate* state where the transport is

dominated by advection. In this case, this determines the flow direction and flow velocity, for example in the *Present Climate* state.

Another important parameter is the sorption of the radionuclides on the sediments. For example, the strongly sorbing radionuclide Zr-93 is retained in all climate states to such a degree that it does not reach the top of the model. In the climate state *Permafrost*, the sorption of Cs-135 is so strong – both in the aquitard and in the upper aquifer – that it is fully retained in the model area (model 2). Here, not only sorption but also the low flow velocity in the upper, frozen aquifer has a decisive influence on the delayed radionuclide transport. However, radionuclides with a low sorption (e. g. I-129) reach the model surface in all climate states. The influence of the degree of groundwater salinity plays an important role if the K_d values for saline groundwater and for fresh water strongly differ from each other, as is the case for Cs-135 and Th-230.

The difference between a delta pulse and a continuous inflow is of particular significance for short-lived radionuclides, e. g. for C-14. While after a delta pulse, C-14 is no longer present in the model area after one million years (model 2), about 0.7 % of the initial mass amount remains in the model area after continuous inflow. Regarding the long-lived radionuclides, the differences between the remaining masses depend on the sorption characteristics. The stronger the sorption on the sediments the smaller the influence of inflow time. For a continuous inflow, the arrival of the maximum concentration at the model surface is delayed in comparison to the delta pulse (Fig. 86 to Fig. 91).

To be able to compare the results of the transport simulations for different climate states, the locations of maximum radionuclide and tracer concentrations at 1 m below the model surface after one million years model time were determined (Tab. 19, Fig. 85) and then the temporal evolution of the concentration at these locations was investigated (Fig. 86 to Fig. 91). The model calculations show that locations of maximum concentrations at the surface do not vary significantly over the model time. Tab. 19 lists the exact locations expressed as the distance from the southern boundary of the model area. Fig. 85 pictures the locations of maximum nuclide concentrations and indicates the location of the hydraulic windows and the source of the pollutants. For a better identification of the different models and climate states, they were plotted on a drawn-out ordinate without a significant scale. Maximum concentrations at the surface indicate the main transport path in each model simulation.

Tab. 19 Locations of maximum radionuclide and tracer concentrations at the model surface after one million years model time, expressed as distances [km] to the southern boundary of the model area. “n.c.” = not calculated

		Tracer		Cs-135		U-Th-Ra	
Inflow time [a]	Model	1	10^6	1	10^6	1	10^6
Constant Climate	1	3.8	3.8	1.6	1.6	1.6	1.6
	2	6.5	5.4	12.6	13.6	11.2	12.5
Sea Water Inundation	1	6.3	6.0	5.0	5.0	n.c.	n.c.
	2	4.8	5.0	5.0	5.0	5.1	n.c.
Permafrost	1	1.7	0.7	0.6	0.50	n.c.	n.c.
	2	5.0	5.2	12.2	12.1	1.2	n.c.

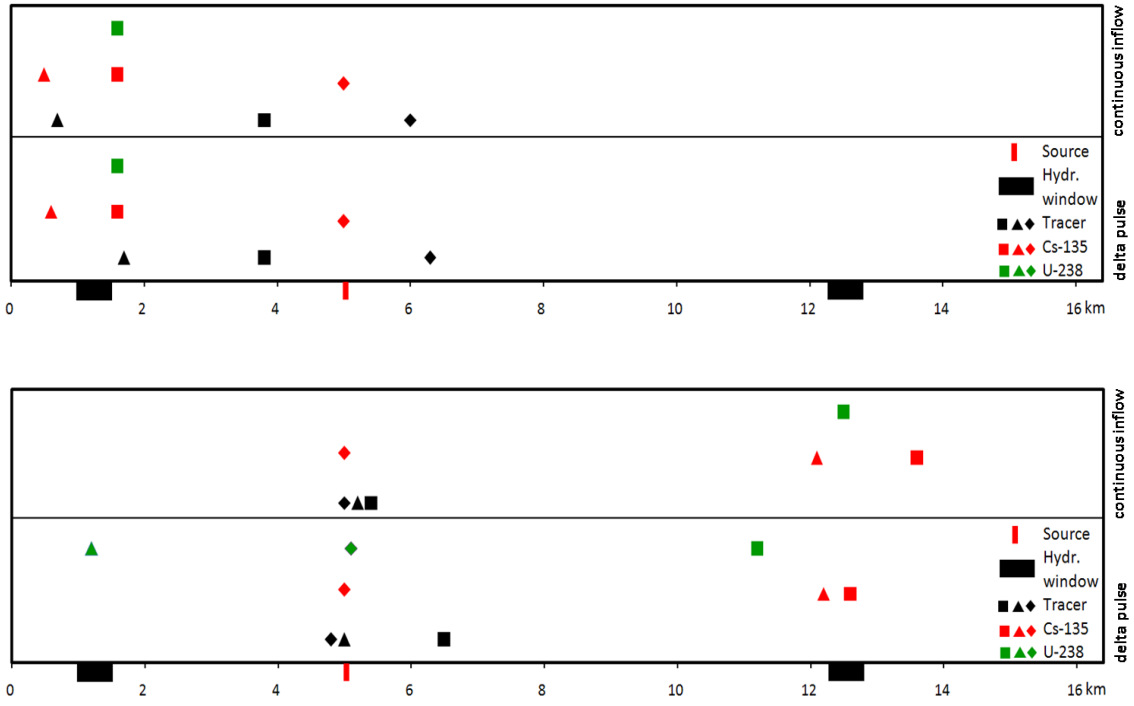

Fig. 85 Locations of maximum radionuclide and tracer concentrations at a depth of 1 m below model surface after one million years model time. Top: Model 1, bottom: Model 2. Ordinate without signification. Squares: *Constant climate*, rhombs: *Sea Water Inundation*, triangles: *Permafrost*

Maximum concentrations at the surface for model 1 are found between 0.5 km and 6.3 km north of the southern boundary for all three climate states. These locations correspond to the locations of the hydraulic window and the taliks in the *Permafrost* climate state respectively. For the *Sea Water Inundation*, the maximum concentration is located directly above the salt dome. For model 2, the locations of the maximum concentration at the

surface vary more. For the *Constant Climate* state, the maximum concentrations of Cs-135 and U-238 at the surface are located above the northern hydraulic window, while the maximum tracer concentration is found above the southern hydraulic window. Likewise in model 1, the maximum concentrations for the *Sea Water Inundation* state are found directly above the salt dome. For the *Permafrost* state, the maximum radionuclide concentrations are found above the northern hydraulic window, while the maximum tracer concentrations are found directly above the salt dome and the maximum U-238 concentration above the southern talik, respectively.

In the following the key characteristics of the different climate states are accentuated.

For the *Present Climate* state, K_d values for saline conditions were defined for all hydrogeological units for both models. The transport is dominated by advection. The impact of the number of hydraulic windows and the inflow rate is quite strong since they cause different flow directions and transport paths of the radionuclides. In model 1, the single hydraulic window in the southern part and the higher inflow rate into the lower aquifer cause a transport in the southern direction and a radionuclide arrival at the surface in the south. In model 2 with two hydraulic windows and a lower inflow rate, the prefered flow direction is northward causing radionuclide arrival at the surface above the northern hydraulic window. This effect is clearly illustrated in Fig. 64, Fig. 65 and Fig. 69 to Fig. 72, where most of the radionuclides considered have reached the aquitard after 1,000 years. After one million years, they arrived – except for Zr-93 – at the model surface through the aquitard and the northern hydraulic window. Smaller mass amounts of the radionuclides remain in the areas of both models than for the state of *Constant Climate*.

The *Constant Climate* state only differs slightly from the *Present Climate* state. However, the salt concentration in the upper aquifer in model 2 is lower. Accordingly, fresh water conditions were defined in the upper aquifer of model 2 and conditions for saline water for the aquitard and the lower aquifer. Model 1 features saline conditions in all of the three units. In the central and northern part of the upper aquifer, lower radionuclide concentrations occur than in the *Present Climate* state for model 1. In model 2, due to the higher sorption, radionuclide transport in the upper aquifer is restricted to the areas above the hydraulic windows for the strong sorbing nuclides. The highest concentrations for Cs-135, U-238 and the tracer at the model surface are found above the southern hydraulic window in model 1 and above the northern hydraulic window in model 2 (Tab. 19). Fig. 86 and Fig. 87 show the temporal evolution of the concentrations at the position of the maximum concentration of the respective radionuclide and the tracer at the surface

(locations given in Tab. 19). Maximum radionuclide concentrations of Cs-135 and U-238 at the model surface are quite similar ranging around $1 \cdot 10^{-8}$ mol m^{-3}. At first, the tracer is detected at the model surface, because it is not subject to sorption. Next, U-238 can be observed here. Due to the stronger sorption of Cs-135 its arrival time at the model surface is strongly delayed. Maximum radionuclide concentrations at the surface of model 2 are observed to occur more than 300,000 years later compared to model 1.

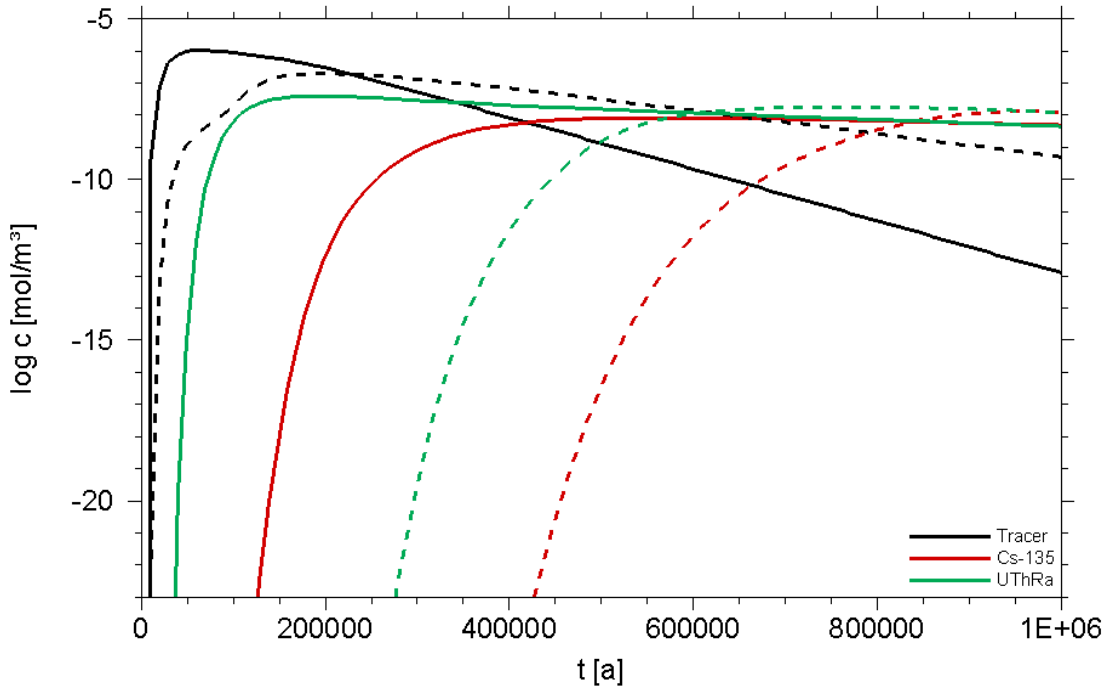

Fig. 86 *Constant Climate* - Delta pulse: Pollutant concentrations at the model surface for Cs-135, U-238 and the tracer. Solid lines: Model 1, dashed lines: Model 2. Locations given in Tab. 19, concentrations at a depth of 1 m below model surface

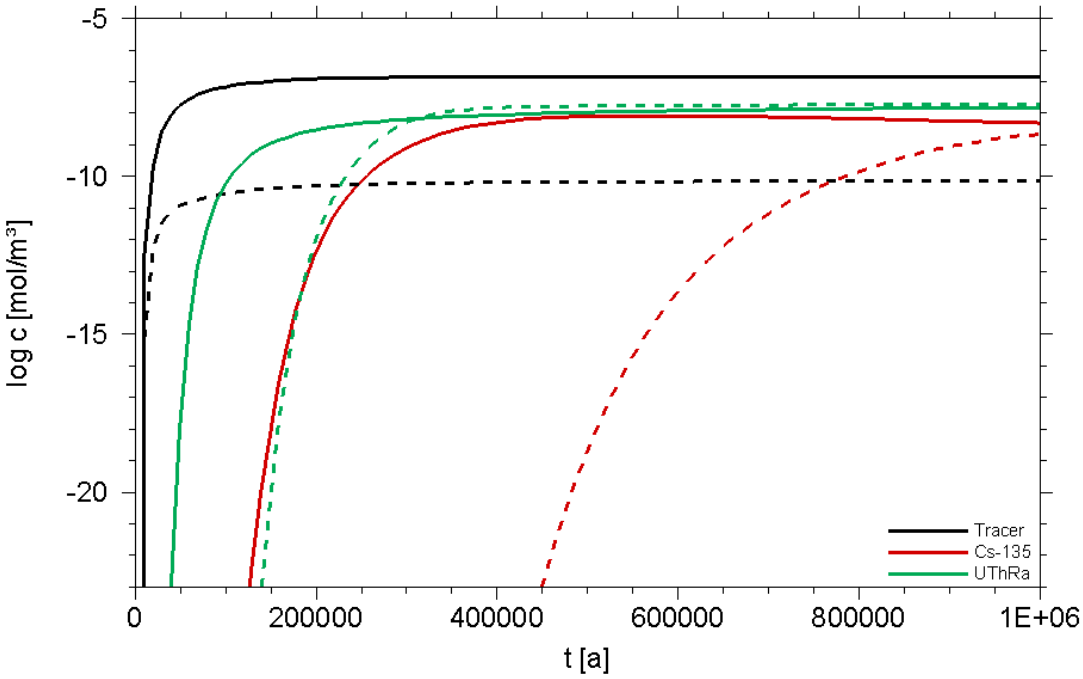

Fig. 87 *Constant Climate* - Continuous inflow: Pollutant concentrations at the model surface for Cs-135, U-238 and the tracer. Solid lines: Model 1, dashed lines: Model 2. Locations given in Tab. 19, concentrations at a depth of 1 m below model surface

In the climate state *Sea Water Inundation* with a 50 m thick column of sea water overlying the reference site, diffusion processes dominate in the whole model area. Groundwater velocities vary only little between aquifers and aquitards. K_d values were set for saline conditions for all units in both models. Radionuclide transport by diffusion is comparably slow, demonstrated by the fact that the radionuclide concentrations at the model surface are significantly lower than for the *Present Climate* and the *Constant Climate* within one million years (Fig. 86, Fig. 87, Fig. 88 and Fig. 89). The transport of the radionuclides from the source first takes place isotropically. They diffuse through the aquitard and reach the top of the model through the hydraulic window later. Since diffusion dominates radionuclide transport, the results for model 1 and 2 are similar, i.e. the number of hydraulic windows in the aquitard is nearly of no relevance for the state of *Sea Water Inundation*. To verify the assumption that the main transport process is the diffusion, the temporal evolution of the tracer concentration was calculated analytically for the one-dimensional transport from the source to the model surface. The temporal evolution of the tracer concentration in 250 m distance of the source is illustrated in Fig. 88 (blue line), in case of an assumed constant tracer concentration of $1 \cdot 10^{-5}$ mol m^3 at the source. The actual concentration of the tracer at the source is varying, but is in the range of the assumed value. The similarity of the graphs indicates that the diffusion is the dominant transport process in the *Sea Water Inundation* state. Due to the slow transport in this climate state, the largest mass amounts remain in the model area after one million years (Tab. 17). The highest substance concentrations at the surface in both models are located above the salt dome in a distance between 4.8 km and 6.3 km from the southern boundary, i. e. above the salt dome (Tab. 19). The impact of the very slow radionuclide transport is also illustrated in Fig. 88 and Fig. 89. The concentrations of Cs-135 and U-238 are still increasing after one million years, thus their concentration maximum at the model surface would be reached after more than one million years model time. The concentration of U-238 is about $1 \cdot 10^{-13}$ mol m^{-3} and of Cs-135 below $1 \cdot 10^{-20}$ mol m^{-3} at the end of the model simulations.

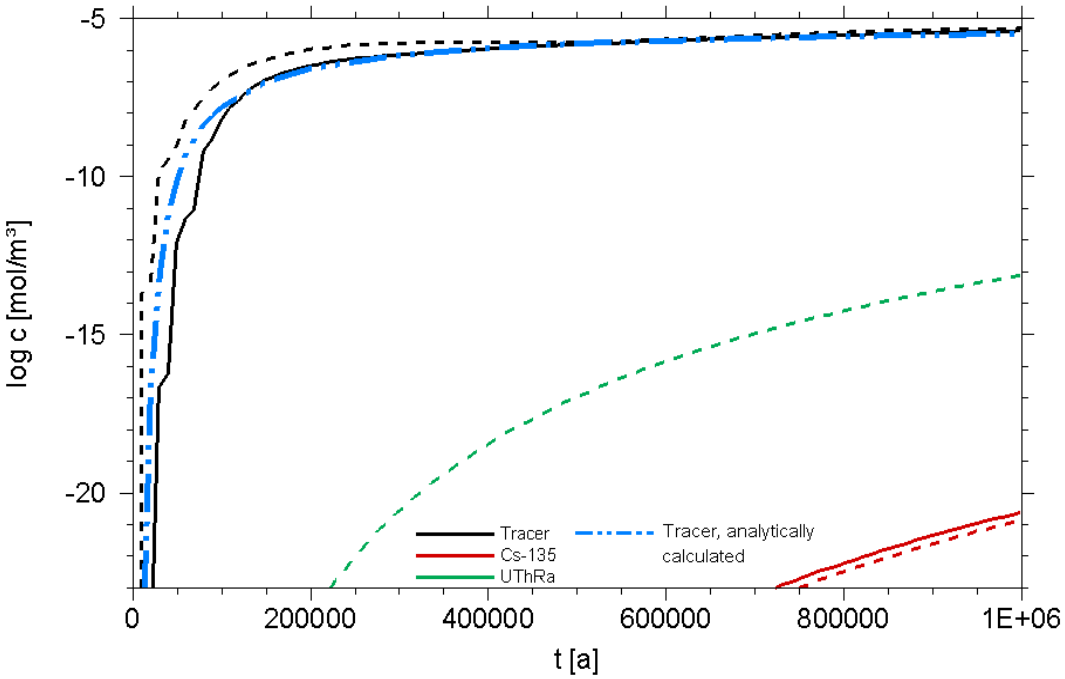

Fig. 88 *Sea Water Inundation* – Delta pulse: Pollutant concentrations at the model surface for Cs-135, U-238 and the tracer. Solid lines: Model 1, dashed lines: Model 2. Locations given in Tab. 19, concentrations at a depth of 1 m below model surface, U-238 calculation for model 1 was not performed

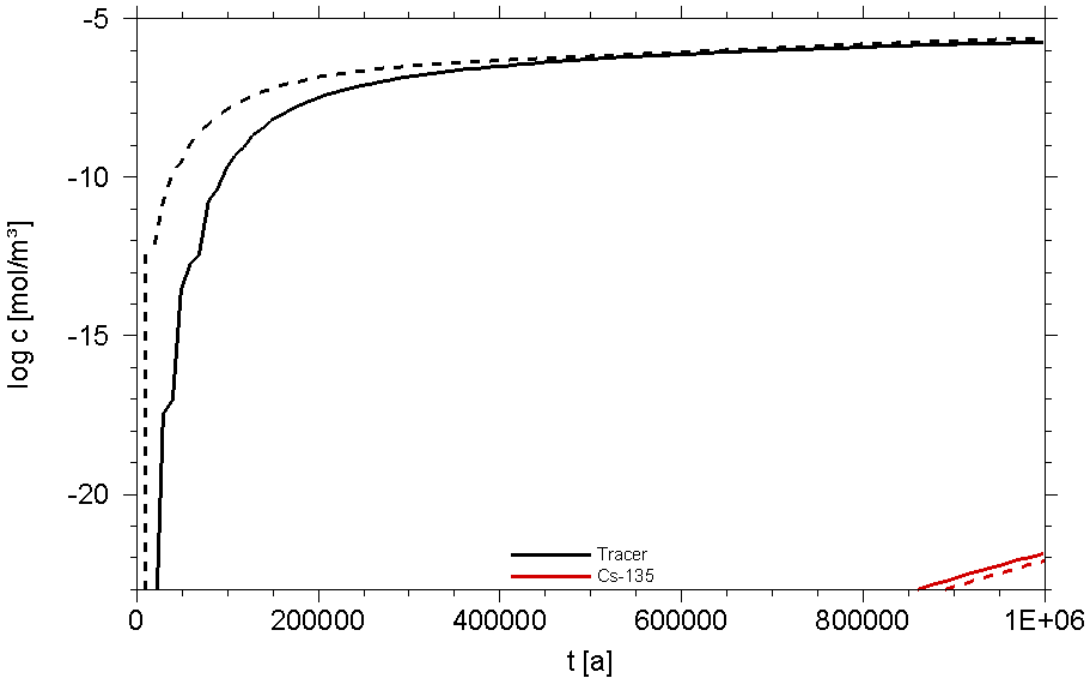

Fig. 89 *Sea Water Inundation* - Continuous inflow: Pollutant concentrations at the model surface for Cs-135 and the tracer. Solid lines: Model 1, dashed lines: Model 2. Locations given in Tab. 19, concentrations at a depth of 1 m below model surface, calculations for U-238 were not performed

In the climate state ***Permafrost*** it is assumed that the permafrost extends over the entire thickness of the upper aquifer of 100 m. For permafrost zones, a reduction of permeability from 10^{-12} m^2 to 10^{-20} m^2 is assumed. However, the frozen zones are interrupted by taliks, which maintain their original permeability of $1 \cdot 10^{-12}$ m^2, in the upper aquifer below the rivers Elbe and Seege. For the aquitard and the lower aquifer no permafrost conditions are assumed. A second characteristic of the model is a high fresh water inflow into the lower aquifer at the northern boundary of the model area caused by the near-by ice sheets. As a result, higher advection velocities in the unfrozen lower aquifer occur than in the other climate states. Under such conditions, the number and the position of the hydraulic windows are also of high relevance, in case they are located at the same positions as the taliks and create a pathway to the surface. Together with the extension and position of the taliks in the upper aquifer, they determine the flow velocity in the lower aquifer and the distribution of the salt concentration. Sorption coefficients for saline conditions were set for all units in model 1 and for the lower aquifer in model 2. The upper aquifer and the aquitard in model 2 feature fresh water conditions. Accordingly the K_d values were set for fresh water conditions here.

In both models, the radionuclides migrate from the source in the lower aquifer in southward direction. In model 2, Cs-135 does not reach the surface due to the increased sorption values under fresh water conditions and, of course, due to the reduced transport velocity in the low permeable frozen upper aquifer. In this climate state, the amounts of radionuclides remaining in the model area are similar to the remaining amounts in the *Present Climate* state (Tab. 17). The highest pollutant concentrations at the model surface occur at the top of the southern talik and above the southern hydraulic window in model 1. For a delta pulse in model 2, the highest radionuclide concentrations occur above the southern hydraulic window, too. For the continous inflow, highest Cs-135 concentrations are found above the northern hydraulic window, while the highest tracer concentrations occur above the salt dome (Tab. 19). Due to the slow transport in the aquitard and the upper aquifer (see above), Cs-135 does not reach the surface, which is illustrated in Fig. 68. The maximum U-238 concentration is $5 \cdot 10^{-11}$ mol m^{-3}, which is lower than in the *Present Climate* state, but higher than in the climate state of *Sea Water Inundation*. The strongest impact of the existence of a second hydraulic window can be observed in this climate state, which is well illustrated for Cs-135. The low concentrations in model 2 are lower than 10^{-23} mol m^3 and cannot be plotted in Fig. 90, while concentrations around $1 \cdot 10^{-10}$ mol m^{-3} are found for model 1 (Fig. 90 and Fig. 91).

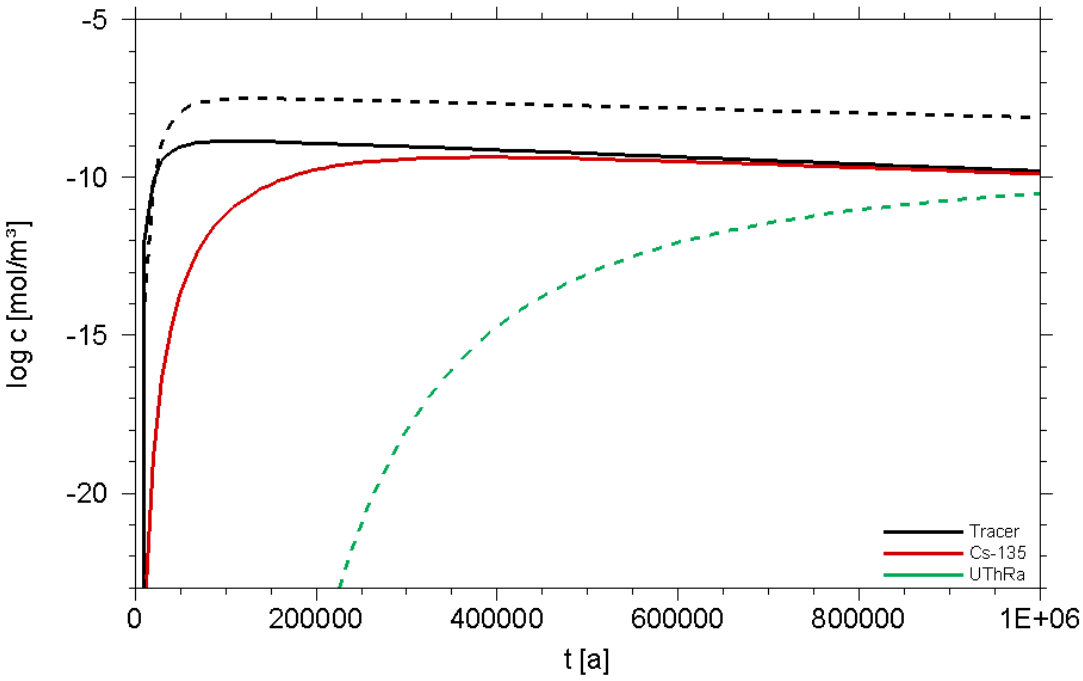

Fig. 90 *Permafrost* – Delta pulse: Pollutant concentrations at the model surface for Cs-135, U-238 and the tracer. Solid lines: Model 1, dashed lines: Model 2. Locations given in Tab. 19, concentrations at a depth of 1 m below model surface, U-238 calculation for model 1 was not performed

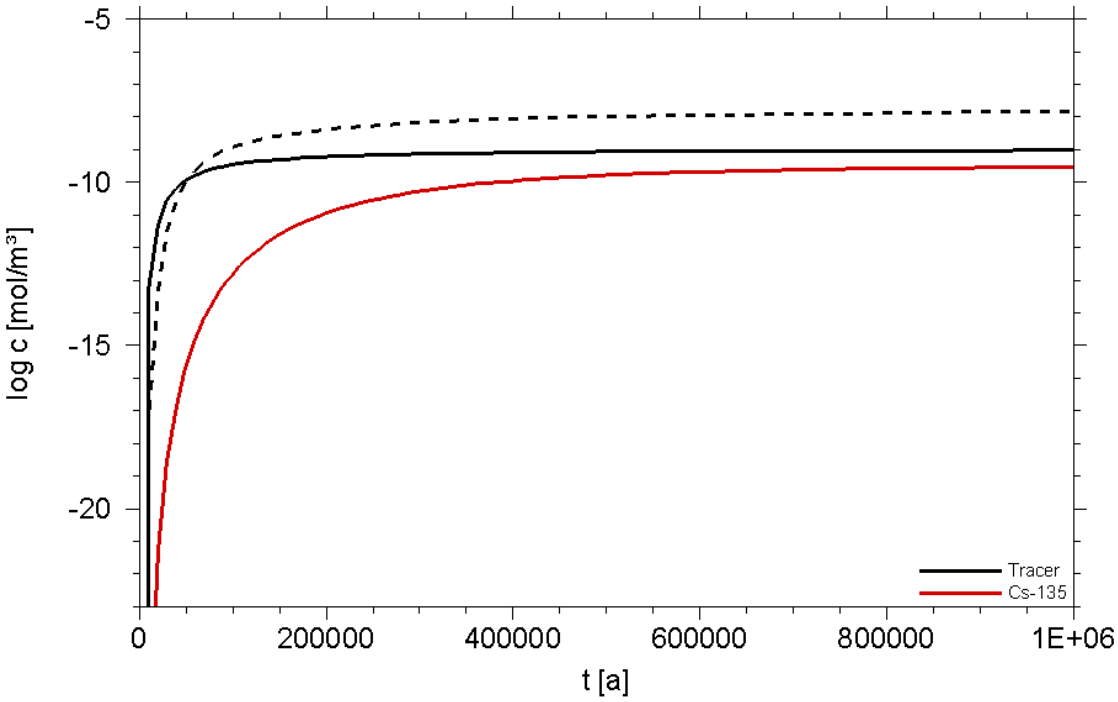

Fig. 91 *Permafrost* – Continuous inflow: Pollutant concentrations at the model surface for Cs-135 and the tracer. Solid lines: Model 1, dashed lines: Model 2. Locations given in Tab. 19, concentrations at a depth of 1 m below model surface, calculations for U-238 were not performed

8 Modelling of climate impact on biosphere processes

8.1 Introduction

After transport through the overburden radionuclides can contaminate the near-surface aquifer and may enter the biosphere via different geosphere-biosphere interfaces as the withdrawal of water from a well or by contamination of surface soil, if the water table is high /CRO 05/. Once entered the biosphere, radionuclides may cause exposures to humans via ingestion of water and food, inhalation of resuspended contaminated soil particles as well as via external exposure from contaminated soils. The resulting radiation exposure potentially arising from the contamination of groundwater is an important safety indicator for the long-term safety assessment. The exposures to humans depend on environmental and climatic conditions, agricultural practices and the habits of potentially exposed people which are difficult to predict for very long periods. This is a key source of uncertainty in estimating doses in the post-closure period of nuclear waste repositories. In this study emphasis is put on investigating the impact of climate changes on the radiation exposures. Therefore, dose conversion factors for a number of specific situations, which reflect different climate conditions at the reference site (see chapter 6), are calculated.

8.2 Methodology

8.2.1 Site characteristics

The current conditions at the reference site investigated in this study are the starting point of the calculations. These include

- climate,
- soil properties
- agricultural practices as
- crops grown,
- irrigation of plants,
- animal husbandry, and feeding regimes,
- habits of people concerning

- food intake and
- duration of stay on contaminated land.

In a first step, exposures from radionuclides entering the biosphere for todays conditions are estimated. In a second step, it is assumed that especially the climate will change. Since those changes are predictable only with high uncertainty, assessments are made for a number of other cases covering a wide spectrum of climatic conditions.

8.2.2 Climate analogue stations

In order to assess the impact of the different future climatic conditions, the potential impact on the base of “what if?” considerations is studied. For this purpose, assessments were made for present day conditions at existing stations with the respective climates, so-called analogue stations. The climate chart for each station considered are shown in Fig. 92. For the classification of climates see chapter 2.1.

The reference site is in the temperate zone, characterised by moderately cool summers and relatively mild winters; conditions are humid during the whole year, i.e. climate Cfb. The distribution of precipitation is relatively homogeneous. Here, the analogue station Magdeburg has been selected as reference station. Climates which might occur at the reference site in the future have been discussed in chapter 6. To simulate the conditions of hot and dry summers with mild and humid winters, Mediterranean climate (Csa) is considered with Rome as analogue station. The analogue station Marrakesh represents steppe climate (BS) with arid conditions during the whole year. Rostow represents a site with pronounced continental climate with very hot summers and cold winters (Dfa). Turku is characterised by cool and short summers and very cold winters (Dfb). Vardo represents tundra climate (ET).

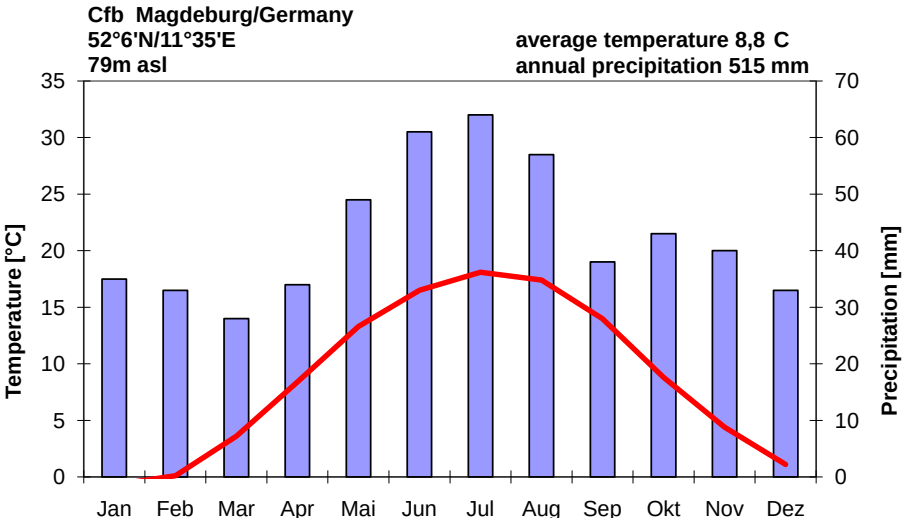

	[° C]	[mm]
Jan	-0,7	35
Feb	0,1	33
Mar	3,6	28
Apr	8,4	34
Mai	13,3	49
Jun	16,5	61
Jul	18,1	64
Aug	17,4	57
Sep	14	38
Okt	8,8	43
Nov	4,4	40
Dez	1,1	33

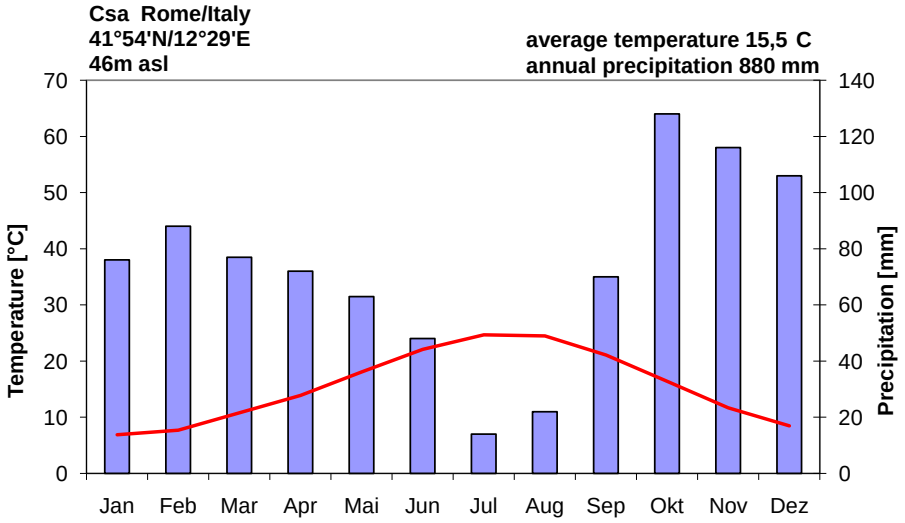

	[° C]	[mm]
Jan	6,9	76
Feb	7,7	88
Mar	10,8	77
Apr	13,9	72
Mai	18,1	63
Jun	22,1	48
Jul	24,7	14
Aug	24,5	22
Sep	21,1	70
Okt	16,4	128
Nov	11,7	116
Dez	8,5	106

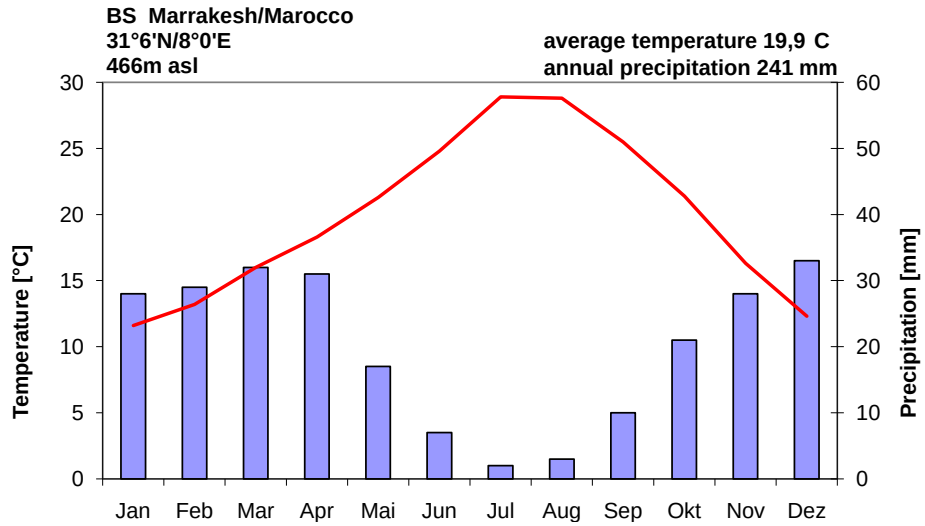

	[° C]	[mm]
Jan	11,6	28
Feb	13,2	29
Mar	16	32
Apr	18,3	31
Mai	21,3	17
Jun	24,8	7
Jul	28,9	2
Aug	28,8	3
Sep	25,5	10
Okt	21,4	21
Nov	16,3	28
Dez	12,3	33

Fig. 92 Climate charts for the analogue stations

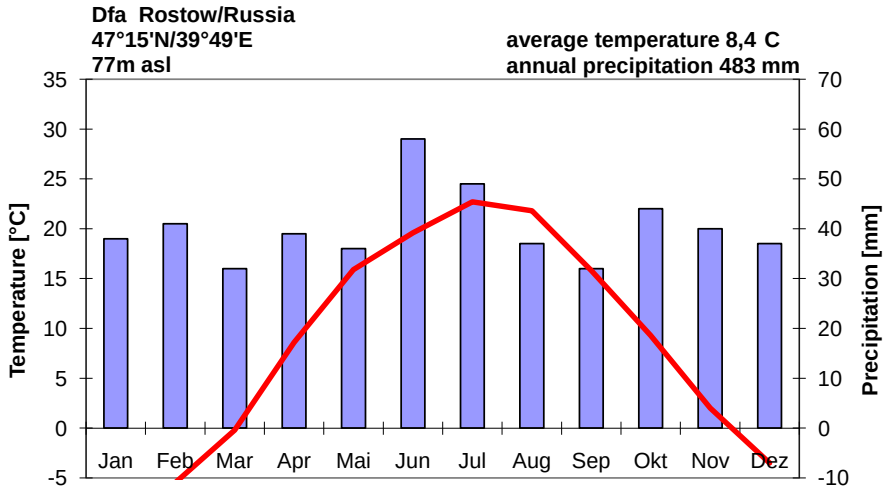

	[° C]	[mm]
Jan	-6,3	38
Feb	-5,5	41
Mar	-0,2	32
Apr	8,6	39
Mai	15,9	36
Jun	19,6	58
Jul	22,7	49
Aug	21,8	37
Sep	15,8	32
Okt	9,3	44
Nov	2	40
Dez	-3,5	37

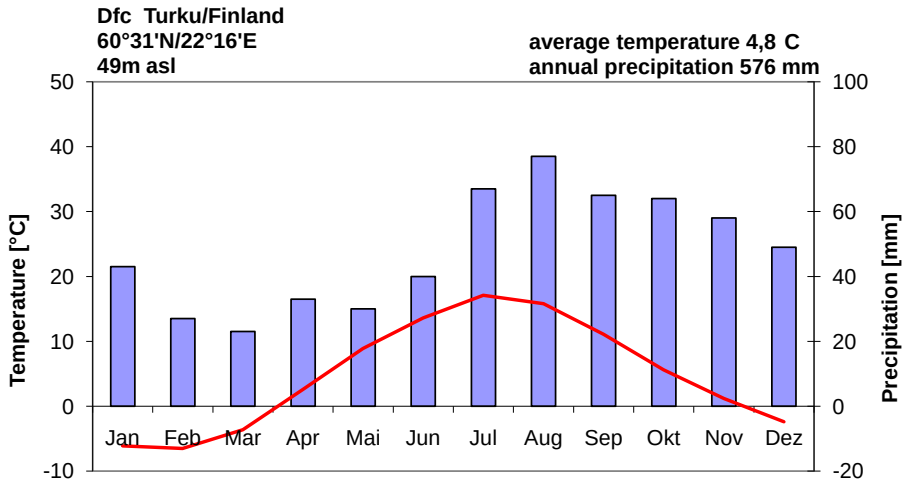

	[° C]	[mm]
Jan	-6,1	43
Feb	-6,5	27
Mar	-3,6	23
Apr	2,6	33
Mai	8,9	30
Jun	13,6	40
Jul	17,1	67
Aug	15,8	77
Sep	11,1	65
Okt	5,6	64
Nov	1,2	58
Dez	-2,4	49

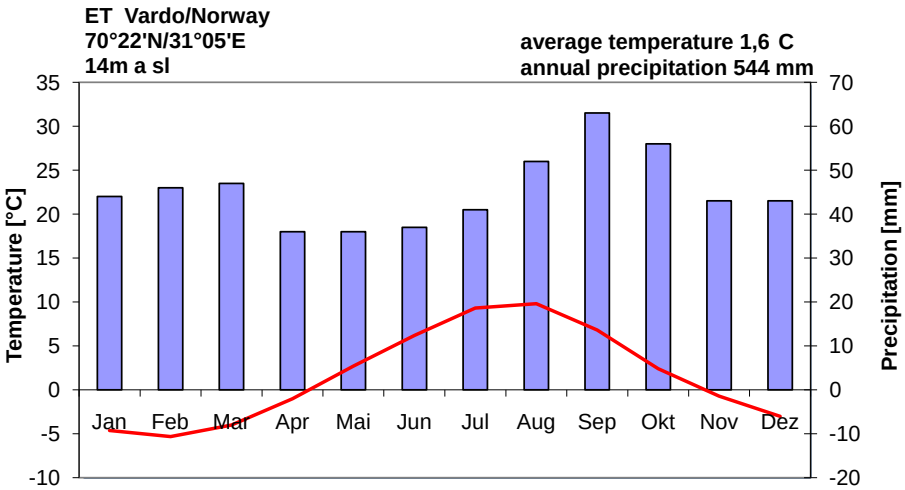

	[° C]	[mm]
Jan	-4,6	44
Feb	-5,3	46
Mar	-4	47
Apr	-1	36
Mai	2,7	36
Jun	6,2	37
Jul	9,3	41
Aug	9,8	52
Sep	6,8	63
Okt	2,4	56
Nov	-0,7	43
Dez	-3	43

Fig. 92 Climate charts for the analogue stations (continued)

8.2.3 Radionuclides

The starting point of the calculation is a reference contamination of the groundwater. The radionuclides considered are summarised in Tab. 20. Some of these radionuclides have radioactive daughters, which are taken into account for the calculations. This list includes the radionuclides that are most important in performance assessments of nuclear waste repositories (e.g. /SAN 05/). Among the actinides, only one representative isotope from each element is considered.

Tab. 20 Radionuclides considered in the calculations

Radionuclide			
C-14	Cl-36	Ni-59	Se-79
Zr-93	Nb-94	Tc-99	Pd-107
Sn-126	I-129	Cs-135	Ra-226
Th-230	Pa-231	U-238	Np-237
Pu-239	Am-234		

8.2.4 Geosphere-biosphere interfaces and climate states

After transport through the overlying rock into near-surface aquifers as described in Chapter 0 radionuclides might enter the biosphere via two principal geosphere-biosphere interfaces (GBIs) (see Fig. 93):

Contaminated groundwater might be withdrawn from a well. It enters the biosphere due the use of well water for drinking and agricultural purposes. In case of high water tables, groundwater may enter the biosphere directly and cause contaminations of soils.

After entering the biosphere, radionuclides may cause radiation exposures to humans. In this chapter the impacts of changing climate and environmental conditions on the transfer of radionuclides through the biosphere for both GBIs are estimated. The possible geosphere-biosphere interfaces for each climate state are given in Tab. 21. The withdrawal of groundwater is likely for all climates. In hot climates, the contamination of surface soils by rising groundwater may in principle be possible, but it is not very likely due to the pronounced aridity. Therefore, the GBI “rising groundwater” is not taken into account for the steppe and the Mediterranean climate.

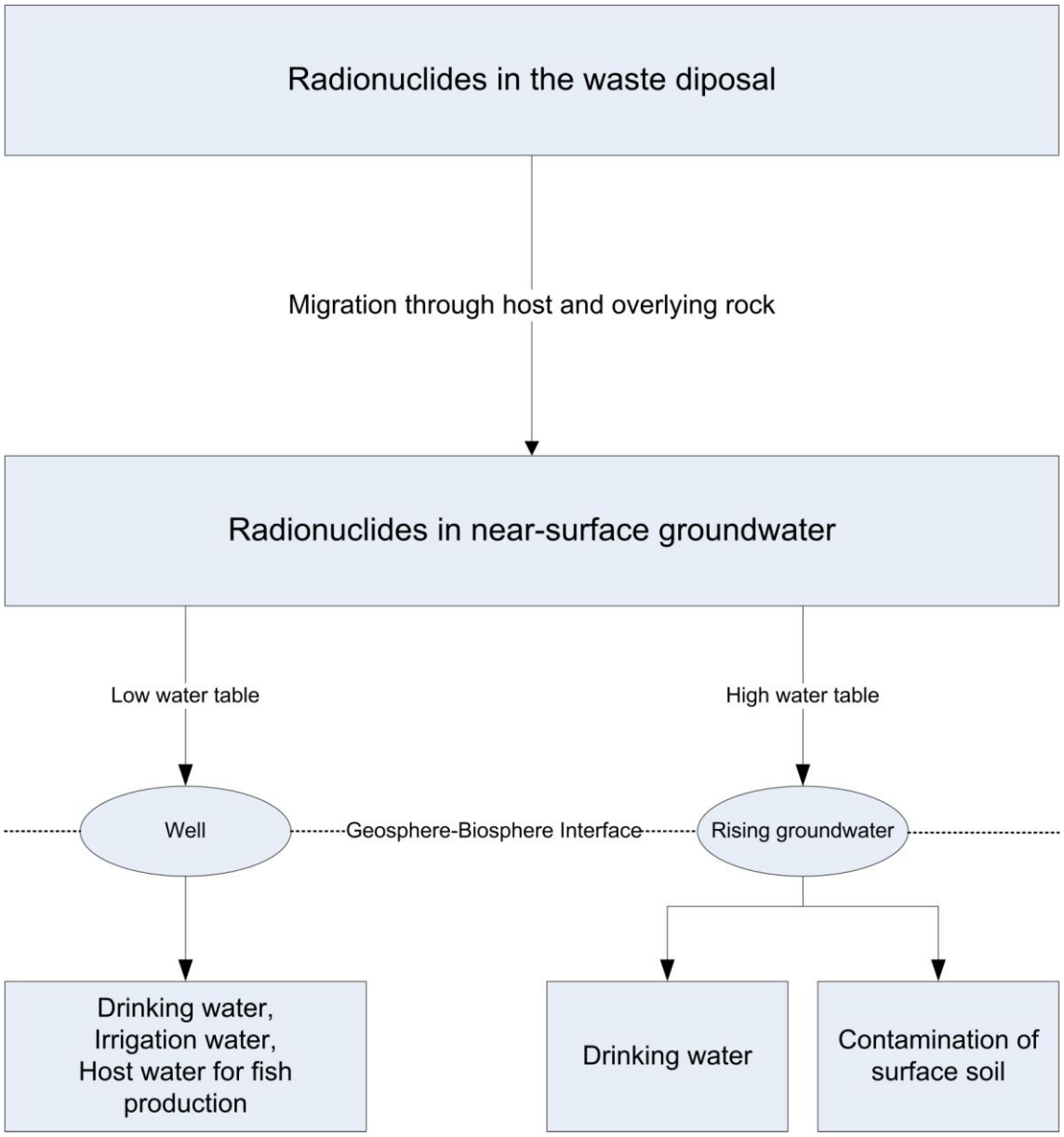

Fig. 93 Principal geosphere-biosphere interfaces for radionuclides entering biosphere

Tab. 21 Climates, analogue stations and GBIs considered

Climate	Climate zone	Analogue climate station	GBI	
			Well	Rising groundwater
Current conditions	Cfb: Temperate	Magdeburg (Germany)	X	X
Hot/dry summers, mild/humid winters	Csa: Mediterran	Rome (Italy)	X	-
Hot summers, warm winters	BS: Steppe	Marrakesh	X	-
Hot summers cold winters	Dfa: Boreal	Rostow (Russia)	X	X
Cold winters, cool and short summers	Dfc: Boreal	Turku (Finland)	X	X
Very cold winter, cool/short summers	ET: Tundra	Vardo (Norway)	X	X

8.2.5 Exposure pathways and endpoint

In the calculations of the radiation exposure, a normalised activity concentration of 1 Bq m^{-3} for each of the radionuclides is assumed. The endpoints of the calculation are the effective dose of an adult reference person. The conceptual models for estimating exposures are shown in Fig. 94 (GBI “well”) and Fig. 95 (GBI “rising groundwater”).

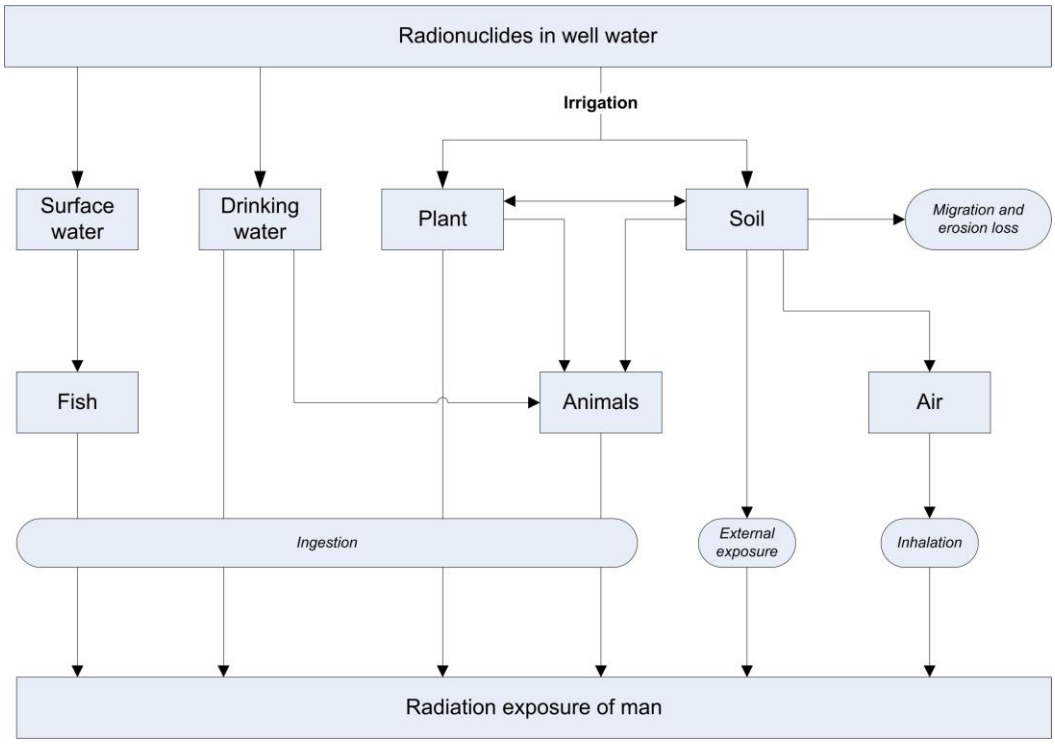

Fig. 94 Conceptual model for estimating the radiation exposure to man, if radionuclides enter the biosphere via well water

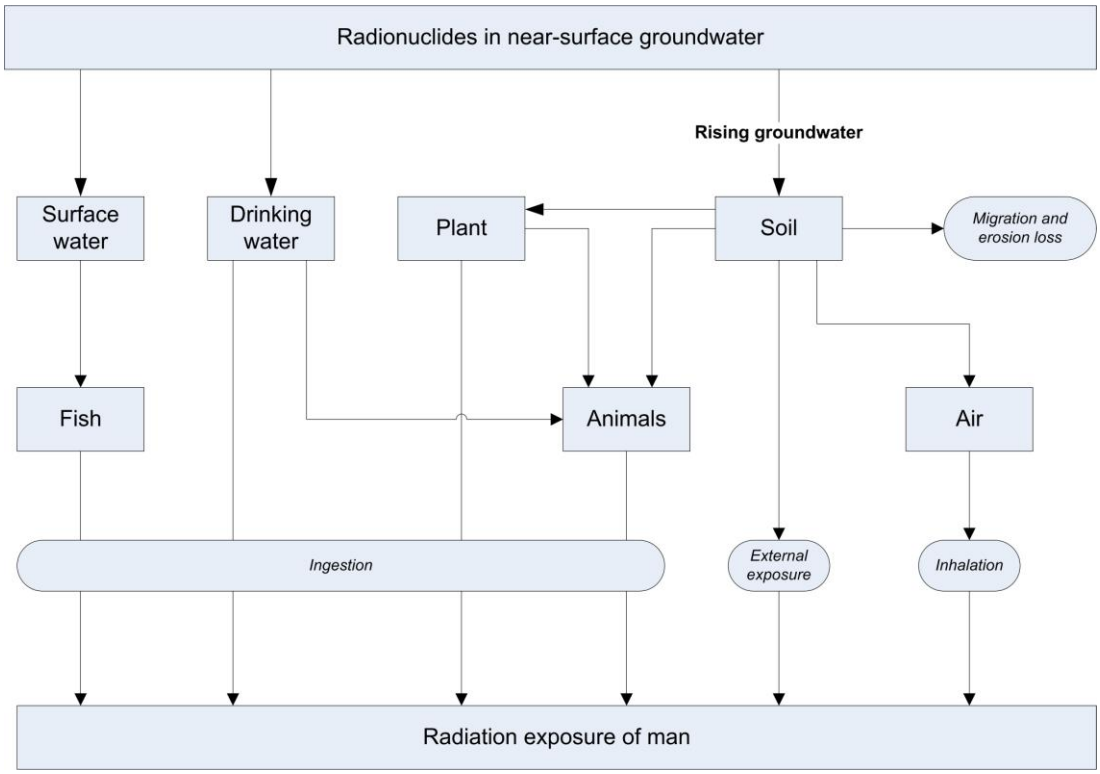

Fig. 95 Conceptual model for estimating the radiation exposure to man if radionuclides enter the biosphere via rising groundwater

For both geosphere-biosphere interfaces the following exposure pathways are considered:

- ingestion,
- inhalation of resuspended contaminated soil particles, and
- external exposure due occupation on contaminated land.

Further it is assumed that contaminated groundwater is used for various purposes:

- drinking water for humans,
- drinking water for cattle,
- irrigation of plants, and
- host water for fish production.

8.2.5.1 Transfer processes

The input of radionuclides to the biosphere via irrigation or rising of groundwater causes the contamination of food and feed stuffs. The contamination processes taken into account are summarised in Tab. 22. The relationships between the compartments involved in the contamination of plants are shown in Fig. 96 and Fig. 97 for both pathways.

Tab. 22 Contamination pathways considered

Contamination process	Geosphere-biosphere interface	
	Well	Rising groundwater
Transfer to plants		
Radionuclide uptake from soil	X	X
Contamination due to resuspension	X	X
Weathering	X	
Interception by plants during application of irrigation water	X	
Translocation (systemic transport within the plant subsequent to foliar deposition)	X	
Loss from soil		
Migration	X	X
Erosion	X	X
Transfer to animals		
Drinking water for cattle	X	X
Use of contaminated feed plants	X	X
Contamination of air by resuspension		
Accumulation of radionuclides in the resuspendable soil fraction	X	X
Transfer to freshwater fish		
Radionuclide uptake by fish	X	X
Attachment of radionuclides to particles and sedimentation	X	X

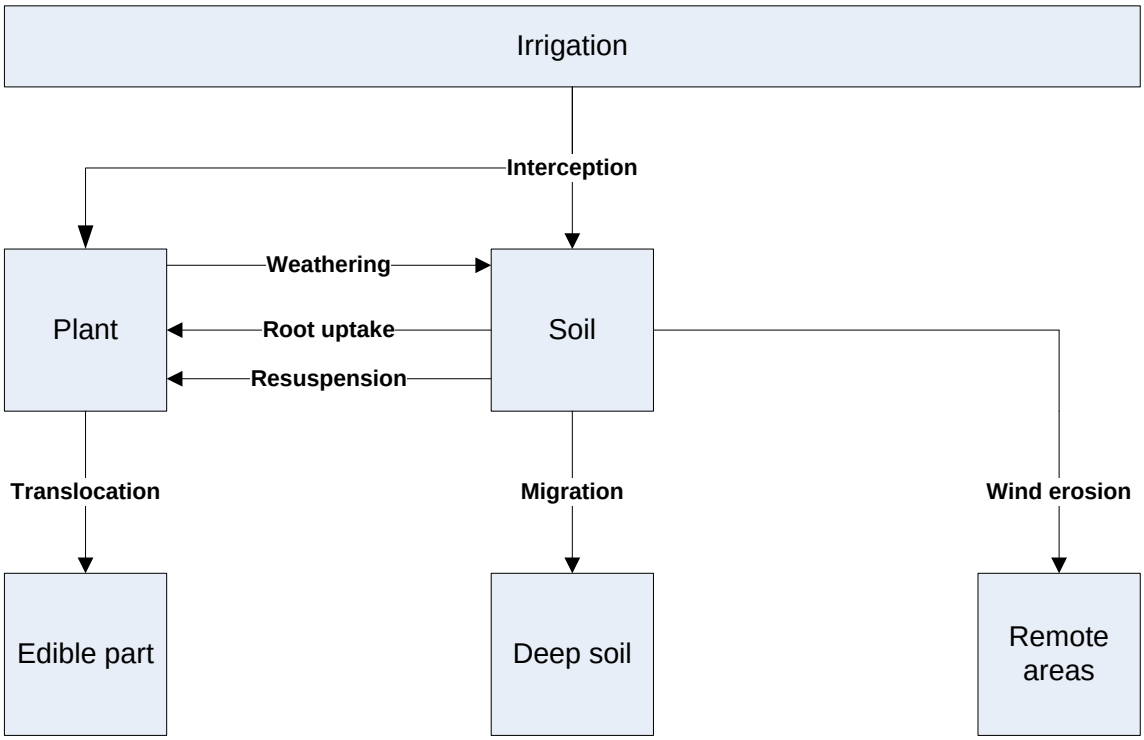

Fig. 96: Processes involved in the transfer of radionuclides to plants subsequent to irrigation with contaminated groundwater

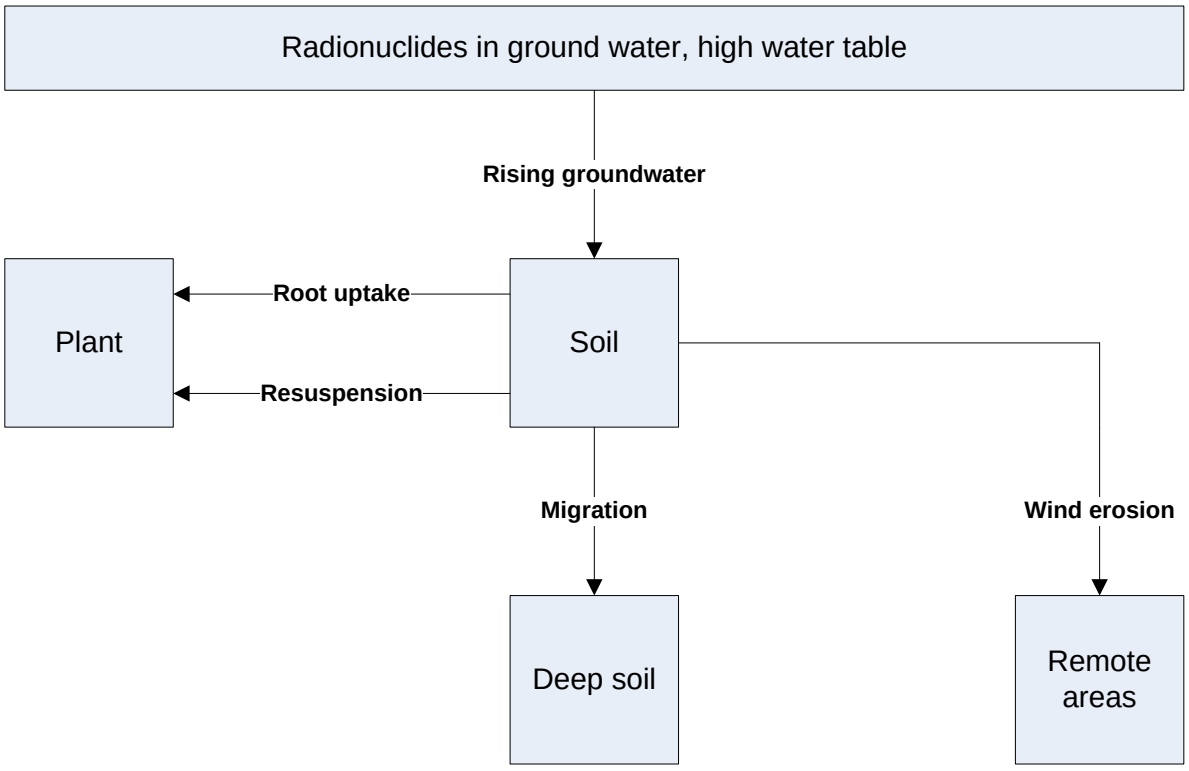

Fig. 97 Processes involved in the transfer of radionuclides to plants due to rising of contaminated groundwater

During irrigation of plants with contaminated water, a fraction of radionuclides is initially retained by the foliage; the rest passes through the canopy and contaminates the soil. Once deposited on the foliage, part of these radionuclides is lost from the plant to the soil by weathering. Furthermore, the systemic transport to the edible parts of plants is taken into account. Processes related to direct plant contamination are not relevant, if radionuclides enter the biosphere via rising groundwater. Radionuclides are lost from soil due to erosion and due to migration to deeper soil layers, where they are no longer available for root uptake.

8.2.5.2 Food and feed products considered

This study takes into account all crops and group of crops that are currently relevant in Europe like cereals, maize, potatoes, root vegetables, fruit vegetables, leafy vegetables and wild berries. All of the crops represent a group of plants rather than a distinct species. The classification follows similarities in modelling, whereas botanical criteria are not considered in this respect.

Cereals represent crops as wheat, barley, oats and rye. These species are very similar concerning morphology and growth. Wheat and barley predominate in Southern Europe, whereas rye and oats are more typical for Northern Europe because they are more adapted to cool summers and poor soils.

Maize represents a crop that is completely used as animal feed.

Potatoes and root vegetables represent crops with an edible plant part that grows below the soil surface. Besides potatoes, crops as carrots, beetroot, radish, celery are considered here.

Fruit vegetables*:* This group includes a wide range of crops with the commonality that all have an edible part growing aboveground as e.g. beans, peas, cucumbers, zucchini, capsicum, and tomatoes.

Leafy vegetables cover a wide range of plants that are used completely by humans as lettuce, field salad, green cabbage, endive, leaf beet and spinach.

Wild berries and mushrooms are considered for the tundra climate only. In this case, the radionuclides enter the biosphere via rising groundwater which might affect also natural land. Ingestion exposure might be due to consumption of wild berries and mushrooms.

Animal food products are an important part of the human diet. In this study, the consumption of beef, pork, lamb, chicken and freshwater fish is considered. For the tundra climate, the ingestion of reindeer meat is taken into account. The specific intake rates of these food items depend on environmental conditions of the site considered. Details are given in Chapter 8.3.2.1.

All food products that are considered to be used at the different climate states are summarised in Tab. 23. The spectrum of products is quite similar for temperate, Mediterranean and boreal climate. For tundra climate the relevance of natural food products as berries, mushrooms and reindeer is of increased importance. In the tundra climate, cereals are not cultivated due to climatic reasons.

Tab. 23 Plant and animal products considered for the different climates

Plant/Animal	Climate					
	Cfb: Temperate	BS: Steppe	Csa Mediterranean	Dfa: Boreal	Dfc: Boreal	ET: Tundra
Grass	X	X	X	X	X	X
Maize	X	X	X	X	-	-
Cereals	X	X	X	X	X	-
Potatoes & roots	X	X	X	X	X	X
Leafy veg.	X	X	X	X	X	-
Fruit veg.	X	X	X	X	X	-
Mushrooms	-	-	-	-	-	X
Berries	-	-	-	-	-	-
Milk	X	X	X	X	X	X
Beef	X	X	X	X	X	-
Pork	X	X	X	X	X	-
Reindeer	-	-	-	-	-	X
Lamb	-	X	X	-	-	-
Fish	X	-	-	X	X	X

8.2.5.3 Growing periods of crops

The growth of crops cultivated at a specific site is dependent on the specific soil and climate conditions. On the long-term, successful production of crops is only possible, if the plants' requirements for temperature, nutrient and water supply are met. For example, the temperature optimum for growth of potatoes is at about 20 °C. At temperatures above 30°C, the growth of tubers is considerably reduced and disrupted /GEI 83/. Nevertheless, potatoes are cultivated from North to South of Europe in quite different climatic zones. This is possible because the growth periods are adjusted accordingly. In Northern Europe, potatoes can be planted only in June due to late frosts and have to be harvested at the latest in early September due to early frosts. In Southern Europe the vegetation period is shifted to the early spring. In North Africa, cultivation of potatoes starts even in January /FRA 82/.

The growing periods of crops are controlled by the different climatic conditions. In general, for optimization of plant production, crop production needs to be adjusted to the climatic conditions. Therefore, the following assumptions are made:

- On the one hand in arid climates, in months with a daily mean of air temperature higher than 35 °C, no plant growth is assumed. It is not impossible to cultivate crops under those conditions, but the effort in terms of irrigation and cost is high and due to the high temperatures the yield is generally reduced. This is the case for the station Marrakesh during the months July, August and September.
- On the other hand plant growth is only assumed, if the average air temperature is above 5 °C. The mean monthly temperature of 5 °C is usually assumed as the start of the vegetation period /GEI 88/.
- In warm and dry climates, growth of crops is managed in a way that the soil water from the winter precipitation can be used and that high temperatures in summer are avoided as far as possible.
- In both, boreal and hot climates, the periods for optimal plant growth (good water supply, moderate temperatures, light conditions) are shorter than in temperate climates. Therefore, in hot climates varieties with short growth periods are preferred.

8.2.5.4 Irrigation

The climate data, the growth and irrigation periods of the crops for each climate state, and the requirements for irrigation are summarised in Tab. 24. In the following it is briefly described how the information is derived.

The irrigation requirements depend on both, the soil and the climatic conditions /ACH 80/. The water storage capacity of soils declines in the order clay > loam > sand. However, in clay soils, a relatively large fraction of water is bound very strongly in micro-pores. Such water is not available for plants, so the best conditions for water storage are provided by loam soils. Due to high permeability in sandy soils, their water storage capacity is lowest. Temperature, precipitation and relative humidity are the key climatic factors that determine the water deficit. With increasing temperature, the evapotranspiration increases: i.e. more water is lost by both, evaporation and transpiration of plants. The humidity depends on temperature and precipitation. In general, with increasing relative humidity the evapotranspiration and, subsequently, the water deficit decrease.

The irrigation requirements are determined according to an empirically derived approach developed by /ACH 80/ that is based on the mean monthly temperature, the mean monthly precipitation and the mean relative humidity in month *i*:

$$B_i = (2 + 0{,}2 \cdot T_i) \cdot T_i - 1{,}2 \cdot (F_i - 80) - P_i \qquad (1)$$

with

B_i irrigation requirement in months *I* (mm)

T_i mean monthly temperature in month *i* (°C)

F_i mean relative humidity in month *i* (%)

P_i mean monthly precipitation in month *i* (mm)

The climatic data are taken from /MUE 96/. The data usually cover the period from 1961 to 1990. Irrigation is assumed only, if the mean monthly temperature is above 5°C, which is usually considered as the start of the vegetation period (s. above). The resulting water deficit during the vegetation period, the annual precipitation and the temperature are shown in Tab. 24. It illustrates very well the relationship between water deficit and temperature and it underlines that the selected analogue station cover a wide range of climatic conditions. The monthly averages of air temperature, precipitation, relative humidity and resulting water

deficit are given in Fig. 98 to 10, respectively. The figures clearly indicate the relation between air temperature, humidity and water deficit.

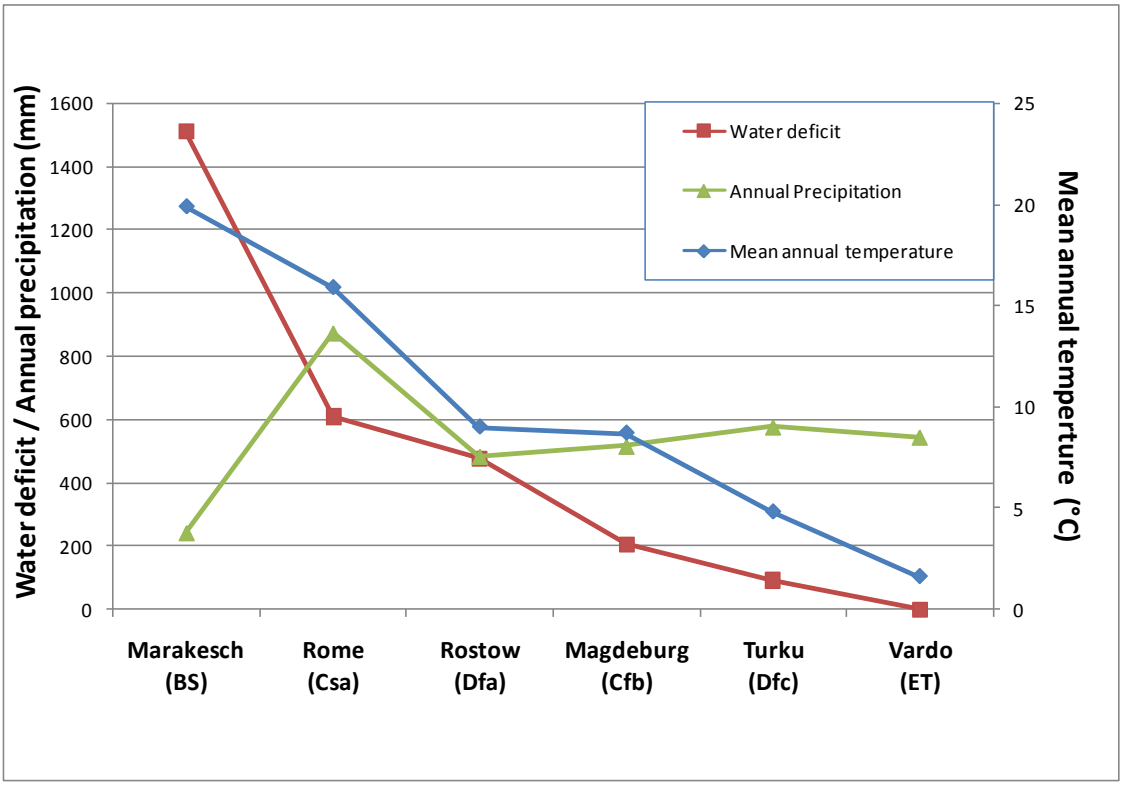

Fig. 98 Mean annual values for precipitation, temperature and water deficit for the analogue stations

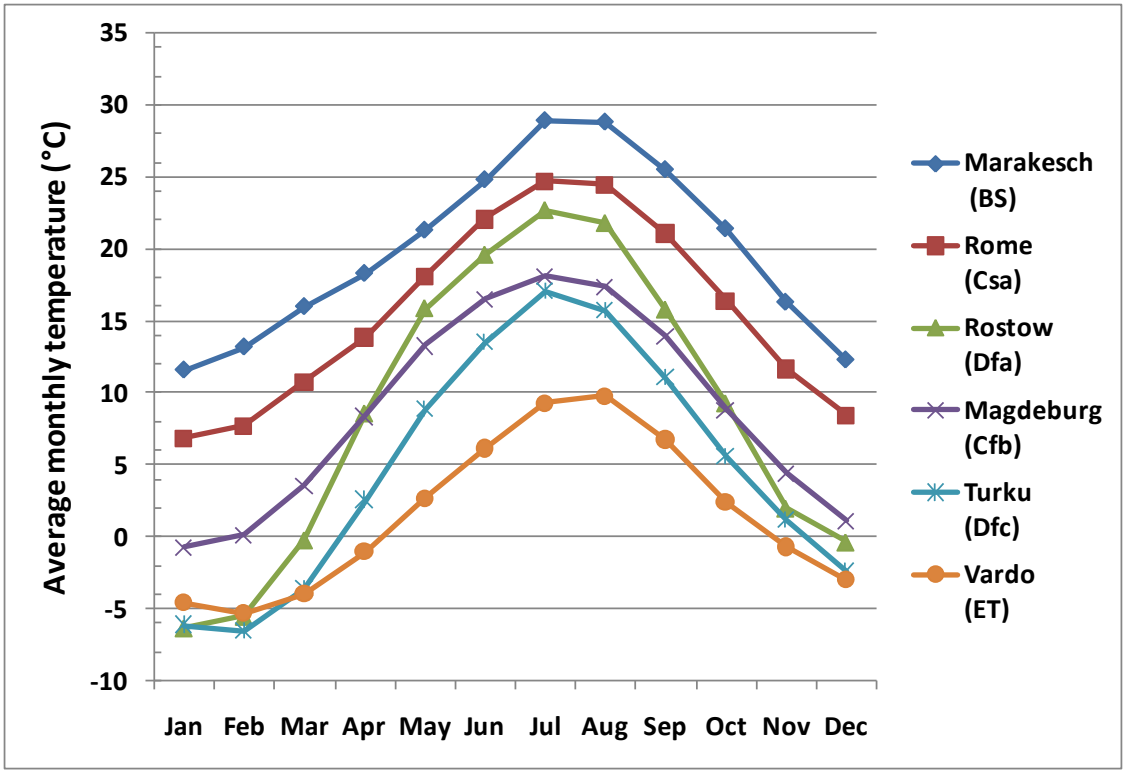

Fig. 99 Average monthly air temperature (°C) for the analogue stations

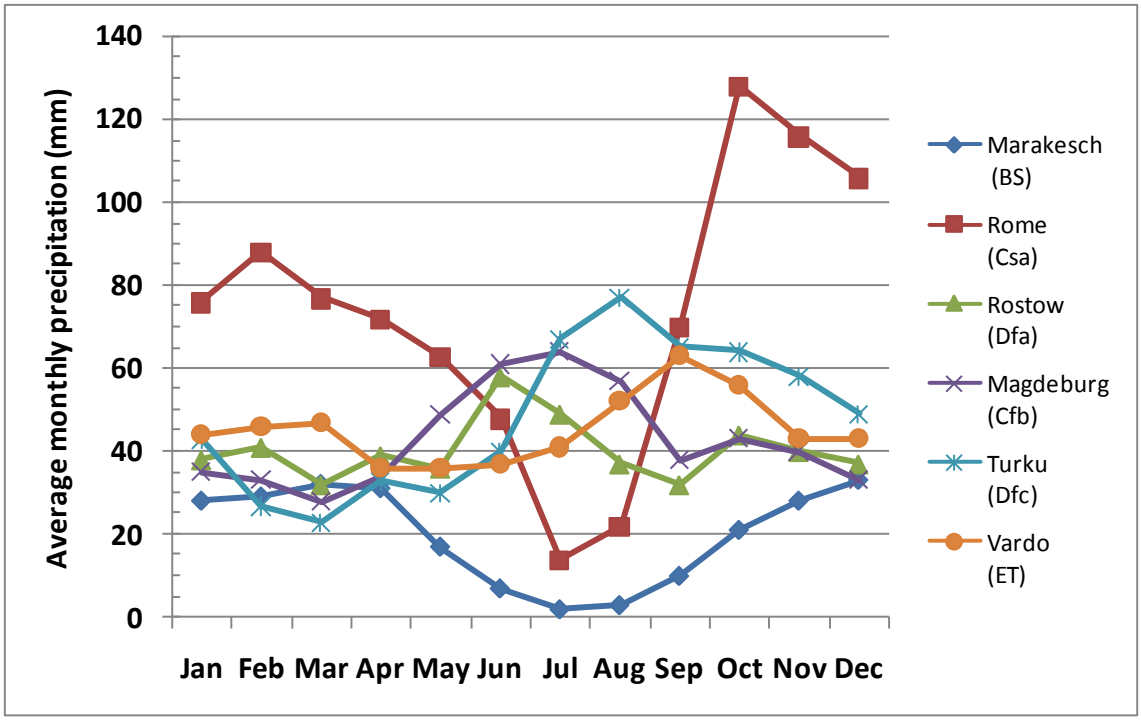

Fig. 100 Average monthly precipitation (mm) for the analogue stations

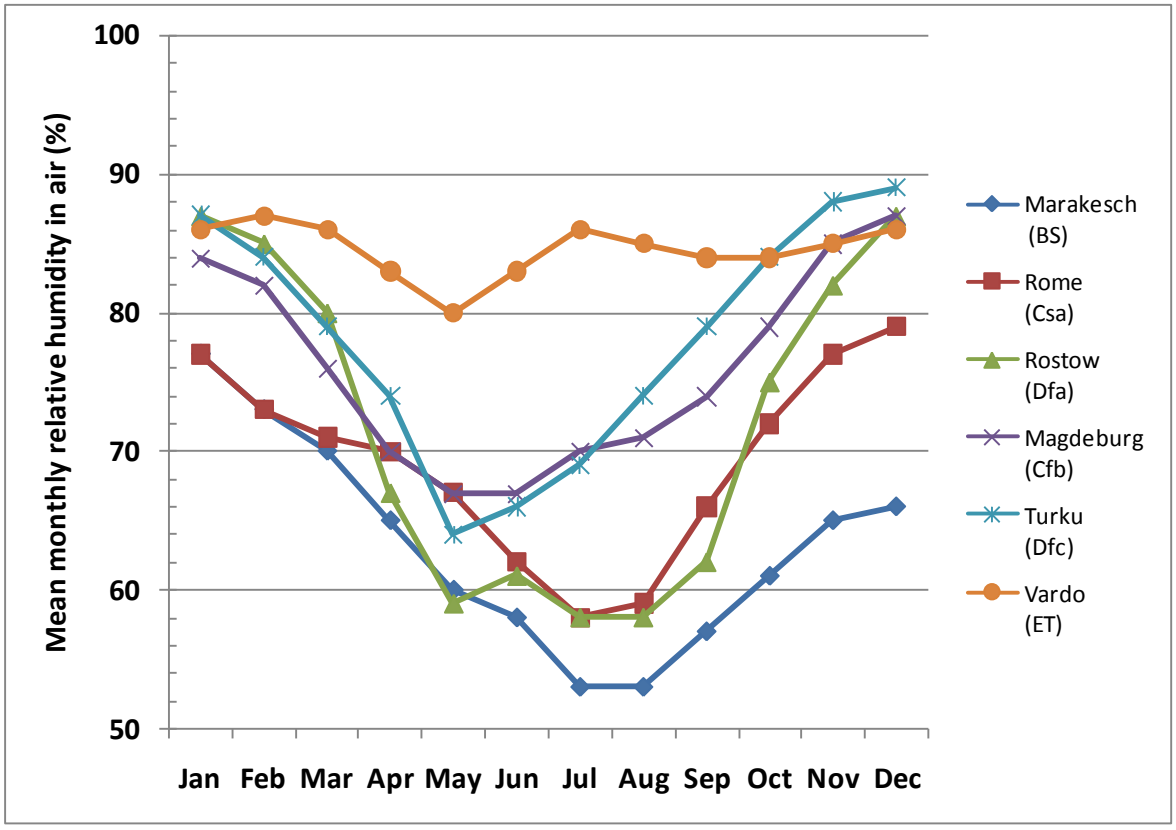

Fig. 101 Average monthly relative humidity (%) for the analogue stations

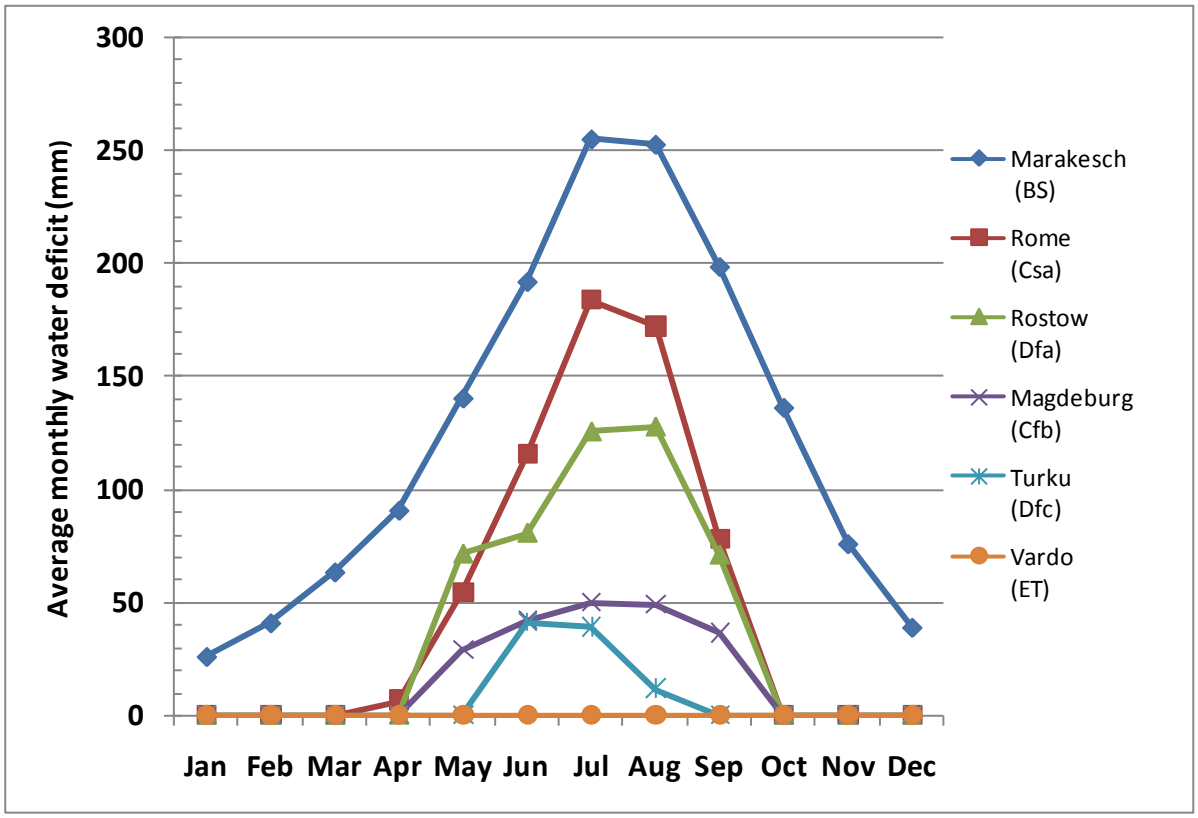

Fig. 102 Average monthly water deficit (mm) for the analogue stations

Tab. 24 Climatic conditions at the analogue stations and irrigation requirements (Marrakesh, Magdeburg)

Marrakesh, Morocco (BS)	Growth period	Month													Irrigation (mm)
		Jan	Feb	Mar	Apr	May	June	July	Aug	Sep	Oct	Nov	Dec	Year	
Climatic parameters															
Temperature (°C)		11.6	13.2	16	18.3	21.3	24.8	28.9	28.8	25.5	21.4	16.3	12.3	19.9	
Precipitation (mm)		28	29	32	31	17	7	2	3	10	21	28	33	241	
Humidity (%)		77	73	70	65	60	58	53	53	57	61	65	66	63	
Water deficit (mm)		26	41	63	91	140	192	255	253	199	136	76	39	1510	
Irrigation requirement		Months with irrigation													
Grass	Oct. - May	x	x	x	x	x					x	x	x		611
Maize	Feb. - June		x	x	x	x	x								527
Cereals	Feb. - June		x	x	x	x	x								527
Potatoes & root veg.	Jan. - May	x	x	x	x	x									360
Leafy vegetables	Feb. - June		x	x	x	x	x								527
Fruit & fruit veg.	Jan.- June	x	x	x	x	x	x								552
Magdeburg, (Cfb)		Jan	Feb	Mar	Apr	May	June	July	Aug	Sep	Oct	Nov	Dec	Year	
Climatic parameters															
Temperature (°C)		-0.7	0.1	3.6	8.4	13.3	16.5	18.1	17.4	14	8.8	4.4	1.1	8.7	
Precipitation (mm)		35	33	28	34	49	61	64	57	38	43	40	33	515	
Humidity (%)		84	82	76	70	67	67	70	71	74	79	85	87		
Water deficit (mm)		0	0	0	0	29	42	50	49	36	0	0	0	206	
Irrigation requirement		Months with irrigation													
Grass	April – Oct.					x	x	x	x	x					206
Maize	May – Oct.					x	x	x	x	x					206
Cereals	April – Aug.					x	x	x	x						170
Potatoes & root veg.	May – Sept.					x	x	x	x	x					206
Leafy vegetables	April – Oct.					x	x	x	x	x					206
Fruit & fruit veg.	April – Oct.					x	x	x	x	x					206

Tab. 24 Climatic conditions at the analogue stations and irrigation requirements (Rome, Rostow) (continued)

Rome, Italy (Csa)	Growth period	Month												Irrigation (mm)
		Jan	Feb	Mar	Apr	May	June	July	Aug	Sep	Oct	Nov	Dec	Year	
Climatic parameters															
Temperature(°C)		6.9	7.7	10.8	13.9	18.1	22.1	24.7	24.5	21.1	16.4	11.7	8.5	15.9	
Precipitation (mm)		76	88	77	72	63	48	14	22	70	128	116	106	880	
Humidity (%)		77	73	71	70	67	62	58	59	66	72	77	79		
Water deficit (mm)		0	0	0	6	54	115	184	172	78	0	0	0	610	
Irrigation requirement		Months with irrigation													
Grass	March – Oct.				x	x	x	x	x	x					610
Maize	April – Sept.				x	x	x	x	x	x					610
Cereals	March - July				x	x	x	x							360
Potatoes & root veg.	March – Oct.				x	x	x	x	x	x					610
Leafy vegetables	March – Oct.				x	x	x	x	x	x					610
Fruit & fruit veg.	March – Oct.				x	x	x	x	x	x					610
Rostow, Russia (Dfa)		Jan	Feb	Mar	Apr	May	June	July	Aug	Sep	Oct	Nov	Dec	Year	
Climatic parameters															
Temperature (°C)		-6.3	-5.5	-0.2	8.6	15.9	19.6	22.7	21.8	15.8	9.3	2	-0.35	9	
Precipitation (mm)		38	41	32	39	36	58	49	37	32	44	40	37	483	
Humidity (%)		87	85	80	67	59	61	58	58	62	75	82	87		
Water deficit (mm)		0	0	0	0	72	81	126	128	71	0	0	0	477	
Irrigation requirement		Months with irrigation													
Grass	April – Oct.					x	x	x	x	x					477
Maize	May- Sept.					x	x	x	x	x					477
Cereals	April – Aug.					x	x	x	x						406
Potatoes & root veg.	May – Sept.					x	x	x	x	x					477
Leafy vegetables	April – Oct.					x	x	x	x	x					477
Fruit & fruit veg.	April – Oct.					x	x	x	x	x					477

Tab. 24 Climatic conditions at the analogue stations and irrigation requirements (continued)

Turku, Finland, (Dfc)	Growth period	Months												Irrigation (mm)
		Jan	Feb	Mar	Apr	May	June	July	Aug	Sep	Oct	Nov	Dec	Year	
Climatic parameters															
Temperature (°C)		-6.1	-6.5	-3.6	2.6	8.9	13.6	17.1	15.8	11.1	5.6	1.2	-2.4	4.8	
Precipitation (mm)		43	27	23	33	30	40	67	77	65	64	58	49	576	
Humidity (%)		87	84	79	74	64	66	69	74	79	84	88	89		
Water deficit (mm)		0	0	0	0	0	41	39	12	0	0	0	0	92	
Irrigation requirement															
Grass	May – Sept.						x	x	x						92
Cereals	May – Aug.						x	x	x						92
Potatoes & root veg.	June – Aug.						x	x	x						92
Leafy vegetables	June – Aug.						x	x	x						92
Fruit & fruit veg.	June – Aug.						x	x	x						92
Vardo, Norway (ET)		Jan	Feb	Mar	Apr	May	June	July	Aug	Sep	Oct	Nov	Dec	Year	
Climatic parameters		Months with irrigation													
Temperature(°C)		-4.6	-5.3	-4	-1	2.7	6.2	9.3	9.8	6.8	2.4	-0.7	-3	1.6	
Precipitation (mm)		44	46	47	36	36	37	41	52	63	56	43	43	544	
Humidity (%)		86	87	86	83	80	83	86	85	84	84	85	86		
Water deficit (mm)		0	0	0	0	0	0	0	0	0	0	0	0	0	
Irrigation requirement		No irrigation													

8.3 Model approaches for exposure calculation

In this section, the model approaches are described that are applied to estimate exposures to humans, if the radionuclides enter the biosphere via the geopshere-biosphere interface “well” and “rising groundwater”. In the first part, the models and parameters are described to estimate the activities in plant and animal foodstuffs. In the second part, the approaches to calculate dose conversion factors for reference persons are described.

8.3.1 Activity in foods

The activity in plant food products is due to direct contamination of the foliage during irrigation and due to uptake of radionuclides from the soil.

Plant contamination by foliar uptake

Plant contamination due to foliar uptake is only relevant, if the contaminated groundwater is used as irrigation water; i.e., this contamination is not relevant, if the radionuclides enter the biosphere due to contamination of surface soil as a consequence of high groundwater table.

8.3.1.1.1 Interception

During the irrigation of plants, a certain fraction of radionuclides applied with the irrigation water is retained by the foliage of plants. This fraction is quantified by the interception factor f_w , which is calculated according to /MUE 93/, /HOF 95/, /PRO 96/:

$$f_{w,rj} = \frac{LAI_j \cdot k_{rj} \cdot S_j}{R} \cdot \left[1 - \exp\left(-\frac{\ln(2)}{3 \cdot k_{rj} \cdot S_j} \cdot R\right) \right] \qquad (2)$$

with

$f_{w,rj}$ interception factor for nuclide *r* and plant *j* [-]

LAI_j leaf area index for plant *j* at time of application (m² leaf area per m² soil area)

S_j water storage capacity of the foliage for plant *j* (mm)

k_{rj} retention factor for nuclide *r* and plant *j* [-]

R amount of irrigation for plant *j* (mm)

The expression above is valid for a wide range of irrigation amounts. The exponential term describes accounts for the built-up of a water film on plant leaves with increasing amount of irrigation. In the case of relatively high irrigation amounts, this term approaches 1 and can be neglected. For low amounts of rainfall and fully developed plant canopies it may occur that f_w yields values higher than 1.0. In this case the value is set to 1.0.

The most important factors for the estimation of the interception factor are the parameters S, LAI and k. According to the review in /PRO 08/, measured values for S for grass, cereals and maize are in the range of 0.1 to 0.3 with a mean of about 0.2. For all other plants (potatoes, root, fruit and leafy vegetables a value of 0.3 is assumed for S /MUE 93/.

The leaf area index LAI is defined as the ratio of leaf area (single-sided) and soil area; i.e, it quantifies the size of the interface plant-irrigation water. It represents the surface of plants which is able to retain irrigation water. The leaf area varies considerably throughout the growing period. From planting or sprouting the leaf area increases rapidly until flowering. During the maturing phase the leaf area decreases again.

Data for LAI are summarised as function of time after start of growth for present day conditions in Tab. 25, /MUE 93/. The values vary from year-to-year due to weather variations and to agricultural practices as fertilization, choice of varieties and the time of seeding. In the model, average values for LAI for the irrigation period are used. The irrigation water is applied in specific periods that depend on crop and climate. During these periods, the applications are evenly distributed, which justifies the use of an average value.

The element dependent retention factor k describes the ability of an element to be fixed on the leaves. A value of $k < 1$ means that the fraction of the element intercepted by the foliage is lower than the intercepted fraction of water in which this element is dissolved. A value of $k > 1$ means that the interception fraction of the element is higher than the interception of water. The retention factor k is controlled by the chemical form. Usually anions have k-values below 1; cations above 1 /ANG 80/, /HOF 95/. The lower values for anions are presumed to be due to the predominantly negative charge of the leaf surfaces /SCH 77/, /ERT 92/.

For the radionuclides in anionic form (I, Cl, Se, Tc), a value for $k = 0.5$ seems to be appropriate /PRO 90/. According to /HOF 95/, for all cations with more than one positive valency (Ni, Mo, Zr, Nb, Pd, Sn, Sm, Pb, Po, Ra, Ac, Pa, Th, U, and the transuranics) a value of $k = 2.0$ is selected. Little information is available about monovalent cations such as cesium and rubidium. The observations of /PRO 90/, /PRO 96/ suggest a k-value of 1.0. For the

calculation of the interception, it has been assumed that per irrigation event 20 mm of water are applied. The resulting interception factors are summarised in Tab. 26.

Tab. 25 **L**eaf area indices (LAI) for present day conditions as function of time and value chosen for the model

Plant	Time after start of growth [d]				
	LAI				Model value
Grass	0	60	230	231	
	0,3	5,5	5,5	0,3	5
Cereals	0	66	112	113	
	0	6	1	0	5
Potatoes	0	42	73	118	
	0	4	4	0	4
Fruit vegetables	0	77	169	200	
	0	5	5	0	5
Leafy vegetables	0	30	213	214	
	0	5	5	0	5

Tab. 26 Interception factors fw,rj calculated by equation (X)

Interception factor	Cl, Se, Tc, I	Cs	Ni, Zr, Nb, Pd,Sn, Ra, Th, Pa, U, Np, Am, Pu
Grass	0,025	0,05	0,1
Maize	0,025	0,05	0,1
Cereals	0,025	0,05	0,1
Potatoes & roots	0,03	0,06	0,12
Leafy vegetables	0,038	0,075	0,15
Fruit vegetables	0,038	0,075	0,15

8.3.1.1.2 Weathering and translocation

For estimating the contamination of plant products subsequent to radionuclide deposition on the foliage, two kinds of plants have to be distinguished with regard to their usage as food:

- plants that are used completely as grass, maize silage, and leafy vegetables,
- other crops, (e.g. cereals or potatoes) , where only a specific part can be used.

For the first group, the contamination at time of harvest is given by the initial contamination at the time of deposition, by loss of activity by weathering (by rain and wind) and by growth dilution during the time between deposition and harvest:

$$C_{rj}(\Delta T) = \frac{C_{wr} \cdot f_{w,rj} \cdot I_j}{E_j} \cdot \exp[-(\lambda_w + \lambda_r) \cdot \Delta T] \quad (3)$$

with

$C_{rj}(\Delta T)$ concentration of activity of nuclide *r* in plant type *j* at harvest (Bq kg^{-1})

C_{wr} activity of nuclide *r* in irrigation water (Bq m^{-3})

$f_{w,rj}$ interception factor for nuclide *r* and plant *j*

E_j yield of plant type *j* at time of harvest (kg m^{-2} fresh weight)

I_j irrigation water applied during an irrigation event to plant j (m³ m^{-2})

λ_w weathering rate (d^{-1})

λ_r radioactive decay constant (d^{-1}) of nuclide *r*

ΔT time between application of irrigation water and harvest (d)

For the weathering rate, a value equivalent to a half-life of 14 d is applied as suggested by the review in /IAE 96/. For plants that are used partly only, the systemic transport from leaves to edible organs (translocation) subsequent to foliar contamination is a key process. It is quantified by the translocation factor, which is defined as the fraction of the activity initially retained by the foliage of the plant and the activity transferred to the edible parts of the plants until harvest:

$$T_{r,j} = \frac{A_{rj}}{C_{rj}} \quad (4)$$

with

T_{rj} translocation factor for nuclide *r* and plant *j*

A_{rj} activity of nuclide *r* on plant *j* initially after irrigation (Bq m^{-2})

C_{rj} concentration of activity of nuclide *r* in plant type *j* at harvest (Bq kg^{-1})

The translocation factor is dependent on the plant type and the time span ΔT from deposition to harvest. In Tab. 27, the elements considered are classified according to their mobility within the plant. This classification is based on several studies /AAR 69/, /AAR 71/, /AAR 72/, /AAR 75/, /VOI 91/. However, no details on the mobility of nickel, palladium, tin and niobium

could be found in the literature. By default, these elements are considered to be mobile, which is a conservative assumption.

The most reliable data for the translocation are available for the mobile element cesium and the immobile element strontium. Therefore, as long as no other quantitative data are available, the translocation data for cesium are considered to be representative for mobile elements. However, the translocation of cesium appears to be relatively high among the mobile elements /LEC 08/. The strontium data are assumed to be typical for the translocation of immobile elements.

Tab. 27 Classification of elements concerning their mobility in plants

Mobile elements	Immobile elements
Nickel	Zirconium
Selenium	Samarium
Rubidium	Lead
Molybdenum	Polonium
Niobium	Radium
Technetium	Actinium
Palladium	Thorium
Tin	Protactinium
Iodine	Uranium
Cesium	Transuranics

The contamination of the edible plant parts at time of harvest is given by:

$$C_{rj}(\Delta T) = \frac{C_{wr} \cdot f_{w,rj} \cdot I_j}{E_j} \cdot T_{rj} \cdot \exp(-\lambda_r \cdot t) \qquad (5)$$

with

$C_{rj}(t)$ concentration of activity of radionuclide *r* in the edible part of plant type *j* resulting from foliar deposition and translocation (Bq kg^{-1})

E_j yield of edible part of plant type *j* (kg m^{-2})

$Tr_j(t)$ translocation factor for nuclide *r* and plant type *j* [-]

t time between deposition and harvest (d)

The translocation of radionuclides also depends on the growth state of the plant. For mobile elements, the maximum can be observed during flowering and begin of the development of

fruit, tubers or grain. However, in this model, the time-dependence of the translocation is not taken into account, since the irrigation occurs more or less uniformly through the whole irrigation period and averaged values can be used. For immobile elements, translocation is very low; it is superimposed by the deposition directly on the edible parts which also causes a contamination of the edible parts. Otherwise, edible plant parts that grow in soil (e.g. potato tubers), are not contaminated by immobile radionuclide that are deposited on the foliage. The translocation factors applied in this study (Tab. 28) are derived from /MUE 93/ as an average over the irrigation period.

Tab. 28 Translocation factors averaged over the irrigation period

Translocation factor	Mobile elements Cl, Ni, Se, Tc, Pd, Sn, I, Cs	Immobile elements Zr, Nb, Ra, Th, Pa, U, Np, Am, Pu
Cereals	0,09	0,005
Potatoes & roots	0,1	0
Fruit vegetables	0,1	0,0033

8.3.1.2 Plant contamination by uptake from soil

The contamination of soil is caused by the application of contaminated irrigation water and by rising of contaminated groundwater. The activity in plants resulting from root uptake is calculated from the activity concentration in the soil, using the transfer factors TF_{rj} which is the ratio of the activity concentration in plants and of the average activity content in the upper 25 cm soil layer. The transfer factors are experimentally derived.

The transfer factor includes all factors influencing the root uptake such as soil type, pH-value, status of the supply with nutrients and sorption capacity of the soil. Furthermore, the transfer factor is based on the total activity in the soil. The activity fractions in the soil being really available for root uptake are not explicitly considered. However, for many radionuclides, considerable fractions are are not accessible, because they are strongly bound to soil particles or precipitated as insoluble compounds. All these factors cause a large variability in activity concentration of plants growing on different soils but with the same activity concentration in the root zone.

Nevertheless, the transfer factors are widely used to quantify radionuclide uptake by crops from soil due to its simple determination and application. Therefore, nearly all information on root uptake is available in terms of transfer factors.

An additional radionuclide uptake process is resuspension, i.e. a transfer of activity from soil to the lower parts of the plant. The plant contamination due to resuspension is estimated from the mass of the soil that is attached to the plant and an element-dependent enrichment factor.

The activity uptake by both processes is described with the equation

$$C_{p,rj} = (TF_{rj} + f_{e,r} \cdot R_j) \cdot C_{s,r} \quad (6)$$

with

$C_{p,rj}$ activity of radionuclide r in plant j resulting from root uptake (Bq kg^{-1} fresh mass)

TF_{rj} soil-plant transfer factor for radionuclide r and plant j

$f_{e,r}$ enrichment factor for radionuclide r

R_j mass load of soil for plant j (g soil per g plant)

$C_{s,r}$ activity of radionuclide r in the rooting zone of soil (Bq kg^{-1} dry mass).

The enrichment factor quantifies the enhancement of the activity concentration of resuspended soil compared to the mean activity concentration in soil. The enrichment is due to the fact that resuspension occurs especially with the fine-grained soil fractions as silt and clay, where radionuclides are preferentially bound to due to the high sorption capacity of these fractions. Therefore, the activity concentration in these soil fractions might be considerably increased compared to the mean soil contamination. The lower the clay and silt content, the higher is the enrichment of activity in the clay and silt fraction.

In general, the enrichment factor is greater than 1 for cationic radionuclides. The enrichment in resuspended soil depends on the specific soil conditions. As discussed above it increases with decreasing clay content. The enrichment factor is applied to the mean activity concentration in soil. According to investigations of /LIV 88/, the typical enrichment of cationic radionuclides in soil fractions that is most likely to be resuspended /GIL 74/ is about a factor of 3. This value is applied for Zr, Sn, Cs, Ra, Th, Pa, U, Np, and Pu. For the anionic elements (Cl, Se, Tc, I) the enrichment factor is assumed to be 1.

The transfer factors soil-plant are summarised in Table 10 for present day conditions. They were selected from /SAN 08/ assuming sandy soils as they are found in the Gorleben region.

The concentration of activity in soil is calculated from the annual activity applied with irrigation water. The activity is assumed to be mixed homogeneously within the upper soil

layer due to soil cultivation. Activity is lost due to physical decay and migration to deeper soil layers. The activity concentration of the mother nuclide after the irrigation period T is then:

$$C_{sr}(T) = \frac{A_r}{L \cdot \rho} \cdot \{1 - \exp[-(\lambda_{s,r} + \lambda_r) \cdot t]\} \quad (7)$$

with

A activity annually applied during irrigation (Bq m^{-2} a^{-1})

L depth of rooting zone (m) (arable land: 0.25 m, pasture 0.1 m)

ρ soil density (kg m^{-3} dry matter)

t time since deposition (d)

λ_r decay constant of radionuclide *r*

λ_s loss rate due to migration (a^{-1})

The half lives equivalent to the loss rates are estimated according to /PRO 05/ and are also listed in Tab. 29. They are based on experimental studies /BUN 92/, /BUN 94/, /BUN 95a/, /BUN 95b/ and they include both, migration of radionuclides in soluble form and fixed to small soil particles.

For dose estimations, the behaviour of long-lived radionuclides in soil is of particular importance, since the soil acts - once contaminated - as a potential long-term source for radionuclides in food and feed. In this study, the applied transfer factors were determined at different sites under present day conditions. However, these conditions will change in the far future, in particular under significantly different climate conditions. Therefore, potential changes in soil properties and their input on radionuclide behaviour is discussed in the following. Basically, the behaviour of radionuclides is nonetheless controlled by physical, biological and chemical constraints with universal and infinite validity /KOC 01/:

- The speciation of radionuclides in soil is mainly controlled by the interaction of redox potential, pH, content and composition of the organic matter and sorption to mineral soil constituents. E.g., for redox sensitive elements like Se, Tc, U, and Np the most mobile forms are found in more or less well aerated soils (E_h > 100 mV) and under moderate pH (5-8), that are typical for intensively managed farmland. Chlorine is very mobile and subject to intensive leaching and good bioavailability over a wide range of E_h/pH combinations.

Tab. 29 Transfer factors soil-plant and half-lives in the upper soil layer for present day conditions

Radionuclide	Transfer factors soil-plant $TFrj$ (Bq/kg fresh mass plant per Bq kg^{-1} dry mass soil)						Half-life in soil (a)	
	Grass	Maize	Cereals	Potatoes & roots	Leafy veget.	Fruit veget.	Arable land (25 cm)	Pasture (10 cm)
Cl-36	2	2	2	2	2	2	1	0.5
Ni-59	0.01	0.05	0.05	$5\cdot10^{-3}$	$5\cdot10^{-3}$	$5\cdot10^{-3}$	100	40
Se-79	0.05	0.02	0.02	$3\cdot10^{-3}$	$3\cdot10^{-3}$	$3\cdot10^{-3}$	50	20
Zr-93	$2\cdot10^{-3}$	$5\cdot10^{-4}$	$1\cdot10^{-3}$	$1\cdot10^{-4}$	$4\cdot10^{-4}$	$4\cdot10^{-4}$	100	40
Nb-94	$4\cdot10^{-3}$	$4\cdot10^{-3}$	$4\cdot10^{-3}$	$1\cdot10^{-3}$	$2\cdot10^{-3}$	$5\cdot10^{-4}$	100	40
Tc-99	1	0.1	0.1	0.1	1	0.3	5	2
Pd-107	0.03	0.03	0.03	$5\cdot10^{-3}$	0.02	$5\cdot10^{-3}$	100	40
Sn-126	$5\cdot10^{-3}$	$5\cdot10^{-3}$	$5\cdot10^{-3}$	$1\cdot10^{-3}$	$3\cdot10^{-3}$	$1\cdot10^{-3}$	100	40
I-129	0.1	0.01	0.01	0.01	0.01	0.01	100	40
Cs-135	0.05	0.02	0.02	0.05	0.05	0.02	100	40
Ra-226	0.02	$1\cdot10^{-3}$	1E-3	0.01	0.01	0.01	100	40
Th-230	0.01	$5\cdot10^{-4}$	$2\cdot10^{-3}$	$2\cdot10^{-4}$	$1\cdot10^{-4}$	$2\cdot10^{-4}$	200	80
Pa-231	$5\cdot10^{-4}$	$2\cdot10^{-4}$	$2\cdot10^{-4}$	$1\cdot10^{-4}$	$3\cdot10^{-4}$	$1\cdot10^{-4}$	200	80
U-238	$2\cdot10^{-3}$	$2\cdot10^{-3}$	$2\cdot10^{-3}$	$1\cdot10^{-3}$	$5\cdot10^{-3}$	$1\cdot10^{-3}$	200	80
Np-237	0.01	$3\cdot10^{-3}$	$3\cdot10^{-3}$	$2\cdot10^{-3}$	$2\cdot10^{-3}$	$2\cdot10^{-3}$	100	40
Am-243	$2\cdot10^{-4}$	$2\cdot10^{-5}$	$2\cdot10^{-5}$	$1\cdot10^{-4}$	$1\cdot10^{-4}$	$1\cdot10^{-4}$	200	80
Pu-239	$1\cdot10^{-4}$	$1\cdot10^{-5}$	$1\cdot10^{-5}$	$1\cdot10^{-5}$	$1\cdot10^{-4}$	$1\cdot10^{-5}$	200	80

- Sustainable farming practices try to optimise and preserve optimal growth conditions. Depending on soil type and texture, the optimal plant growth is found for E_h-values between 100 and 600 mV, and for pH from 5,5 to 7,5. With the exception of iodine, these conditions coincide with those under which mobile forms are found.

- An important part of the exposure scenarios is the irrigation of crops with contaminated water. However, the irrigation of soils with a redox potential persistently lower than 100 mV is unlikely, since such soils are either water-logged or have severe structural problems /SCH 02/.

- The upper limit of the optimal redox potential is near the maximum that can be achieved under normal atmospheric conditions; this will also be a constraint for any future conditions.

Assuming agricultural practices, which aim at sustainable land use and optimal conditions for cultivation of crops, it is unlikely that radionuclides in future behave completely different than observed today on sites that are considered to be an appropriate analogue for future soil systems. Therefore, present day data are in principal appropriate to estimate root uptake also under sustainable future agricultural systems.

8.3.1.3 General interactions of climate and soil processes

However, the question is in how far the environmental conditions change and which consequences on the long-term radionuclide behaviour may be expected. Although it is impossible to predict the detailed changes at a given site, some trends can be identified.

The development of soil is driven by the interaction of the host material with climatic and anthropogenic factors. The host material from which soils are formed will not change, but on the long-term, climate and soil management may differ from present conditions, therefore the discussion will be limited to these factors. A lot has been speculated about future climatic changes and it is not intended to continue this debate here. The subject of interest in this context is, how different climatic conditions would be able to change soils characteristics and, consequently, would alter radionuclide turnover, irrespective of the probability with which such a change may occur.

The soils are affected by climate change, directly via changes of water balance and temperature, indirectly via changes of the growth conditions for plants and the activity of soil organisms, and due to modifications of soil management. The adaptation of soils as a response to changing environmental conditions need different time periods. Soil characteristics, such as redox potential, water content and temperature may change within days or weeks. Changes of the organic matter content and quality happen within decades to centuries, whereas changes in weathering and paedogenesis occur over longer time frames, say within millennia. Such time scales have to be taken into consideration regarding further climatically induced alteration of soils.

To account for possible changes of soil characteristics for different climatic states, it has to be differentiated in particular between increasing and decreasing temperatures as well as arid and humid conditions. General trends have already been illustrated in chapter 2.2 and are compiled in

Tab. 30. These developments may be slightly modified by site-specific factors as specific annual course of temperature and precipitation, the soil type, the topography and the site-specific water balance and the soil use.

Tab. 30 Possible modifications in relation to present conditions at the reference site

Issue	Possible modification in relation to conditions at reference site	
Climate	Steppe BS), Mediterranean (Csa) Boreal (Dfa)	Boreal (Dfc), Tundra (ET)
Development of climate	Increased temperature and aridity	Decreased temperature, higher humidity
General development of soil	Lower decomposition of organic matter Increase of pH	Increasing content of organic matter, Decrease of pH
Migration in soil	Reduced water leaching due to low precipitation and high evaporation	Increased leaching of water, precipitation comparable to present Gorleben site conditions, but evaporation is lower
Specific behavior of radionuclides		
Selenium	More available Se-forms as selenate and selenite predominate	Lower root uptake due to predominance of less available Se-forms as selenide and elemental Se
Iodine	No clear trend	Higher uptake on water–logged soils due to existence of iodide
Uranium	Tends to form mobile uranyl complexes	U(IV) in wet soils, strongly bound to organic matter and precipitates
Neptunium	Trend to mobile Np(V) forms	Trend to form less available Np(IV) in wet soils, complexation by inorganic and organic ligands
Technetium	Trend to mobile and available pertechnetate	Trend to less available forms under reductive conditions
Radium	No clear trend	Strongly bound to organic matter

Increase of temperature

Under humid conditions, increasing temperatures lead to an acceleration of all soil processes. The soil formation driven by weathering of soil minerals, leaching of weathering products and the decrease of soil pH-value are faster at a high temperature and at humid conditions. The higher turnover of organic matter could lead to a mobilisation of radionuclides incorporated in the humus fraction and to an increased biological availability. Due to the potentially higher leaching, the migration to deeper soil layers may be enhanced as well.

Under dryer arid conditions with increased temperatures decomposition of organic matter is reduced and weathering slower compared to present day conditions. In general, the mobilisation of radionuclides sorbed to organic and mineral soil components should decrease. Aridity is associated with a predominantly upward movement of soil water caused

by the high evapotranspiration, which causes an accumulation of cations and anions in the upper soil layer. Due to the increase of salinity, the pH potentially rises. The decrease of infiltration reduces migration of radionuclides into deeper soil layers. In general, the radionuclide turnover in soil is reduced.

Decrease of temperature

In colder climate conditions with enhanced humidity, the degradation of organic matter is inhibited and the sorption and incorporation of radionuclides to the organic soil fraction potentially increases. On the other hand, the pH value tends to decrease due to the leaching of alkaline cations. With increasing soil acidity, the formation of low molecular weight organic acids (e.g., fulvic acids) is promoted which act as complexing agents. This process could potentially increase mobility and so the loss to deeper soil layers. However, it depends on the site and which of these two processes is more important.

In cool and dry climates the soil productivity drops drastically and – compared to temperate climates - the possibilities for land-use are limited to an extensive management. In general, the soil processes, such as decomposition of organic matter, weathering of the parent material, and leaching are inhibited.

Soil erosion

Erosion processes cause a relocation of soil material due to wind and rain. In case of a contaminated area that is surrounded by uncontaminated or less contaminated land, erosion causes an enhanced activity loss for the contaminated land, since the activity losses from the contaminated land are not compensated by activity inputs from the outside. At the reference site in the Gorleben area, due to the flat terrain, erosion by water is not relevant. However, the sandy soils in this area are very vulnerable to wind erosion due to the soil texture and the relatively low precipitation.

According to /SCH 02/, about 3 t ha^{-1} a^{-1} may be lost due to wind erosion on sandy soils in Northern Germany. This corresponds for a 25 cm soil layer (density: 1.6 kg dm^{-3}) to an annual loss rate of 0.00085 a^{-1}; i.e. which is equivalent to a half-live of around 800 a. Thus, for temperate climates, activity losses due to wind erosion are less relevant. It should be noted that relevant soil losses due to wind erosion occur during very single events that may be very seldom; however, during those events large amounts of soil might be removed. It needs the coincidence of dried up sandy soils, a poor vegetation cover and high wind speeds to enable relevant wind erosion. For example on four sites in Northern Germany, soil losses from 16 – 170 t ha^{-1} a^{-1} were observed during one single day on sandy podsols /NEE 91/. For

all cultivated crop land in the United States, /KEG 94/ estimated mean soil losses due to wind erosion of 7.8 t ha^{-1} a^{-1} /LEE 96/.

For arid regions, soils are much more vulnerable to wind erosion, since usually during relatively long periods soils are dried up and have no or only a thin vegetation cover. /ZOB 00/ estimated wind erosion losses on irrigated land in Texas. Highest erosion rates were found for sandy soils, ranging from 38 – 570 t ha^{-1} a^{-1} depending on crop type. On clay and loamy soils, wind erosion is by more than a factor 10 less. In a semi-arid dry farming region in Texas with predominantly sandy and loamy soils, erosion rates were determined of about 50 t ha^{-1} a^{-1} /SCO 06/.

Consequence for transfer, erosion and migration

Higher mobility of radionuclides in soil may generally induce two processes: First, the potential root uptake of radionuclides increases. Second, the potential loss of radionuclides to deeper soil layers increases as well. These two processes compensate each other at least to some extent. From this point of view, it is unlikely that changing climatic conditions would impact the total transfer of radionuclides to plants in a way that the results would drastically enhance or decrease the integrated uptake of radionuclides by plants. An exception is cesium: On acid soils, low in potassium and clay and high in organic matter, the opposite observations are made. Under these conditions, high uptake by plants is observed although the migration to deeper soil layers is low. Cesium is prevented from leaching due to the incorporation in organic matter and micro-organisms.

A recently finished compilation of transfer factors soil-plant is given in /IAE 08/. It is a comprehensive summary of transfer factors on the base of about 9000 single data. The data in this compilation are categorised according to soil type and crop. The soil type is characterised by the soil texture; so, the transfer factors are given for sand, loam, clay and organic soils. However, the number of data varies considerably dependent on crop and radionuclide. Most data are available for grass and cereals, the radionuclides with most entries are cesium and strontium. Unfortunately, many of the radionuclides relevant for waste disposal are less well studied. In Fig. 103 the average transfer factors for different radionuclide and different soil types are plotted. For this comparison cereal data were used, because the most comprehensive data set was available for this crop. Despite the large underlying data set, there are still gaps; e.g., there are no data for uranium and thorium in organic soils or plutonium in sandy soils. The figure indicates that for cationic elements (U, Th, Cs, Am, Np, Pu) transfer factors in general decrease in the order sand > loam > clay. This is an expected result, since the cation exchange capacity increases in the same order.

The differences between the different soil types are in the order of a factor 2 - 5. For anionic radionuclides (Cl, Se, Tc, I), the soil texture is less important. Especially selenium, technetium and iodine are subject to a pronounced speciation that is controlled by redox potential and pH /KOC 01/ (see also above).

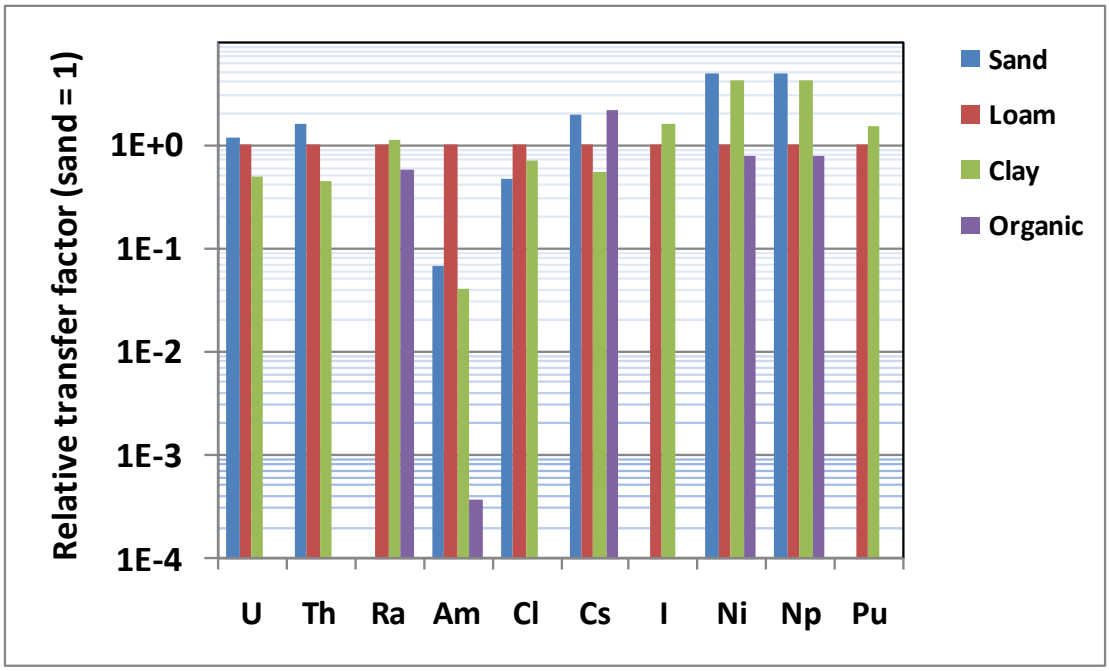

Fig. 103 Average transfer factors soil-plant for sand, loam, clay and organic soils

In Fig. 104 the K_d-values are plotted for the different soil types /VID 08/. The K_d-value increases with the strength of the sorption of a radionuclide to soil. It is not a direct measure of the bio-availability of a radionuclide; however, increasing K_d-values usually indicate decreasing root uptake and decreasing loss rates from the upper soil.

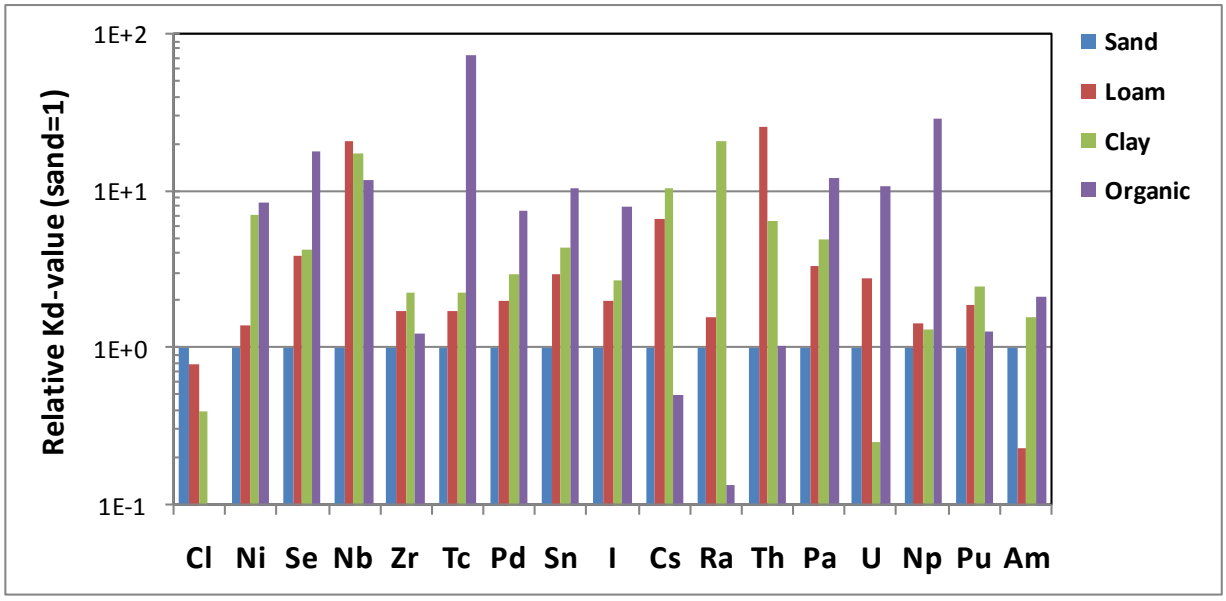

Fig. 104 Average Kd-values for sand, loam, clay and organic soils

The results are in general consistent with those drawn from the comparison of transfer factors: For cationic radionuclides, K_d-values – in general - increase in the order sand > loam > soil. In some cases, highest K_d-values are found for organic soils (Se, Tc, Np, Pd, Sn, I, Pa, Np, Am). However, the sorption strength of radionuclides to organic matter is lower than to inorganic soil constituents; i.e. a high K_d-value does not necessarily mean a low root uptake. The exchange between radionuclides pools that differ in bioavailability may be easier than in organic soils. As a result, the root uptake in organic soils may be high although the K_d-value is high. Furthermore, the fulvic and humic acids act as complexing agents that keep radionuclides in a relative mobile and available form, although the K_d-values may be relatively high.

In order to quantify the impact of climatic conditions, the transfer factors used in the models are modified according to Tab. 31. Parameters for erosion and migration are modified as shown in Tab. 32. The vulnerability of soil to wind erosion increases with aridity and dryness of a site. The modification factors for erosion are consistent with the wind erosion rates discussed above.

For the migration in soil, the water infiltration is the driving force; i.e. with increasing aridity, migration of radionuclides to deeper layers decreases. In continuously arid regions, there is no migration at all. However, with increasing aridity, there is a trend to salinisation of the upper soil: Due to the low humidity, there is an upwards movement of water, which evaporates at the surface and the salts originally dissolved remain at the surface. With the

application of irrigation water, this process may even be intensified, since there is an additional input of minerals with the irrigation water. In the Mediterranean climate, this problem is less severe, since there is sufficient precipitation during winter, which leads a relevant downward migration of water (and therewith enriched salts) in soil. In areas with pronounced aridity, excess irrigation water has to be applied during the cold season to enforce dissolution of salts and a downward movement of the water in order to prevent salinisation /BOG 81/. Therefore, to enable sustainable agriculture, leaching of radionuclides will occur in any case, but it will be less than under temperate climates. The reduction factors listed in Tab. 31 and Tab. 32 should be considered as a first rough estimate.

It should be noted that the loss processes - migration and erosion - compensate each other – at least to some extent. Under dry conditions, migration to deeper soil layers is in general less than under humid climates, but the radionuclide loss due to wind erosion is higher and vice versa. Mushrooms and berries are specific to the tundra climate. The transfer factors soil-plant applied are summarised in Tab. 33

Tab. 31 Modification factors (to be applied to transfer factor soil-plant for present day conditions) to estimate the root uptake of radionuclides for the other climates

Radionuclide	Modification factor			
	Well		Rising groundwater	
	Steppe(BS), Mediterranean (Csa) Boreal (Dfa)	Boreal (Dfc), Tundra (ET)	Temperate (Cfb) Boreal (Dfa)	Boreal (Dfc), Tundra (ET)
Cl-36	1	1	1	1
Ni-59	1	1	1	1
Se-79	10	1	1	0.3
Zr-93	0.5	1	1	1
Nb-94	0.5	1	1	1
Tc-99	10	0.1	1	0.1
Pd-107	0.5	1	1	1
Sn-126	0.5	1	1	1
I-129	0.5	1	10	10
Cs-135	0.5	50	0.5	50
Ra-226	0.5	0.5	1	0.5
Th-230	0.5	1	1	1
Pa-231	0.5	1	1	1
U-238	3	1	1	1
Np-237	5	1	1	1
Am-243	0.5	1	1	1
Pu-239	0.5	1	1	1

Tab. 32 Modification of further parameters for the other climates

Climate	Value
Erosion (a^{-1})	
Temperate (Cfb)	$5 \cdot 10^{-4}$
Mediterranean (Csa)	$2 \cdot 10^{-3}$
Steppe (BS)	$5 \cdot 10^{-3}$
Boreal (Dfa)	$2 \cdot 10^{-3}$
Boreal (Dfc)	$5 \cdot 10^{-4}$
Tundra (ET)	$5 \cdot 10^{-4}$
Migration (relative values)	
Temperate (Cfb)	1
Mediterranean (Csa)	0.5
Steppe (BS)	0.2
Boreal (Dfa)	0.5
Boreal (Dfc)	1
Tundra (ET)	1

Tab. 33 Transfer factors soil-plant for tundra climate

Radionuclide	Transfer factors soil-plant TF_{rj} (Bq kg^{-1} fresh mass plant per Bq kg^{-1} dry mass soil)	
	Mushrooms	Berries
Cl-36	2	2
Ni-59	$5 \cdot 10^{-3}$	$5 \cdot 10^{-3}$
Se-79	$3 \cdot 10^{-3}$	$3 \cdot 10^{-3}$
Zr-93	$4 \cdot 10^{-4}$	$4 \cdot 10^{-4}$
Nb-94	$2 \cdot 10^{-3}$	$5 \cdot 10^{-4}$
Tc-99	0.1	0.3
Pd-107	0.02	$5 \cdot 10^{-3}$
Sn-126	$3 \cdot 10^{-3}$	$1 \cdot 10^{-3}$
I-129	0.1	0.1
Cs-135	10	1.0
Ra-226	0.1	0.01
Th-230	0.01	$2 \cdot 10^{-4}$
Pa-231	$3 \cdot 10^{-4}$	$1 \cdot 10^{-4}$
U-238	0.05	$1 \cdot 10^{-3}$
Np-237	$2 \cdot 10^{-3}$	$2 \cdot 10^{-3}$
Am-243	$1 \cdot 10^{-4}$	$1 \cdot 10^{-4}$
Pu-239	0.01	$1 \cdot 10^{-5}$

Soil contamination due to rising groundwater

In case of a high groundwater table, irrigation of plants is usually not necessary. However, under those circumstances, soils may be contaminated due to rising groundwater. Since the contamination of surface soils is a long-term process, equilibrium conditions between the activity in soil and water are assumed. Then, the contamination of soil C_s can be estimated from the water contamination C_w and the distribution coefficient K_d. The contamination of plants results from the soil contamination and element-specific transfer factors soil-plant TF_{rj} (see above):

$$C_{p,r} = C_{w,r} \cdot K_{d,r} \cdot TF_{rj} \qquad (8)$$

During continuous humid conditions, radionuclides would accumulate in the upper soil horizon, since the rising water transports radionuclides to the soil surface. The water evaporates and the radionuclides remain. However, wet and water-logged soils are difficult to

use for agricultural purposes due to problems in mechanical soil cultivation. Such soils are often very wet, which impedes their cultivation. Therefore, on the long term, such soils can only be used, if due to the implementation of drainage, the soil is dewatered to avoid water logging with all its related problems. This also causes – at least temporarily – a downward movement of the soil water, which is a driving force for radionuclide leaching /VID 08/.

8.3.1.4 Transfer of radionuclides to animal products

The intake of radionuclides by animals with water, feed and soil causes a contamination of animal food products. The concentration of activity in meat and milk can be estimated from the intake of activity by animals, considering the kinetics of the radionuclides in the animals' metabolism. Subsequent to intake and resorption in the gut, radionuclides are distributed in the animals' body while part of it is excreted via urine and faeces. After a single intake, the time-dependence of the activities in the different organs is very pronounced. However, in case of a long-term contamination of groundwater as expected in a release scenario, radionuclides are taken up over a long period. Under those conditions it is justified to assume that steady state conditions of the activity are achieved in tissues and organs.

The intake rate of activity is calculated from the activity concentrations in the different foodstuffs and the feed consumption rates:

$$A_{drk} = C_w \cdot I_w + \sum_{m=1}^{M} C_{rm} \cdot I_{mk} \qquad (9)$$

with

A_{drk} activity intake rate of nuclide r by animal k (Bq d^{-1})

C_w activity concentration of nuclide r in water (Bq kg^{-1})

I_w water intake of animal k (l d^{-1})

C_{rm} activity concentration of activity of nuclide r in feedstuff m (Bq kg^{-1})

I_{mk} intake rate of feedstuff m by animal k (kg d^{-1})

For grass and forage, the soil intake of cattle is considered by the factor S_j. This parameter is defined as the amount of soil that is ingested by cattle per unit of grass or forage intake. Since during the soil ingestion of animals, no fractionation occurs as during the resuspension, it is assumed that the contamination of soil ingested is equal to the mean activity in the soil; therefore the enrichment factor is not applied. The resuspension and soil ingestion by cattle is formally used as the transfer factor for root uptake.

The feed and water intake of the animals is summarised in Tab. 34 /PRO 05/. The data represent typical values. However, feeding regimes of animals cover a wide range of possibilities and depend on the specific conditions at a site or farm.

Tab. 34 Feeding rations for calculating activities in animal food products

Animal	Feed	Climate					
		Temperate Cfb	Medit. Csa	Steppe BS	Boreal Dfa	Boreal Dfc	Tundra ET
Lactating cow	Grass	70	70	70	70	70	70
	Water	75	75	75	75	75	75
Beef	Grass	0	25	25	25	50	-
	Maize	25	10	10	10	0	-
	Cereals	0	0	0	0	1	-
	Water	40	40	40	40	40	-
Pork	Cereals	4	4	4	4	4	-
	Water	8	8	8	8	8	-
Lamb	Grass	5	5	5	5	5	-
	Water	4	4	4	4	4	-
Reindeer	Grass	-	-	-	-	-	70
	Water	-	-	-	-	-	40

The transfer to the animal products under equilibrium conditions is described by the transfer factor fodder-animal product TF_{ik}, which is defined as the ratio of concentration of activity in the animal product (Bq kg^{-1}) and the daily intake of activity by the animal (Bq d^{-1}) for equilibrium conditions. Then, the concentration of activity in milk, meat and eggs is given by:

$$C_{rk} = A_{drk} \cdot TF_{rk} \tag{10}$$

with

C_{rk} activity concentration of nuclide r in animal product k at equilibrium (Bq kg^{-1}, Bq l^{-1})

TF_{rk} transfer factor feed - animal product k for the radionuclide r (d l^{-1}, d kg^{-1})

As discussed above equilibrium conditions can be assumed which allows the application of transfer factors without consideration of the time-dependence of activities in animal food products. The transfer factors are summarised in /PRO 05/, /PRO 96,/ IAE 08/.

Tab. 35 Transfer factors feed-animal products

Radionuclide	Transfer factors feed (d l^{-1}, d kg^{-1})				
	Milk	Beef	Pork	Lamb	Reindeer
Cl-36	0.02	0.02	0.3	0.3	0.02
Ni-59	$1 \cdot 10^{-3}$	$5 \cdot 10^{-3}$	0.01	0.05	$5 \cdot 10^{-3}$
S·10-79	$1 \cdot 10^{-3}$	$5 \cdot 10^{-3}$	0.01	0.05	$5 \cdot 10^{-3}$
Zr-93	$1 \cdot 10^{-6}$	$1 \cdot 10^{-6}$	$5 \cdot 10^{-6}$	$1 \cdot 10^{-5}$	$1 \cdot 10^{-6}$
Nb-94	$1 \cdot 10^{-6}$	$1 \cdot 10^{-6}$	$3 \cdot 10^{-6}$	$1 \cdot 10^{-5}$	$1 \cdot 10^{-6}$
Tc-99	$1 \cdot 10^{-4}$	$5 \cdot 10^{-4}$	$1 \cdot 10^{-3}$	$5 \cdot 10^{-3}$	$5 \cdot 10^{-4}$
Pd-107	$1 \cdot 10^{-3}$	$1 \cdot 10^{-3}$	$3 \cdot 10^{-3}$	0.01	$1 \cdot 10^{-3}$
Sn-126	$5 \cdot 10^{-4}$	$1 \cdot 10^{-3}$	$3 \cdot 10^{-3}$	0.01	$1 \cdot 10^{-3}$
I-129	$5 \cdot 10^{-3}$	0.02	0.03	0.03	0.02
Cs-135	$5 \cdot 10^{-3}$	0.02	0.4	0.5	0.02
Ra-226	$3 \cdot 10^{-4}$	$3 \cdot 10^{-3}$	$2 \cdot 10^{-3}$	$5 \cdot 10^{-4}$	$3 \cdot 10^{-3}$
Th-230	$5 \cdot 10^{-6}$	$1 \cdot 10^{-5}$	$3 \cdot 10^{-5}$	$1 \cdot 10^{-4}$	$1 \cdot 10^{-5}$
Pa-231	$5 \cdot 10^{-6}$	$1 \cdot 10^{-5}$	$3 \cdot 10^{-5}$	$1 \cdot 10^{-4}$	$1 \cdot 10^{-5}$
U-238	$1 \cdot 10^{-4}$	$1 \cdot 10^{-4}$	$3 \cdot 10^{-4}$	$1 \cdot 10^{-3}$	$1 \cdot 10^{-4}$
Np-237	$5 \cdot 10^{-6}$	$1 \cdot 10^{-4}$	$3 \cdot 10^{-4}$	$1 \cdot 10^{-3}$	$1 \cdot 10^{-4}$
Am-243	$1 \cdot 10^{-6}$	$1 \cdot 10^{-4}$	$3 \cdot 10^{-4}$	$1 \cdot 10^{-3}$	$1 \cdot 10^{-4}$
Pu-239	$1 \cdot 10^{-6}$	$1 \cdot 10^{-4}$	$3 \cdot 10^{-4}$	$1 \cdot 10^{-3}$	$1 \cdot 10^{-4}$

8.3.1.5 Contamination of fish

Under equilibrium conditions, the activity concentration in fish is estimated from the activity in water, the element-specific concentration factor water-fish according to:

$$C_{f,r} = C_{w,r} \cdot CF_{wf,r} \tag{11}$$

with

$C_{f,r}$ activity concentration in fish (Bq kg^{-1})

$CF_{wf,r}$ concentration factor water-fish (l kg^{-1})

$C_{w,r}$ activity concentration in water (Bq l^{-1})

The activity concentration in the lake water is estimated from the activity of the inflowing water, the turnover of the water body λ_t and the sedimentation rate λ_{sed}. The activity of the

inflowing water is assumed to be the same as that of the contaminated near-surface water.

$$C_{Lw} = \frac{C_w}{\lambda_{sed} + \lambda_t} \quad (12)$$

with

λ_t rate for the loss due to turnover (d^{-1})

$\lambda_{r,s}$ rate of nuclide r for the loss due to sedimentation (d^{-1})

The sedimentation rate λ_{sed} is estimated from the particulates suspended in water and the distribution coefficient water-sediment:

$$\lambda_s = \frac{S_a \cdot K_{d,ws}}{d \cdot (1 + C_p \cdot K_{d,ws})} \quad (13)$$

with

λ_s sedimentation rate (d^{-1})

S_a annual sedimentation (kg m^{-2} a^{-1})

$K_{d,ws}$ distribution coefficient water-sediment (m^3 kg^{-1})

d depth of the water body (m)

C_p particulate concentration in water (kg m^{-3})

The nuclide-independent parameters to estimate the activity in lake water are listed in Tab. 36. The K_d-values and the concentration factors water-fish are summarised in Tab. 37. The values represent a simplified reference lake /PRO 05/. The turnover rate is only 2 a^{-1}, and the depth of the water is only 3 m. These assumptions are cautious.

Tab. 36 Element independent parameters to estimate the activity in lake water

Parameter	Unit	Value
Turnover of water	a^{-1}	2
Sedimentation rate	a^{-1}	0.2
Annual sedimentation	kg m^{-2} a^{-1}	5
Annual sedimentation	m a^{-1}	0.005
Sediment density	kg m^{-3}	1000
Depth of water body	m	3
Particulate concentration	kg m^{-3}	0.1

Tab. 37 Concentration factors water-fish and Kd water-sediment

Radionuclide	Concentration factor water-fish (l kg^{-1})	Kd-water sediment (m^3 kg^{-1})
Cl-36	50	0.1
Ni-59	100	30
Se-79	200	0.1
Zr-93	200	10
Nb-94	200	30
Tc-99	15	0.1
Pd-107	10	30
Sn-126	3000	30
I-129	10	10
Cs-135	1000	10
Ra-226	70	30
Th-230	100	30
Pa-231	10	30
U-238	50	30
Np-237	30	30
Am-243	30	30
Pu-239	30	30

8.3.2 Dose calculation

8.3.2.1 Calculation of the ingestion dose

The annual effective dose is calculated for an adult reference person. It is the sum of the contributions from ingestion, inhalation, and external exposure. The annual ingestion dose is calculated from the activity intake with food and water exposure $D_{ing,n}$ due to ingestion of the foodstuff n is given by

$$D_{ing,n} = V_{n,r} \cdot C_{nr} \cdot g_{ing,r} \quad (14)$$

with

$V_{n,r}$ annual intake rate of foodstuff n (kg d^{-1})

$C_{n,r}$ annual average of food activity in food n (Bq kg^{-1})

$g_{ing,r}$ ingestion dose coefficient for effective dose for ingestion of nuclide r (Sv Bq^{-1})

The intake rates for the different climate states are summarised in Tab. 38. The data represent present day average intake rates for countries which are located in the climate zones considered as reference for the different climates.

Tab. 38 Food intake rates for the different climate states considered. RG = Rising Groundwater

Food item	Food intake rates (l a-1, kg a-1)						
	Well; RG	Well, GW	Well	Well	Well, GW	Well	GW
	Temperate Cfb	Mediterr. Csa	Steppe BS	Boreal Dfa	Boreal Dfc	Tundra ET	Tundra ET
Drinking water	730	1100	1100	730	730	730	730
Cereals	110	115	105	110	71	-	-
Potatoes/root veg.	55	107	93	55	84	-	113
Leafy vegetables	13	56	34	13	51	-	7.7
Fruit vegetables	75	84	12	75	-	-	16
Milk	130	100	87	130	115	37a	37
Beef	30	28	22	30	72	110 a	110
Pork	60	28	22	60	0	0	-
Lamb	0	1.5	12	0	0	0	-
Fish	1	0	0	1	14	0	36.5
Fungi	-	-	-	-	-	-	7.7
Berries	-	-	-	-	-	-	16
Reindeer	-	-	-	-	-	-	110
Reference	/PRO 05/		/EUR 91/	/PRO 05/		/TRA 02/	
Analogue station	Germany	Spain	Greece	Germany	Sweden	Kola peninsula	

For the temperate climate, German intake rates are applied as a reference. To represent the Mediterranean climate, Spanish data are used. No data are available for Steppe climate which is represented by the site Marrakesh. In lieu, Greek data were used, which are thought to be appropriate in view on climatic conditions. The data for tundra were surveyed by an investigation of laps on the Kola Peninsula. The water intake is assumed to be 2 l d^{-1}, which is consistent with the physiological water demand /KLE 99/. In warmer climates, water demand and intake are higher. Therefore, for the Mediterranean climate, and the Steppe climate a daily water consumption of three litres is assumed. In view of various sources that contribute to water intake, this is a very cautious assumption. The dose coefficients for ingestion and inhalation are taken from /BMU 02/ (Tab. 39).

Tab. 39 Dose coefficients for ingestion, inhalation and internal exposure

Dose coefficient	Ingestion (Sv Bq^{-1})	External exposure (Sv s^{-1} pro Bq m^{-2})	Inhalation (Sv Bq^{-1})	Inhalation class
C-14 (organic)	$5.8 \cdot 10^{-10}$		-	
C-14 (anorganic)	$2.9 \cdot 10^{-11}$	0	$6.2 \cdot 10^{-12}$	
Cl-36	$9.3 \cdot 10^{-10}$	0	$7.3 \cdot 10^{-09}$	M
Ni-59	$6.3 \cdot 10^{-11}$	$3.1 \cdot 10^{-19}$	$4.4 \cdot 10^{-10}$	
Se-79	$2.9 \cdot 10^{-09}$	0	$2.6 \cdot 10^{-09}$	M
Zr-93	$1.1 \cdot 10^{-09}$	$4.6 \cdot 10^{-19}$	$1.0 \cdot 10^{-08}$	M
Nb-94	$1.7 \cdot 10^{-09}$	$1.5 \cdot 10^{-15}$	$1.1 \cdot 10^{-08}$	
Tc-99	$6.4 \cdot 10^{-10}$	0	$4.0 \cdot 10^{-09}$	M
Pd-107	$3.7 \cdot 10^{-11}$	0	$8.5 \cdot 10^{-11}$	
Sn-126	$7.1 \cdot 10^{-08}$	$1.9 \cdot 10^{-15}$	$3.1 \cdot 10^{-08}$	M
I-129	$1.1 \cdot 10^{-07}$	$2.0 \cdot 10^{-17}$	$3.6 \cdot 10^{-08}$	F
Cs-135	$2.0 \cdot 10^{-09}$	0	$6.9 \cdot 10^{-10}$	F
Ra-226	$2.8 \cdot 10^{-07}$	$1.6 \cdot 10^{-15}$	$3.5 \cdot 10^{-06}$	M
Th-230	$3.1 \cdot 10^{-07}$	$3.8 \cdot 10^{-19}$	$4.3 \cdot 10^{-05}$	M
Pa-231	$7.1 \cdot 10^{-07}$	$4.0 \cdot 10^{-16}$	$1.4 \cdot 10^{-04}$	M
U-238	$4.8 \cdot 10^{-08}$	$1.6 \cdot 10^{-15}$	$2.9 \cdot 10^{-06}$	M
Np-237	$1.1 \cdot 10^{-07}$	$2.1 \cdot 10^{-16}$	$2.3 \cdot 10^{-05}$	M
Am-243	$2.0 \cdot 10^{-07}$	$2.0 \cdot 10^{-16}$	$4.1 \cdot 10^{-05}$	
Pu-239	$2.5 \cdot 10^{-07}$	$3.2 \cdot 10^{-19}$	$5.0 \cdot 10^{-05}$	M

8.3.2.2 Inhalation dose due to resuspended soil particles

The resuspension of contaminated soil particles depends on a variety of factors such as weather, particle size spectrum in air, characteristics of the surface (soil, vegetation, urban environment) and climatic conditions. These influencing factors lead to a pronounced variability of resuspension. The key assumption for the estimation of exposure due to inhalation of resuspended particles for an adult reference person is that the inhaled particles have the same activity concentration as the soil from which it is resuspended. The effective dose is estimated according to:

$$D_{inh,r} = C_{s,r} \cdot L_s \cdot I_A \cdot f_{e,r} \cdot g_{inh,r} \quad (15)$$

with

$D_{inh,r}$ effective annual inhalations dose due to nuclide r (Sv a^{-1})

$C_{s,r}$ activity concentration of the soil (Bq kg^{-1})

L_s dust in air (g m^{-3})

I_A breathing rate (m^3 a^{-1})

$f_{e,r}$ enrichment factor for the resuspendable soil fraction

$g_{inh,r}$ inhalation dose coefficient for effective dose of the radionuclide r (Sv Bq^{-1})

The breathing rate for an adult person is 8,100 m^3 a^{-1} /BMU 01/. The dust concentration in air in rural areas is about 20 µg m^{-3} for temperate climates /SEI 86/. For dry conditions, resuspension and wind erosion are higher /SEI 86/. The respective values are given in Tab. 40 and are in consistence with the assumptions on activity loss due to wind erosion.

The dose coefficients for inhalation are taken from /BMU 02/ (Tab. 39). The dose coefficients are derived for a particle size around 1 µm. The particle size spectrum of resuspended material covers a wide range from less than 1 µm to some ten µm. Most particles have diameters below 10 µm /SEI 86/, which is considered as the respirable fraction. This assumption is cautious because it implies that the total resuspended activity contributes to the inhalation dose.

Tab. 40 Parameters for estimating exposures from inhalation of resuspended particles

Parameter	Value
Dust concentration (µg m^{-3})	
Temperate (Cfb)	20
Mediterranean (Csa)	100
Steppe (BS)	200
Boreal (Dfa)	100
Boreal (Dfc)	20
Tundra (ET)	20
Enrichment factor	
Cl, Se, Tc, I	1
Zr, Sn, Cs, Ra, Th, Pa, U, Np, Pu	3

8.3.2.3 External exposure

The external exposure from activity deposited on soil during the application of irrigation water is calculated from the activity in soil, the effective thickness of the soil layer, the exposure time during which the reference person stays on contaminated soil and the dose coefficient for external exposure.

$$D_{ext,r} = C_{s,r} \cdot d_{b,r} \cdot T_{ext} \cdot g_{ext,r} \quad (16)$$

with

$D_{ext,r}$ annual effective dose due to external exposure (Sv a^{-1})

$d_{b,r}$ effective thickness of the soil layer that contributes to external exposure from radionuclide *r* in soil (m)

$g_{ext,r}$ dose coefficient for external exposure from the ground (Sv s^{-1} per Bq m^{-2})

T_{ext} exposure time (s a^{-1})

The parameter $d_{b,r}$ is a nuclide-dependent correction factor that is necessary because dose coefficients for external exposure relate to a planar radionuclide source on the soil surface, but the radionuclides are homogeneously distributed over the soil profile.

The application of these dose coefficients to radionuclides at a depth < 0.5 cm overestimates the external exposure, since the radiation is shielded by the overlying soil layers. The shielding effect increases with the penetration depth of the radionuclides. Furthermore, the photon energy is important: Low-energy photons are attenuated by a few mm of soil, whereas the mean free path of high energy photons is several cm.

The parameter $d_{b,r}$ gives the thickness of a soil layer to calculate the equivalent activity inventory per unit area for the applications of the dose coefficients of a planar radionuclide source.

8.3.3 Estimation of C-14 activity in foods

The estimation of C-14 in food subsequent to application of irrigation water that contains C-14 requires a special consideration. For this assessment, it is assumed that C-14 occurs as $^{14}CO_2$, $H^{14}CO_3^-$ or $^{14}CO_3^{2-}$. The key process for the fate of carbon dioxide is the photosynthesis, during which CO_2 is converted to carbohydrates. The photosynthesis

depends on the environmental conditions as day time, insolation, temperature, water supply and plant species. Part of the carbohydrates is lost in the short-term by respiration which enables the metabolism of the plant. Part of it is stored in specific parts of the plant as e.g. tubers or grain /GIS 90/, /SHE 06a/, /SHE 06b/.

Carbon dioxide is metabolised by the photosynthesis of the plant and enters via this pathway the human food chain and causes ingestion exposures due to the intake of contaminated food. The use of ^{14}C contaminated water for irrigation of crops is modelled assuming a conceptual model as shown in Fig. 105. The model assumptions are applied:

- The soil area that receives the C-14 contaminated irrigation water is 100,000 m².
- During or after irrigation, $^{14}CO_2$ degasses from the water.
- $^{14}CO_2$ is metabolised during photosynthesis increasing the natural C-14/C-12 ratio.
- Over the area that releases $^{14}CO_2$, the $^{14}CO_2$ is homogeneously distributed in the mixing layer with the height h. As default, it is assumed that this mixing layer is 20 m. The CO_2 in this 20 m-layer is assimilated on a sunny summer day during photosynthesis by a well developed canopy, which is able to assimilate daily 2 – 3 g CO_2 per m² soil /GEI 80/. However, on sunny days, the effective mixing layer is much higher. The insolation causes a convective boundary layer, which may increase to a height of up to 1000 m from morning to early afternoon /GRU 01/, i.e. the assumption of a mixing height of 20 m is conservative.
- The $^{12}CO_2$-content in air is 0.04 wt.-% which corresponds to 0.176 g C-12 m^{-3} air. This $^{12}CO_2$ is assumed for the whole mixing layer. In reality, there is a gradient of $^{12}CO_2$ in air, since, due to the photosynthesis, the canopy is an effective CO_2-sink that causes a permanent flux of $^{12}CO_2$ from upper atmosphere layers to the ground. However, this effect is not taken into account.
- There is a horizontal air exchange within this layer due to wind. The exchange rate of air is the ratio of wind speed v and radius r of the area r ($\lambda_{ex} = v/r$).
- The mean annual wind speed in a height of 10 m is in the order of 3 – 5 m s^{-1}, depending on the site characteristics. The wind speed increases with height following an exponential wind profile. Following a Gaussian plume model for a neutral stability class of the atmosphere, a wind speed of 2 m s^{-1} on the ground corresponds to a wind speed of about 3.5 m s^{-1} in a height of 10 m /TRO 91/.

- The radius r corresponds to the radius of the CO_2 release area. In this estimation a default area of 100,000 m² is assumed. Accordingly the radius is app. 178 m.

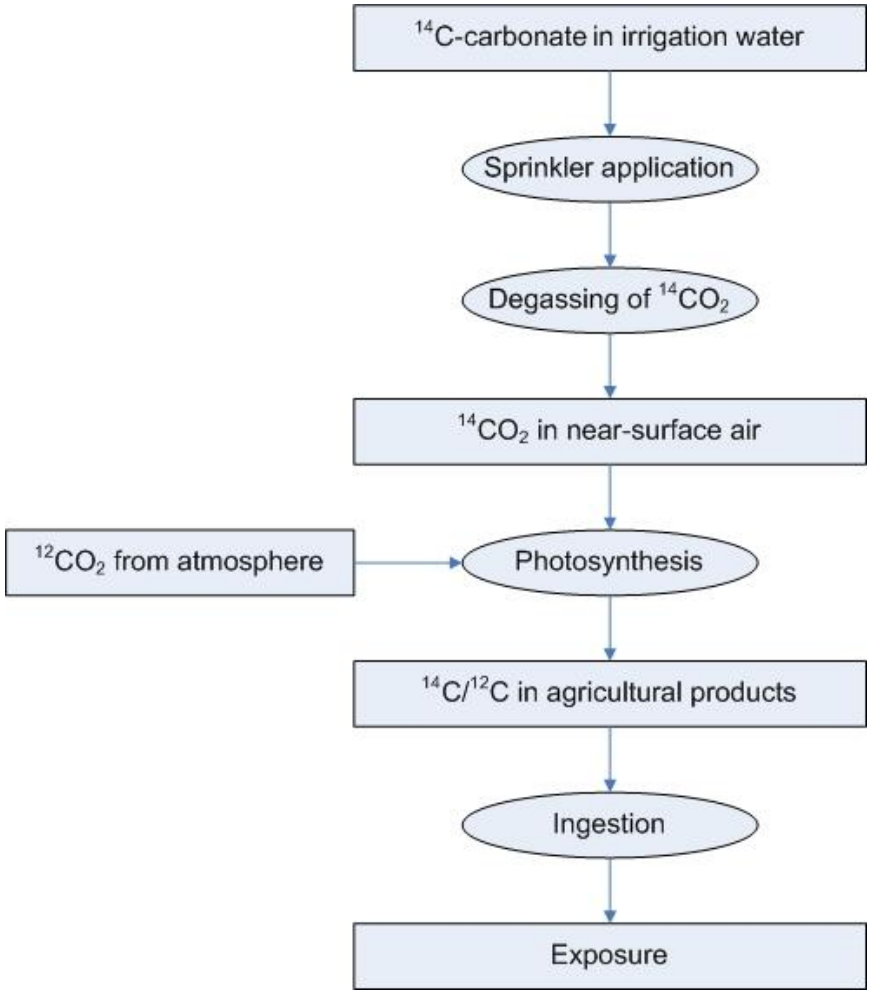

Fig. 105 Flowchart of the model to assess exposures due to use of water containing C-14 for irrigation of agricultural crops

The excess C-14/C-12 ratio in the mixing layer for a continuous $^{14}CO_2$ release can be calculated according to

$$R_{^{14}C/^{12}C} = \frac{E}{h \cdot \lambda_{ex} \cdot C_{^{12}C}} \qquad (17)$$

with

$R_{^{14}C/^{12}C}$ C-14/C-12 ratio in air (Bq g^{-1})

E input of C-14 during the vegetation period with irrigation (Bq m^{-2} s^{-1})

h mixing height (m)

$C_{^{12}C}$ C-12 content of air (0.176 g m^{-3})

According to /UNS 88/, a natural C-14/C-12 ratio of 0.227 (Bq C-14)(g C-12)$^{-1}$ corresponds to an effective dose of 12 µSv a^{-1}, resulting in an effective dose factor of 52.9 µSv a^{-1} per (Bq C-14) (g C-12)$^{-1}$. The factor in /UNS 88/ is derived from the global specific activity of carbon. However, in this estimation, a relatively small area of 10 ha is considered, on which all consumed plant and animal food products are produced. The exposure due to ^{14}C is then estimated as product of the excess C-14/C-12 ratio and the dose factor derived from /UNS 88/. Details for the parameters are given in Tab. 41.

Tab. 41 Details for the estimation of the exposure due to releases of C-14 to agricultural and forest soils

Parameter	Mean	Remark
Release rate (Bq a^{-1})	$1.0 \cdot 10^{8}$	Predefined
Area affected (m²)	$1.0 \cdot 10^{5}$	Predefined
Wind speed (m s^{-1})		
Agriculture	2	Mean wind speed
Irrigation	1	Irrigation performed at lower wind speeds to minimise drift losses
Mixing height (m)		
Irrigation	10	

For agricultural land, the wind speed is represented by the mean value at a height of 10 m. The wind speed is relatively well known from meteorological monitoring, but no data for representative wind speeds during irrigation are available. However, it is thought that plants are irrigated during periods with lower wind speed to prevent a water loss with the wind drift. Therefore a lower wind speed of 1 m^{-2} s^{-1} is applied for the calculation.

The mixing heights described above are derived from the total assimilation during a whole day (see above). Irrigation water is applied only during a few hours per day, thus the mixing height is reduced to 10m. Furthermore, the irrigation has a cooling effect, which reduces the turbulence above the canopy. For these circumstances, the dose coefficient for C-14 applied with irrigation water is adapted to $1.8 \cdot 10^{-17}$ Sv Bq^{-1}.

8.4 Results

8.4.1 Dose conversion factors for different climates

The dose conversion factors for the radionuclides are summarised for the GBI “well” for temperate, steppe Mediterranean, boreal (Dfa and Dfc) and tundra climate in Tab. 42. For the GBI “rising groundwater”, the results are given in Tab. 44 for temperate, boreal (Dfa and Dfc) and tundra climate. To facilitate the comparison among the climates, the results are also given in relative units. The differences between the climates vary dependent on radionuclide and geosphere-biosphere interface by factors in a range of 2-2000.

The contributions of the pathways for both geosphere-biosphere interfaces are shown in Tab. 43 and Tab. 45. The contributions are given for ingestion, external exposure, and inhalation of resuspended soil particles. Ingestion is differentiated according to the intake of drinking water, plant food products (cereals, potatoes and root vegetables, fruit and fruit vegetables, leafy vegetables) and animal food products (meat, milk) and fish.

The results are discussed in detail in chapter 8.5.

Tab. 42 Dose conversion factors for the different climates for GBI “well”

Climate	Dose conversion coefficient (Sv a^{-1} per Bq m^{-3})																	
	C -14	Cl -36	Ni -59	Se -79	Zr -93	Nb -94	Tc -99	Pd -107	Sn -126	I -129	Cs -135	Ra -226	Th -230	Pa -231	U -238	Np -237	Am -243	Pu -239
Absolute values																		
Temperate Cfb	$7.5\cdot10^{-7}$	$2.3\cdot10^{-6}$	$1.2\cdot10^{-7}$	$3.3\cdot10^{-6}$	$9.0\cdot10^{-7}$	$2.6\cdot10^{-5}$	$7.1\cdot10^{-7}$	$6.2\cdot10^{-8}$	$1.2\cdot10^{-4}$	$1.8\cdot10^{-4}$	$5.3\cdot10^{-6}$	$3.7\cdot10^{-4}$	$2.6\cdot10^{-4}$	$6.3\cdot10^{-4}$	$4.2\cdot10^{-5}$	$9.5\cdot10^{-5}$	$1.7\cdot10^{-4}$	$2.0\cdot10^{-4}$
Mediterran Csa	$1.2\cdot10^{-6}$	$7.4\cdot10^{-6}$	$2.9\cdot10^{-7}$	$5.1\cdot10^{-4}$	$1.2\cdot10^{-6}$	$8.6\cdot10^{-5}$	$6.1\cdot10^{-5}$	$1.2\cdot10^{-7}$	$2.3\cdot10^{-4}$	$3.5\cdot10^{-4}$	$9.7\cdot10^{-6}$	$9.7\cdot10^{-4}$	$4.0\cdot10^{-4}$	$1.3\cdot10^{-3}$	$9.5\cdot10^{-5}$	$2.6\cdot10^{-4}$	$2.8\cdot10^{-4}$	$3.2\cdot10^{-4}$
Steppe BS	$1.0\cdot10^{-6}$	$5.5\cdot10^{-5}$	$2.4\cdot10^{-7}$	$6.2\cdot10^{-4}$	$1.2\cdot10^{-6}$	$7.4\cdot10^{-5}$	$8.0\cdot10^{-5}$	$1.0\cdot10^{-7}$	$2.1\cdot10^{-4}$	$3.4\cdot10^{-4}$	$9.7\cdot10^{-6}$	$8.4\cdot10^{-4}$	$3.8\cdot10^{-4}$	$1.4\cdot10^{-3}$	$7.2\cdot10^{-5}$	$2.2\cdot10^{-4}$	$2.8\cdot10^{-4}$	$3.2\cdot10^{-4}$
Boreal Dfa	$1.3\cdot10^{-6}$	$7.0\cdot10^{-6}$	$2.4\cdot10^{-7}$	$1.9\cdot10^{-5}$	$1.0\cdot10^{-6}$	$7.9\cdot10^{-5}$	$2.7\cdot10^{-5}$	$1.0\cdot10^{-7}$	$2.2\cdot10^{-4}$	$3.2\cdot10^{-4}$	$8.8\cdot10^{-6}$	$7.1\cdot10^{-4}$	$3.4\cdot10^{-4}$	$1.1\cdot10^{-3}$	$6.9\cdot10^{-5}$	$2.0\cdot10^{-4}$	$2.4\cdot10^{-4}$	$2.7\cdot10^{-4}$
Boreal Dfc	$4.2\cdot10^{-6}$	$1.5\cdot10^{-6}$	$7.4\cdot10^{-8}$	$6.2\cdot10^{-6}$	$1.2\cdot10^{-6}$	$1.0\cdot10^{-5}$	$5.7\cdot10^{-7}$	$3.9\cdot10^{-8}$	$2.8\cdot10^{-4}$	$5.5\cdot10^{-4}$	$5.2\cdot10^{-5}$	$2.8\cdot10^{-4}$	$2.7\cdot10^{-4}$	$5.8\cdot10^{-4}$	$4.1\cdot10^{-5}$	$9.1\cdot10^{-5}$	$1.6\cdot10^{-4}$	$2.0\cdot10^{-4}$
Tundra ET	$2.1\cdot10^{-8}$	$7.6\cdot10^{-7}$	$4.7\cdot10^{-8}$	$2.2\cdot10^{-6}$	$8.0\cdot10^{-7}$	$1.2\cdot10^{-6}$	$4.7\cdot10^{-7}$	$2.7\cdot10^{-8}$	$5.2\cdot10^{-5}$	$8.8\cdot10^{-5}$	$1.6\cdot10^{-6}$	$2.1\cdot10^{-4}$	$2.3\cdot10^{-4}$	$5.2\cdot10^{-4}$	$3.5\cdot10^{-5}$	$8.0\cdot10^{-5}$	$1.5\cdot10^{-4}$	$1.8\cdot10^{-4}$
Min	$2.1\cdot10^{-8}$	$7.6\cdot10^{-7}$	$4.7\cdot10^{-8}$	$2.2\cdot10^{-6}$	$8.0\cdot10^{-7}$	$1.2\cdot10^{-6}$	$4.7\cdot10^{-7}$	$2.7\cdot10^{-8}$	$5.2\cdot10^{-5}$	$8.8\cdot10^{-5}$	$1.6\cdot10^{-6}$	$2.1\cdot10^{-4}$	$2.3\cdot10^{-4}$	$5.2\cdot10^{-4}$	$3.5\cdot10^{-5}$	$8.0\cdot10^{-5}$	$1.5\cdot10^{-4}$	$1.8\cdot10^{-4}$
Max	$4.2\cdot10^{-6}$	$5.5\cdot10^{-5}$	$2.9\cdot10^{-7}$	$6.2\cdot10^{-4}$	$1.2\cdot10^{-6}$	$8.6\cdot10^{-5}$	$8.0\cdot10^{-5}$	$1.2\cdot10^{-7}$	$2.8\cdot10^{-4}$	$5.5\cdot10^{-4}$	$5.2\cdot10^{-5}$	$9.7\cdot10^{-4}$	$4.0\cdot10^{-4}$	$1.4\cdot10^{-3}$	$9.5\cdot10^{-5}$	$2.6\cdot10^{-4}$	$2.8\cdot10^{-4}$	$3.2\cdot10^{-4}$
Ratio Max/Min	198.2	72.8	6.0	286	1.5	69.1	170	4.6	5.3	6.3	31.8	4.7	1.8	2.6	2.7	3.2	1.9	1.8
Relative values (Temperate = 1)																		
Temperate Cfb	1.00	1.00	1.00	1.00	1.00	1.00	1.00	1.00	1.00	1.00	1.00	1.00	1.00	1.00	1.00	1.00	1.00	1.00
Mediterran Csa	1.64	3.17	2.45	155.92	1.35	3.35	85.80	2.02	1.92	1.95	1.85	2.66	1.54	2.15	2.29	2.72	1.69	1.60
Steppe BS	1.4	23.7	2.0	189.5	1.29	2.89	112.37	1.69	1.69	1.90	1.84	2.29	1.44	2.17	1.73	2.29	1.68	1.58
Boreal Dfa	1.78	3.00	2.07	5.63	1.15	3.07	38.10	1.65	1.82	1.78	1.68	1.94	1.30	1.77	1.66	2.10	1.43	1.35
Boreal Dfc	5.62	0.66	0.63	1.89	1.29	0.40	0.80	0.63	2.27	3.07	9.88	0.78	1.05	0.92	0.98	0.96	0.98	1.00
Tundra ET	0.03	0.33	0.41	0.66	0.90	0.05	0.66	0.44	0.43	0.49	0.31	0.57	0.87	0.83	0.84	0.85	0.88	0.90

Tab. 43 Contributions of the exposure pathways for the different climates for the GBI “well”

Climate	Pathway	Pathway contribution (%)																	
		C -14	Cl -36	Ni -59	Se -79	Zr -93	Nb -94	Tc -99	Pd -107	Sn -126	I -129	Cs -135	Ra -226	Th -230	Pa -231	U -238	Np -237	Am -243	Pu -239
Temperate	Ingestion	100	100	100	100	100	6	100	100	76	100	100	93	99	95	98	96	95	98
Cfb	Drinking water	3	29	40	64	90	87	66	44	56	45	28	60	88	87	85	88	92	92
	Plant foods	46	22	55	23	8	11	33	52	27	22	31	38	11	13	14	12	8	8
	Animal foods	12	48	5	4	0.0	0.0	0.6	4	1	33	38	2	0.0	0.0	0.4	0.1	0.1	0.1
	Fish	39	0.9	0.4	8	2	2	0.6	0.0	16	0.1	4	0.4	0.8	0.1	0.4	0.2	0.3	0.3
	Inhalation	0.0	0.0	0.0	0.0	0.0	0.0	0.0	0.0	0.0	0.0	0.0	0.1	1	4	0.5	0.9	2.1	1.6
	Ext. exposure	0.0	0.0	0.5	0.0	0.0	94	0.0	0.0	24	0.0	0.0	7	0.0	1	1	3	3	0.0
Mediterran	Ingestion	100	100	99	100	99	2	100	100	56	100	100	91	89	73	96	91	79	86
Csa	Drinking water	2	9	16	0.4	67	63	0.8	22	39	23	15	23	63	52	38	34	66	66
	Plant foods	85	42	79	90	33	37	98	74	58	32	51	75	37	48	61	66	34	34
	Animal foods	13	49	5	10	0.0	0.0	2	4	2	45	34	2	0.1	0.0	0.8	0.2	0.1	0.1
	Fish	0.0	0.0	0.0	0.0	0.0	0.0	0.0	0.0	0.0	0.0	0.0	0.0	0.0	0.0	0.0	0.0	0.0	0.0
	Inhalation	0.0	0.0	0.0	0.0	0.5	0.0	0.0	0.0	0.0	0.0	0.0	0.5	11	25	3	5	17	14
	Ext. exposure	0.0	0.0	0.7	0.0	0.0	98	0.0	0.0	44	0.0	0.0	9	0.0	2	1	4	4	0.0
Steppe	Ingestion	100	100	99	100	99	2	100	100	57	100	100	90	86	66	94	85	74	81
BS	Drinking water	2	1	19	0.3	70	67	0.6	26	44	24	15	27	69	58	52	43	70	70
	Plant foods	84	40	73	82	30	33	96	68	52	25	36	70	30	42	47	56	30	30
	Animal foods	14	58	8	17	0.0	0.0	3	6	4	52	49	3	0.1	0.1	1	0.4	0.2	0.2
	Fish	0.0	0.0	0.0	0.0	0.0	0.0	0.0	0.0	0.0	0.0	0.0	0.0	0.0	0.0	0.0	0.0	0.0	0.0
	Inhalation	0.0	0.0	0.1	0.0	1.0	0.0	0.0	0.1	0.0	0.0	0.0	0.9	14	33	5	11	23	19
	Ext. exposure	0.0	0.0	0.7	0.0	0.0	97	0.0	0.0	43	0.0	0.0	9	0.0	1	1	4	3	0.0

Tab. 43 Contributions of the exposure pathways for the different climates for the GBI “well” (continued)

Climate	Pathway	Pathway contribution (%)																	
		C -14	Cl -36	Ni -59	Se -79	Zr -93	Nb -94	Tc -99	Pd -107	Sn -126	I -129	Cs -135	Ra -226	Th -230	Pa -231	U -238	Np -237	Am -243	Pu -239
Boreal Dfa	Ingestion	100	100	99	100	99	2	100	100	58	100	100	89	88	70	95	89	77	85
	Drinking water	2	10	19	11	79	75	2	26	41	25	17	32	75	66	54	45	79	79
	Plant foods	61	30	74	65	19	23	95	68	45	25	35	65	24	33	45	54	20	20
	Animal foods	16	60	6	22	0.0	0.0	3	6	2	49	46	3	0.1	0.1	1	0.2	0.1	0.1
	Fish	22	0.3	0.2	1	2	1	0.0	0.0	12	0.0	2	0.2	0.7	0.1	0.3	0.1	0.2	0.2
	Inhalation	0.0	0.0	0.0	0.0	0.6	0.0	0.0	0.0	0.0	0.0	0.0	0.6	12	28	4	7	18	15
	Ext. exposure	0.0	0.0	0.8	0.0	0.0	98	0.0	0.0	42	0.0	0.0	11	0.0	2	2	4	4	0.0
Boreal Dfc	Ingestion	100	100	100	100	100	16	100	100	96	100	100	97	100	98	99	99	98	99
	Drinking water	0.5	44	62	34	70	75	82	70	19	15	3	74	83	91	86	90	91	91
	Plant foods	2	10	25	4	4	6	7	26	3	12	41	16	6	7	8	7	6	6
	Animal foods	0.6	27	5	2	0.0	0.0	0.3	3	0.3	73	51	3	0.0	0.0	0.2	0.1	0.1	0.1
	Fish	97	19	8	60	26	20	11	0.9	77	0.3	5	7	11	1	6	4	4	4
	Inhalation	0.0	0.0	0.0	0.0	0.0	0.0	0.0	0.0	0.0	0.0	0.0	0.0	0.4	2	0.2	0.3	0.8	0.6
	Ext. exposure	0.0	0.0	0.3	0.0	0.0	84	0.0	0.0	4	0.0	0.0	3	0.0	0.5	0.4	1	0.9	0.0
Tundr ET	Ingestion	100	100	100	100	100	100	100	100	100	100	100	100	100	100	100	100	100	100
	Drinking water	100	89	97	97	100	100	100	99	99	92	89	98	100	100	100	100	100	100
	Plant foods	0.0	0.0	0.0	0.0	0.0	0.0	0.0	0.0	0.0	0.0	0.0	0.0	0.0	0.0	0.0	0.0	0.0	0.0
	Animal foods	0.0	11	3	3	0.0	0.0	0.3	0.6	0.6	8	11	2	0.0	0.0	0.1	0.1	0.1	0.1
	Fish	0.0	0.0	0.0	0.0	0.0	0.0	0.0	0.0	0.0	0.0	0.0	0.0	0.0	0.0	0.0	0.0	0.0	0.0
	Inhalation	0.0	0.0	0.0	0.0	0.0	0.0	0.0	0.0	0.0	0.0	0.0	0.0	0.0	0.0	0.0	0.0	0.0	0.0
	Ext. exposure	0.0	0.0	0.0	0.0	0.0	0.0	0.0	0.0	0.0	0.0	0.0	0.0	0.0	0.0	0.0	0.0	0.0	0.0

Tab. 44 Dose conversion factors for the different climates for the GBI “rising groundwater”

Climate	Dose conversion coefficient (Sv a^{-1} per Bq m^{-3})																	
	C -14	Cl -36	Ni -59	Se -79	Zr -93	Nb -94	Tc -99	Pd -107	Sn -126	I -129	Cs -135	Ra -226	Th -230	Pa -231	U -238	Np -237	Am -243	Pu -239
Absolute values																		
Temperate Cfb	$2.4\cdot10^{-8}$	$1.1\cdot10^{-6}$	$1.3\cdot10^{-7}$	$3.1\cdot10^{-6}$	$9.3\cdot10^{-7}$	$1.3\cdot10^{-4}$	$9.5\cdot10^{-7}$	$3.8\cdot10^{-8}$	$1.4\cdot10^{-4}$	$1.1\cdot10^{-4}$	$3.6\cdot10^{-6}$	$4.4\cdot10^{-3}$	$2.8\cdot10^{-4}$	$7.5\cdot10^{-4}$	$3.8\cdot10^{-5}$	$8.1\cdot10^{-5}$	$1.9\cdot10^{-4}$	$2.0\cdot10^{-4}$
Boreal Dfa	$2.1\cdot10^{-8}$	$1.1\cdot10^{-6}$	$1.3\cdot10^{-7}$	$2.9\cdot10^{-6}$	$9.1\cdot10^{-7}$	$1.3\cdot10^{-4}$	$9.5\cdot10^{-7}$	$3.8\cdot10^{-8}$	$1.2\cdot10^{-4}$	$1.1\cdot10^{-4}$	$3.5\cdot10^{-6}$	$4.4\cdot10^{-3}$	$2.8\cdot10^{-4}$	$7.5\cdot10^{-4}$	$3.8\cdot10^{-5}$	$8.1\cdot10^{-5}$	$1.9\cdot10^{-4}$	$2.0\cdot10^{-4}$
Boreal Dfc	$8.2\cdot10^{-8}$	$1.3\cdot10^{-6}$	$1.2\cdot10^{-7}$	$6.2\cdot10^{-6}$	$1.2\cdot10^{-6}$	$1.4\cdot10^{-4}$	$5.9\cdot10^{-7}$	$3.7\cdot10^{-8}$	$3.3\cdot10^{-4}$	$4.8\cdot10^{-4}$	$3.3\cdot10^{-4}$	$3.8\cdot10^{-3}$	$3.0\cdot10^{-4}$	$7.4\cdot10^{-4}$	$4.1\cdot10^{-5}$	$8.4\cdot10^{-5}$	$1.9\cdot10^{-4}$	$2.1\cdot10^{-4}$
Tundra ET	$2.3\cdot10^{-7}$	$1.7\cdot10^{-6}$	$8.3\cdot10^{-8}$	$1.2\cdot10^{-5}$	$1.6\cdot10^{-6}$	$1.4\cdot10^{-4}$	$6.6\cdot10^{-7}$	$3.1\cdot10^{-8}$	$6.5\cdot10^{-4}$	$1.6\cdot10^{-2}$	$3.2\cdot10^{-3}$	$2.3\cdot10^{-3}$	$3.4\cdot10^{-4}$	$7.0\cdot10^{-4}$	$6.7\cdot10^{-5}$	$8.9\cdot10^{-5}$	$2.0\cdot10^{-4}$	$2.2\cdot10^{-4}$
Min	$2.1\cdot10^{-8}$	$1.1\cdot10^{-6}$	$8.3\cdot10^{-8}$	$2.9\cdot10^{-6}$	$9.1\cdot10^{-7}$	$1.3\cdot10^{-4}$	$5.9\cdot10^{-7}$	$3.1\cdot10^{-8}$	$1.2\cdot10^{-4}$	$1.1\cdot10^{-4}$	$3.5\cdot10^{-6}$	$2.3\cdot10^{-3}$	$2.8\cdot10^{-4}$	$7.0\cdot10^{-4}$	$3.8\cdot10^{-5}$	$8.1\cdot10^{-5}$	$1.9\cdot10^{-4}$	$2.0\cdot10^{-4}$
Max	$2.3\cdot10^{-7}$	$1.7\cdot10^{-6}$	$1.3\cdot10^{-7}$	$1.2\cdot10^{-5}$	$1.6\cdot10^{-6}$	$1.4\cdot10^{-4}$	$9.5\cdot10^{-7}$	$3.8\cdot10^{-8}$	$6.5\cdot10^{-4}$	$1.6\cdot10^{-2}$	$3.2\cdot10^{-3}$	$4.4\cdot10^{-3}$	$3.4\cdot10^{-4}$	$7.5\cdot10^{-4}$	$6.7\cdot10^{-5}$	$8.9\cdot10^{-5}$	$2.0\cdot10^{-4}$	$2.2\cdot10^{-4}$
Ratio Max/Min	11.0	1.5	1.6	4.2	1.8	1.0	1.6	1.2	5.3	144.8	937.4	1.9	1.2	1.1	1.7	1.1	1.0	1.1
Relative values (Temperate = 1)																		
Temperate Cfb	1.00	1.00	1.00	1.00	1.00	1.00	1.00	1.00	1.00	1.00	1.00	1.00	1.00	1.00	1.00	1.00	1.00	1.00
Mediterran Csa	0.88	0.98	0.99	0.92	0.98	1.00	1.00	1.00	0.89	1.03	0.97	1.01	0.99	1.00	1.00	1.00	1.00	1.00
Steppe BS	3.41	1.12	0.85	1.98	1.27	1.00	0.63	0.97	2.39	4.38	92.46	0.87	1.05	0.99	1.06	1.04	1.01	1.03
Boreal Dfa	9.67	1.51	0.61	3.91	1.74	1.00	0.69	0.82	4.77	144.8	906	0.53	1.18	0.93	1.74	1.10	1.04	1.10
Boreal Dfc	1.00	1.00	1.00	1.00	1.00	1.00	1.00	1.00	1.00	1.00	1.00	1.00	1.00	1.00	1.00	1.00	1.00	1.00
Tundra ET	0.88	0.98	0.99	0.92	0.98	1.00	1.00	1.00	0.89	1.03	0.97	1.01	0.99	1.00	1.00	1.00	1.00	1.00

Tab. 45 Contributions of the exposure pathways for the different climates for the GBI "rising groundwater"

Climate	Pathway	Pathway contribution (%)																	
		C -14	Cl -36	Ni -59	Se -79	Zr -93	Nb -94	Tc -99	Pd -107	Sn -126	I -129	Cs -135	Ra -226	Th -230	Pa -231	U -238	Np -237	Am -243	Pu -239
Temperate Cfb	Ingestion	100	100	99	100	100	1	100	100	56	100	100	84	97	87	99	100	88	96
	Drinking water	88	60	34	68	87	72	49	72	68	73	41	6	82	80	93	99	88	95
	Plant foods	0.0	8	60	18	11	27	49	26	12	8	21	93	17	20	7	0.4	12	5
	Animal foods	0.0	29	5	5	0.0	0.0	1	2.7	1	19	33	2	0.0	0.0	0.1	0.0	0.0	0.0
	Fish	12	2	0.3	9	2	1	0.5	0.1	19	0.1	5	0.0	0.8	0.1	0.4	0.3	0.2	0.3
	Inhalation	0.0	0.0	0.0	0.0	0.2	0.0	0.0	0.0	0.0	0.0	0.0	0.2	3	10	0.4	0.1	0.0	4
	Ext. exposure	0.0	0.0	1	0.0	0.0	99	0.0	0.0	44	0.0	0.0	16	0.0	3	0.9	0.2	12	0.0
Boreal Dfa	Ingestion	100	100	99	100	100	1	100	100	51	100	100	84	97	87	99	100	88	96
	Drinking water	100	61	35	74	89	73	49	72	84	71	42	6	83	80	93	100	88	95
	Plant foods	0.0	9	60	19	11	27	49	26	15	7	21	92	17	20	7	0.4	12	5
	Animal foods	0.0	30	5	7	0.0	0.0	1	3	1	22	37	2	0.0	0.0	0.1	0.0	0.1	0.1
	Fish	0.0	0.0	0.0	0.0	0.0	0.0	0.0	0.0	0.0	0.0	0.0	0.0	0.0	0.0	0.0	0.0	0.0	0.0
	Inhalation	0.0	0.0	0.0	0.0	0.2	0.0	0.0	0.0	0.0	0.0	0.0	0.2	3	10	0.4	0.1	0.0	4
	Ext. exposure	0.0	0.0	1	0.0	0.0	99	0.0	0.0	49	0.0	0.0	16	0.0	3	0.9	0.2	12	0.0
Boreal Dfc	Ingestion	100	100	99	100	100	1	100	100	82	100	100	81	97	87	99	100	89	96
	Drinking water	26	54	41	34	68	63	79	74	19	17	0.4	7	78	81	87	96	87	92
	Plant foods	0.0	6	48	2	6	20	10	22	3	14	52	89	11	18	7	0.3	10	4
	Animal foods	0.0	16	6	2	0.0	0.0	0.6	3	0.4	69	47	4	0.1	0.0	0.2	0.0	0.2	0.1
	Fish	74	24	5	61	25	17	10	1.0	77	0.3	0.8	0.6	10	1	6	4	3	4
	Inhalation	0.0	0.0	0.0	0.0	0.1	0.0	0.0	0.0	0.0	0.0	0.0	0.2	3	10	0.4	0.1	0.0	4
	Ext. exposure	0.0	0.0	1	0.0	0.0	99	0.0	0.0	18	0.0	0.0	19	0.0	3	0.9	0.2	11	0.0
Tundra ET	Ingestion	100	100	98	100	100	2	100	100	91	100	100	69	97	86	99	100	89	97
	Drinking water	9	40	57	17	50	55	71	87	9	0.5	0.0	13	69	86	53	90	84	86
	Plant foods	0.0	3	12	0.3	2	6	3	6	0.4	9	46	71	7	11	38	0.2	7	5
	Animal foods	0.0	11	12	2	0.0	0.0	0.8	3	0.2	90	54	13	0.1	0.0	0.2	0.1	0.4	0.2
	Fish	91	46	20	80	48	38	25	3	91	0.0	0.2	3	24	3	9	9	9	9
	Inhalation	0.0	0.0	0.0	0.0	0.1	0.0	0.0	0.0	0.0	0.0	0.0	0.3	3	10	0.2	0.1	0.0	3
	Ext. exposure	0.0	0.0	2	0.0	0.0	98	0.0	0.0	9	0.0	0.0	31	0.0	3	0.5	0.2	11	0.0

8.4.2 Additional considerations

8.4.2.1 Water requirements for the different climate states

The climate states considered depend on the existence of sufficient groundwater resources. The consideration of a geosphere-biosphere interface “rising groundwater” only makes sense, if the water table is close to the surface over an area that is large enough to enable sustainable food production for a small community. Whereas the annual consumption of plant food products can be produced on a relatively small area of a few 100 m² (see Tab. 46), the production of milk and meat requires much larger areas. To ensure sustainable animal husbandry, herds are needed that include animals for breeding, meat and milk production. E.g., in temperate environments, a dairy cow that is fed only on locally produced grass, hay and silage, needs an area of about 5,000 m². Thus, for a herd of 30 dairy cows, an area of 150,000 m^2 is needed. Beef cattle, fattened on the basis of maize silage require an area of about 2,000-3,000 m² per animal. Pigs fattened on cereals require an area of about 600 m². These numbers illustrate that sustainable production of both plant and animal food products for a small community needs at least some hundred thousands of square meters.

In case of the GBI “well”, the capacity of the well needs to be sufficient enough to ensure a sustainable water supply. The area needed is comparable to that for the GBI “rising groundwater”. Assuming a minimum area requirement of 50 ha and an irrigation requirement for the temperate zone of approximately 200 mm a^{-1} (Tab. 47), the minimum capacity of the well is about 12 m^3 h^{-1} (3.2 l s^{-1}). Additional water is needed in the household for cooking, cleaning and personal hygiene in the order of 100-150 l per person and day. Assuming a community of 50 people this requires an additional well capacity of about 0.3 m^3 h^{-1} (0.1 l s^{-1}); i.e. the water requirement of the agriculture is by far dominating the total water use. For steppe, which has the highest water requirement among the climates in this study, a well capacity of 33 m^3 h^{-1} (9.2 l s^{-1}) is estimated. However, in total such well capacities are relatively low, it should be no problem to withdraw such amounts of water even from small aquifers.

Tab. 46 Annual water need for a group of 50 people in the household and for irrigation of all plant food products for temperate climate

Item	Annual consumption (kg a^{-1}, l a^{-1})	Yield (kg m^{-2})	Irrigation (mm m^{-2} a^{-1})	Requirement (m^3 a^{-1})	
				Single person	Group of 50 people
Drinking water	730	-	-	0.73	36.5
Cereals	110	0,5	170	37	1,870
Potatoes & root veg.	55	3	210	3.9	193
Leafy vegetables	13	2	210	1.4	68
Fruit vegetables	75	2	210	7.9	394
Household	54,750	-	-	55	2,750
Total	-	-	-	106	5,300

Tab. 47 Annual water requirement to enable sustainable animal husbandry

Animal Herd size	Feed	Annual intake (kg a^{-1}, l a^{-1})	Yield (kg m^{-2})	Area requirement (m^2)	Irrigation (mm m^{-2} a^{-1})	Water requirement (m^3 a^{-1})	
						Per animal	Per herd
Dairy cow	Grass	25,550	5	5110	210	1,070	32,000
30	Water	27,400	-	-	-	27	810
Beef cattle	Maize	9,100	3	3000	210	630	19,000
30	Water	14,600	-	-	-	15	450
Pigs	Cereals	1,095	0.5	2190	170	370	37,000
100	Water	2,190	-	-	-	2.2	220
Lamb	Grass	1,825	5	365	210	77	7,700
100	Water	1,460	-	-	-	1.5	150

8.4.2.2 Dose calculations for population groups with other consumption habits

To estimate exposures for representative persons in the different climates, diets are assumed that are derived from mean consumption habits. However, human habits are subject to pronounced variations. The calculations were made for diets consisting of a balanced mix of plant and animal foodstuff. However, some diets largely deviate from those average intake rates. In order to estimate the possible impact of such specific habits, exemplarily calculations are made for a vegan (consuming no milk and meat, but exclusively

plant food products) and a person with a large focus on meat consumption. Detailed surveys on the intake rates of vegans and meat-eaters are not available. Therefore, the diets were defined with the following underlying assumptions (Tab. 48):

- The energy intake with the normal diet is about 9000 kJ d^{-1}.
- The vegan eats only plant products. The intake rates are enhanced for all plant food products by a factor of 1.6, so that the energy intake is the same as for the normal diet.
- In the diet of the meat-eater, the intake of plant food products is supposed to be a factor of 2 less and the intake of meat and milk a factor of 2 higher than for the normal diet. The energy intake is about a 10 % higher than for the normal diet.

The resulting dose conversion coefficients for normal, vegan and meat-enhanced diet are compared in

Tab. 49. It indicates that the specific diets are of minor importance, if the intake rates stay within physiologically reasonable limits. The ratio of maximum and minimum is only for ^{36}Cl higher than a factor of two, for the other radionuclides the difference is about 10 to 50%. The impact is relatively low, since among the diets, the similarities are still significant. There are compensating effects, since higher meat intake is compensated by lower intake of plant food products and vice versa. Furthermore, the total intake is limited by the energy content of the diet.

Tab. 48 Diets for vegans and person with an enhanced consumption of meat and milk

Food item	Intake (kg a^{-1})	Modification factor	Modified intake		Energy (kJ g^{-1})	Energy intake (kJ d^{-1})
			kg a^{-1}	g d^{-1}		
Normal diet						
Cereals	110	1	110	301	15	4521
Potatoes & root veg.	55	1	55	151	3,6	542
Leafy vegetables	13	1	13	36	1	36
Fruit vegetables	75	1	75	205	1	205
Milk	130	1	130	356	2,8	997
Beef	30	1	30	82	8,5	699
Pork	60	1	60	164	12	1973
Total	**-**	**-**	**-**	**-**	**-**	**8973**
Vegan diet						
Cereals	110	1,6	176	482	15	7504
Potatoes & root veg.	55	1,6	88	241	3,6	900
Leafy vegetables	13	1,6	20,8	57	1	59
Fruit vegetables	75	1,6	120	329	1	341
Milk	130	0	0	0	2,8	0
Beef	30	0	0	0	8,5	0
Pork	60	0	0	0	12	0
Total	**-**	**-**	**-**	**-**	**-**	**8805**
Meat diet						
Cereals	110	0,5	55	151	15	2260
Potatoes & root veg.	55	0,5	27,5	75	3,6	271
Leafy vegetables	13	0,5	6,5	18	1	18
Fruit vegetables	75	0,5	37,5	103	1	103
Milk	130	2	260	712	2,8	1995
Beef	30	2	60	164	8,5	1397
Pork	60	2	120	329	12	3945
Total	**-**	**-**	**-**	**-**	**-**	**9989**

Tab. 49 Comparison of dose conversion factors for different diets (normal, vegan, enhanced meat) for the temperate climate

Radionuclide	Dose conversion coefficient (Sv a^{-1} per Bq m^{-3})			Max/Min
	Normal diet	Vegan diet	Meat diet	
C-14	$7.5 \cdot 10^{-7}$	$5.7 \cdot 10^{-7}$	$9.5 \cdot 10^{-7}$	1.66
Cl-36	$2.3 \cdot 10^{-6}$	$1.5 \cdot 10^{-6}$	$3.2 \cdot 10^{-6}$	2.14
Ni-59	$1.2 \cdot 10^{-7}$	$1.5 \cdot 10^{-7}$	$9.1 \cdot 10^{-8}$	1.65
Se-79	$3.3 \cdot 10^{-6}$	$3.3 \cdot 10^{-6}$	$3.3 \cdot 10^{-6}$	1.01
Zr-93	$9.0 \cdot 10^{-7}$	$9.2 \cdot 10^{-7}$	$8.8 \cdot 10^{-7}$	1.04
Nb-94	$2.6 \cdot 10^{-5}$	$2.6 \cdot 10^{-5}$	$2.6 \cdot 10^{-5}$	1.01
Tc-99	$7.1 \cdot 10^{-7}$	$8.4 \cdot 10^{-7}$	$6.0 \cdot 10^{-7}$	1.40
Pd-107	$6.2 \cdot 10^{-8}$	$7.9 \cdot 10^{-8}$	$4.8 \cdot 10^{-8}$	1.65
Sn-126	$1.2 \cdot 10^{-4}$	$1.2 \cdot 10^{-4}$	$1.3 \cdot 10^{-4}$	1.04
I-129	$1.8 \cdot 10^{-4}$	$1.4 \cdot 10^{-4}$	$2.2 \cdot 10^{-4}$	1.53
Cs-135	$5.3 \cdot 10^{-6}$	$4.1 \cdot 10^{-6}$	$6.6 \cdot 10^{-6}$	1.63
Ra-226	$3.7 \cdot 10^{-4}$	$4.4 \cdot 10^{-4}$	$3.1 \cdot 10^{-4}$	1.42
Th-230	$2.6 \cdot 10^{-4}$	$2.8 \cdot 10^{-4}$	$2.5 \cdot 10^{-4}$	1.11
Pa-231	$6.3 \cdot 10^{-4}$	$6.7 \cdot 10^{-4}$	$5.9 \cdot 10^{-4}$	1.14
U-238	$4.2 \cdot 10^{-5}$	$4.5 \cdot 10^{-5}$	$3.9 \cdot 10^{-5}$	1.14
Np-237	$9.5 \cdot 10^{-5}$	$1.0 \cdot 10^{-4}$	$9.0 \cdot 10^{-5}$	1.13
Am-243	$1.7 \cdot 10^{-4}$	$1.7 \cdot 10^{-4}$	$1.6 \cdot 10^{-4}$	1.08
Pu-239	$2.0 \cdot 10^{-4}$	$2.1 \cdot 10^{-4}$	$1.9 \cdot 10^{-4}$	1.08

8.5 Discussion and conclusions

In this study, the impact of different climates on dose conversion factors for assessing radiation exposures to reference persons is calculated. Two geosphere-biosphere interfaces (GBIs) are considered:

- Radionuclides enter the biosphere via withdrawal of contaminated groundwater
- In case of a high water table, radionuclides enter the biosphere directly and cause contaminations of soils

For both GBIs, the exposure via ingestion, inhalation of resuspended contaminated soil particles and external exposure due to stay on contaminated land is taken into account. For the estimation of the ingestion dose, it is assumed that contaminated groundwater is used as drinking water for humans and cattle, irrigation water and host water for fish production.

In order to address the influence of the climate, the dose conversion factors were determined for a wide spectrum of climates. Detailed calculations were done for steppe, Mediterranean, boreal and tundra climate. Data for temperature, precipitation, and humidity were taken from analogue stations which are today characterised by those climates.

The calculations of the dose conversion factors are performed for the radionuclides C-14, Cl-36, Ni-59, Se-79, Zr-93, Nb-94, Tc-99, Pd-107, Sn-126, I-129, Cs-135, Ra-226, Th-230, Pa-231, U-238, Np-237, Am-243, and Pu-239. From the calculations, the following conclusions can be drawn:

Present day climate (temperate)

- For the GBI “well”, ingestion is the most important pathway with the exception of Nb-94, for which external exposure is by far dominating.
- Among ingestion, the intake of drinking water is most important but C-14, Cl-36, Ni-59, Pd-107, I-129, and Cs-135.
- In general, the ingestion of plant food products is more important than the intake of animal food products.
- Fish is only a relevant contributor for C-14.

- The inhalation of resuspended soil particles is of minor importance for all radionuclides. The highest contributions are about 2 % for Pu-239 and Am-243 respectively.
- For the GBI “rising groundwater”, the ingestion pathway is by far dominating with the exception of Nb-94 and Sn-126. Among ingestion, the intake of contaminated drinking water is the most important contributor but for Cl-36, Ni-59, Tc-99, Pd-107, Cs-135, Ra-226.
- The ingestion of plant food products is important for Ni-59, Se-79, Tc-99, Cs-135, Ra-226, and Pa-231. Animal food products are relevant especially for Cl-36 and Cs-135.
- The inhalation of resuspended soil particles is an important pathway for Th-230, Pa-231, U-238, Np-237 and Am-243. The highest contribution is found for Pa-231. This is due to the high accumulation of Pa-231 in soil caused by high K_d-value and a rapidly achieved equilibrium with its daughter nuclide Ac-227, which has a very high inhalation dose factor.

Modified climates

For modified climates, the dose conversions factors vary considerably. For analysing the impact, the geosphere-biosphere interfaces “well” and “rising groundwater” have to be considered separately.

For the GBI “well”, the highest variations between the different climates are found for C-14, Cl-36, Nb-94, Cs-135 and for the redox-sensitive radionuclides Se-79, Tc-99, and I-129. The variations are caused especially by several factors:

- Due to the different climatic conditions the input of radionuclides to soil via irrigation of crops varies considerably by a factor of about 6, which has a direct impact on the exposure via ingestion of foods (except drinking water), inhalation and external exposure.
- The root uptake and migration of Se-79, Tc-99, and I-129 depends largely on the soil characteristics. The root uptake of selenium and technetium is enhanced on well aerated and dry soil, as it is the case for steppe climate. In this case selenate and pertechnetate are the predominating chemical species which are readily available for root uptake. At the same time, due to the aridity, the migration to deeper soil layers is reduced compared

to the other climates. For I-129, root uptake is highest in wet and water-logged soils which occur especially under cold climates.

- The intake rates for the reference climates are different. For steppe climate a daily water consumption of 3 l d^{-1} is assumed compared to 2 l d^{-1} for the other climates to account for the higher water demand under hot conditions. Furthermore, in the steppe climate, the husbandry of small ruminants as sheep and goat is relevant. The transfer of some elements to sheep and goat is much higher than to beef, which causes an increased radionuclide intake by humans. Among the radionuclides considered in this study, this is especially the case for cesium and iodine.

The variations among all climates for Ra-226, Th-230, Pa-231, U-238, Np-237, Am-243, and Pu-239 are relative small; mostly the differences are less than a factor of 5. In general, the transfer for these radionuclides through food chains is relatively low, and the mobility within the plant subsequent to foliar deposition is low as well. Therefore, the intake of radionuclides with drinking water dominates over the other ingestion pathways. This does not mean that root uptake and migration are not influenced by environmental conditions, but even under conditions that cause enhanced transfers of actinides, the transfer to man remains relatively low.

For the GBI „rising groundwater", the steppe climate is not taken into account, since the assumption of hot climate and agriculture on areas affected by groundwater appears somewhat contradictory. For this interface, the variations among the climates are low, with the exception of the radionuclides C-14, I-129, and Cs-135, whose dose conversion factors are by far highest for tundra climate.

- For C-14, the high exposure for tundra climate is due to the high consumption of fish, which accumulates C-14 considerably.

- For I-129, and Cs-135 the strong increase is caused by their different behaviour in soil. Under the conditions of tundra climate, in wet and water-logged soils, the predominant iodine species is iodide which is readily available for root uptake. The transfer factors of cesium are also considerably enhanced for the low pH and high organic matter found in tundra climate, which causes high concentrations in grass and reindeer, berries and mushrooms.

The exposure due to inhalation of resuspended soil particles is less important than for the GBI “well”. The erosion and therewith the resuspension of contaminated soil particles is reduced due to the wetter soil surfaces caused by the high groundwater levels.

The processes causing radionuclide transfer to man vary considerably among the climates, and they vary to a larger extent than the results of the nuclide-specific dose conversion factors may suggest. Some of the processes compensate each other at least to some extent:

- In general, with increasing sorption capacity, the bioavailability of radionuclides decreases, i.e. the long-term accumulation is high, but the uptake by plants is low. This is especially valid for mineral soils. However, in organic soils, the sorption capacity is high as well, but the sorption is relatively weak and the radionuclides are still available for root uptake.
- In arid climates, migration to deeper soil layers is reduced due to the decreasing downward water movement, which causes a higher accumulation in soil. However, at the same time, dry soils are more vulnerable to wind erosion, which may cause considerable soil losses and therefore compensates the higher accumulation.
- Food intake rates widely vary in different population groups and climates. Some foods are well known for their potential to accumulate large amounts of radionuclides. Examples are the accumulation of cesium in berries and mushroom, of iodine in milk, and of selenium and technetium in plants. However, if people consume more from one food item, they usually eat less from another. Therefore, the impact of increased radionuclide contents in specific foods is mostly less than linear, since the exposure is always due to different pathways.

In many cases, the intake of drinking water is an important, if not the dominating pathway. This is especially true for radionuclides with a low transfer through the food chain. Drinking water consumption varies only little in the different climate states. The consideration of drinking water has a “smoothing” effect. Since it is nearly constant, it reduces the relative differences among the climate-GBI-combinations.

Impact of specific diets

For the GBI “well” in the temperate climate, the impact of modified intake rates on the resulting dose conversion factors was investigated. For this purpose, the dose conversion factors for an average diet are compared with a vegan and a meat-enhanced diet. The

energy intake in all diets considered varies within 10 %. The maximal impact was a about a factor of 2, for most radionuclides considered the difference is in the range of 10 to 50 %.

Impact of geosphere-biosphere interface

The dose conversion factors for the GBIs “well” and “rising groundwater” differ considerably for C-14, Cl-36, Ni-59, Se-79, Nb-94, Tc-99, Sn-126, I-129, Cs-135, Ra-226, and Np-237. For the same climate, the ratios of the dose conversion factors for “well” and “rising groundwater” vary from 0.0005 to 63. For the temperate and the boreal climates, in general, the GBI “well” causes higher dose conversion factors, whereas in case of the tundra climate, dose conversion factors are higher, if the radionuclides enter the biosphere via GBI “rising groundwater”.

Requirement of well water

The requirement of water has been estimated for the GBI “well”. For this purpose, a group of 50 people is assumed that consume only locally produced foods. To enable sustainability, an area of 10,000 m^2 is assumed for herds of cattle. The water use in the household is taken into account. Under those circumstances a well with a relatively little capacity of less than 5 l s^{-1} is needed in case of temperate climate, the most arid climate considered in this study, a well capacity of less than 10 l s^{-1} is needed.

Other studies

In a comparative study, /BEC 03/ compared the radiological impact of radionuclide releases from waste repositories based on generic biosphere models. Geosphere-biosphere interfaces considered are the withdrawal of water from a well and flooding of both, natural and agricultural land. In this study, it is assumed that radionuclides enter the biosphere due to withdrawal of contaminated well water and due to flood events. Contamination of the biosphere by rising water is not taken into account. The modelling of the transfer processes is mainly based on the draft of a simple radioecological model that is used in Germany during licensing of nuclear facilities. Interactions of the radionuclide processes as root uptake, migration and climatic features are not taken into consideration.

In the framework of the long-term performance assessment study for a nuclear waste disposal in Sweden, the interaction of climatic conditions and changes in the landscape with the potential exposure is considered in great detail /AVI 06/, /JAN 06/, /KAR 06/. The radionuclide flux through an evolving landscape is modelled. The biosphere changes during the temperate of an interglacial period are simulated by biosphere models for the projected sequence of environmental conditions. The transfer of radionuclides is simulated by a series of connected dynamic models representing ecosystems as sea, lakes, rivers, mires, agricultural land and forest. The uncertainty of the characteristics of the geosphere-biosphere interface is taken into account, the radionuclide access to the biosphere is assumed to vary in time and space. The transformation between different environmental situations is simulated by discrete events occurring every thousand years. Finally, the potential contributions of the different ecosystems to the exposure of man are estimated.

Remaining problems and future needs

For radionuclides which are strongly sorbed in soil, the dose conversion factors vary only relatively little among different climate states and geosphere-bisophere interface. However, the variations are much more pronounced for a number of anionic, redox-sensitive radionuclides and for C-14, Nb-94 and Cs-135. This holds for both geosphere-biosphere interfaces considered.

The key parameters for all radionuclides and geosphere-biosphere interfaces are especially those that control the long-term behaviour of radionuclides in soil, i.e. the transfer factors soil-plant, migration parameters in soil and wind erosion. In this context, the radionuclide speciation in soil is of particular importance. However, data on the interaction of radionuclide speciation, soil characteristics, climate and agricultural practice are poor; therefore predictions of the long-term behaviour in soil are associated with large uncertainties.

In the framework of this study, deterministic calculations were made. The results do not allow an estimation of the uncertainties, which would be needed for a more comprehensive evaluation of the results.

In order to estimate the influence of climate changes on the potential radiological impact to man, the calculations were made for selected stationary climates. However, this approach neglects the climatic and environmental conditions of transition periods, which may be short in relation to geological developments but long in relation to the lifetime of humans. During

those transition periods, the rapid change of environmental conditions may cause the mobilization of strongly bound radionuclides due to drastic modifications of the chemical milieu. This may cause much higher radiation exposures than those calculated for the stationary climates considered in this study. Examples for those transition periods are the aggradation of lakes with subsequent use for agriculture, the development of steppe and deserts, or the alteration of terrestrial ecosystems to aquatic ecosystems subsequent to flooding. These examples are far from being complete, but they underline that a systematic analysis of environmental changes and their implications for long-term performance studies of nuclear repositories is needed.

Those issues are already addressed in long-term performance assessment studies as e.g. carried out in Sweden /AVI 06/, /JAN 06/, /KAR 06/. This approach appears to be most comprehensive for assessing the radiological impact due to releases of radionuclides from nuclear waste repositories to the biosphere.

9 Summary and conclusions

The objective of this study was to assess possible effects of climatic changes on a hypothetical repository in salt at a potential site in Northern Germany. Main focus was to study the impact on flow and transport processes in the overburden of the salt dome and on processes in the biosphere. It is not relevant for a normal evolution of a repository for heat generating waste, where a complete confinement of the waste is reached by closure of all void volumes and transport pathways due to convergence of rock salt. However, in a safety case also altered scenarios with radionuclide mobilisation and release from the host rock, which cannot be fully excluded, need to be considered.

Due to the comprehensive information about geological, hydrological and near-surface characteristics available the Gorleben site was chosen as reference site for this study. The work comprised

- a description of the main factors influencing the climate,
- an evaluation of paleodata and a compilation of ancient climates within the last several 100,000 years and their impacts on the reference site,
- a brief discussion of climate models, their capabilities and prognoses performed for very long time scales relevant for performance assessment,
- identification and characterisation of potential future climate states at the reference site, and
- development of flow and transport models as well as biosphere models for the selected climate states and numerical calculations with these models to identify the impact of the respective climate states.

The primary factors affecting the long-term climate evolution for time scales > 10,000 years up to one million years are the orbital parameters. The impact of the orbital parameters on the average insolation and the resulting cyclic changes between glacials and interglacials can be described by the Milankovich theory. Due to this theory, the occurrence of glacials is correlated with insolation minima in summer in 65° Northern altitude. Corresponding climate data from Antarctic ice cores can be reproduced by model calculations, assuming a transition into an ice age when summer insolation at 65°N fell below a critical value. Currently, the impact of anthropogenic factors on the climate evolution, especially of the greenhouse gases, raises increasing interest. It is discussed and shown by some model calculations that

very high anthropogenic emissions in the next decades/centuries might cause long-term changes of the climate over several tens of thousand up to hundred thousand years. Furthermore, the amplitude of insolation (and therewith the insolation minima) is comparably low for the next 50,000 years due the currently low eccentricity of the earth's orbit. As a consequence, most climate scientists and modellers do not expect the next glacial within the coming 50,000 years.

However, due to the high uncertainty covered with climate modelling, especially over such long time frames, special attention was also drawn to paleo-climatological information about glacials and interglacials from Quaternary and Holocene. During the Quaternary cycles the time frame of glacials has exceeded those of interglacials by far. The last interglacials covered time frames of app. 10,000 years, whereas interglacials occurred over time periods of 60,000 to 100,000 years. The analyses also showed that there is no representative glacial/interglacial cycle for the considered site, but distinct differences between the cycles occurred.

The Elsterian and the Saalian glacials caused a several 100 m thick ice cover above the reference site for a time period of about 10,000 years, whereas the glaciers of the last glacial (Weichselian) did not extend that far and left the site without an ice cover. During such glacial time periods without ice cover, periglacial conditions with permafrost down to a depth of 40 m to 140 m have prevailed for several ten thousand years at the site. The formation of glaciers led to a strong subsidence of the sea-level, which caused values about 110 m to 140 m lower than today at the past glacial maxima. The increasing distance of several 100 km to the sea led to an increasingly continental climate at the reference site.

There appeared also strong differences between the last interglacials. Whereas during the warmest period of the Holsteinian interglacial a transgression of the North Sea occurred at the reference site, this was not the case during the Eemian Interglacial. Whether a future climate optimum will lead to a transgression of the site mainly depends on the amount of deglaciation of currently existing glaciers. A retreat of all glaciers existing today, which may not be expected according to the actual state of knowledge but occurred in earlier times, would result in a sea level rise of about 70 m. Due to the low elevation of the region Gorleben this might cause a maximum sea-level of 50 m above today´s ground.

Flow and transport modelling in the overburden of the salt dome requires a large effort for the development of models and in particular high computing costs for modelling of each climate state. Therefore this part of the investigation was restricted to few selected models for

extreme climate states, where significant differences in the models and the simulation results have been expected. Based on the paleoclimatic information discussed above the following climate stages have been selected:

- continuation of the climate conditions occurring today (as reference),
- a warmer interglacial state with a potential maximum sea level (leading to transgression of the reference site), and
- a glacial state accompanied by the formation of a glacier similar to a Weichselian one with formation of permafrost in front of the glacier.

In order to analyse the effects of the selected climate states conceptual models for flow and transport have been developed, implemented into the codes d^3f and r^3t, and exploratory calculations have been performed for the three climate states. A simplified 2D hydrogeological model of 16.4 km lateral extension and 400 m thickness with an upper and lower aquifer and a separating clay aquitard in between was applied. Due to uncertainties about the location of hydraulic connections in the argillaceous aquitard layer between the upper and lower aquifer two models, model 1 with only one and model 2 with two hydraulic windows, have been applied. The calculations have been performed for time periods of several 100,000 years. It was assumed, that each climate state did not change during this time. This allowed the detailed investigation of relevant effects and processes and principle differences in flow and transport caused by each climate state. For the transport calculations a limited number of radionuclides with different sorption properties was regarded and the impact of changes in groundwater mineralisation on the K_d-values was taken into account.

The results show that groundwater flow and radionuclide transport are strongly different in the models for the different climate states. Major differences occur in the dominating transport mechanism (advection vs. diffusion) but also in flow direction and radionuclide retardation causing different arrival locations in the near-surface aquifer. The important role of sorption is illustrated by the difference between the strongly sorbing radionuclide Zr-93 and the weakly sorbing I-129. Whereas Zr-93 in no case reaches the model surface within 1 million years, I-129 arrives their in all climate states.

Under climate conditions, as they occur today, stationary states of the flow field and salt concentrations are reached after about 150,000 to 200,000 years. The dominant transport process is advection. The impact of hydraulic windows is quite strong, since they cause different flow directions of the groundwater. In model 1 the single hydraulic window in the

southern part causes transport in southern direction and radionuclide arrival at the surface in the south, whereas in model 2 with two hydraulic windows the preferred flow direction is northwards causing radionuclide arrival at the surface above the northern hydraulic window. However, all radionuclides except Zr-93 reach the surface within 1 million years.

In the warmer climate state assuming a flooding of the reference site with a 50 m high column of sea water diffusion processes dominate in the whole model area so that more than 700,000 years are required to reach stationary salt concentrations. A stationary flow field, however, is reached after less than 50,000 years. Radionuclide transport by diffusion is comparably slow demonstrated by the fact that only weakly sorbing I-129 and the uranium isotopes (with their daughters) reach the model surface within 1 million years. Since diffusion dominates the results for model 1 and 2 are similar, i.e. the number of hydraulic windows in the aquitard is nearly of no relevance for this climate state.

For the cold climate with periglacial conditions it is assumed that the permafrost extends over the entire thickness of the upper aquifer of 100 m. For permafrost zones a reduction of permeability from 10^{-12} m² to 10^{-20} m² is assumed. However, unfrozen zones, so-called taliks, form in the upper aquifer below the river Elbe and Seege which maintain their original permeability of $1 \cdot 10^{-12}$ m². For the aquitard and the lower aquifer no permafrost conditions are assumed. A second characteristic of the model is a high freshwater inflow into the lower aquifer at the northern edge of the model area caused by the nearby glaciers. As a result higher advection velocities in the unfrozen lower aquifer occur than in the other climate states. Under such conditions the number and the position of the hydraulic windows are also of high relevance. Together with the extension and position of the taliks in the upper aquifer, they determine the flow velocity in the lower aquifer and the distribution of the salt concentration. For model 2 fresh water conditions occur in the aquitard and the upper aquifer. In this case Cs-135 do not reach the surface due to its increased sorption values under freshwater conditions and of course due to the reduced transport velocity in the low permeable frozen upper aquifer.

For biosphere modelling in total six different climate states, i.e., steppe (BS), Mediterranean (Cs), temperate (Cfb), boreal (Dfa/Dfb), and tundra (ET), have been considered, respectively. Data for potential future distribution of temperature, precipitation, and humidity were taken from so-called analogue stations, which are characterised by those climates today: Marrakesh, Rome, Magdeburg, Rostow, Turku and Vardo, respectively. The conditions of the reference site have been also considered by the current soil properties and potential developments.

Two geosphere-biosphere interfaces (GBIs) have been considered:

- Radionuclides enter the biosphere via withdrawal of contaminated groundwater (“well”)
- radionuclides enter the biosphere directly in case of a high water table and cause contaminations of soils (“rising groundwater”)

For both GBIs, the exposure via ingestion, inhalation of resuspended contaminated soil particles and external exposure due to stay on contaminated land was taken into account. For the estimation of the ingestion dose, it was assumed that contaminated groundwater is used as drinking water for humans and cattle, irrigation water and host water for fish breeding.

For all climate states dose conversion factors were calculated by different biosphere models. The impact of the climate state on the biosphere modelling was considered by differences in the

- consumption habits,
- required irrigation amounts and duration of the growth period,
- considered exposition pathways and GBIs,
- parameters for radionuclide behaviour in soils (migration and transfer to the plant), for erosion and resuspension, and feeding rations for animals.

The results show that the variations among all climates for Ra-226, Th-230, Pa-231, U-238, Np-237, Am-243, and Pu-239 are relatively small; mostly the differences are less than a factor of 5. In general, the transfer for these radionuclides through food chains is relatively low, and the mobility within the plant subsequent to foliar deposition is low as well. Therefore, the intake of radionuclides with drinking water dominates over the other ingestion pathways. This does not mean that root uptake and migration are not influenced by environmental conditions, but even under conditions that cause enhanced transfers of actinides, the transfer to man changes only slightly.

The results further show that the dose conversions factors for other radionuclides vary considerably for the different climate states. This variation is strongly dependent on the different geosphere-biosphere interfaces. For the temperate and the boreal climates, the interface “*well*” causes higher dose conversion factors, whereas in case of the tundra climate, dose conversion factors are higher for the interface “*rising groundwater*”.

For the GBI “well”, the highest variations between the different climates are found for C-14, Cl-36, Nb-94, Cs-135 and for the redox-sensitive radionuclides Se-79, Tc-99, and I-129. Variations are caused especially by the following factors:

- Due to the differences in temperature, precipitation and evapotranspiration at the analogue stations the irrigation rates and therewith the input of radionuclides to soil varies considerably by a factor of about 6, which has a direct impact on the exposure via ingestion of foods, inhalation and external exposure.
- The root uptake and migration of Se-79, Tc-99, and I-129 depends largely on the soil characteristics. The root uptake of selenium and technetium is enhanced on well aerated and dry soil, as it is the case for steppe climate. In this case selenate and pertechnetate are the predominating chemical species which are readily available for root uptake. At the same time, due to the aridity, the migration to deeper soil layers is reduced compared to the other climates. On the other hand for I-129, root uptake is highest in wet and water-logged soils which occur especially under cold climates.
- The intake rates for the reference climates are different. For steppe climate a daily water consumption of 3 l d^{-1} is assumed compared to 2 l d^{-1} for the other climates to account for the higher water demand under hot conditions. Furthermore, in the steppe climate, the husbandry of small ruminants as sheep and goat is relevant. The transfer of some elements to sheep and goat is much higher than to beef, which causes an increased radionuclide intake by humans. Among the radionuclides considered in this study, this is especially the case for Cs-135 and I-129.

These factors cause maximum differences of more than two orders of magnitude in the dose conversion factors for the interface “well”. Highest differences occur for the radionuclides Se-79, C-14, Tc-99, Cl-36, Nb-94 and Cs-135.

For the GBI “rising groundwater”, the steppe climate is not taken into account, since the assumption of hot climate and agriculture on areas affected by groundwater appears somewhat contradictory. For this interface, the variations among the climates are low, with the exception of the radionuclides C-14, I-129, and Cs-135, whose dose conversion factors are by far highest for tundra climate.

- For C-14, the high exposure for tundra climate is due to the high consumption of fish, which accumulates C-14 considerably.

- For I-129, and Cs-135 the strong increase is caused by their different behaviour in soil. Under the conditions of tundra climate, in wet and water-logged soils, the predominant iodine species is iodide which is readily available for root uptake. The transfer factors of cesium are also considerably enhanced for the low pH and high organic matter found in tundra climate, which causes high concentrations in grass and reindeer, berries and mushrooms.

For the GBI “rising groundwater” by far highest differences in dose conversion factors for the different climate states are found for Cs-135 with nearly three orders of magnitude and for I-19 with more than two orders of magnitude. The differences for all other radionuclides are below one order of magnitude.

This first study on the implications of different future climate states on the long-term safety of radioactive waste repository in rock salt was restricted to the processes in the overburden and the biosphere, where highest impact is expected. It was also restricted to the consideration of single discrete climate states. However, yet it is not clear, which effects the transfer between different climate states might cause. Therefore, in a future project the investigation of transient conditions for flow and transport in the overburden as well as for the biosphere processes is planned. It is also foreseen to further study potential repercussions of the geosphere on the biosphere processes.

Moreover, in a later step, a complex flow and transport model representing a more detailed description of the hydrogeological characteristics at the site should be used to simulate flow and transport. It will be evaluated if additional effects and processes might play a role, which do not occur in the simplified model applied here.

10 References

/AAL 98/ Aalbergsberg, G.; Litt, T.: Multiproxy climate reconstructions for the Eemian and Early Weichselian. Journal of quaternary science, Vol. 13(5), S. 367-390, 1998.

/AAR 69/ Aarkrog, A.; Lippert, J.: The direct contamination of rye, barley, wheat and oats with Sr-85, Cs-134, Mn-54 and Ce-141. Rad. Bot. 9:357-366; 1969.

/AAR 71/ Aarkrog, A.; Lippert, J.: Direct contamination of barley with Cr-51, Fe-59, Co-58, Zn-65, Hg-203, and Pb-210. Rad. Bot. 11:463-472; 1971.

/AAR 72/ Aarkrog, A.: Direct contamination of barley with Be-7, Na-22, Cd-115, Sb-125, Cs-134 and Ba-133. Risø, Denmark: Risø National Laboratory, Risø-R-256:163-175; 1972.

/AAR 75/ Aarkrog, A.: Radionuclide levels in mature grain related to radiostrontium content and time of direct contamination. Health Physics 28(1975), 557-562.

/ACH 80/ Achtnich, W.: Bewässerungslandbau. Ulmer Verlag, 1980.

/AKE 02/ AKEND: Auswahlverfahren für Endlagerstandorte – Empfehlungen desArbeitskreis Auswahlverfahren Endlagerstandorte (AKEND), Abschlußbericht. Langfassung, 260 p., Dezember 2002.

/ALL 02/ Alley, R.; Bender, M.L.: Grönlands eisige Klima-Archive. Spektrum der Wissenschaft, Dossier: Klima, S. 42-47, 2002.

/ANG 77/ Angeletti, L.; Levi, E.: Etude comparative des facteurs de transfert de l`eau, de l'iode et du strontium sur le ray-´grass et le trèfle. Centre d'Etude Nucléaires, Fontenay-aux-Roses, France, Rapport CEA-R-4860, (1977).

/ARC 05a/ Archer, D.; Ganopolski, A.: A movable trigger: Fossil fuel CO2 and the onset of the next glaciation. Geochem. Geophys. Geosys. 6, Q05003, doi:10.1029/2004GC000891, 2005.

/ARC 05b/ Archer, D.: Fate of fossil fuel CO2 in geologic time. J. Geophys Res. doi:10.1029/2004JC002625, 2005.

/AVI 06/ Avila, R.; Kautsky; U.; Ekström, P.A.: Modeling the long-term transport and accumulation of radionuclides in the landscape for derivation of dose conversion factors. Ambio, 35, 513-523, 2006.

/BAT 99/ Bath, A.; Boulton, G.; Marivoet, J.; Bloomqvist, R.: “What Approach and Tools Do We Have For Understanding the Past Evolution of Groundwater Systems as a Guide to Future Evolution for Repository Performance Assessment?” In Euradwaste 1999 ‘Radioactive Waste Management Strategies and Issues’ (C. Davies, ed.), Proc. Conference Luxembourg, CEC Report EUR 19143 EN, S. 257-273, 1999.

/BEC 03/ Becker, A.: Beitrag zur Erstellung einer Referenzbiosphäre zur Berechnung der in der Nachbetriebsphase eines Endlagers für radioaktive Stoffe hervorgerufenen potentiellen Strahlenexposition unter Berücksichtigung des Einflusses des Klimas. BMU (Ed.), Schriftenreihe Reaktorsicherheit und Strahlenschutz, BMU-2003-623, 2003.

/BEH 04/ Behre, K.-E.: Eine neue Meeresspiegelkurve für die südliche Nordsee-Transgressionen und Regressionen in den letzten 10 000 Jahren. Probleme der Küstenforschung im südlichen Nordseegebiet 28, S. 9-63, Oldenburg 2003.

/BER 04/ Berner, U.; Streif, H.J. (eds.): Klimafakten, Der Rückblick – Ein Schlüssel für die Zukunft. BGR, GGA, NLfB, 4. Auflage,. Schweizerbart'sche Verlags-buchhandlung, Stuttgart 2004.

/BER 97/ Berger, A.; Loutre, M.F.: Paleoclimate sensitivity to CO2 and insolation. Ambio, 26, 32-37, 1997.

/BER 02/ Berger, A.; Loutre, M.F.: An exceptionally long interglacial ahead? Science 297, 1287-1288, August 2002.

/BGR 07a/ Bundesamt für Geowissenschaften in http://www.bgr.bund.de/cln_006/DE/Themen/Boden/Produkte/Karten/Downloads/BAG5000,templateId=raw,property=publicationFile.pdf/BAG5000.pdf, date of access: 2007.

/BGR 07b/ Bundesamt für Geowissenschaften in http://www.bgr.bund.de/cln_006/DE/Themen/Boden/Produkte/Karten/Downloads/BGL5000,templateId=raw,property=publicationFile.pdf/BGL5000.pdf, date of access: 2007.

/BIO 01a/ BIOCLIM: Modelling sequential biosphere systems under climate change for radioactive waste disposal. Environmental change analysis. Deliverable D1, 2001.

/BIO 01b/ BIOCLIM: Global climatic features over the next million years and recommendation for specific situations to be considered. Deliverable D3, 2001.

/BIO 04/ BIOCLIM: Development and Application of a Methodology for Taking Climate-Driven Environmental Change into Account in Performance Assessments. Deliverable D10-12. 2004.

/BIR 04/ Birthler, H.; Schneider, A.: Modellrechnungen zur großräumigen dichteabhängigen Grundwasserbewegung. GRS-191, ISBN3-931995-59-3, 2003.

/BIR 00/ Birthler, H., Fein, E., Schneider, A.: Validierung von Einzeleffekten in Grundwassermodellen. GRS-150, Gesellschaft für Anlagen- und Reaktorsicherheit (mbH), Braunschweig 2000.

/BMU 05/ BMU (Bundesminister für Umwelt, Naturschutz und Reaktorsicherheit): Allgemeine Verwaltungsvorschrift zu § 47 Strahlenschutzverordnung: Ermittlung der Strahlenexposition durch die Ableitung radioaktiver Stoffe aus kerntechnischen Anlagen oder Einrichtungen. Bundesanzeiger 42 (Nr. 64a), 1990, Uberarbeiteter Entwurf vom Mai 2005.

/BOG 81/ Bogenrieder, A.: Bodenversalzung in der Bewässerungslandwirtschaft arider Zonen. Naturwissenschaftliche Rundschau, 35(1982), 103-109.

/BON 02/ Bond, G., Kromer, B., Beer, J., Muscheler, R., Evans, M.N., Showers, W., Hoffmann, S., Lotti-Bond, R., Hajdas, I., and Bonani, G.: Persistent solar influence on North Atlantic climate during the Holocene. Science, 294, 2130-2136, 2001.

/BOS 01/ Bos, J.A.A.; Bohncke, S.J.P.; Kasse, C.; Vanderberghe, J.: Vegetation and climate during the Weichselian Early Glacial and Pleniglacial in the Niederlausitz, eastern Germany-macrofossil and pollen evidence. Journal of quaternary science, Vol. 16(3), S. 269-289, 2001.

/BUH 08a/ Buhmann, D., Mönig, J., Wolf, J.: Untersuchungen zur Ermittlung und Bewertung von Freisetzungsszenarien. Teilbericht zum Projekt ISIBEL "Überprüfung und Bewertung des Instrumentariums für eine sicherheitliche Bewertung von Endlagern für HAW". GRS-233, Gesellschaft für Anlagen- und Reaktorsicherheit (mbH), Braunschweig, 2008.

/BUH 08b/ Buhmann, D.; Mönig, J.; Wolf, J.; Keller, S.; Weber, J. R.; Eberth, S.; Kreienmeyer, M.; Krone, J.; Tholen, M.: FEP-Katalog für einen HAW-Standort im Wirtsgestein Salz. Version 01. Gemeinsamer Bericht von DBE TECHNOLOGY GmbH, BGR und GRS. Peine, Hannover, Braunschweig, April 2008.

/BUN 92/ Bunzl, K.; Kracke, W.; Schimmack, W.: Vertical migration of 239/240Pu, 241Am and 137Cs fallout in a forest soil under spruce. Analyst. 117, 469-474, 1992.

/BUN 94/ Bunzl, K.; Förster, H.; Kracke, W.; Schimmack, W.: Residence times of fallout 239/240Pu, 238Pu, 241Am and 137Cs in the upper horizons of an undisturbed grassland soil. J. Environm. Radioact. 22, 11-27, 1994.

/BUN 95a/ Bunzl, K.; Kracke, W.; Schimmack, W.; Auerswald, K.: Migration of 239/240Pu, 241Am and 137Cs in the various horizons of a forest soil under pine. J. Environm. Radioact. 28, 17-34, 1995a.

/BUN 95b/ Bunzl, K.; Kofuji, H.; Schimmack, W.; Tsumura, A.; Ueno, K.; Yamamoto, M.: Residence times of global weapons testing fallout Np-237 in a grassland soil compared to Pu-239/240, Am-241 and Cs-137. Health Physics, 68, 89-93, 1995b.

/CAS 01/ Caspers, G.; Freund, H.: Vegetation and climate in the Early- and Pleni-Weichselian in northern central Europe, Journal of quaternary science. 16(1), 31-48, 2001.

/CED 04/ Cedecreutz, J.: Future climate scenarios for Olkiluoto with emphasis on permafrost. Posiva 2004-06, December 2004.

/CHO 83/ Chorlton, W.: Eiszeiten - Der Planet Erde. ISBN 9-06-182-488-5, Time Life Bücher, Amsterdam, 1983.

/CLA 02/ Claussen, M.; Mysak, L.A.; Weaver, A.J.; Crucifix, M.; Fichefet, T.; Loutre, M.-F.; Weber, S.L.; Alcamo, J.; Alexeev, V.A.; Berger, A.; Calov, R.; Ganopolski, A.; Goosse, H.; Lohmann, G.; Lunkeit, F.; Mokhov, I.I.; Petoukhov, V.; Stone, P.; Wang, Z.: Earth system models of intermediate complexity: closing the gap in the spectrum of climate models. Climate Dynamics 18, 579-586, 2002.

/CRO 05/ Crossland, I.; Pinedo P.; Kessler, J.H.; Torres-Vidal, C.; Walters, B.: "Reference biospheres" for solid radioactive waste disposal. J. Environmental Radioact. 84, 135-150, 2005.

/CRU 02/ Crucifix, M., Loutre, M.F.; Tulkens, P.; Fichefet, T.; Berger, A.: Climate evolution during the Holocene: a study with an Earth system model of intermediate complexity, Climate Dynamics, 19(1), 43-60, 2002.

/DAH 98/ Dahl-Jensen, D.; Mosegard, N.; Gundestrup, N.; Clow, G.D.; Johnson, S.J.; Hansen, A.W.; Balling, N.: Past temperatures directly from the Greenland Ice Sheet. Science, 282(5387), 268-271, 1998.

/DAV 67/ Davies, S. & De Wiest, R.: Hydrogeology. John Wiley & Sons Inc. New York – London – Sydney. 463 p., 1967.

/DEL 08/ http://www.bgr.bund.de/cln_011/nn_335066/sid_5D32BFBE1D64C00298F288C586EAA21D/DE/Themen/MeerPolar/Polarforschung/Arktis/Permafrost/permafrost__inhalt.html?__nnn=true, date of access: 2008.

/DEL 98/ Delisle, G.: Numerical simulation of permafrost growth and decay. Journal of Quarternary Science 13 (4), 325-333, 1998.

/DEL 91/ Delisle, G.: Causes and consequences of the advance of a continental ice sheet from Scandinavia to Northern Germany, Geol. Jb., A127, S. 507-517, Hannover 1991.

/DUA 07/ Duan, K. et al: A 1000 year history of atmospheroc sulfate concentrations in southern Asia as recorded by a Himalayan ice core. Geophysical Research Letters 34, L01810, doi:10.1029/2006GL027456, 2007.

/DUP 83/ Duphorn, K.; Schneider, U.: Zur Geologie und Geomorphologie des Naturparks Elbufer-Drawehn. erschienen in Abh. Naturwiss. Ver. (NF) 25: Mittelelbe und Drawehn-Lebensräume, Flora und Fauna im Hannoverschen Wendland (Kreis Lüchow-Dannenberg). S. 9-40, Verlag Paul Parey, Hamburg 1983.

/EHR 86/ Ehrlich, D. (1986): Entsorgung-Langzeitsicherheit von Endlagern Zeitrahmen für Sicherheitsbetrachtungen-Bewertung der Subrosion des Salzstocks Gorleben. Atomwirtschaft, S. 231-236, Mai 1986.

/EIS 08/ http://www.Eistobel.net, date of access: 2008.

/EMI 57/ Emiliani, C.: Temperature and Age Analysis of Deep-Sea Cores. Science 125, 383-87, 1957.

/EMI 66/ Emiliani, C.: Isotopic Paleotemperatures. Science 154, 851-57, 1966.

/ERT 92/ Ertel, J.; Paretzke, H.G.; Ziegler, H.: Cs-137 penetration by contact exchange through isolated plant cuticles: cuticles as asymmetric transport membranes. Plant, Cell and Environ. 15, 211-219, (1992).

/EUR 91/ EU (1991): Underlying data for derived emergency reference levels; Report EUR 12553, Luxembourg; ISBN 92-826-3116-8.

/FEI 04/ Fein, E. [Hrsg.]: Software Package r³t. Model for Transport and Retention in Porous Media. GRS-192, Gesellschaft für Anlagen- und Reaktorsicherheit (mbH), Braunschweig 2004.

/FEI 99/ Fein, E. & Schneider, A. [Hrsg.]: d³f – Ein Programmpaket zur Modellierung von Dichteströmungen. GRS-139, Gesellschaft- für Anlagen- und Reaktorsicherheit (mbH), Braunschweig 1999.

/FLU 09/ Flügge, J.: Radionuclide Transport in the Overburden of a Salt Dome – The Impacts of Extreme Climate States. Dissertation, TU-Braunschweig, in preparation.

/FOE 00/ Förster, M.-B.; Fraedrich, W.: Felseninsel Helgoland. Ein geologischer Führer.- Ferdinand Enke Verlag, Stuttgart 2000.

/FRA 82/ Franke, G.: Nutzpflanzen der Tropen und Subtropen. Hirzel Verlag Leipzig, 1982.

/GAN 07/ Ganopolski, A.: Persönliche Mitteilung vom 12.06.2007.

/GAN 01/ Ganopolski, A; Petoukhov, V.K.; Rahmstorf, S.; Brovkin, V., Claussen, M.; Eliseev, A.; Kubatzki, C.: CLIMBER-2: A climate system model of intermediate complexity. Part II: Model sensitivity. Clim. Dyn. 17, 735-751, 2003.

/GEI 83/ Geisler, G.: Ertragsphysiologie von Kulturarten des gemäßigten Klimas, Verlag Paul Parey Berlin und Hamburg 1983.

/GEI 88/ Geisler, G.: Pflanzenbau. Ein Lehrbuch – Biologische Grundlagen und Technik der Pflanzenproduktion. Verlag Paul Parey Berlin und Hamburg, 1988.

/GEO 06/ GEOkompakt, Nr.9: Wetter und Klima, 2006.

/GIL 74/ Gillette, D.; Blifford, I.; Fryrear, D.: The influence of wind velocity on the size distributions of aerosols generated by the wind erosion of soils. Journal of Geophysical Research 79, 4068-4075, 1974.

/GIS 90/ Gisi, U.: Bodenökologie. Georg Thieme Verlag, Stuttgart and New York, 1990.

/GOO 08/ Google Earth, date of access 2007.

/GOO 99/ Goodess, C.M.; Watkins, S.J.; Burgess, P.E., Palutikof, J.P.: Assessing the Long-Term Future Climate of the British Isles in Relation to the Deep Underground Disposal of Radioactive Waste. Climatic Research Unit, University of East Anglia, Norwich, NR47TJ, 12/1999.

/GRA 99/ GRAPE Manual. SFB 256, University of Bonn, 1999 http://www.iam.unibonn.de/grape/main.html. Bonn.

/GRO 06/ Grobe, H., AWI, http://de.wikipedia.org/wiki/Eiszeit, date of access 2006.

/GRU 01/ Grünhage, L.; Jäger, H.: Austausch von Stoffen zwischen Atmosphäre und Biosphäre. In: Guderian, R. (ed).: Handbuch von Umweltveränderungen und Ökotoxikologie, Band 2a. Terrestrische Ökosysteme: Immissionsökologische Grundlagen – Wirkungen auf Boden – Wirkungen auf Pflanzen, Springer Verlag Berlin, 2001.

/HAR 01/ Harff, J.; Frischbutter, A.; Lampe, R. & Meyer, M.: Sea-Level Change in the Baltic Sea: Interrelation of Climatic and Geological Processes. In: Gerhard, J. et al. [eds.]: Geological Perspectives of Climate Change. Amer. Ass. Petrol. Geol. Bull., Special Publ.: p. 231-250; Tulsa, Oklahoma. 2001.

/HAU 02/ Haug, G.H.; Tiedemann, R.; Zahn, R: Vom Panama-Isthmus zum Grönlandeis. Spektrum der Wissenschaft, Dossier: Klima, S. 50-52, 2002.

/HAU 05/ Haug, G.H.; Ganopolski, A. et al: North Pacific Seasonality and the Glaciation of North America 2.7 Million Years ago. Nature 433, 821-825, 2005.

/HER 00/ Herget, J.: Klimaänderungen in Mitteleuropa seit dem Tertiär. Petermanns Geographische Mitteilungen 144, 4/2000.

/HOF 95/ Hoffman, F.O.; Thiessen, K.M.; Rael, R.M.: Comparison of interception and initial retention of wet-deposited contaminants on leaves of different vegetation types, Atmospheric Environment 29, 1771-1775, 1995.

/HOH 05/ Hohl V.: Northern European long term climate archives, SKB TR-05-01, S. 391-417, 2005.

/HUI 98/ Huijzer, B.; Vandenberghe, J.: Climatic reconstruction of the Weichselian Pleniglacial in northwestern and central Europe. Journal of quaternary science, Vol. 13(5), 1998.

/IAE 08/ International Atomic Energy Agency: Radioecological models and parameters for radiological assessments. TECDOC, to be published, 2008.

/IAE 96/ International Atomic Energy Agency: Modelling of radionuclide interception and loss processes in vegetation and of transfer in semi-natural ecosystems, IAEA-TECDOC, Vienna, 1996.

/IMB 80/ Imbrie, J.; Imbrie, J.Z.: Modelling the climate response to orbital variations. Science 207, 943-953, 1980.

/ING 98/ Ingram, C.: Palaeoecology and geochemistry of shallow marine ostracoda from the Sand Hole Formation, Inner Silver Pit, southern North Sea. Quat. Sci. Rev. 17: 913-929, 1998

/IPC 01/ IPCC: University Press Cambridge, ISBN 0521014956, 2001.

/IPC 07/ IPCC: Climate Change 2007 - The Physical Science Basis. Contribution of Working Group I to the Fourth Assessment Report of the IPCC. 2007.

/JAN 06/ Jansson, U.; Kautsky, U.; Milliander, S.: Rural landscape, production and consumption: past, present and future. Ambio 35, 505-512, 2006.

/JAR 93/ Jaritz, W.: Die geowissenschaftliche Untersuchung des Salzstocks Gorleben auf seine Eignung für ein Endlager für radioaktive Abfälle - Stand 1993. Geologisches Jahrbuch A142, 295-304, 1993.

/JAR 80/ Jaritz, W.: Einige Aspekte der Entwicklungsgeschichte der nordwestdeutschen Salzstöcke, Z. dt. geol. Ges., No: 131, 387-408, Hannover 1980.

/JOU 07/ Jouzel, J. et al: Orbital and Millennial Antarctic Climate Variability over the Past 800.000 Years. Science 317, 793-796, 2007.

/KAP 61/ Kappelmeyer, O.: Geothermik. In: A. Bentz: Lehrbuch der Angewandten Geologie, 1: 863-889, Stuttgart, Enke 1961.

/KAR 06/ Karlberg, L.; Gustafsson, D.; Jansson, P.E.: Modelling carbon turnover in five terrestrial ecosystems in the boreal zone using multiple criteria of acceptance; Ambio, 35,448-458, 2006.

/KEE 05/ Keesmann, S., Noseck, U., Buhmann, D., Fein, E., Schneider, A.: Modellrechnungen zur Langzeitsicherheit von Endlagern in Salz- und Granitformationen. GRS-206, Gesellschaft für Anlagen- und Reaktorsicherheit (mbH), Braunschweig 2005.

/KEL 02/ Keller, S.: Ermittlung und Analyse von Szenarien für Endlagerstandorte mit unterschiedlichen Wirtsgesteinen (Deutschland) – Zusammenstellung von geologischen, klimatischen und hydrogeologischen ZEP. 1. Zwischenbericht, BGR, Hannover 2002.

/KEL 98/ Keller, S.: Permafrost in der Weichsel-Kaltzeit und Langzeitprognose der hydrogeologischen Entwicklung der Umgebung von Gorleben / NW-Deutschland. Z. Angew. Geol. 48, 111-119, 1998.

/KEL 94/ Kellogg, R.L.; TeSelle, G.; Goebel, J.J: Highlights from the 1992 national resources inventory. J. Soil and Water conservation, 49, 521-527, 1994.

/KLE 99/ Kleiner, S.: Water - An Essential But Overlooked Nutrient; J. of the American Dietetic Association, 99, 200-206, 1999.

/KLI 07/ Klinge, H., Boehme, J., Grissemann, C., Houben, G., Ludwig, R.-R., Rübel, A., Schelkes, K., Schildknecht, F. / Suckow, A.: Standortbeschreibung Gorleben, Teil 1: Die Hydrogeologie des Deckgebirges des Salzstocks Gorleben. Geologisches Jahrbuch: Reihe C, Hydrogeologie, Ingenieurgeologie, 71, 147 p., 2007.

/KLI 02/ Klinge, H.; Köthe, A.; Ludwig, R.-R.; Zwirner, R.: Geologie und Hydrogeologie des Deckgebirges über dem Salzstock Gorleben. Z. Angew. Geol. 48, 7-15, 2002.

/KOC 01/ Koch-Steindl, H.; Pröhl, G.: Considerations on the behaviour of long-lived radionuclides in the soil. J. Environm. Biophysics, 40,93-104, 2001.

/KOE 07/ Köthe, A., Hoffmann, N., Krull, P., Zirngast, M, Zwirner, R.: Gorleben, Teil 2: Die Geologie des Deckgebirges des Salzstocks Gorleben. Geologisches Jahrbuch: Reihe C, Hydrogeologie, Ingenieurgeologie: 72, 201 p., 2007.

/KOE 02/ Kösters, E., Vogel, P., Schelkes, K. 2D-Modellierung der paläohydrogeologischen Entwicklung des Grundwassersystems im Elberaum zwischen Burg und Boitzenburg. Fachbericht der Bundesanstalt für Geowissenschaften und Rohstoffe. Hannover. 61 S., 2000.

/KRA 83/ Kraus, O.: Abhandlungen des Naturwissenschaftlichen Vereins in Hamburg: (NF) 25; Mittelelbe und Drawehn-Lebensräume, Flora und Fauna im Hannoverschen Wendland (Kreis Lüchow-Dannenberg). Verlag Paul Parey Hamburg und Berlin, 1983.

/KUB 00/ Kubatzki, C.: Wechselwirkungen zwischen Klima und Landoberfläche im Holozän - Modellstudien. Dissertation, FU Berlin, September 2000.

/LEC 08/ Leclerc, E.; Colle, C.; Madoz-Escande, C.; Choi, Y.H.: Translocation. In: International Atomic Energy Agency: Radioecological models and parameters for radiological assessments, TECDOC, To be published. 2008.

/LEE 96/ Lee, J.L.; Phillips, D.L.; Dodson, R.F.: Sensitivity of the US Corn Belt to climate change and elevated CO2: II. Soil erosion and organic carbon. Agricultural Systems, 52, 503-521, 1996.

/LEE 01/ Leermakers, M., Galletti, S., De Galan, S., Brion, N., Baeyens, W.: Mercury in the Southern North Sea and Scheldt estuary. Mar. Chem. 75: 229–248, 2001

/LEG 04/ Legarth, B., Tischner, T., Huenges, E.: Stimulating for Productivity: Hydraulic Proppant Fracturing Treatments in Rotliegend Sandstones. In: Huenges, E., Wolfgramm, M. [Hrsg.]: Sandsteine im In-situ-Geothermielabor Groß Schönebeck – Reservoir-Charakterisierung, Stimulation, Hydraulik und Nutzungskonzepte. Scientific Technical Report STR04/03. GeoForschungsZentrum Potsdam. Potsdam 2004. Erhältlich unter: http://www.gfz-potsdam.de/bib/zbstr.htm (Stand: 02/2008).

/LEI 89/ Leijnse, A., Glasbergen, P., Nijhoff-Pan, I., Sauter, F. J.: Calculation of groundwater flow and particle tracking for the Gorleben site with METROPOL. Report 728516001. National Institute of public health and environmental protection, Bilthoven, 1989.

/LEM 03/ Lemke, P.; Hilmer, H.; Meereismodelle. promet, Jahrgang 29, Nr. 1-4, Deutscher Wetterdienst, S. 90-97, 6/2003.

/LEV 00/ Leverington, D.W.; Mann, J.D.; Teller, J.T.: Changes in the Bathymetry and Volume of Glacial Lake Agassiz Between 11,000 and 9300 14C yr B.P. Quaternary Res. 54 (2), 174-181, 2000.

/LIV 88/ Livens, F.; Baxter, M.: Chemical association of artificial radionuclides in West Cumbrian soils. J. Environmental Radioactivity, 7, 75-86, 1988.

/LOH 00/ Lohmann, G.; Lorenz, S.: On the hydrological cycle under paleoclimatic conditions as derived from AGCM simulations. Journal of Geophysical Research 105, (D13), 17,417-17,436, 2000.

/LOU 04/ Loutre, M.F.; Paillard, D.; Vimeux, F.; Cortijo, E.: Does mean annual insolation have the potential to change the climate? Earth and Planetary Sci. Let. 221, 1-14, 2004.

/LOU 03/ Loutre, M.F.: Clues from MIS11 to predict the future climate – A modelling point of view. Earth and Planetary Science Letters, 212, 213-224, 2003.

/LOU 00/ Loutre, M.F.; Berger, A.: Future climate changes: Are we entering an exceptionally long interglacial?. Climatic Change 46, 61-90, 2000.

/LUD 02/ Ludwig, R. & Kösters, E.: Hydrogeologisches Modell Gorleben – Entwicklung bis zum paläohydrogeologischen Ansatz. Schriftenreihe der Deutschen Geologischen Gesellschaft. 24, 69-77, 2002.

/MAG 06/ Magill, J., Pfennig, G., Galy, J.: Karlsruher Nuklidkarte, 7. Auflage, 2006.

/MEY 01/ Meyer, M.; Harff, J.: Modellierung der Küstenentwicklung in der südwestlichen Ostsee. Projekt HA1834/5-1, Zwischenbericht 2001.

/MEY 94/ Meyer, K.-D. et al: Neuere Untersuchungen an Interglazialen in Niedersachsen. Geologisches Jahrbuch Reihe A, Heft 134, 9-69, Hannover 1994.

/MEY 07/ Meyer, K.D.; persönliche Mitteilung vom 21. August 2007.

/MOE 02/ Mölders, N.; Elbern, H.: Bodenfrost und Schneemetamorphose-Simulationen für die Baltex-Region mit einem komplexen Hydro-Thermodynamischen Bodenvegetationsschema. DEKLIM Kickoff Meeting 2002, S. 68-71.

/MUE 86/ Müller, H.: Altquartäre Sedimente im Deckgebirge des Salzstocks Gorleben. Z. dt. geol. Ges., No: 137, 85-95, Hannover 1986.

/MUE 93/ Müller, H.; Pröhl, G.: ECOSYS – A dynamic model for assessing radiological consequences of nuclear accidents. Health Physics, 64, 232-252, 1993.

/MUE 96/ Müller, M.: Handbuch ausgewählter Klimastationen. Universität Trier, Forschungsstelle Bodenerosion. Trier, 1996.

/MUR 07/ Munier-Lamy, C.; Deneux-Mustin, S.; Mustin, C.; Merlet, D.; Berthelin, J.; Leyval, C.: Selenium bioavailability and uptake as affected by four different plants in a loamy clay soil with particular attention to mycorrhizae inoculated rye-grass; J. Environm. Radioactivity 97, 148-158, 2007.

/NAE 07/ Näslund, J.O.: Climate Change and Its Potential Impact on Mechanical, Hydraulic and Chemical Conditions. In: Proceedings of the IGSC "Geosphere Stability" Workshop on the Stability and Buffering Capacity of the Geosphere for Long-term Isolation of Radioactive Waste: Application to Crystalline Rock. Manchester, 15.-17. November 2007.

/NEE 91/ Neemann, W.: Bestimmung des Bodenerodierbarkeitsfaktors für winderosionsgefährdete Böden Norddeutschlands – Ein Betrag zur Quantifizierung der Bodenverluste; Geologisches Jahrbuch, Reihe F, Heft 25, 1991.

/PAG 01/ /PAGES-International Geosphere-Biosphere Programme: Environmental Variabiliy and Climate Change. IGBP Science No.3, 2001.

/PAI 98/ Paillard, D.: The timing of Pleistocene glaciations from a simple multiple-state climate model. Nature 391, 378-381, 1998.

/PET 99/ Petit, J.R.; Jouzel, J.; Raynaud, D.; Barkov, N.I.; Barnola, J.M.; Basile, I.; Bender, M.; Chapellaz, J.; Davis, M.; Delaaygue,G.; Delmotte, M.; Kotlyakov, V.M.; Legrand, M.; Lipenkov, V.J.; Lorius, C.; Pépin, L.; Ritz, C.; Saltzmann, E.; Stievenand, M.: Climate and atmospheric history of the past 420 000 years from Vostok ice core, Antarctica. Nature, 399(6735), 429-436, 1999.

/PET 00/ Petoukhov, V., Ganopolski, A., Brovkin, V., Claussen, M., Eliseev, A., Kubatzki, C., Rahmstorf, S.: CLIMBER-2: A climate system model of intermediate complexity. Part I: Model description and performance for present climate. Clim. Dyn. 16, 1–17, 2000.

/PIN 05/ Pinedo, P.; Thorne, M.; Egan, M.; Calvez, M.; Kautsky, U.: Consideration of environmental change in performance assessment. J. Environmental Radioact. 84, 185-210, 2005.

/PRO 90/ Pröhl, G., Modellierung der Radionuklidausbreitung in Nahrungsketten nach Deposition von Strontium-90, Cäsium-137 und Jod-131 auf landwirtschaftlich genutzte Flächen; München-Neuherberg, GSF-Bericht 29/90, (1990).

/PRO 96/ Pröhl, G.; Hoffman, F.O.: “Radionuclide, interception and loss processes in vegetation, Modelling of radionuclide interception and loss processes in vegetation and of transfer in semi-natural ecosystems. IAEA-TECDOC-857, 9-47, Vienna 1996.

/PRO 96/ Pröhl, G.; Müller, H.: Radiation exposure from radionuclides in ground water: an uncertainty analysis for selected exposure scenarios. J. Environm. Biophysics, 35, 205-218, 1996.

/PRO 05/ Pröhl, G.; Olyslaegers, G.; Kanyar, B.; Pinedo, P.; Bergström, U.; Mobbs, S.; Eged, K.; Katona, T.; Simon, I.; Hallberg, U.B.; Chen, Q.; Kowe, R. and Zeevaert T.: Development and comparison of five site-specific biosphere models for safety assessment of radioactive waste disposal. J. Radiol. Prot. 25, 343-373, 2005.

/PRO 08/ Pröhl, G.: Interception of dry and wet deposited radionuclides by vegetation. Submitted to Journal Environmental Radioactivity, 2008.

/RAH 07/ Rahmstorf, S.; Schnellnhuber, H.J.: Der Klimawandel. Diagnose, Prognose, Therapie. 144 S., Verlag C.H. Beck, München 2007.

/RAH 02/ Rahmstorf, S.: Ocean circulation and climate during the past 120.000 years. Nature 419, 207-214, 9/2002.

/RAH 02b/ Rahmstorf, S.: Warum das Eiszeitklima Kapriolen schlug. Spektrum der Wissenschaft, Dossier: Klima, S. 48-49, 2002.

/RUD 01/ Ruddiman, W.F.: Earth´s climate: past and present. W. H. Freeman Publishers, 465 pp., 2001.

/RUE 76/ Rühberg, N.: Probleme der Zechsteinbewegung. Z. angew. Geol. 22 (9): 413-420, 1976

/SAN 05/ Santucci, P.; Kontic, B.; Coughtrey, P.; McKenny, C.; Smith, G.: Use of contaminated well water, example reference biospheres 1 and 2A. J. Environmental Radioact., 84, 151-170, 2005.

/SAN 08/ Sanzharova, N.; Shubina, O.; Vandenhove, H.; Olyslaeghers, G.; Fesenko, S.; Uchida, S.; Tagami, K.; Reed, E.;Velasco, H.; Ayub, J.;.Choi, Y.H; Shang, Z.R.: Agricultural ecosystems: root uptake. In: International Atomic Energy Agency: Radioecological models and parameters for radiological assessments, TECDOC, To be published. 2008.

/SCH 07a/ Schönwiese, D.: Untersuchungen eines Uranvorkommens in der Oberpfalz auf Eignung als Natürliches Analogon für das Verhalten radioaktiver Elemente im Fernfeld eines hypothetischen Endlagers. Braunschweiger Geowissenschaftliche Arbeiten. Braunschweig (Institut für Umweltgeologie, Technische Universität Braunschweig), 29: 146, 2007

/SCH 07b/ Schwalb, A.: Persönliche Mitteilung vom 21.08.2007.

/SCH 06/ Persönliche Mitteilung Prof. Dr. A. Schwalb, Prof. K.D. Meyer, TU Braunschweig, 2006.

/SCH 04/ Schwentker, B.: Verstaubte Klimamodelle, Wissenschaftsteil der Frankfurter Allgemeinen Zeitung am 15.08.2004.

/SCH 03/ Schneider, R.; Lohmann, G.: Das Klima der letzten 11.000 Jahre. Klimastatusbericht, 35-54, 2003.

/SCH 02/ SCHULTZ, J.: Die Ökozonen der Erde. 3. Auflage. 320 S., Ulmer UTB 1514, Stuttgart 2002.

/SCH 02/ Scheffer, F.; Schachtschabel, P.: Lehrbuch der Bodenkunde. Ferdinand Enke Verlag 2002.

/SCH 77/ Schönherr, J.: Plant cuticles are polyelectrolytes with isoelectric points around three. Plant Physiol. 59, 145-150, 1977.

/SCH 74/ Schwarzbach, M.: Das Klima der Vorzeit - Eine Einführung in die Paläoklimatologie. 3. Auflage Stuttgart Enke Verlag 1974.

/SCO 07/ Scott Van Pelt, R.; Zobeck, T.M.; Ritchie, J.C.; Gill, T.: Validating the use of 137Cs to estimate rates of soil redistribution by wind. CATENA, 70, 455-464, 2007.

/SCO 05/ © Paleontology Science Center in http://www2.tu-berlin.de/~kehl/project/lv-twk/002-eiszeiten.htm, date of access: 2005.

/SEI 03/ Seiler, W.: Der globale Klimawandel: Ursachen, Wirkungen und Maßnahmen. Institut für Meteorologie und Klimaforschung (IMK-IFU), Forschungszentrum Karlsruhe, Vortrag vom 08.10.2003 im Geiger-Haus, Oberstdorf.

/SEI 86/ Seinfeld, J.: Atmospheric chemistry and physics of air pollution; John Wiley & Sons, New York, 1986.

/SHE 06a/ Sheppard, S.C.; Ciffroy, P.; Siclet, F.; Damois, C.; Sheppard, M.I.; Stephenson, M.: Conceptual approaches for the development of dynamic specific activity models of 14C transfer from surface water to humans, J. Environmental Radioactivity, 87, 32-51, 2006.

/SHE 06b/ Sheppard, S.C.; Sheppard, M.I.; Siclet, F.: Parameterization of a dynamic specific activity model of 14C transfer from surface water-to-humans. J. Environmental Radioactivity, 87, 15-31, 2006.

/SIR 02/ Sirocko, F.; Böttger, F.; Böttger, T.; Claussen, M.: Verbund: Klimaänderungen am Ende einer Warmzeit (EEM), DEKLIM Kickoff Meeting 2002, S. 36-39.

/STR 07/ Streif, H.: Das Quartär in Niedersachsen und benachbarten Gebieten - Gliederung, geologische Prozesse, Ablagerungen und Landschaftsformen. Mit Beiträgen von Caspers, G., Freund, H., Geyh, M. A., Kleinmann, A., Merkt, J., Meyer, K.-D., Müller, H., Rohde, P, Schwarz, C. Aktualisiert nach LITT et al. (2005, 2007), 2007. http://cdl.niedersachsen.de/blob/images/C38300508_L20.pdf date of access: 2008

/SUT 98/ Suter, D., Biehler, D., Blaser, P., Hollmann, A.: Derivation of a sorption data set fort he Gorleben overburden. Proceedings DisTec ,98, International Conference on Radioactive Waste Disposal, Hamurg. 581- 584, 1998.

/TEL 02/ Teller, J. T., Leverington, D. W., Mann, J. D.: Freshwater outbursts to the ocean from Lake Agassiz and their role in climate change during the last deglaciation. Quat. Sci. Rev. 21: 879-887, 2002

/TEX 03/ Texier, D.; Degnan, P.; Loutre, M.F.; Paillard, D.; Thorne, M.: Modelling Sequential BIOsphere systems under CLIMate change for radioactive waste disposal. Proceedings of the International High-Level Waste Management Conference (March30-April 2, 2003), Projekt BIOCLIM, Las Vegas, USA.

/THE 74/ Thenius, E.: Eiszeiten - einst und jetzt Ursachen und Wirkungen. Kosmos Bibliothek, Franck'sche Verlagsbuchhandlung, 1974.

/THO 02/ Thompson, L. et al: Kilimanjaro Ice Core Records : Evidence of Holocene Climate Change in Tropical Africa. Science 298, S. 589-593, 2002.

/THO 03/ Thompson, L. et al: Tropical Glacier and Ice Core Evidence of Climate Change on Annual to Millennial Time Scales. Climatic Change 59, S. 137-155, 2003.

/TRA 02/ Travnikova, I.: Assessment of current exposure levels in different population groups of the Kola Peninsula. J. Environmental Radioactivity, 60, 235-248, 2002.

/TRO 91/ Troen & Erik Lundtang Petersen: European Wind Atlas. Risoe National Laboratory, Risoe, Denmark, ISBN 87-550-1482-8, 1991.

/UNS 88/ UNSCEAR (United Scientific Committee on the Effects of Atomic Radiation): Sources and effects of ionizing radiation. Report to the General Assembly 1988; United Nations, New York, 1993.

/VET 04/ Vettoretti G.; Peltier, W.R.: Orbital insolation and carbon dioxide concentration effects on the process of glacial inception. Quat. Sci. Rev. 23, 499-519, 2004.

/VID 08/ Vidal, M.; Rigol, A.; Gil-García, C.J.: Agricultural ecosystems: radionuclide mobility in soil. In: International Atomic Energy Agency: Radioecological models and parameters for radiological assessments. TECDOC, to be published. 2008.

/VOG 91/ Vogel, P., Schelkes, K., Giesel, W.: Modellrechnungen zur Grundwasserbewegung mit variabler Dichte für einen Aquifer über einem Salzstock – Dokumentation erster Ergebnisse. Bundesanstalt für Geowissenschaften und Rohstoffe (BGR), Hannover 1991.

/VOI 91/ Voigt, G.; Müller, H.; Pröhl, G.: Experiments on the seasonality of the cesium translocation in cereals, potatoes and vegetables. Radiat. Environm. Biophysics, 30, 295-303, 1991.

/VUW 08/ http://koeppen-geiger.vu-wien.ac.at/, date of access: 2008.

/WAL 92/ Walter, R.: Geologie von Mitteleuropa, Schweizerbart'sche Verlagsbuch-handlung, 1992.

/WIK 08/ http://de.wikipedia.org/wiki/Drawehn, date of access: 2008.

/WOL 09/ Wolf, J., Rübel, A., Noseck, U., Becker, D.: Safety and performance indicators for repositories in salt and clay formations. GRS-240. Braunschweig (Gesellschaft für Anlagen- und Reaktorsicherheit (mbH)), 104, 2009

/ZIR 91/ Zirngast, M. (1991): Die Entwicklung des Salzstocks Gorleben - Ergebnis einer strukturgeologischen Bearbeitung. Geologisches Jahrbuch Reihe A, Band A 132.

/ZOB 00/ Zobeck, T.M.; Parker, N.C.; Haskell, S.; Guoding, K.: Scaling up from field to region for wind erosion prediction using a field scale wind erosion model and GIS, Agriculture. Ecosystem and Environment, 82, 247-259, 2000.

List of Figures

List of Tables

Gesellschaft für Anlagen- und Reaktorsicherheit (GRS) mbH

Schwertnergasse 1
50667 Köln
Telefon +49 221 2068-0
Telefax +49 221 2068-888

Forschungsinstitute
85748 Garching b. München
Telefon +49 89 32004-0
Telefax +49 89 32004-300

Kurfürstendamm 200
10719 Berlin
Telefon +49 30 88589-0
Telefax +49 30 88589-111

Theodor-Heuss-Straße 4
38122 Braunschweig
Telefon +49 531 8012-0
Telefax +49 531 8012-200

www.grs.de

ISBN 978-3-939355-15-1